Spring 2011

Development of engineering tools to analyze and design flexible structures in open ocean environments

Judson Decew
University of New Hampshire, Durham

DEVELOPMENT OF ENGINEERING TOOLS TO ANALYZE AND DESIGN FLEXIBLE STRUCTURES IN OPEN OCEAN ENVIRONMENTS

BY

JUDSON DECEW

B.S., University of New Hampshire, 1999
M.S., University of New Hampshire, 2002

DISSERTATION

Submitted to the University of New Hampshire
in partial fulfillment of the requirements
for the degree of

Doctor of Philosophy

in

Ocean Engineering

May 2011

This Dissertation has been examined and approved.

Dissertation Co-Director, Igor Tsukrov
Professor of Mechanical and Ocean Engineering

Dissertation Co-Director, Barbaros Celikkol
Professor of Mechanical and Ocean Engineering

Kenneth Baldwin
Professor of Ocean Engineering

David Fredriksson
Associate Professor of Ocean Engineering,
U.S. Naval Academy

M. Robinson Swift
Professor of Mechanical and Ocean Engineering

Yannis Korkolis
Assistant Professor of Mechanical Engineering

7/18/2011
Date

DEDICATION

To Oliver and Rowan

ACKNOWLEDGMENTS

The research presented in this dissertation spanned numerous funded and unfunded projects. Funding for the initial high density polyethylene material and finite element modeling of the near shore net pens was provided, in part, through a Saltonstall-Kennedy grant (number NA03NMF4270183) to the University of New Hampshire. Upgrades to the Aqua-FE software and field experiments were funded, in part, by NOAA grant no. NA040AR4600155 to the University of New Hampshire (UNH) Cooperative Institute for New England Mariculture and Fisheries (CINEMAR). The Ocean Cage Aquaculture Technology research was supported by the American Soybean Association International Marketing (ASAIM) and the U.S. Soybean Export Council (USSEC). Funding for the submerged grid mooring design, analysis and deployment was provided by the NOAA grant #NA16RP1718 to CINEMAR.

The guidance from my supervisory committee, professors Igor Tsukrov, Barbaros Celikkol, Ken Baldwin, M. Robinson Swift and Yannis Korkolis of the University of New Hampshire and David Fredriksson of the U.S. Naval Academy, on the modeling approach, material testing and field experiments is highly appreciated. I would also like to thank fellow graduate students Andrew Drach and Graham Cullen for their help with the Instron machine set-up and testing. Paul Lavoie, thank you for all your help in the machine shop, especially for setting up the mill on multiple occasions and developing a jig to ease my time "making chips." Thank you to those graduate students who graduated before me, but were never the less influential in my success: Glen Rice, Glen McGillicuddy, and Chad Turmelle to name a few. I would also like to thank those who supplied HDPE pipe specimens taken from previously used fish cages from aquaculture farms around the world: Oystein Patursson of Fiskaaling, Faeroe Islands, Jeff King of Marine Harvest, British Columbia, Canada, and Joe Santamaria of Bristol, NH.

Finally, I want to thank my family for their support and patience throughout this research, specifically my wife, Mandy, who, on occasion, took up additional house responsibilities on those long nights in the laboratory.

TABLE OF CONTENTS

DEDICATION iii

ACKNOWLEDGMENTS iv

LIST OF TABLES viii

LIST OF FIGURES x

ABSTRACT xvii

1. INTRODUCTION 1

2. ADVANCEMENTS IN NUMERICAL MODELING 8

2.1 Previous Technical Work 9

2.1.1 Numerical Modeling of Flexible Structures 9

2.1.2 Hydrodynamic Fluid-Structure Interaction 14

2.2 Numerical Model Enhancement. Incorporation of Spherical Element 16

2.2.1 Drag Forces on Spherical Element 16

2.2.2 Validation for Buoyancy and Node Assignment Scheme 20

2.2.3 Comparison of Truss and Sphere Elements. Behavior under Currents and Waves 26

2.3 Numerical Model Enhancement. Implementation of Hydrodynamic Effects 31

2.3.1 Wave Theory 32

2.3.2 Evaluation of Performance of Subroutine 36

2.4 Numerical Model Enhancement. Implementation of Shadowing Effects 39

2.5 Numerical Model Enhancement. Transition from Subcritical to Critical Reynolds Numbers 41

2.5.1 Drag Forces on Cylindrical Elements 42

2.5.2 Validation of Drag Forces 44

2.5.3 Coefficient of Drag Sensitivity Study 46

3. CASE STUDY. FIELD TESTS AND NUMERICAL MODELING OF A SPHERICAL FISH CAGE SYSTEM 52

3.1 Marine Fish Cage System 53

3.2 Instruments and Calibration 54

3.3 Preparation and Set-up 56

3.4 Towing of the Cage 59
3.5 Results of Tow Test 61
3.6 Tow Test Discussion 64
3.7 Numerical Model Comparison 65
4. CASE STUDY. DYNAMICS OF SINGLE POINT MOORED FISH CAGE 70
4.1 Introduction to Single Point Moorings 70
4.2 Description of the Small-Volume Ocean Cage Aquaculture Technology System 72
4.3 Physical Model and Experimental Setup 74
4.4 Fish Cage and Mooring Numerical Model 77
4.5 Load Cases 80
4.6 Validation of Numerical Model 81
4.7 Numerical Model Results and Discussion 83
4.8 Conclusions 87
5. DEVELOPMENT OF STRUCTURAL MODELING TECHNIQUES 88
5.1 Previous Technical Work: Structural Modeling in Marine Aquaculture 89
5.2 Aquaculture in Broad Cove, Maine 91
5.3 Finite Element Procedure and Material Modeling 95
5.4 Finite Element Analysis of HDPE Pipes 98
5.5 Circular Ring Experiments 100
5.6 Boundary Conditions and Geometric and Material Properties 106
5.7 Broad Cove Farm Case Study 110
5.8 Structural Modeling Results 113
5.9 Estimated Maximum Load 116
5.10 Conclusions 121
6. MECHANICAL BEHAVIOR OF HDPE IN MARINE APPLICATIONS 123
6.1 Previous HDPE Research 124
6.2 Evaluation of Strain Rates in HDPE Cage Frames 125
6.2.1 Aqua-FE Mesh 126
6.2.2 Dynamic Modeling Results 133
6.2.3 Structural Modeling of the Cage Frame 134

6.3 Experimental Program 140
6.3.1 HDPE Specimens 141
6.3.2 Experimental Procedure 143
6.3.3 Data Processing 147
6.3.4 Results 148
6.4 Discussion 159
7. DESIGN CONSIDERATIONS AND PRACTICAL APPLICATIONS OF FLEXIBLE STRUCTURES IN MARINE ENVIRONMENTS 161
7.1 Design Criteria 162
7.2 Engineering Analysis 167
7.4 Results 170
7.4.1 System Hydrostatics 170
7.4.2 Dynamic Simulations 171
7.5 Component Specification and Deployment 173
7.6 Research Activities and Environmental Conditions at the Submerged Mooring 181
7.7 Mooring Recovery and Inspection 186
7.8 Review of the System 190
8. RESEARCH CONCLUSIONS 192
LIST OF REFERENCES 195
APPENDIX A: MODIFIED AQUA-FE SUBROUTINES A1
FINITE ELEMENT ANALYSIS PROGRAM (FEAP) A1
OPT File Description A2
Aqua-FE Code Modifications A3
MACRO - FDAT A3
MACRO - WETTEST A10
MACRO - SURFELEV A12
MACRO - AVCURR A12
MACRO - UPDCD A15

LIST OF TABLES

Table 2.1: The geometric and material properties of the spherical element mode assignment verification model. 22
Table 2.2: The geometric and material properties of the spherical element buoyancy verification model. 25
Table 2.3: The truss and spherical element dynamic behavior models geometric and material properties. The effective density is defined as the mass divided by the volume enclosed by the outside surface. 27
Table 2.4: The output model tension results from the sphere and cylindrical float behavior response investigation. 28
Table 2.5: Analytical calculations compared to the Aqua-FE output result for wave properties associated with Stokes 2nd order wave. 37
Table 2.6: The truss and spherical element dynamic behavior model's geometric and material properties. 38
Table 2.7: Geometric and material properties of the model. 45
Table 2.8: Aqua-FE output and analytical calculations verifying the Aqua-FE output values. 46
Table 2.9: The geometric and material properties of the buoy and mooring analyzed in this sensitivity study. 47
Table 2.10: The geometric and material properties of the SeaStation^{TM} fish cages analyzed in the sensitivity study. 48
Table 2.11: Summarized output mooring tension results of the simulations. 51
Table 3.1: Comparison test results between the Marsh-McBirney and Aquadopp current meters. 56
Table 3.2: Water velocities measured by Marsh-McBirney and Aquadopp current meters during the first six minutes of the experiment. 64
Table 3.3: The fish cage and tow line properties utilized in Aqua-FE. 66
Table 3.4: Comparing the average drag force with the predicted numerical model. 68
Table 4.1: The cage and mooring full and model scale components. 75
Table 4.2: Net pen solidities utilized in the numerical model submergence study. 80
Table 4.3: Current velocity input parameters for physical scaled model testing. 81
Table 5.1: Young's Modulus values obtained during tensile testing using weathered HDPE samples. 98
Table 5.2: Geometric and material properties of HDPE pipe used in the FEM calculations for the weathered ring experiments. 103
Table 5.3: The geometric and material properties of the net pen flotation structure FEM. 107
Table 5.4: The current velocity measurements obtained from the current meter located outside of the farm for two selected load cases. 111

Table 5.5: The average and maximum load cell results from each of the Y-line attachments....113
Table 5.6: The Von Mises Stress calculated using the structural model for each load case and boundary condition.....113
Table 5.7: The estimated failure loads for the three attachment locations.....117
Table 6.1:Geometric and material properties of a standard gravity net pen.....127
Table 6.2: Geometric and material properties of the cage system used in the sensitivity study. 128
Table 6.3: Geometric and material properties of the mooring system used in the sensitivity study.....129
Table 6.4: The net properties utilized in the Aqua-FE sensitivity study.....131
Table 6.5: The environmental conditions, bridle line materials and net chamber solidities analyzed in the sensitivity study. 132
Table 6.6 : The output parameters for the forcing equation required for the structural analysis. 134
Table 6.7: The geometric and material properties of the net pen flotation structure FEM.....135
Table 6.8 : The predicted strain rate, as defined by equation 6.4, from the structural analysis. The maximum and minimum values are highlighted.....140
Table 6.9: The geometric properties, origin and deployment history for the acquired pipe specimens.....142
Table 6.10 : The displacement rates utilized for the material testing. 144
Table 6.11: The sampling rates of the instruments utilized in the tension testing.....146
Table 6.12: The subset and step parameter values examined in the DIC sensitivity study.....150
Table 6.13: The Young's Modulus results of specimen obtained from PIPE A1. 154
Table 6.14: The Young's Modulus results of specimen obtained from PIPE A2. 155
Table 6.15: The Young's Modulus results of specimen obtained from PIPE B.....155
Table 6.16: The Young's Modulus results of specimen obtained from PIPE C.....155
Table 6.17: The Young's Modulus results of specimen obtained from PIPE D. 156
Table 6.18: The Young's Modulus results of specimen obtained from PIPE N (new, unused). ...156
Table 6.19: Tensile Strength at Yielding for specimens obtained from PIPE A1.....157
Table 6.20: Tensile Strength at Yielding for specimens obtained from PIPE A2.....157
Table 6.21: Tensile Strength at Yielding for specimens obtained from PIPE B. 157
Table 6.22: Tensile Strength at Yielding for specimens obtained from PIPE C. 158
Table 6.23: Tensile Strength at Yielding for specimens obtained from PIPE D.....158
Table 6.24: Tensile Strength at Yielding for specimens obtained from PIPE N (New, unused). ..158
Table 7.1: Pre-determined design values utilized in the catenary analysis. These parameters were established due to geometric constraints (for example, permit area), availability of equipment and past experience. 169
Table 7.2: Analytical and Numerically modeling static load results.....171
Table 7.3: The mooring system particulars.....177

LIST OF FIGURES

Figure 1.1: The University of New Hampshire's submerged grid mooring with 4 fish cages. The bays of the mooring are suspended 18 meters below the surface and provide a platform for investigating various structures. The SeaStation™ fish cage has a steel central spar and octagonal rim. The net is tensioned between these components, forming a rigid structure. Ballast is suspended below the net pen to provide a restoring force to the net pen. Additional information on the grid mooring can be found in Chapter 7 2
Figure 1.2: A single point moored Ocean Cage Aquaculture Technology (OCAT) fish cage is shown on left. On right: The OCAT is presented without the net chamber for clarity. 2
Figure 1.3: A typical gravity fish cage. The net pen consists of an HDPE superstructure supporting a flexible net and a weighted lower rim. 3
Figure 2.1: Relative fluid velocity components acting on a cylindrical element. The n and t subscripts represent the normal and tangential directions, respectively. 11
Figure 2.2: Dependence of drag coefficient of a sphere on Reynolds Number. Obtained from Donley, 1991. 18
Figure 2.3: A schematic of the change of the drag force in the critical range of Reynolds numbers. Adopted from "Hydrodynamics around cylinder structures" by M. Sumar and J. Fredsoe. 19
Figure 2.4: Drag coefficients for a sphere. The experimental values are compared to equation (2.10). Experimental values were obtained from Hoerner (1965) and numerical approximation by DeCew et al., 2010 20
Figure 2.5: The spherical element consists of two nodes: the active node where the mass and characteristics are applied, and the connecting node. 21
Figure 2.6: A sphere was placed in line of a rope and analyzed under a constant with depth water velocity (top). The cases were investigated where the sphere's active node was moved and the underlying elements connectivity reversed. 23
Figure 2.7: The output tension results from the elements. The tension values are shown above the FEA mesh 24
Figure 2.8: A buoyant spherical float placed at the end of a line (left) was modeled in Aqua-FE (right). Note that the buoy and stiffener elements overlay each other in the Aqua-FE model 25
Figure 2.9: The output line tension results. The transient and steady state tension regions are also shown 26
Figure 2.10: The truss and spherical floats were modeled using similar mooring lines in Aqua-FE. The deformed geometry is shown for the 1 m/s water velocity as an example. 27
Figure 2.11: The models constructed in Aqua-FE to analyze the spherical and cylindrical floats response in waves. 29

Figure 2.12: Element tension results of the model under 1 meter, 5.64 second waves. The full time series is shown on left, a 20 second section of the data is presented on right. 30
Figure 2.13: Element tension results of the model under an irregular wave field having a significant wave height of 1 meter, and dominate period of 5.64 second waves. The full time series is shown on left, a 40 second section of data on right. 30
Figure 2.14: The Stokes 2nd order wave surface elevation (top), vertical water particle velocity (bottom left) and acceleration (bottom right) compared Airy waves. The waves had the following properties: T = 5 seconds, H = 3.654 meters, h = 10 meters, L = 36.54 meters, H/L = 1/10. 36
Figure 2.15: The surface wave elevation and Aqua-Fe model position. 38
Figure 2.16: Coefficient of Drag versus Reynolds for a smooth circular cylinder. Choo and Casarella approximations work well at Re number below 3 $x10^5$, however neglect the reduction in coefficient of drag in critical flow regions. 42
Figure 2.17: Normal drag coefficients for a cylinder. The experimental values are compared to the Choo and Casarella approximation and equation (2.29). 44
Figure 2.18: Aqua-FE model of cylindrical truss element generated to verify the drag predictions of the software 45
Figure 2.19: The offshore site boundary marker analyzed in this sensitivity study 47
Figure 2.20: FEA models of two SeaStation™ fish cages were constructed in Aqua-FE. One had a net chamber (lower right), where the second one only had the rims and tensioned stays (upper left). 49
Figure 2.21: The site marker mooring tension and buoy tilt angle under the 1 m/s water velocity. The system was analyzed with the original and updated software. 49
Figure 2.22: The fish cage drag force results under the 1 m/s water velocity. The cage with a net chamber (on left) and without (on right) was analyzed with the original and updated Aqua-FE software. 50
Figure 2.23: The site marker mooring tension and buoy tilt angle under the 2 m/s water velocity. The system was analyzed with the original and updated software. 50
Figure 2.24: The fish cage drag force results under the 2 m/s water velocity. The cage with a net chamber (on left) and without (on right) was analyzed with the original and updated Aqua-FE software. 50
Figure 3.1: The open ocean aquaculture site is located off the coast of New Hampshire, USA in the southwest corner of the Gulf of Maine (Figure downloaded from http://spo.nos.noaa.gov and annotated) 53
Figure 3.2: The 9.75 meter Aquapod™ fish cage. 54
Figure 3.3: View of the Marsh-McBirney current meter and support. 57
Figure 3.4: The load cell and tow line components. 58
Figure 3.5: The A/D and vi utilized during the tow test. The power cables for the instruments ran to the A/D board, which was powered by the power supply. The data was then sent to the computer for viewing and analysis. 58

Figure 3.6: The Aquadopp current meter placed in the Aquapod™ cage (left) and orientation of the device to the tow direction (right).....59
Figure 3.7: The cage was deployed from the NH Port Authority and towed out to the UNH Open Ocean Aquaculture Farm site with the R/V Meriel B.....60
Figure 3.8: Water velocity and load cell readings during the experiment.....61
Figure 3.9: A subset of load cell tension measurements and wave characteristics present of the day of the tow. The tow test was initiated at 16:00 EST.....62
Figure 3.10: The GOMOOS buoy was located at 70° 25'40'' W, 43° 10'51'' N, approximately 22 km to the Northeast of the tow test site. 62
Figure 3.11: The measured water velocity reduction and tow line tension. 63
Figure 3.12: The field test set-up was recreated in Aqua-FE. The cage in the dotted box is zoomed in above.....66
Figure 3.13: The full ambient water velocity was applied to the front half of the cage system. The water velocities measured inside the cage were applied to the aft portions of the model.....67
Figure 4.1: (a) The OCAT truncated pyramid cage frame constructed with HDPE pipes. Ballast hangs below the system providing additional stability to the system. (b) The single point mooring secured with a deadweight anchor, mooring chain, surface float and two pairs of bridle lines. 73
Figure 4.2: 1:10 Froude scale model of the OCAT cage 74
Figure 4.3: The experimental setup for physical scaled model current testing. Note that bridle lines (left) were digitally enhanced for viewing purposes. 77
Figure 4.4: Finite element model of the cage and bridle line components.....78
Figure 4.5: Finite element model of the full OCAT cage and single point mooring system. The cage and bridle line components are similar to those shown in Figure 6. The tensions within four elements were recorded to provide mooring component tension. 79
Figure 4.6: Comparison between full scale numerical and (recalculated to full scale) physical model predictions of the drag on the OCAT cage system.....82
Figure 4.7: Submergence depth of the OCAT system for various netting solidities and water velocities. Note that the 9%, 10%, 12%, 16% with velocity gradient, 18% and 21% solidities were only examined at 1.5 m/s.....85
Figure 4.8: Submerged configurations of the OCAT system at 1.5 m/s currents.....85
Figure 4.9: Variation of the mooring chain tension with water velocity for different net solidities. 86
Figure 5.1: Two failed cage rims, resulting in a loss of structural integrity. The rims were constructed of standard HDPE material and deployed in near-shore farms.....89
Figure 5.2: Three element types representing the same length of pipe. (a) 2 node line element, (b) 2D shell elements, and (c) 3D brick elements. 90
Figure 5.3: The farm was located in Broad Cove, Eastport, Maine.....92

Figure 5.4: The fish farm consisted of 20 net pans each with an approximate diameter of 31.8 m. Instrumentation was deployed in the southwest portion of the farm. Load cells were installed on the SW anchor and bridle lines. 93
Figure 5.5: The cage frame and brackets are shown (with a attached bridle line load cell recorder)....94
Figure 5.6: Samples of HDPE pipe were placed in an Instron tensile testing device. 97
Figure 5.7: Stress strain data results when loaded at 0.0127mm/s, 0.127 mm/s and 1.27 mm/s. 97
Figure 5.8: The four-node shell element with 6 degrees of freedom per node. 99
Figure 5.9: Approximation of polymer material behavior by linearly elastic – perfectly plastic curve....100
Figure 5.10: Experimental test set-up of the circular ring experiments. 101
Figure 5.11: The tensioning connection point with a localized failure observed. 102
Figure 5.12: The results of the circular ring experiment. The force and associated circular ring diameter are shown. The diametric deflection was measured with a tape measure between the load application point and midpoint between the supporting bridles. 102
Figure 5.13: Using the values in Table 5.2, FEM calculations were performed to simulate the weathered ring experiments. Note that the ropes pull inward, present in the laboratory experiment, was not replicated in the FEM. The displacement, in meters, in the horizontal position (Y) is shown along the deformed geometry (right). 104
Figure 5.14: A visual comparison between the kinking and localized failure of the circular ring. Note that the yield stress of HDPE is 2.417×10^7 Pa. 105
Figure 5.15: The load versus percentage of pipe circumference element failure. The progression of stress contours using the localized failure technique is also shown. 106
Figure 5.16: An FEM model of a portion of the surface rings used in a net pen. 108
Figure 5.17: The first load case: the drag was assumed to be evenly distributed over "major arc" the inner and outer rims. The two additional bridle line supports (would be present in the "minor arc" of the cage frame), were not taken into consideration for this analysis. 109
Figure 5.18: The tensions in the mooring line are represented by point loads applied to ½ the pipe circumference and evenly distributed on the inner and outer rims. The two additional bridle line supports (would be present in the "minor arc" of the cage frame), were not taken into consideration for this analysis....110
Figure 5.19: The load cell data sets from 5-may-2004 at 1400 UTC. 112
Figure 5.20: The tensions in the y-lines measured on 16-may-2004 at 2200 UTC. 112
Figure 5.21: Von Mises Stresses in the net pen structure using environmental loading data of 5-may 2004 at 1200 with the 1st load case boundary conditions. The maximum stress occurred on the inside rim in the middle of the distributed loads as seen in Figure 5.18....114

Figure 5.22: Von Mises Stresses in the net pen structure using environmental loading data of 5-may 2004 at 1200 with the 2nd load case boundary conditions. The maximum stress occurred at the SW y-line load application point (maximum y-line tension).....115
Figure 5.23: Von Mises Stresses in the net pen structure using environmental loading data of 16-may 2004 at 2200 with the 1st load case boundary conditions. The maximum stress occurred on the inside rim in the middle of the distributed loads as seen in Figure 5.18.....115
Figure 5.24: Von Mises Stresses in the net pen structure using environmental loading data of 16-may 2004 at 2200 with the 2nd load case boundary conditions. The maximum stress occurred at the SE y-line load application point (maximum y-line tension). 116
Figure 5.25: The attachment configurations were modeled where the net pen was secured with one (a), two (b) and four (c) point locations. 117
Figure 5.26: The von mises stress distribution on the net pen rim when 53 kN is applied as a distributed load. 118
Figure 5.27: The von mises stress distribution on the net pen rim when one full y-line (shown superimposed above the results) is utilized.....119
Figure 5.28: The von mises stress distribution on the net pen rim when two, symmetrical y-lines (shown superimposed above the results) are utilized. 119
Figure 5.29: The stress distribution on the cage frame when y-lines are moved such they are not longer equally spaced around the cage circumference. 120
Figure 6.1: A standard circular gravity fish cage. Two main flotation pipes are connected by brackets, forming the upper superstructure.....126
Figure 6.2: The Aqua-FE cage-grid mooring system model. A gravity fish cage was placed in a submerged grid, 18 meters below the surface in 45 meters of water. The lower ends of the anchor chain were fixed points. 128
Figure 6.3: Wave direction was aligned with one sole anchor leg in each simulation. 130
Figure 6.4: The output bridle line tension results with 2 net solidities under two regular wave regimes. The 8% solidity net chamber in 4 second, 1.66 meter waves (left) and 24% solidity in 12 second, 13.5 meter waves (right).....133
Figure 6.5: The FEM constructed in MSC.MARC/Mentat. The full rim is shown on left, a portion of the mesh on right.....136
Figure 6.6: The boundary conditions applied to the FEM.....137
Figure 6.7: Strain in the material was monitored in four nodal positions along the cage frame. 138
Figure 6.8: The output strain results from the structural analysis of the thin wall pipe under forcing described by equation 6.2.....138
Figure 6.9: The output strain results from the structural analysis of the thin wall pipe under forcing described by equation 6.3.....139
Figure 6.10: Twenty specimens were fabricated from each pipe segment. The samples were 101.6 mm long, 12.7 mm wide and 3.8 mm thick. The testing gage length, L_o, was 9.5 mm.....143

Figure 6.11: The test set-up of the experiments performed on the Instron tensile testing machine. The force straining the HDPE specimen was recorded from the load cell. The specimens strain was calculated from the Instron cross head movement and DIC measurements 146
Figure 6.12: The specimens were speckled in contrasting paint for DIC measurement....147
Figure 6.13: The linear portion of the stress-strain curve was utilized to calculate the Young's Modulus, E....147
Figure 6.14: The tensile strength at yielding, σ_y, was obtained for each specimen. 148
Figure 6.15: An undeformed and deformed specimen tested subjected to uniaxial tensile loading. 149
Figure 6.16: Sensitivity test results comparing the strain in a sample from the unused pipe at displacement rate 1, 9.525 x 10^{-1} mms^{-1} for the 6 load cases. Left: The total specimen strain. Top Right: The strain in the linear elastic region of the specimen. Bottom Right: The strain at the yield stress. 151
Figure 6.17: The axial strain distribution of the specimen under load. From left to right: The unloaded, undeformed specimen; and strain distribution during the linearly elastic deformation. 152
Figure 6.18: The stress-strain curves for a specimen obtained from pipe sample 2 under displacement rate 2. The curves were obtained using the calculated crosshead and DIC measured strains. 153
Figure 6.19: The stress-strain curve obtained from tensile testing of HDPE specimen 1 of Pipe A1. 154
Figure 7.1: The SS600 and SS3000 cages each consist of a central spar and rim held together with tensioned stays. The spar on the SS600 has a length of 9 meters, while the spar on the SS3000 is about 15 meters. The nominal rim diameter of the SS600 is 15 meters, while on the SS3000 it is 25 meters. Each cage incorporates a ballast weight suspended with a pendent line from the spar weighing 19 and 53 kN (dry) for the SS600 and the SS3000 cages, respectively. 164
Figure 7.2: An isometric view of the submerged 4-cage grid system. 166
Figure 7.3: A top view of the submerged grid mooring system. It consisted of 8 corner anchor legs, 4 side anchor legs, 1 center anchor line, 12 grid lines, and 16 bridle lines. The anchors on the north and east sides are numbered for load identification. 166
Figure 7.4: Anchor leg definition schematic. Note that the float assembly consists of the float, a length of chain and the rope ring corner connections (not shown). 167
Figure 7.5: Selected mooring line load results using one of the UNH design conditions. Anchors are identified in Figure 7.3. 172
Figure 7.6: The maximum load distribution in the mooring using one of the UNH design conditions. The current and waves are applied from the northeast direction. 172
Figure 7.7: Component details of the side grid mooring assembly. Some items are not to drawn to scale. 174

Figure 7.8: Component details of the corner grid mooring assembly. Some items are not to drawn to scale. 175
Figure 7.9: Component details of the center grid mooring assembly. Some items are not to drawn to scale. The center node is held down by a 1800 kg steel deadweight. 175
Figure 7.10: Component details of the crown line assembly. Some items are not to drawn to scale....176
Figure 7.11: The F/V Nobska, operated by Stommel Fisheries, deployed the four-grid mooring. 178
Figure 7.12: The gear was faked on the deck and streamed behind the deployment vessel....179
Figure 7.13: The grid lines can be seen organized on the water surface....179
Figure 7.14: The mooring corner and anchor locations depicted on the UNH site bathymetry. The solid black diamonds represent the designed location of the anchors. The pink are the deployed locations as measured from the vessel GPS. The numbers are the distances between the deployed and designed positions. During deployment, it became apparent from the indicator floats that the designed anchor locations were not sufficient to get the grid to the designed depth. As a result, the anchors out further than designed....180
Figure 7.15: Cage systems deployed at the site include the SeaStation™ (top left), Aquapod™ (top right), OCAT (lower left), and the JPS prototype (lower right)....181
Figure 7.16: Feeding buoys deployed within or coupled to the grid: (a) 1/4 ton feed capacity, (b) 1 ton feed capacity or (c) 20 ton feed capacity....182
Figure 7.17: Several of the fish species grown at the site include Atlantic halibut (top left), Atlantic cod (top right), Haddock (lower left), and Steelhead Trout (lower right). 183
Figure 7.18: The environmental monitoring buoy deployed at the offshore site. 184
Figure 7.19: Typical winter storm waves in 2005-2006 with significant wave heights of 4 to 6 m. 185
Figure 7.20: The April 2007, 9 meter, 12 second storm event at the UNH offshore site. 185
Figure 7.21: The observed currents at the UNH site over one year. 186
Figure 7.22: Two anchors recovered from the mooring. Some of the anchors were in excellent shape, with paint present on the flukes and little material loss (a), whereas others had some material loss at the edges of the flukes (b)....187
Figure 7.23: The grid lines were found to have some wear around the thimbles, near the rope rings. The lines must have come in contact with the rope rings, fraying the line over the seven year deployment. 188
Figure 7.24: The center connection rope ring and shackles. The rope rings and shackles were found to be in good shape, with minimal wear. 189
Figure 7.25: The connections on the floats were found to be in excellent condition. 190

ABSTRACT

DEVELOPMENT OF ENGINEERING TOOLS TO ANALYZE AND DESIGN FLEXIBLE STRUCTURES IN OPEN OCEAN ENVIRONMENTS

By

Judson DeCew

University of New Hampshire, May 2011

Methods to effectively predict system response in marine settings are critical in the engineering design process. The high energy ocean environment can subject structures to large wave and current forces, causing complex coupled motions and loads. This research focused on the development of effective methods to predict flexible system response and the structural integrity of marine High Density Polyethylene (HDPE) components. Numerical modeling tools were developed to analyze and design flexible structures in open ocean environments. Enhancements to the University of New Hampshire's Aqua-FE finite element computer program were performed, including expansion of the element library to include spherical geometries and implementation of various hydrodynamic effects such as Stokes 2nd order waves and water velocity reduction due to component shadowing. Two case studies, involving laboratory and field experiments, were performed evaluating the software modifications and examining the response of flexible systems in various environmental conditions. Practical applications of the numerical model are presented, focusing on the design, analysis and deployment of a submerged grid mooring 10 km from Portsmouth, NH. The system was recovered after a seven year deployment and inspected. The numerical model proved to be a valuable engineering tool

for investigating a system's motion dynamics and mooring tension response in marine environments.

High density polyethylene is a primary structural component for marine systems such as fish containment, wave attenuators and marine defense barrier systems. The fundamental engineering issues with the compliant HDPE material are associated with how the material changes its stiffness and strength depending upon the service life, load rate and temperature. Structural modeling techniques were developed to determine effective methods of analyzing marine systems constructed of HDPE. This included the investigation of the mechanical behavior of new and environmentally fatigued HDPE specimens, obtained from commercial fish farms, at different strain rates and validation of the modeling approach with laboratory experiments. The operational limits, loads and modes of a failure of the HDPE cage frame were estimated, providing valuable information on the survivability of these large, flexible systems in offshore environments.

CHAPTER 1

INTRODUCTION

Methods to effectively predict system response in marine settings are critical in the engineering design process. The high energy ocean environment can subject structures to large wave and current forces, causing complex coupled motions and loads. Most systems deployed in the ocean can be characterized as flexible, i.e. moored systems that can endure large displacements. Navigational buoys and moorings, oil platform risers, wave energy devices and aquaculture equipment are a few examples. Aquaculture farms present an ideal case study of a complex flexible system. They utilize traditional and modern equipment throughout the mooring and structural elements. Typical aquaculture moorings employ anchors, chain, rope, various shaped flotation, and surface or submerged fish cages throughout the water column (Figure 1.1). In these systems, fish cages are the largest structures in terms of water blockage, mass and buoyancy and typically dominate the mooring's dynamic and load response. These rigid or flexible net pens can be secured in grid arrays (Figure 1.1) or single point moored (Figure 1.2).

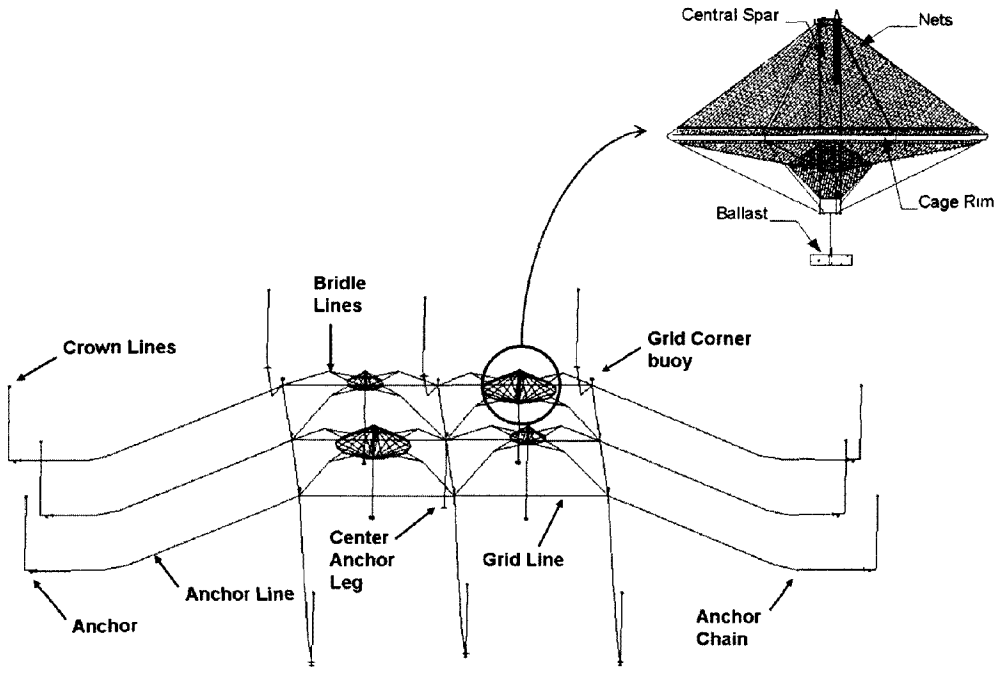

Figure 1.1: The University of New Hampshire's submerged grid mooring with 4 fish cages. The bays of the mooring are suspended 18 meters below the surface and provide a platform for investigating various structures. The SeaStation™ fish cage has a steel central spar and octagonal rim. The net is tensioned between these components, forming a rigid structure. Ballast is suspended below the net pen to provide a restoring force to the net pen. Additional information on the grid mooring can be found in Chapter 7.

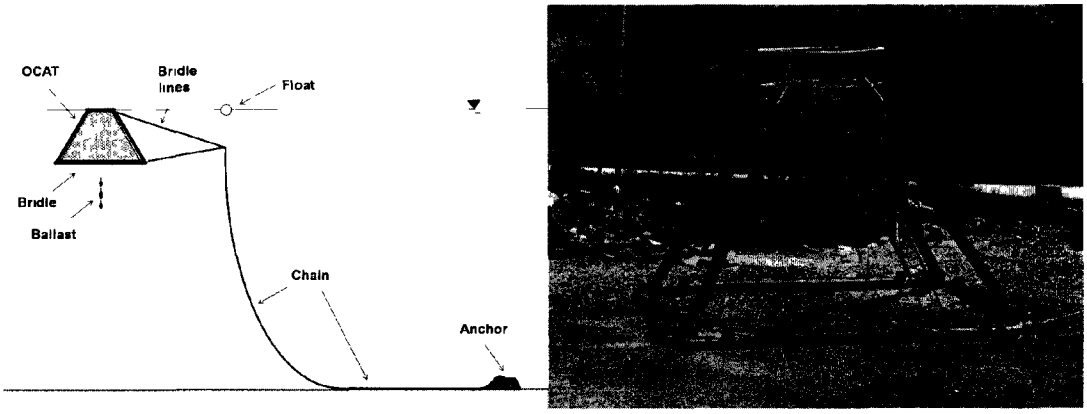

Figure 1.2: A single point moored Ocean Cage Aquaculture Technology (OCAT) fish cage is shown on left. On right: The OCAT is presented without the net chamber for clarity.

Aquaculture is an expanding worldwide industry of which the grow-out of finfish species represents an area of significant expansion (Food and Agricultural Organization, 2004). The vast majority of the world's finfish species are grown in surface gravity cages as seen in Figure 1.3. These systems consist of one to three buoyant rims, a net chamber and weights to retain the nets volumetric integrity (can be individual weights or weighted lower rim). Presently the majority of fish farms are located in protected sites such as bays or rivers. Fish farmers in the sheltered sites are running into various environmental and multi-user conflicts as they try to expand their operations. As a result, the industry has begun to develop aquaculture farms in more exposed sites, but it is unclear how the existing equipment will be able to withstand these higher energy environments. Therefore understanding the characteristics of fish cage and mooring motion and load response is essential to minimize system failure and allow the successful stocking, grow-out and harvesting of fish in an offshore environment.

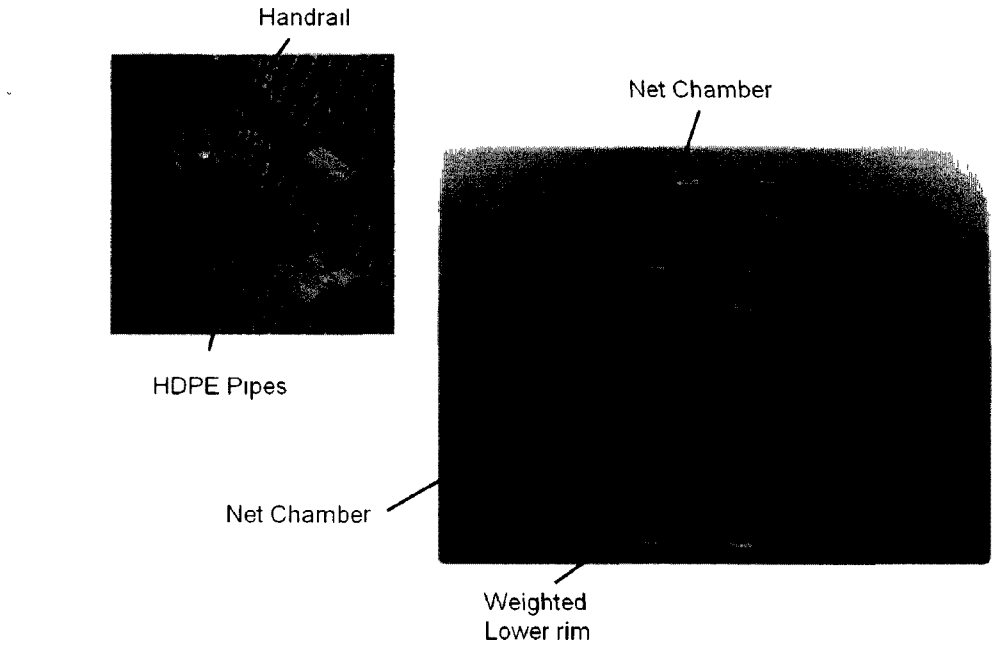

Figure 1.3: A typical gravity fish cage. The net pen consists of an HDPE superstructure supporting a flexible net and a weighted lower rim.

High density polyethylene (HDPE) pipe is the primary structural component for fish containment. The use of HDPE as a structural member has also grown in other industries (docking material, wave attenuators, marine defense barrier systems, etc). It is advantageous because the components are relatively easy to fabricate and repair, the plastic has outstanding corrosion characteristics and the material is compliant and (historically) inexpensive. The fundamental engineering issues with HDPE are associated with how the material changes its stiffness and strength depending upon the service life, load rate and temperature. A better understanding of the structural integrity of HDPE components, specifically of pre-used material, is important as cage failure can result in a considerable loss of product. For example, according to the Directorate of Fisheries in Norway, 170,000 Atlantic cod (*Gadus morhua)* escaped in 2005. It is known that the HDPE cage rim integrity loss was the cause of 30% of net pen failures in Norway from 2001 through 2006. This has significant impacts on the local environment and native fish species (possible cross-breeding) as well as economic consequences (loss of fish product). Knowledge of proper mechanical properties and weathering of HDPE material utilized in net pens can reduce rim failure and prevent fish escapement.

Various other operational or research components may also be deployed throughout the farm: instrument packages, automatic feeding buoys or hoses, load cells, etc. These highly coupled systems have a unique dynamic motion response when loaded by currents, waves, etc. Therefore understanding not only the relative motion between components, as it may increase wear and component tension, but also how objects respond in changing water flow fields caused, in part, by blockage or shadowing effects of nearby structures is critical.

This research develops and investigates engineering methods to predict flexible system response and the structural integrity of HDPE components. It was, in a large part, motivated by

the successful design, deployment and utilization of a submerged offshore mooring grid described in detail in Chapter 7. The use of the mooring as a research platform provided insight into the modeling process and technique that could be improved. Primarily these improvements focused on extension of the element library and improved modeling of the hydrodynamic effects.

Updates and enhancements were introduced to the software package developed by the University of New Hampshire (UNH) called Aqua-FE. This program has been successfully employed to design and analyze various flexible marine structures, and has been calibrated with laboratory and field measurements (Fredriksson, 2001; DeCew et al., 2005; Risso, 2007). As new technology is employed offshore, the program has to be continuously upgraded and validated. Therefore, the software was enhanced by including spherical elements and various hydrodynamic effects such as Stokes 2^{nd} order waves, shadowing effects and proper coefficient of drag values at high Reynolds numbers for flow around cylinders. Two case studies were performed to evaluate the software modifications and examine the response of flexible systems in various environmental conditions. Structural modeling techniques were developed to predict performance of HDPE components in marine. In addition, investigations into the mechanical behavior of pre-used HDPE specimens were performed. Tensile tests were conducted on specimens obtained from new and previously deployed HDPE structures at different strain rates to obtain the material's Young's Modulus and tensile strength at yielding. This research increased the numerical modeling capability and provided a better understanding of HDPE net pen response. Finally, a practical application of the knowledge gained from this research is presented and discussed.

Chapter 2 is dedicated to enhancement of numerical modeling techniques used in the design and analysis of flexible moored installations. A new spherical element type was incorporated into the Aqua-FE program increasing its versatility. Additional hydrodynamic effects were implemented into the software including Stokes 2nd order waves and water velocity shadowing effects. Cylindrical truss elements were upgraded to have more accurate coefficient of drag values at high Reynolds numbers. All of these enhancements to the software were verified by comparison to analytical calculations.

In Chapter 3, the numerical drag force predictions of a spherical fish cage were compared to tow test field measurements of a similar structure, taking into account water velocities outside and inside the net pen. Chapter 4 presents the dynamic response of a small scale, rigid fish cage system, secured by a single point mooring. It was analyzed under a variety of water velocities. To insure accuracy of the results, the numerical model data was compared to physical scale model tow test data performed in the Jere A. Chase Ocean Engineering Laboratory. The validated numerical model was then utilized to investigate the net pen dynamics and mooring loads under currents.

Chapter 5 is dedicated to the development of structural modeling techniques to analyze HDPE structures in marine environments. A finite element analysis of a circular HDPE frame was performed and compared to similar laboratory experiments. A localized failure modeling technique was proposed to simulate the load and mode of failure of the frame. The technique was then used to examine net pen frames under environmental forces typical for a farm located in Eastport, Maine. Field measurements of mooring loads were obtained and used as input. The cage frame stress was predicted and compared to the tensile strength. Additional analysis was

then performed to predict the failure envelope of the cage frame superstructure and the corresponding load and mode of failure.

Chapter 6 focuses on the mechanical behavior of new and previously used HDPE material obtained from net pen frames from three fish farms located in the Faeroe Islands, British Columbia and New Hampshire. It is known that the material was subjected to several years of cyclic (fatigue) loading and exposure to the marine environment during regular service. Numerical modeling was employed to analyze the overall dynamic behavior of fish farms under various sea conditions and the stress within the structural HDPE fish cage components. The results were used to predict the material's strain rate, which helped identify displacement rates used in the laboratory testing. Uniaxial tensile tests were performed on the HDPE specimens fabricated from the new and previously deployed cage components.

Chapter 7 presents a practical application of the numerical modeling approach presented in this dissertation. The design, analysis, and deployment of the University's offshore mooring grid is described, highlighting the importance of a thorough engineering approach. The submerged mooring, deployed for seven years, was recovered and inspected. A systematic review of the design is presented with a discussion of the system's successes and failures.

CHAPTER 2

ADVANCEMENTS IN NUMERICAL MODELING

This chapter presents advancements in numerical modeling techniques aimed at better prediction of the dynamic behavior of flexible marine structures subjected to wave and current environmental loading. These advancements have been implemented in the UNH developed software package Aqua-FE. This finite element analysis (FEA) program has the ability to simulate wave, currents and storm events acting on complex mechanical systems to predict motion dynamics and mooring loads (Gosz et al., 1997 and Tsukrov et al., 2003). An important feature of Aqua-FE is its ability to handle the non-linear dynamics associated with large displacements. The software is equipped with an element library developed for marine structures, which includes truss, stiffener, non-linear and net elements. Regular and irregular waves can be applied, along with a linear current profile. A more detailed description of Aqua-FE is provided in section 2.1.1.

The enhancements of the Aqua-FE software include three major developments: expansion of the menu of elements, implementation of additional hydrodynamic effects and validation for new applications.

2.1 Previous Technical Work

2.1.1 Numerical Modeling of Flexible Structures

Computer models are extremely useful in analyzing flexible structures in open ocean environments. The models can be easily modified to account for different designs and a range of loading conditions. The two most common numerical modeling approaches to represent dynamic deformation of flexible structures are mass/spring and finite element analysis (FEA) models (Garett, 1982; Haritos and He, 1992; Webster, 1995; Gignoux and Messier, 1999; Gobat et al., 2001; and Tsukrov et al., 2000). In mass/spring models, components are discretized into a series of lumped masses, while the stiffness of the component is represented by the spring (Rao, 2004). The lumped masses are assigned based on the component geometric and material properties. It is assumed that the internal and external forces are applied to the system at the lumped mass locations. Mass / spring models are relatively straightforward to develop, however, they can become cumbersome if the system is large and complex. In addition, modifying the spring values to represent a nonlinear response or have a bending stiffness can be difficult.

In FEA models, a system is discretized into a series of simple geometric shapes appropriate for a particular structure (for example, line and/or quad elements). The material properties, element interaction and loads are expressed at the element nodes. Compared to mass/spring models, FEA can better simulate and more accurately predict the mechanics of a system, including taking into consideration Poisson's effect, nonlinear responses and, if needed, bending stiffness. Both mass /spring and FEA models can simulate nonlinear loads. However the implementation of non-linear effects such as partial submergence and material properties is typically easier in FEA.

Mass/spring and FEA models have been implemented in software packages developed by research and commercial groups. A majority of mass / spring models associated with aquaculture systems have focused on the hydrodynamic response of nets with applications to other areas (Lee et al., 2004; Li et al., 2006; Huang et al., 2006; Zhan et al., 2005; Lader et al., 2006; *etc*). There are presently two commercial software packages used to analyze marine aquaculture systems, Orcaflex™ (http://www.orcina.com) and Aquastructures™ (http://www.aquastructures.no). Orcaflex™ is a mass spring model which employs the Morrison approximation (Morrison et al., 1950) for wave and current loading. The numerical procedure used in Aquastructures™ is not publically available. These software packages have been used to predict the system dynamic response, net deformations and tensions in the mooring lines. However, they are limited in their ability to estimate stresses in the structural components and to utilize the correct material models necessary to predict failure of cages.

The UNH group developed an FEA software package that utilizes truss, stiffener, net and nonlinear elements to investigate mooring load and dynamic system response (Gosz et al., 1996; Swift et al., 1998; and Tsukrov et al., 2000). The program is based on the Finite Element Analysis Program (FEAP) originally programmed by Professor R.L. Taylor from the Department of Civil Engineering at the University of California, Berkeley. Hydrodynamic forces on the structural elements are calculated using the Morison equation modified to account for relative motion between the structural element and the surrounding fluid. Following Haritos and He (1992), the fluid force per unit length acting on a cylindrical element is represented as

$$\mathbf{f} = C_1 \mathbf{V}_{Rn} + C_2 \mathbf{V}_{Rt} + C_3 \dot{\mathbf{V}}_n + C_4 \dot{\mathbf{V}}_{Rn}, \qquad (2.1)$$

where $\mathbf{V}_{Rn}$ and $\mathbf{V}_{Rt}$ are the normal and tangential components of the fluid velocity relative to the structural element (see Figure 2.1), $\dot{\mathbf{V}}_n$ is the normal component of total fluid acceleration and $\dot{\mathbf{V}}_{Rn}$ is the normal component of fluid acceleration relative to the structural element. The coefficients in the formula above are given by $C_1 = \frac{1}{2}\rho_w D C_n V_{Rn}$, $C_2 = C_t$, $C_3 = \rho_w A$ and $C_4 = \rho_w A C_a$, where D and A are the diameter and the cross-sectional area of the element in the deformed configuration, ρ_w is the water density, C_n and C_t are the normal and tangential drag coefficients. A value of one was used for the added mass coefficient (C_a) following the work of Bessoneau and Marichal (1998), however the value can be changed depending upon the shape characterisitcs. Note that C_n and C_a are dimensionless, while C_t has the dimension of viscosity. Equation (2.1) is known to adequately predict the hydrodynamic force on a submerged cylindrical element whose diameter is small compared to the wave length (Haritos and He, 1992; Webster, 1995; Tsukrov et al., 2000).

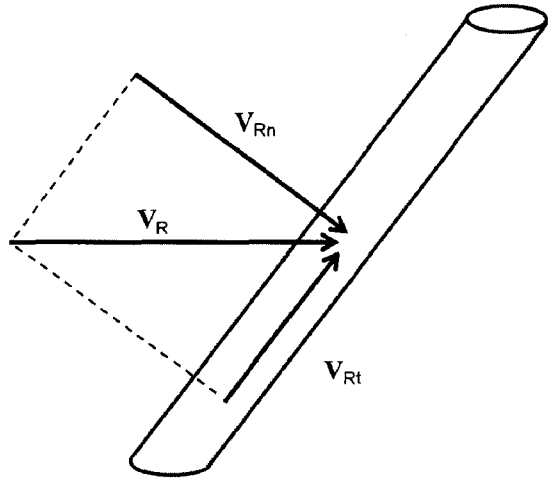

Figure 2.1: Relative fluid velocity components acting on a cylindrical element. The n and t subscripts represent the normal and tangential directions, respectively.

The numerical procedure calculates C_n and C_t, using a method described by Choo and Casarella (1971), that updates the drag coefficients based on the Reynolds number (Re_n) according to,

$$C_n = \begin{cases} \dfrac{8\pi}{\mathrm{Re}_n\, s}\left(1 - 0.87 s^{-2}\right) & \left(0 < \mathrm{Re}_n \le 1\right), \\ 1.45 + 8.55\,\mathrm{Re}_n^{-0.90} & \left(1 < \mathrm{Re}_n \le 30\right), \\ 1.1 + 4\,\mathrm{Re}_n^{-0.50} & \left(30 < \mathrm{Re}_n \le 10^5\right) \end{cases} \tag{2.2}$$

$$C_t = \pi\mu\left(0.55\,\mathrm{Re}_n^{1/2} + 0.084\,\mathrm{Re}_n^{2/3}\right) \tag{2.3}$$

where $\mathrm{Re}_n = \rho_w D V_{Rn}/\mu$, $s = -0.077215665 + \ln\left(8/\mathrm{Re}_n\right)$ and μ is the water viscosity.

The Aqua-FE element library consists of truss, truss with non-linear material properties (referred to as "nonlinear" in this document), stiffener, net and spherical elements. At the beginning of the research described here, however, the spherical elements were not functioning. The truss and non-linear elements are subjected to normal and tangential components of hydrodynamic loading and experience four types of force: buoyancy forces due to fluid displacement, dynamic forces due to the motion of the element with respect to the fluid, gravity forces and point loading. A stiffener element is a "specialized" truss element that has the following properties:

- Possesses high stiffness (Young's Modulus)
- Can experience point loading
- Is not subject to buoyancy forces due to fluid displacement
- Is not subject to dynamic forces due to relative element and fluid motion
- Is not subject to gravity force
- Possesses zero mass and does not contribute to inertia forces

The incorporation of stiffener elements into Aqua-FE was necessary as there are no beam elements in the software program. Truss members have six degrees of freedom with endpoints characterized by pin attachments, so in certain formations, structures made of these elements will collapse upon themselves without the addition of stiffeners for stability.

One element unique in representing aquaculture systems, developed specifically for the Aqua-FE software, is the consistent net element. Direct numerical modeling of the nets can require an excessive amount of computational capacity if every twine is represented. The consistent net element (Tsukrov et al., 2003) was developed to address this issue enabling the use of fewer elements, but maintaining (1) fluid drag, (2) inertia, (3) buoyancy, (4) weight and (5) elastic forces. The consistent net element approach allows the net structure to be modeled using fewer elements than straight geometric modeling, necessary to accurately model net panels while sustaining computational efficiency. The final element that was originally developed but not implemented or verified in the software was the spherical element. More information on this element type is presented in section 2.2.

To understand portions of the enhancements presented in this chapter, it is important to have an understanding of Aqua-FE's operating procedure. The underlying code is a general purpose finite element program (see Appendix A for more information). Subroutines, such as the fluid-structure interaction, were added into the base code. The resulting program requires the mesh geometry, element and nodal connectivity and material property and fluid loading information. This data is stored in three main files: model structural and connectivity data file (**.out*), material property and fluid data file (**.opt*) and the I/O information file (*feap.in*).

To analyze a system in Aqua-FE, first the finite element mesh is created in a standard FEA package such as MSC.MARC / MENTAT. This mesh is then exported and processed in the

preaquafe subroutine , obtaining the model's nodal and element connectivity and boundary condition data (forming the **.out* file). The **.opt* file contains the material properties, fluid loading, numerical time steps and controls various operating MACRO's (a MACRO is a sequence of commands, discussed in greater detail in Appendix A). Note that the following material property data is required: the effective density, defined as the total mass of the item divided by its volume (kg/m^3), the Young's Modulus (Pa) and the cross-sectional area of the element (m^2). Net elements are the exception, requiring a fourth input parameter. This value is geometrically calculated and allows the program to model netting members with respect to their solidity (Tsukrov et al., 2003), where solidity is the ratio of the projected area to the outline area. Finally the I/O information file contains data on the file location of the input data and provides the name of the file where the results of the simulation are to be stored.

Aqua-FE has been extensively used to study a variety of different marine systems and has compared well with physical model testing and *in-situ* experiments for different structures and mooring configurations (DeCew et al., 2005; Fredriksson et al., 2005a;, Tsukrov et al., 2003; Fredriksson et al., 2003). More information on the software can be found in Tsukrov et al. 2005.

2.1.2 Hydrodynamic Fluid-Structure Interaction

The primary forcing mechanisms of flexible oceanic structures are wind, waves and current. The focus of this dissertation is aquaculture systems, which have a vast majority of their structure below the waterline. Therefore wind forcing will not be considered. Waves can be represented using a variety of methods, such as Airy wave theory, non-linear waves, etc. Fluid drag forces, associated with current, have been extensively studied and are relatively straightforward to predict (see, for example, Hoerner, 1965). There are three primary hydrodynamic methods to simulate the structures response to these forcings: undisturbed

hydrodynamic loading, loading with approximate representation of shadowing effects (through empirically derived coefficients), and fluid flow analysis based models.

In undisturbed hydrodynamic loading (non-interactive) models, it is assumed that presence of elements does not influence the water flow or wave parameters. Component shadowing (blockage), surface wave effects due to waves breaking on structures, wave creation by the structure, and alteration of the wave or current path are not included. The majority of these models use Airy wave theory (see, for example, Dean and Dalrymple, 1991) and a modified version of the Morrison equation (Morrison et al., 1950) to represent the wave and water velocity induced drag on the component (Tsukrov et al., 2003; Li et al., 2006; Ladar and Fredheim, 2003; Huang et al., 2006; *etc*). Some models use different wave loadings, such as Stokes 2^{nd} or 5^{th} order approximations to represent the wave parameters (Fenton, 1985; Rahman, 1998).

The non- interactive hydrodynamical models can be modified to allow component shadowing. Fredriksson et al. 2007a used measured velocity reductions within a system to investigate the tension response within a 20 cage near-shore farm. The tidal current was reduced as it progressed through the farm, decreasing the drag force on in-line cage systems. The results of the analysis compared well with field measurements. However, all altered water particle velocity values used in this approach must be pre-determined.

Fluid flow analysis based models account for the structure's influence on the surrounding fluid. As systems become larger, they may affect the local wave and water velocity path and/or magnitude (Patursson, 2008). Fredriksson et al. (2008) preformed preliminary diffraction analysis using analytical methods to investigate the flow around a closed containment (i.e. floating tanks) fish farm. Lee (1995) presented a method for analysis of large

offshore structures where wave diffraction may be found. Other diffraction models can be found that model wave run-up on structures (Issacson and Cheung, 1994) or the diffracted wave properties (Lee and Kim, 2006; Clark et al., 1991). However, presently these programs are not computationally efficient for the modeling of large porous flexible systems.

2.2 Numerical Model Enhancement. Incorporation of Spherical Element

Spherically shaped elements are commonly used in marine engineering. These can be floats suspending gear at or below the surface, weights used to provide a restoring or damping force, or a rigid fairing material built around a structure to reduce its drag. From an engineering perspective, a sphere is ideal in that it has uniform drag characteristics regardless of the fluid flow direction. Since this shape is so prevalent in marine environments, the first enhancement of the Aqua-FE software was the incorporation of a spherical element. In 2004, the element was created for the software based upon flow around a sphere (Kestler, 2004). Portions of the operating code for the element were generated but not completed or incorporated into the software. In this work, an effort was made to implement the element, validate it, and develop operating protocols to insure proper use of the element.

2.2.1 Drag Forces on Spherical Element

A submerged spherical body, under dynamic flow (or motion) can have five force components acting upon it: gravity, mass inertia, buoyancy, fluid drag and fluid acceleration. The gravitational force is constant, the mass inertia force component is dependent upon the unit's acceleration and the buoyancy on the submerged volume. The fluid drag and acceleration forces change depending upon the relative motion between the fluid and the spherical body.

The dynamic fluid force contributions acting on a submerged spherical body are similar to the forces acting on cylindrical element:

$$\mathbf{f}_b = C_1\mathbf{V}_R + C_2\dot{\mathbf{V}} + C_3\dot{\mathbf{V}}_R \tag{2.4}$$

where

$$C_1 = \frac{1}{2}\rho_w A C_d \{\mathbf{V}_R \cdot \mathbf{V}_R\}^{\frac{1}{2}} \tag{2.5}$$

$$C_2 = \rho_w V \tag{2.6}$$

$$C_3 = \rho_w V C_m \tag{2.7}$$

where C_d is the drag coefficient, C_m is the added mass coefficient, A is the buoy cross-sectional area, V is the buoy volume, and ρ_w is the mass density of the fluid. Bold faced letters represent vectors: $\mathbf{f_b}$ is the total force on the buoy, $\mathbf{V}_R$ is the relative velocity, $\dot{\mathbf{V}}$ is the total acceleration, and $\dot{\mathbf{V}}_R$ is the relative acceleration. The primary difference between equations 2.1 and 2.4 is the lack of tangential drag acting on the sphere. To insure accurate drag force values, the numerical procedure in Aqua-FE updates the coefficient of drag for each element at each time step. The coefficient of drag is a function of the Reynolds number (Re), defined as:

$$Re = \frac{\rho_w U d}{\mu} \tag{2.8}$$

where d is the characteristic diameter, U is the water velocity, and μ is the fluid dynamic viscosity. The relationship between the coefficient of drag and Reynolds number has been well established (see, for example, White, 1999 or Berteaux, 1991), and is shown in Figure 2.2.

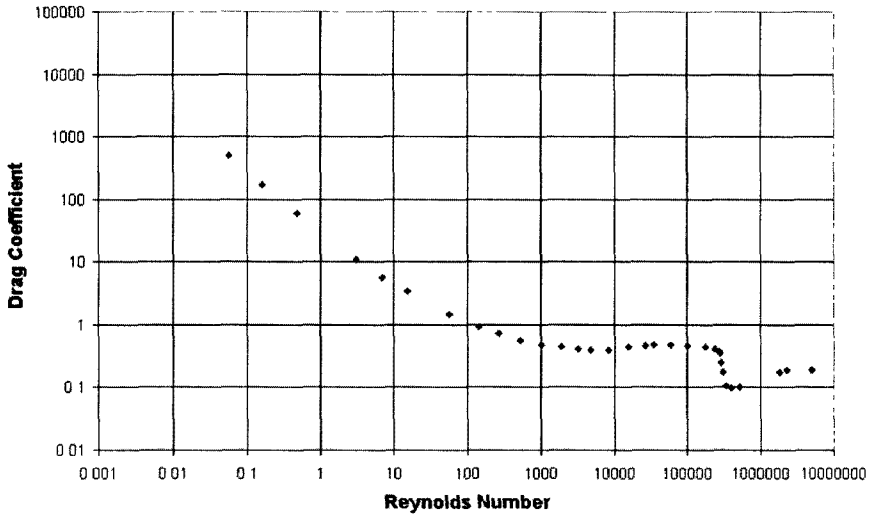

Figure 2.2: Dependence of drag coefficient of a sphere on Reynolds Number. Obtained from Donley, 1991.

At Reynolds numbers less than one the drag coefficient curve is generated by Stokes law (1851), described as:

$$C_d = \frac{24}{Re}, \qquad Re \leq 1 \qquad (2.9)$$

This relation assumes that the sphere is smooth and the primary drag on the body is the surface drag associated with the spherical body's boundary layer. At Reynolds numbers greater than 1, flow seperation is initated, and pressure drag is formed. The coefficient of drag for smooth spherical bodies in this region was determined experimentally. Several obervations of the curve can be made:

- The drag coefficients are relatively constant between Reynolds Numbers of 10^4 to 10^5.
- At Reynolds numbers greater than 4×10^5, the coefficient of drag has a significant reduction, decreasing to approximately 20% of its previous value. This drop occurs at the "critical" Reynolds number, where the boundary layer becomes fully turbulent and

the location of flow seperation moves back. Generalized regimes of the curve near the critical Reynolds number are shown in Figure 2.3.

- The drag coefficient rebounds and levels off at Reynolds numbers greater than 10^7.

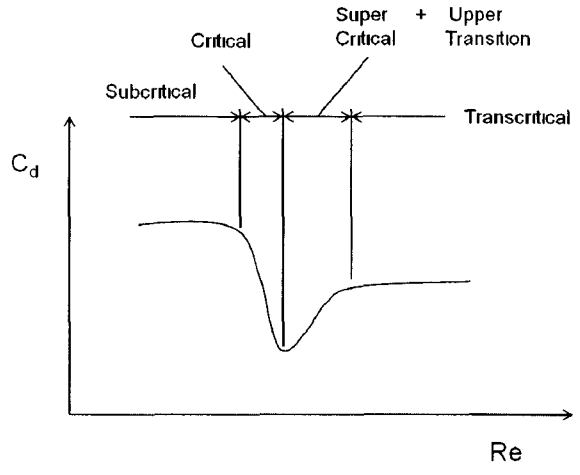

Figure 2.3: A schematic of the change of the drag force in the critical range of Reynolds numbers. Adopted from "Hydrodynamics around cylinder structures" by M. Sumar and J. Fredsoe.

This reduction in drag coefficient can have significant implications for the dynamics of a spherical body and, therefore, needs to be properly implemented in the Aqua-FE software. The following approach has been proposed by DeCew et al. 2010 to represent the coefficient of drag. The curve is divided into five sections, with each section approximated by linear or exponential functions, with a continuity condition imposed:

$$C_d = \begin{cases} 30.824Re^{-0.8465} + 0.4347, \ 0 < Re \leq 3.803 \cdot 10^5 \\ -9.222 \cdot 10^{-6}(Re - 4.3025 \cdot 10^5), \ 3.803 \cdot 10^5 < Re \leq 4.165 \cdot 10^5 \\ 0.0928 + 0.8\left(e^{\left(1-\frac{Re}{1.3201\,10^5}\right)}\right), \ 4.165 \cdot 10^5 < Re \leq 1.259 \cdot 10^6 \\ 0.1488\left(1 - e^{\frac{-Re}{1.286\,10^6}}\right), \ 1.259 \cdot 10^6 < Re \leq 10^8 \end{cases} \quad (2.10)$$

Figure 2.4 presents the analytical curve given by (2.10) compared to the experimentally measured drag coefficient values. Formulae (2.10) have been implemented in the program Aqua-FE together with the updated formulation of the sphere element.

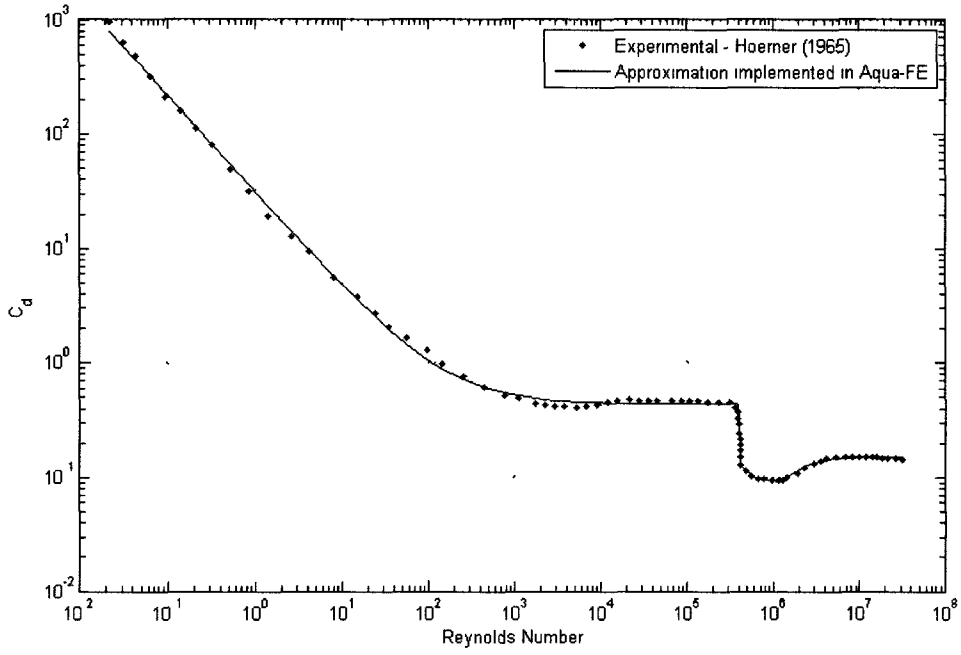

Figure 2.4: Drag coefficients for a sphere. The experimental values are compared to equation (2.10). Experimental values were obtained from Hoerner (1965) and numerical approximation by DeCew et al., 2010.

2.2.2 Validation for Buoyancy and Node Assignment Scheme

With the spherical element incorporated into the Aqua-FE software, proper use and output results of the element, specifically the location of the mass and buoyancy contributions of the element, were then verified. The Aqua-FE program utilizes 2 node elements for the assembly of the finite element mesh (Tsukrov et al., 2000). Therefore, to incorporate the spherical element into the software, it must also have 2 nodes. All the mass and buoyancy characteristics of the element are lumped around a single node (referred to as the *active* node).

The current and wave forces are applied to the same node. The second node of the element (*connecting* node) has no sphere properties associated with it and is used strictly for the element connectivity. This set-up can be seen more clearly in Figure 2.5.

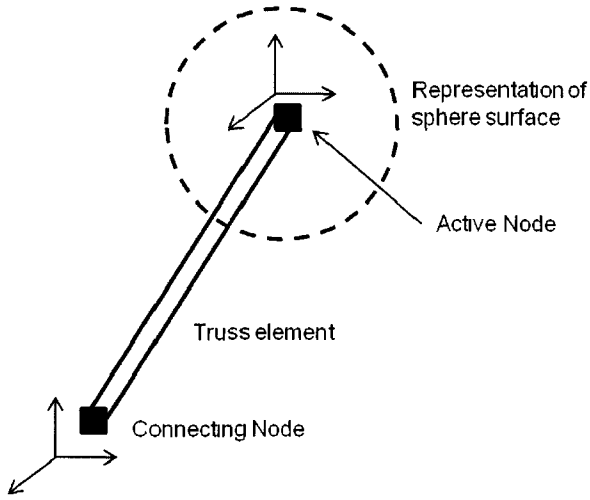

Figure 2.5: The spherical element consists of two nodes: the active node where the mass and characteristics are applied, and the connecting node.

Since the sphere's geometric and material properties are located at one node, the underlying truss element does not have any stiffness. Thus, a second truss element must be added in order for the sphere to retain its position relative to the other elements in the model. It is important to note that the sphere material property information supplied to the **.opt* file is different from that of a truss element. The spherical element only requires the effective density (similarly defined as the total mass of the sphere divided by its volume) and diameter information. An example of the **.opt* file is shown below. In this example, the material set 2 is the spherical element. The effective density (set to be neutrally buoyant, 1025 kg/m^3) and diameter (0.5000 m) were set. A full **.opt* file containing the description of required input properties is presented in Appendix A.

```
MATE
    1     1                                                        Cylindrical
Truss
        0      9.8062          1 1.037E+03 1.172E+09 1.075E-01
    2     2                                                          Sphere
        0      9.8062          1 1.025E+02 5.000E-01
```

To insure the element was properly incorporated into the software, a simple numerical study was initiated for which the drag of a sphere was investigated. A sphere was placed mid-way on a rope, fixed at both ends, and subjected to an inline steady water velocity (Figure 2.6). The model was comprised of 6 nodes and 6 elements (the sphere and a truss element overlap). The material and geometric properties for this model are shown in Table 2.1. The output rope tensions were monitored to verify the sphere location and monitor any possible influence of the underlying truss element's connectivity on the output results. The system was subjected to 10 cms^{-1} constant-with-depth water velocity.

Table 2.1: The geometric and material properties of the spherical element mode assignment verification model.

Component	Parameter	Value
Line	Effective Density	1025 kg/m^3
	Young's Modulus	1.0×10^9 Pa
	Cross sectional Area	1.0×10^{-2} m^2
Sphere	Effective Density	1025 kg/m^3
	Diameter	0.5 m

The boundary conditions and element's geometric and material properties were identical for each load case. Three geometrical arrangements of the system were considered:

- Case 1: The sphere located at the 3rd node in the mesh.
- Case 2: The sphere located at the 4th node in the mesh.

- Case 3: Similar to load case 2, except that the underlying truss element's connectivity was reversed.

Together, these investigations examined the location of the sphere (in relation to the active and connecting nodes selected during the mesh construction) and the influence of the underlying elements connectivity.

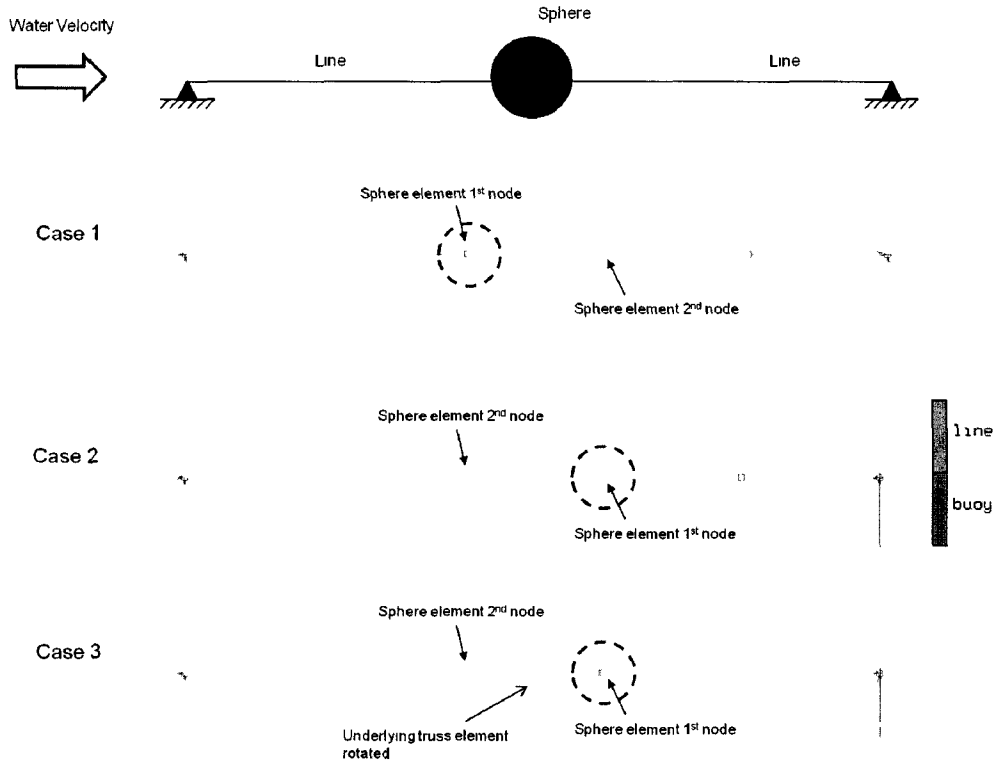

Figure 2.6: A sphere was placed in line of a rope and analyzed under a constant with depth water velocity (top). The cases were investigated where the sphere's active node was moved and the underlying elements connectivity reversed.

The output tension results for the elements are shown in Figure 2.7. It can be seen that the sphere is located at the 1st node of the elements connectivity (active node). In addition, the connectivity associated with the truss element used with spherical element did not influence the model's output tension results.

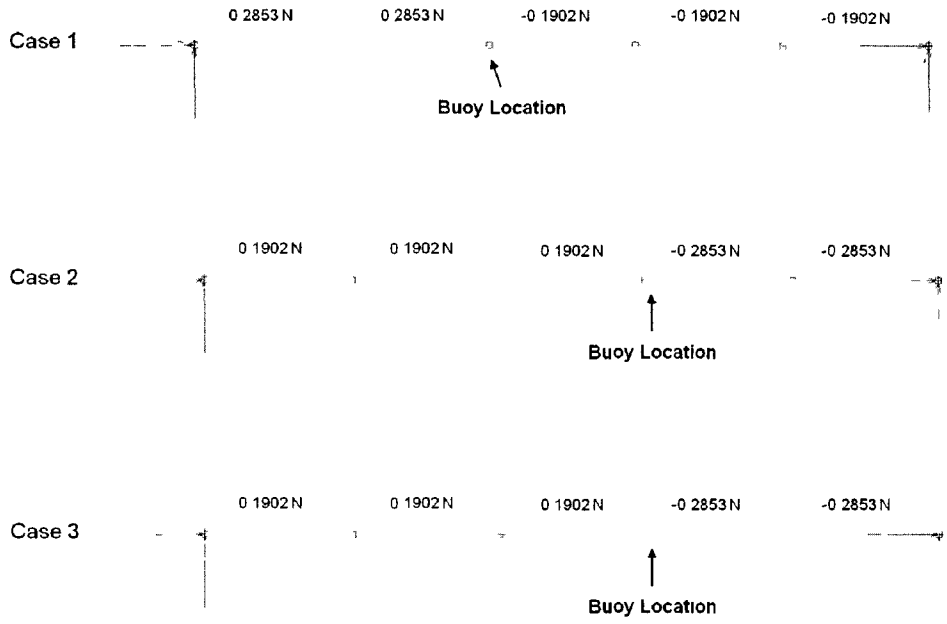

Figure 2.7: The output tension results from the elements. The tension values are shown above the FEA mesh.

With the proper location of the sphere known, the buoyancy output of the element was verified. A model consisting of a fully submerged spherical float connected to a line was created and tested in Aqua-FE. The sphere was connected to the line via a stiffener element. The model can be seen in Figure 2.8. The geometric and material properties are shown in Table 2.2.

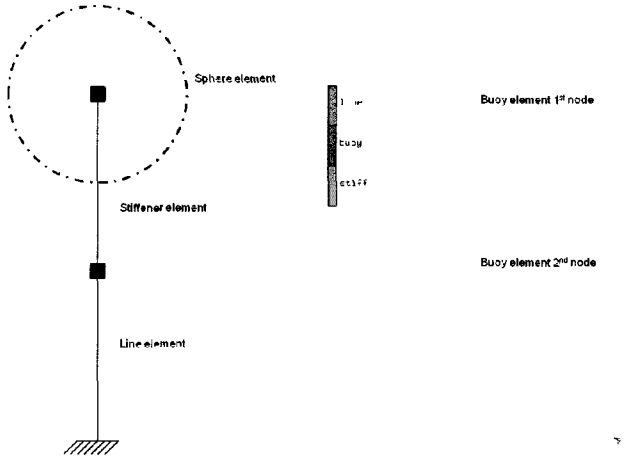

Figure 2.8: A buoyant spherical float placed at the end of a line (left) was modeled in Aqua-FE (right). Note that the buoy and stiffener elements overlay each other in the Aqua-FE model.

Table 2.2: The geometric and material properties of the spherical element buoyancy verification model.

Component	Parameter	Value
Line	Effective Density	1025 kg/m^3
	Young's Modulus	1.0 x 10^9 Pa
	Cross sectional Area	1.0 x 10^{-6} m^2
	Length	0.25 m
Sphere	Effective Density	1025 kg/m^3
	Diameter	0.5 m

The steady state output tension in the line was compared to analytical values. The results of this analysis are shown in Figure 2.9. Note that for the purpose of this research, the "steady state" portion of the output does not include the system's initial transient response or deformation. It can be seen that the numerical prediction and analytical calculations were within 0.06%. The response of the spherical element for various levels of submergence was also verified by considering 4 levels of submergence: 100% (fully submerged), 75%, 50% and 25%. For all cases, the buoyancy forces in still water were found to be as expected from static equilibrium.

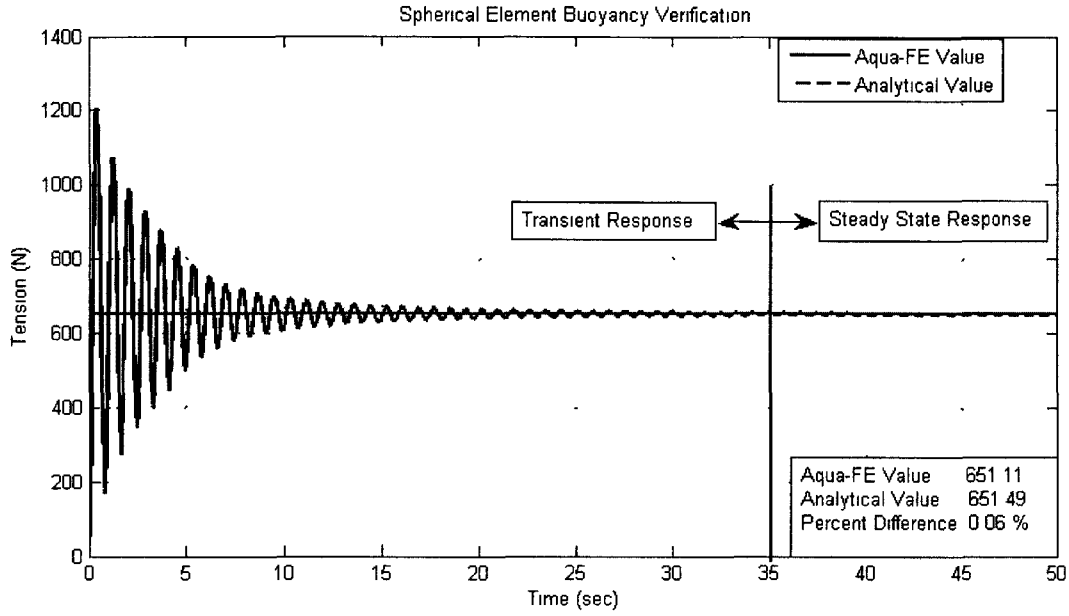

Figure 2.9: The output line tension results. The transient and steady state tension regions are also shown.

2.2.3 Comparison of Truss and Sphere Elements. Behavior under Currents and Waves

Once the element was fully implemented in the software, a comparison study was initiated between spherical and cylindrical shaped flotation members. These shapes are the dominant flotation geometries for marine applications, thus understanding their dynamic response under currents and waves is important.

Three load cases were analyzed using two numerical models. First, a comparison of the surge (horizontal) motion and mooring line load response was performed. The line and float models, constructed in Aqua-FE, are shown in Figure 2.10. Each assembly was assembled using 101 elements and 102 nodes. Buoyant steel spherical and cylindrical elements, having similar projected areas and volumes, were placed at the top of separate line arrays. The centers of both buoyant elements were placed at the waterline.

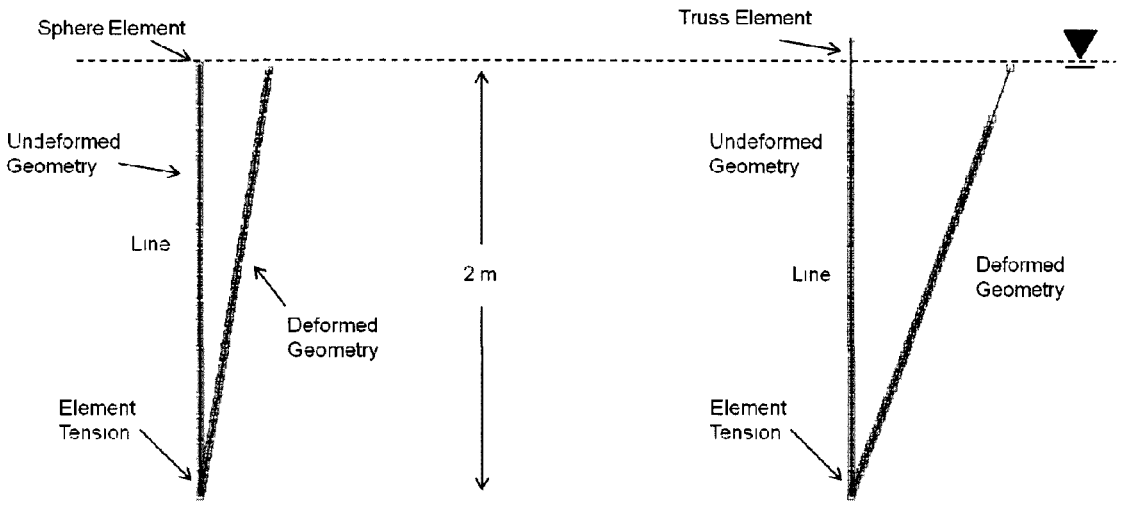

Figure 2.10: The truss and spherical floats were modeled using similar mooring lines in Aqua-FE. The deformed geometry is shown for the 1 m/s water velocity as an example.

The geometric and material properties of the model are shown in Table 2.3. The tension at the base of the line (adjacent to the fixed boundary condition) was recorded for comparison. The horizontal displacement of the float was also monitored. The models were analyzed in eight constant-with-depth currents ranging from 0 to 1 ms^{-1}, in 0.125 ms^{-1} increments. The output mooring tensions and deflections of the floats are given in Table 2.4.

Table 2.3: The truss and spherical element dynamic behavior models geometric and material properties. The effective density is defined as the mass divided by the volume enclosed by the outside surface.

Component	Parameter	Value
Line	Effective Density	1025 kg/m^3
	Young's Modulus	2.0×10^{11} Pa
	Cross sectional Area	1.0×10^{-6} m^2
Sphere	Effective Density	100 kg/m^3
	Diameter	0.25 m
Cylinder	Effective Density	100 kg/m^3
	Young's Modulus	2.0×10^{11} Pa
	Cross sectional Area	3.27×10^{-2} m^2
	Length	0.25 m

Table 2.4: The output model tension results from the sphere and cylindrical float behavior response investigation.

	Sphere Float Model		Cylinder Float Model	
Current (ms^{-1})	Mooring Tension (N)	Horizontal Deflection (m)	Mooring Tension (N)	Horizontal Deflection (m)
0	74.209	0	74.209	0
0.125	74.214	0.005	74.208	0.020
0.25	74.229	0.021	74.189	0.077
0.375	74.228	0.047	74.104	0.173
0.50	74.267	0.082	73.879	0.304
0.625	74.348	0.127	73.418	0.468
0.75	74.492	0.182	72.630	0.659
0.875	74.726	0.245	71.451	0.865
1.00	75.077	0.317	69.872	1.078

It can be seen that the sphere and cylindrical floats have a similar mooring tension for a majority of the applied water velocities. As the water velocities increase, however, the spherical float has more tension in the line. This is a result of the cylindrical float changing its orientation to the water flow, reducing the projected area normal to the applied current. It is interesting to note that at the higher water velocities, the spherical float has approximately 70% less deflection, due mostly to the lower coefficient of drag.

Understanding the differences in the dynamics of a spherical versus cylindrical shaped object in the ocean is also important. Therefore, the response of a similar buoyant sphere and cylinder was investigated under regular and irregular waves. A similar model to that used for the steady current flow analysis was employed, however two modifications to the model were made: (1) the water depth and line lengths were increased from 2 meters (nominal) to 10 meters and (2) the Young's Modulus of the line was changed from 2.0×10^{11} Pa to 2.0×10^{9} Pa. The centerline of each float remained at the waterline. The model is shown in Figure 2.11.

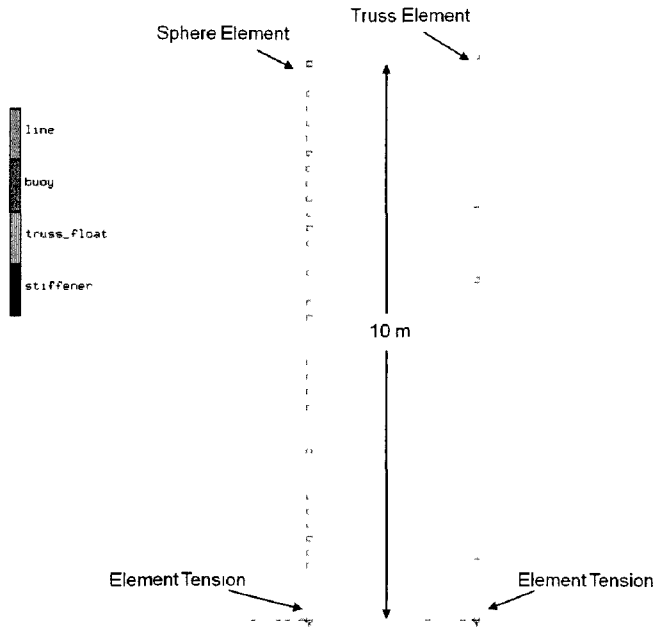

Figure 2.11: The models constructed in Aqua-FE to analyze the spherical and cylindrical floats response in waves.

Two wave regimes based on Airy wave theory were then applied to the model. Regular waves having a height of 1 meter and period of 5.64 seconds were first applied. Then, an irregular wave field, represented by a Joint North Sea Wave Project (JONSWAP) spectrum, having a significant wave height of 1 meter and dominate period of 5.64 seconds was generated. The analytical expression for the spectrum, $G_{JONSWAP}$, modified by Goda (1985), is:

$$G_{JONSWAP}(f) = \alpha H_s^2 T_p^{-4} f^{-5} exp\left[-1.25\left(T_p f\right)^{-4}\right] \lambda^Y \tag{2.11}$$

$$Y = e^{\left[-(T_p f - 1)^2 / 2\sigma^2\right]} \tag{2.12}$$

$$\alpha = \frac{0.0624}{0.23 + 0.0336\gamma - 0.185(1.9+\lambda)^{-1}} \tag{2.13}$$

$$\sigma = \begin{Bmatrix} \sigma_a f \leq f_p \\ \sigma_b f > f_p \end{Bmatrix} \tag{2.14}$$

where H_s is the significant wave height, T_p is the dominate period, f_p is the frequency at the spectral peak ($1/T_p$), and σ and λ are shaping parameters used to adjust the height and width of the peak of the curve. More information on the generated wave spectrum used in this analysis can be found in Fredriksson et al. 2003. The output mooring line tension was recorded for this analysis and is presented in Figures 2.12 and 2.13.

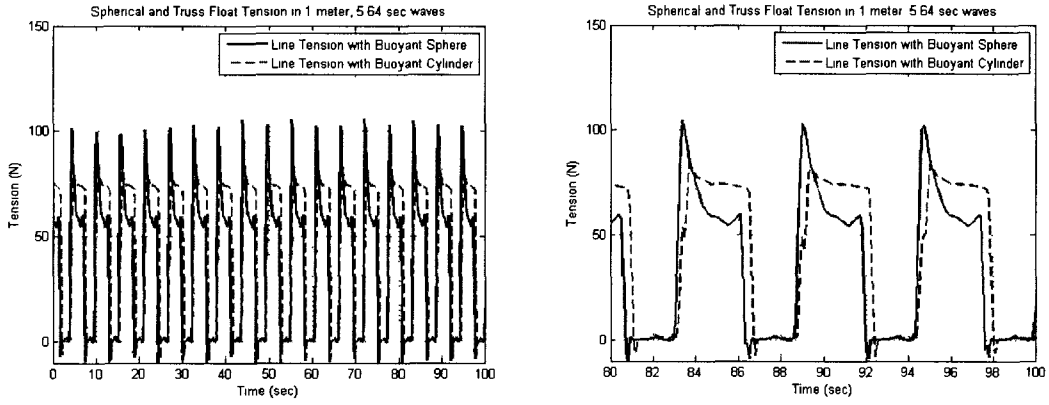

Figure 2.12: Element tension results of the model under 1 meter, 5.64 second waves. The full time series is shown on left, a 20 second section of the data is presented on right.

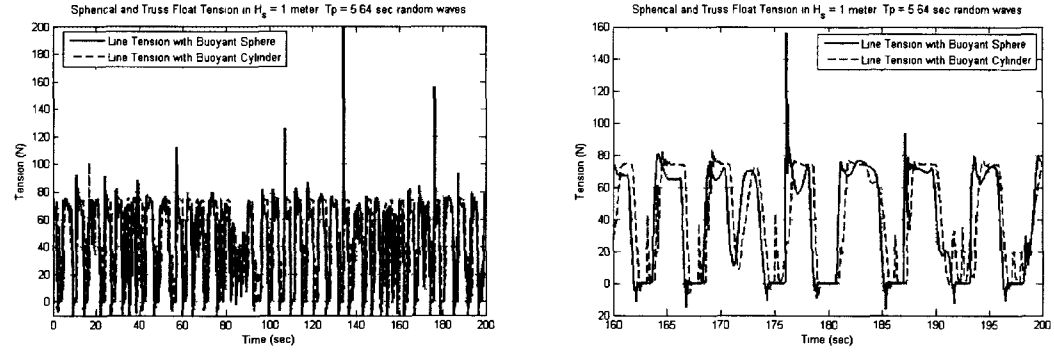

Figure 2.13: Element tension results of the model under an irregular wave field having a significant wave height of 1 meter, and dominate period of 5.64 second waves. The full time series is shown on left, a 40 second section of data on right.

The models were run for 100 and 200 seconds in the regular and irregular waves, respectively, to allow the system to enter a steady state load response. The following observations can be made from the results:

- The spherical float consistently has larger initial peak loads associated with the float's initial response to the waves.
- This force is amplified up to a factor of three in the irregular waves.
- One explanation of the differences in the mooring line tension results is the waterline location and the concentrated buoyancy around the center of the spherical element. The truss element's buoyancy is distributed along its length, thereby generating linear change in tension response as the surface elevation rises or falls. However, the spherical float has the majority of its volume (and thus buoyancy) around its center. Thus small changes in water surface elevation significantly changes the buoyancy forces in the mooring.

2.3 Numerical Model Enhancement. Implementation of Hydrodynamic Effects

Gravity waves are a dominate forcing parameter in the marine environment. Therefore it is important to properly describe these in the Aqua-FE software. Most numerical models use Airy wave theory to describe the wave motion (Airy, 1845). Airy waves have the following three general properties:

- The wave surface is a two-dimensional simple harmonic wave,
- The theory is based on irrotational flow of an inviscid, incompressible fluid,

- Current may be superimposed to determine fluid velocity.

Two primary assumptions of the theory are that the wave height is assumed to be small compared to wavelength and the fluid depth is assumed to be uniform. Aqua-FE was originally developed to utilize this linear, small amplitude wave theory for regular and irregular waves. In an effort to expand the dynamic loading scenarios, Stokes 2nd order waves were incorporated into the software. The governing equations were first written into the program. Then the output surface elevation was verified. Finally, error checks were incorporated to ensure proper use of the subroutine, for example, by not allowing super positioning of multiple Stokes 2nd order wave frequencies.

2.3.1 Wave Theory

The Aqua-FE software has the capability to generate waves based upon linear, small amplitude wave theory (see, for example, Dean and Darymple, 1991) to approximate regular and irregular wave characteristics. According to this theory, the surface elevation, η, of small amplitude, linear waves is given by

$$\eta = \frac{H}{2}\cos(\mathrm{kx} - \sigma t) \tag{2.15}$$

where H is the wave height, k is the wave number, x is the horizontal position, σ is the radian frequency, and t is time. Following small amplitude wave theory, the velocity potential, ϕ, is

$$\phi = -\frac{H}{2}\frac{\sigma}{k}\frac{\cosh[k(h+z)]}{\sinh(kh)}\sin(kx - \sigma t) \tag{2.16}$$

where h is the water depth and z is measured from the surface (positive upward), which is used to obtain the x and y components of the water particle velocity vector according to $u =$

$-\frac{\partial\phi}{\partial x}$ and $w = -\frac{\partial\phi}{\partial z}$, respectively. The relationship between the wave number and radian frequency (dispersion relation) is

$$\sigma^2 = gktanh(kh) \tag{2.17}$$

Taking the derivative of equation (2.16) with respect to the horizontal direction, x, results in the horizontal water particle velocity, u:

$$u = \frac{H}{2}\frac{gk}{\sigma}\frac{\cosh[k(h+z)]}{\cosh(kh)}\cos(kx - \sigma t) \tag{2.18}$$

where g is the gravitational constant. Similarly, the vertical water particle velocity can be found by taking the derivative with respect to the vertical direction, z:

$$w = \frac{H}{2}\sigma\frac{\sinh[k(h+z)]}{\sinh(kh)}\sin(kx - \sigma t) \tag{2.19}$$

The horizontal and vertical water particle accelerations can also be determined by taking the derivative of the water particle velocities in the horizontal and vertical directions:

$$\frac{du}{dt} = \frac{H}{2}\sigma^2\frac{\cosh[k(h+z)]}{\sinh(kh)}\sin(kx - \sigma t), \tag{2.20}$$

$$\frac{dw}{dt} = -\frac{H}{2}\sigma^2\frac{\sinh[k(h+z)]}{\sinh(kh)}\cos(kx - \sigma t). \tag{2.21}$$

These equations are required by Aqua-FE software to determine the forces acting on the finite element mesh. Note that irregular waves in Aqua-FE are modeled as a superposition of sinusoids with different wave amplitudes (a), radian frequencies (σ), and phases (ε), so that

$$\eta(t) = \sum_{n=1}^{N} a_n \cos(\sigma_n t - \varepsilon_n) \tag{2.22}$$

where N is the number of sinusoids, σ_n are regularly spaced radian frequencies, and ε_n is a random number.

The software requires similar parameters to calculate the surface elevation, horizontal and vertical water particle velocities and accelerations to properly implement the Stokes 2nd order waves (see, for example, Dean and Darymple, 1991). Using a perturbation approach, the velocity potential and surface elevation can be shown to be

$$\phi = -\frac{Hg}{2\sigma}\frac{\cosh[k(h+z)]}{\cosh(kh)}\sin(kx-\sigma t) - \frac{3}{32}H^2\sigma\frac{\cosh 2[k(h+z)]}{\sinh^4(kh)}\sin 2(kx-\sigma t) \qquad (2.23)$$

$$\eta = \frac{H}{2}\cos(\mathrm{kx}-\sigma t) + \frac{H^2 k\cosh(kh)}{16\sinh(kh)^3}[2+\cosh(2kh)]\cos[2(kx-\sigma t)] \qquad (2.24)$$

Note that the dispersion equation remains similar to small amplitude wave theory for Stokes 2nd order waves. Taking the derivative of equation 2.23 with respect to the horizontal distance x, and vertical direction z, results in the horizontal and vertical water particle velocities, respectively:

$$\mathrm{u} = \frac{H}{2}\frac{gk}{\sigma}\frac{\cosh[k(h+z)]}{\cosh(kh)}\cos(kx-\sigma t) + \frac{3}{16}H^2\sigma k\frac{\cosh[2k(h+z)]}{\sinh(kh)^4}\cos[2(kx-\sigma t)] \qquad (2.25)$$

$$\mathrm{w} = \frac{H}{2}\frac{gk}{\sigma}\frac{\sinh[k(h+z)]}{\cosh(kh)}\sin(kx-\sigma t) + \frac{3}{16}H^2\sigma k\frac{\sinh[2k(h+z)]}{\sinh(kh)^4}\sin[2(kx-\sigma t)] \qquad (2.26)$$

The horizontal and vertical acceleration terms can then be found by taking the total derivative of the particle velocities,

$$\frac{Du}{Dt} = \frac{du}{dt} + u\left(\frac{du}{dx}\right) + v\left(\frac{du}{dy}\right) + w\left(\frac{du}{dz}\right) \qquad (2.27)$$

$$\frac{Dw}{Dt} = \frac{dw}{dt} + u\left(\frac{dw}{dx}\right) + v\left(\frac{dw}{dy}\right) + w\left(\frac{dw}{dz}\right) \qquad (2.28)$$

which result in the following horizontal and vertical water particle accelerations:

$$\frac{\mathrm{Du}}{\mathrm{Dt}} = \frac{1}{2}Hgk\frac{\cosh[k(h+z)]}{\cosh(kh)}\sin(kx-\sigma t) - \frac{1}{4}H^2gk^2\frac{\sin[2(kx-\sigma t)]}{\sinh[2kh]}$$
$$+\frac{3}{8}H^2\sigma^2k\frac{\cosh[2k(h+z)]}{\sinh(kh)^4}\sin[2(kx-\sigma t)]$$

(2.29)

$$\frac{\mathrm{Dw}}{\mathrm{Dt}} = -\frac{1}{2}Hgk\frac{\sinh[k(h+z)]}{\cosh(kh)}\cos(kx-\sigma t) + \frac{1}{4}H^2gk^2\frac{\sinh[2k(h+z)]}{\sinh[2kh]}$$
$$-\frac{3}{8}H^2\sigma^2k\frac{\sinh[2k(h+z)]}{\sinh(kh)^4}\cos[2(kx-\sigma t)]$$

(2.30)

The nonlinear portions of the Stokes wave's surface elevation have steeper crests and flatter troughs compared to linear waves (shown in Figure 2.14). The horizontal velocities are also greater under the wave crest and reduced under the trough. The horizontal particle accelerations have a slight increase for the Stokes 2nd order waves, with the maximum and minimum values having a slight phase shift.

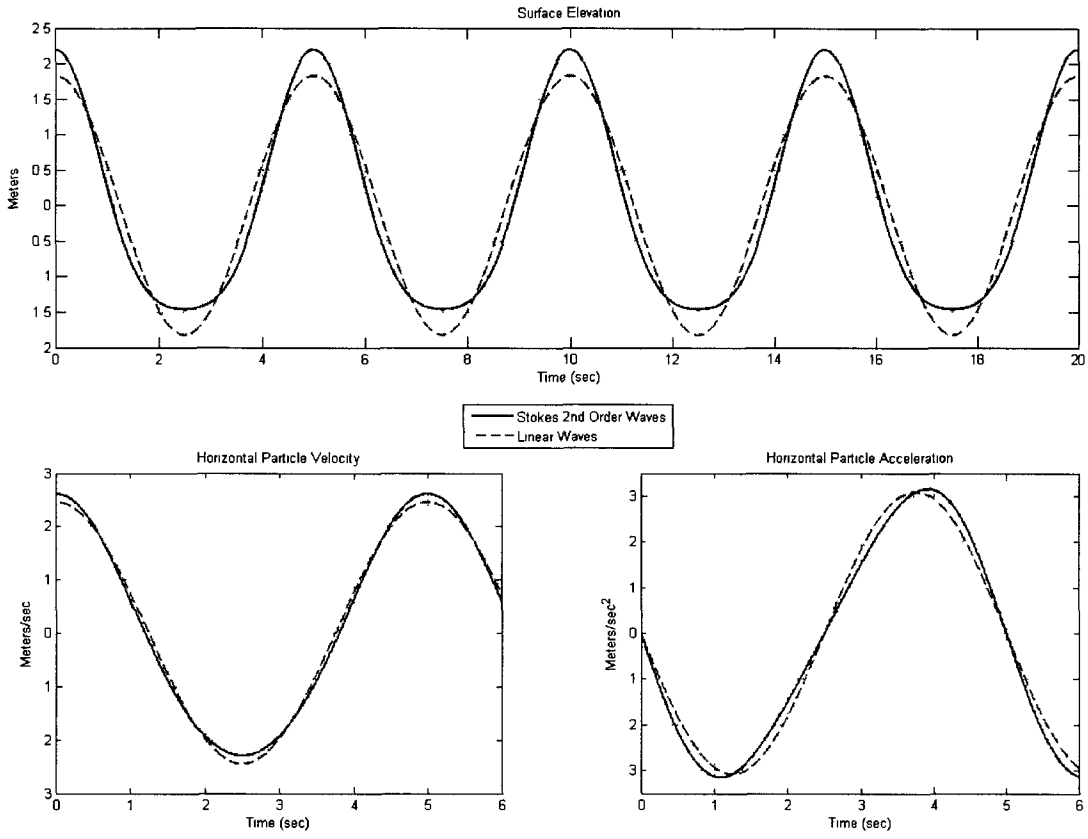

Figure 2.14: The Stokes 2nd order wave surface elevation (top), vertical water particle velocity (bottom left) and acceleration (bottom right) compared Airy waves. The waves had the following properties: T = 5 seconds, H = 3.654 meters, h = 10 meters, L = 36.54 meters, H/L = 1/10.

2.3.2 Evaluation of Performance of Subroutine

Once Stokes 2nd order waves were incorporated into the software, the subroutine's performance was verified. Stokes 2nd order waves are initiated in Aqua-FE in the fluid properties section of the **.opt* file. The *iwave* parameter controls the application of wave forces in the software. A value of 0 does not apply waves to the model, where a value of 1 applies Airy waves. An example of the **.opt* file formatting for Airy and Stokes 2nd order waves is shown below (a

single wave frequency is shown having a height and length of 0.25 m and 10.214 m, respectively). For Stokes 2nd order waves, a value of 2 should be utilized.

No Wave Loading

```
wave loading iwave =    0
no. freq.    nfreq =    0
```

Airy Wave Loading

```
wave loading iwave =    1
no. freq.    nfreq =    1
1: height, length   0.250E+00,
10.214
```

Stokes 2nd Order Wave Loading

```
wave loading iwave =    2
no. freq.    nfreq =    1
1: height, length   0.250E+00,
10.214
```

The horizontal and vertical water particle velocity and acceleration output by the software were first compared to analytical solutions for nonlinear waves with a height of 0.25 m and period of 2.8 seconds. These values were compared at various water depths, times and horizontal positions. For brevity, sample output results are provided in Table 2.5 for a location 0.5825 meters below the surface at x = 0, t = 0.1 sec.

Table 2.5: Analytical calculations compared to the Aqua-FE output result for wave properties associated with Stokes 2nd order wave.

Parameter	Analytical Value	Aqua-FE Output	% Difference
Horizontal Velocity	0.2663 m/s	0.2663 m/s	0.0
Vertical Velocity	-2.260×10^{-3} m/s	-2.260×10^{-3} m/s	0.0
Horizontal Acceleration	-7.184×10^{-3} m/s^2	-7.184×10^{-3} m/s^2	0.0
Vertical Acceleration	-0.422 m/s^2	-0.422 m/s^2	0.0

To verify the surface elevation and model response under Stokes 2nd order waves, a simple model of a wave following a 0.25 m diameter sphere on a 10 meter long line was

considered. The model was constructed of 102 nodes and 102 elements. The geometric and material properties of the model are presented in Table 2.6. The mooring line was selected to minimize its influence on the heave motion of the float. Figure 2.15 presents the results of this simulation. Good correspondence with expected wave following behavior was observed.

Table 2.6: The truss and spherical element dynamic behavior model's geometric and material properties

Component	Parameter	Value
Line	Effective Density	1025 kg/m^3
	Young's Modulus	2.0 x 10^{09} Pa
	Cross sectional Area	1.0 x 10^{-3} m^2
Sphere	Effective Density	100 kg/m^3
	Diameter	0.25 m
Stiffener	Effective Density	1025 kg/m^3
	Young's Modulus	2.5 x 10^{11} Pa
	Cross sectional Area	1.0 x 10^{-7} m^2

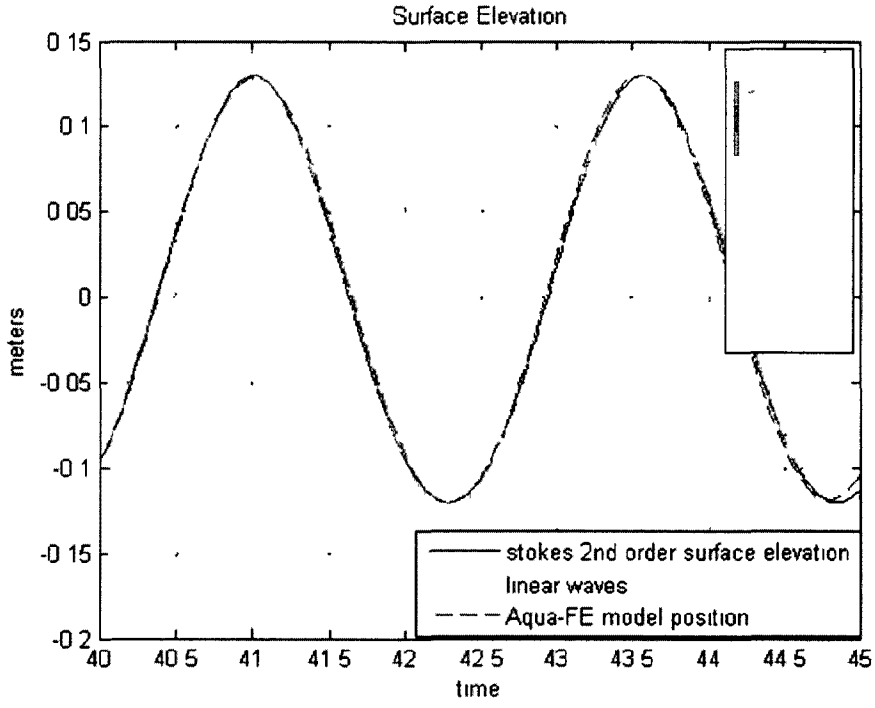

Figure 2.15: The surface wave elevation and Aqua-Fe model position.

Finally, unlike linear waves, Stokes 2nd order waves cannot be superimposed in Aqua-FE due to the addition of the nonlinear term. Therefore, a special control command was introduced in the subroutine *iwave*. This command stops the Aqua-FE simulation and outputs an error message when multiple wave frequencies are prescribed in the *nfreq* input in the **.opt* file. For example, if the **.opt* file shows the following:

wave loading iwave = 2
no. freq. nfreq = 1
1: height, length 0.250E+00, 10.214, 2.435
2: height, length 0.200E+00, 14.511, 5.056

the simulation will terminate and the following message is outputted to the **.res* file:

```
*ERROR* MULTIPLE WAVE FREQUENCIES NOT ALLOWED
```

The full Stokes 2nd order wave subroutine is presented in Appendix A.

2.4 Numerical Model Enhancement. Implementation of Shadowing Effects

An interdependent relationship exists between a partially or fully submerged object and the surrounding fluid. The object is displaced and deformed by the fluid, while motion of the fluid is altered by the presence of the object. From an engineering perspective, the fluid modification phenomenon should be taken into consideration because reduced water velocities occur behind structures due to blockage or shadowing effects and will impact subsequent components / structures. In the case of fish netting, this is discussed in Aarnses et al. 1990, Loland (1991) and Patursson et al. 2010, where a velocity reduction typically occurs behind nets

of various solidities. This can have significant influence on system motion and component loads as relative water velocities are reduced in these areas.

To rigorously model this phenomenon, a coupled fluid-structure interaction problem would have to be solved. The analytical solution of the coupled problem exists only for very basic geometries (see, for example, Patursson et al., 2008; Wang and Tan, 2008). In addition, numerical solutions of the coupled problem are computationally intensive and are mostly done for 2D and simple 3D geometries (Patursson et al., 2010). Thus, semi-empirical techniques to evaluate current shadowing must be resorted to in order to provide an efficient approach to modeling complex marine installations.

Aqua-FE was initially developed to apply the same environmental fluid conditions to every submerged element in the model, regardless of wake effects or blockage that may be occurring. This approach can provide good accuracy in the case of standard flexible systems such as oil risers, surface buoy moorings and small fish cages. However, recent studies into larger systems and net chamber water blockage and subsequent velocity reductions provide evidence that the code should be modified to account for a horizontal change in water velocity (Fredriksson et al., 2007a; Patursson, 2008).

Two approaches were considered to account for steady horizontal current velocity changes. The first was to develop a new element that incorporates a specific velocity reduction characteristic. This approach was used with a certain degree of success, but only a single cage system was modeled (Fredriksson et al., 2003). For a large system, however, this "reduced velocity" element would have to be generated for each existing element type (truss, buoy, net, etc) increasing the number of elements used in the model. In addition, if multiple velocity reduction locations exist, even more element types would be required, which would further

reduce the computational efficiency. The second approach was to allow multiple horizontal current profiles to be generated and applied to specific elements. Therefore, several different current values could be applied to different elements. If the current reduction is known, it can be incorporated into the model as different current velocities. This approach allows a horizontal current profile feature to be used in the model.

The code was modified to accommodate up to 25 horizontal current profile points. This allows for a variety of applications to be investigated and, if needed, a large current reduction in a complex system. The code was altered to produce a specifically generated file, which contains all the wave (height, length, and phase) and current (velocity, depth) information for each profile. The program then assigns the proper profile to the associated element for processing. This repeats for each element at each time step. Modifying the code in this manner allowed for the most versatile use of the model, without compromising the efficiency of the program.

Case studies verifying the proper implementation of this enhancement are presented in Chapters 3 and 4. The code modifications implemented in Aqua-FE was incorporated into the subroutine *pmesh*, presented in Appendix A.

2.5 Numerical Model Enhancement. Transition from Subcritical to Critical Reynolds Numbers

The final enhancement of the Aqua-FE software was the incorporation of the decrease in drag coefficients for cylindrical elements at high Reynolds Numbers. Whereas the spherical element has an accurate representation of the drag coefficient (DeCew et al., 2010), the cylindrical elements employ an approximation based upon Choo and Casarella (1971). This approximation does not incorporate the decrease in coefficient of drag at Reynolds numbers

approaching 10^5, as seen in Figure 2.16. This over-prediction of drag coefficients can result in increased drag forces and altered motion responses of a structure.

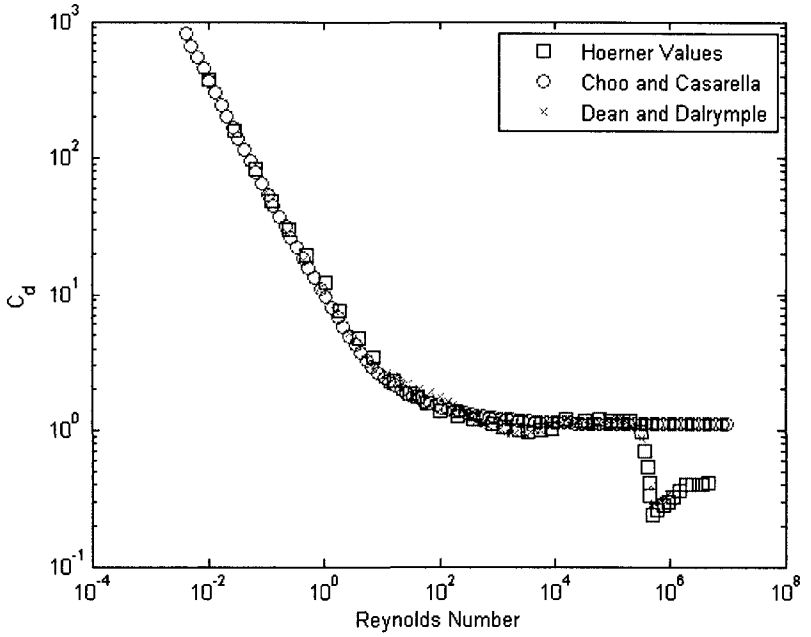

Figure 2.16: Coefficient of Drag versus Reynolds for a smooth circular cylinder. Choo and Casarella approximations work well at Re number below 3 x10^5, however neglect the reduction in coefficient of drag in critical flow regions.

2.5.1 Drag Forces on Cylindrical Elements

Recall that Aqua-FE incorporates both wave and current loadings on truss elements using a Morrison equation (Morison et al., 1950) formulation modified to include relative motion between the structural element and the surrounding fluid. The program calculates both the normal and tangential drag coefficients, at each time step, based upon the value of the Reynolds number. The experimentally observed variations of the normal coefficient of drag with Reynolds number for cylinders were presented, for example, by Hoerner (1965) and are shown in Figure 2.16. In numerical simulations, the drag coefficient for cylindrical elements has usually been approximated by formulations of Choo and Casarella (1971) (see Fredriksson et al., 2005c;

Haritos and He, 1992; Lader et al., 2007). However this approximation does not take into account the reduction in coefficients at high Reynolds numbers which is a result of the fluid boundary layer becoming fully turbulent causing the separation points to move aft. The point at which the steep reduction in drag coefficients occurs is referred to as the critical Reynolds number. Following the idea of Choo and Cadarella's, the coefficient of drag curve was divided into five sections, with each section approximated by linear or exponential functions, with a continuity condition imposed. This resulting relationship is as follows:

$$C_{dn} = \begin{cases} \frac{8\pi}{Re\, s}(1 - 0.87s^{-2}), & 0 < Re < 1 \\ 1.45 + 8.55Re^{-0.90}, & 1 < Re \leq 30 \\ 1.1 + 4Re^{-0.5}, & 30 < Re \leq 2.33 \cdot 10^5 \\ -3.41 \cdot 10^{-6}(Re - 5.78 \cdot 10^5), & 2.33 \cdot 10^5 < Re \leq 4.92 \cdot 10^5 \\ 0.401\left(1 - e^{\frac{-Re}{5\,99\,10^5}}\right), & 4.92 \cdot 10^5 < Re \leq 10^7 \end{cases} \quad (2.29)$$

$$C_{dt} = \pi\mu\left(0.55Re^{1/2} + 0.084Re^{2/3}\right) \quad (2.30)$$

where C_{dn} is the normal coefficient of drag, C_{dt} is the tangential drag coefficient, Re_n is the Reynolds Number, s = -0.077215655 + ln(8/Re) and μ is the fluid viscosity. Alternatively, for Reynolds numbers less than 2.33 x 10^5, the following approximation can be used, although not employed in this research: $C_{dn} = 10.435\ Re^{-0.761} + 1.083$. Figure 2.17 shows the normal coefficient of drag for cylinders along with the Choo and Casarella values and those utilized in the new numerical model. The Choo and Casarella expression for the tangential drag coefficient for cylinders was not modified.

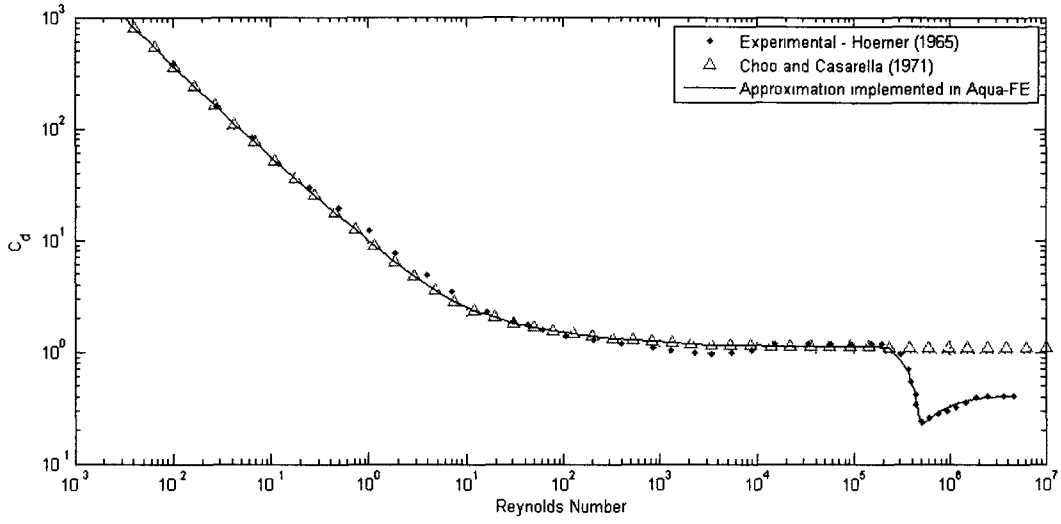

Figure 2.17: Normal drag coefficients for a cylinder. The experimental values are compared to the Choo and Casarella approximation and equation (2.29).

2.5.2 Validation of Drag Forces

The truss elements utilizing the drag coefficients (eq. 2.29) were verified by analyzing a cylinder, aligned perpendicular to the flow, in Aqua-FE and comparing the software's drag coefficient output data. A simple model was constructed of a fully submerged truss element as shown in Figure 2.18. The model consisted of 4 elements and 4 nodes. The geometric and material properties of the model are presented in Table 2.7. Seventeen constant with depth water velocities were applied to the model, selected to produce Reynolds numbers from 0.75 to 5×10^6. The output coefficients of drag values were compared to those predicted by equation 2.29 and are presented in Table 2.8. As expected, good correspondence is observed, verifying the proper implementation of this software enhancement.

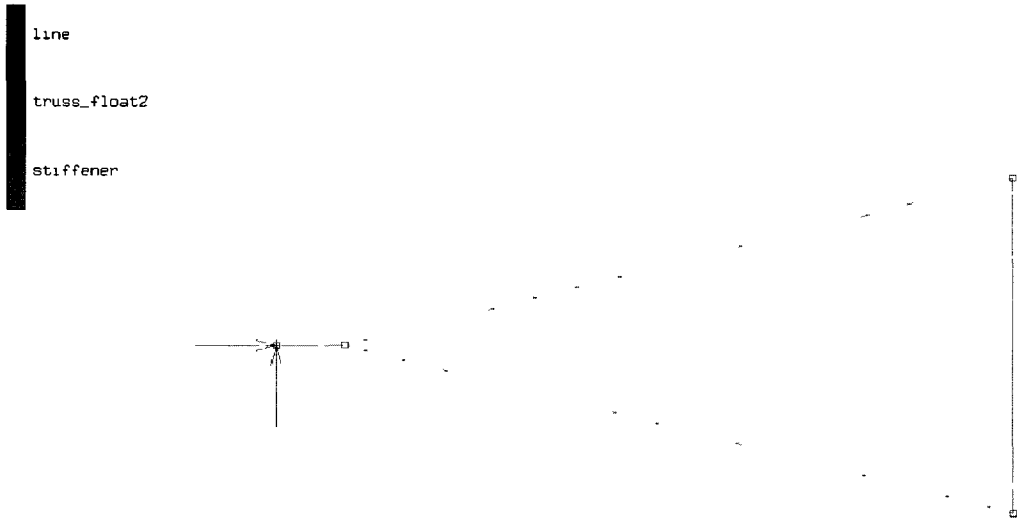

Figure 2.18: Aqua-FE model of cylindrical truss element generated to verify the drag predictions of the software

Table 2.7: Geometric and material properties of the model.

Component	Parameter	Value
Line	Effective Density	1025 kg/m^3
	Young's Modulus	2.0 x 10^{11} Pa
	Cross sectional Area	1.0 x 10^{-6} m^2
Truss	Effective Density	1025 kg/m^3
	Young's Modulus	2.0 x 10^{11} Pa
	Cross sectional Area	1.96 x 10^{-1} m^2
Stiffener	Effective Density	1025 kg/m^3
	Young's Modulus	2.5 x 10^{11} Pa
	Cross sectional Area	1.0 x 10^{-7} m^2

Table 2.8: Aqua-FE output and analytical calculations verifying the Aqua-FE output values.

Velocity (m/s)	Reynolds Number	Analytical C_d Calculations	Aqua-FE C_d Output	% difference
1.654×10^{-6}	0.7502	12.20	12.20	0.0 %
3.307×10^{-5}	15	2.18	2.18	0.0 %
0.441	2×10^5	1.109	1.109	0.0 %
0.706	3.2×10^5	0.9402	0.9402	0.0 %
0.816	3.7×10^5	0.688	0.688	0.0 %
0.904	4.1×10^5	0.517	0.517	0.0 %
0.97	4.4×10^5	0.397	0.397	0.0 %
1.036	4.7×10^5	0.309	0.309	0.0 %
1.102	5.0×10^5	0.243	0.243	0.0 %
1.433	6.5×10^5	0.262	0.262	0.0 %
1.764	8×10^5	0.283	0.283	0.0 %
2.205	1.0×10^6	0.302	0.302	0.0 %
2.866	1.3×10^6	0.327	0.327	0.0 %
3.748	1.7×10^6	0.368	0.368	0.0 %
4.41	2×10^6	0.400	0.400	0.0 %
6.615	3×10^6	0.405	0.405	0.0 %
11.024	5×10^6	0.408	0.408	0.0 %

2.5.3 Coefficient of Drag Sensitivity Study

With the drag coefficient for the truss element properly implemented, a sensitivity study was initiated to investigate the effect of the updated algorithms on two marine structures: a buoy used at the UNH offshore site as a boundary marker and a 600 m^3 Ocean Spar Technologies SeaStation™ fish cage. Both were placed using simplified moorings and analyzed under similar water velocities. The models were analyzed with the original and enhanced Aqua-FE software.

The offshore site marker consisted of a cylindrical float approximately 1.5 m long, 0.61 m in diameter and with a mass of approximately 160 kg (see Figure 2.19). These are placed at the corners of the demonstration site as navigational buoys. A model of the buoy was created in Aqua-FE and placed on a 25 meter line. The model consisted of 50 elements and 51 nodes. The

geometric and material properties are shown in Table 2.9. The waterline was placed similar to those in the field, half way up the cylinder.

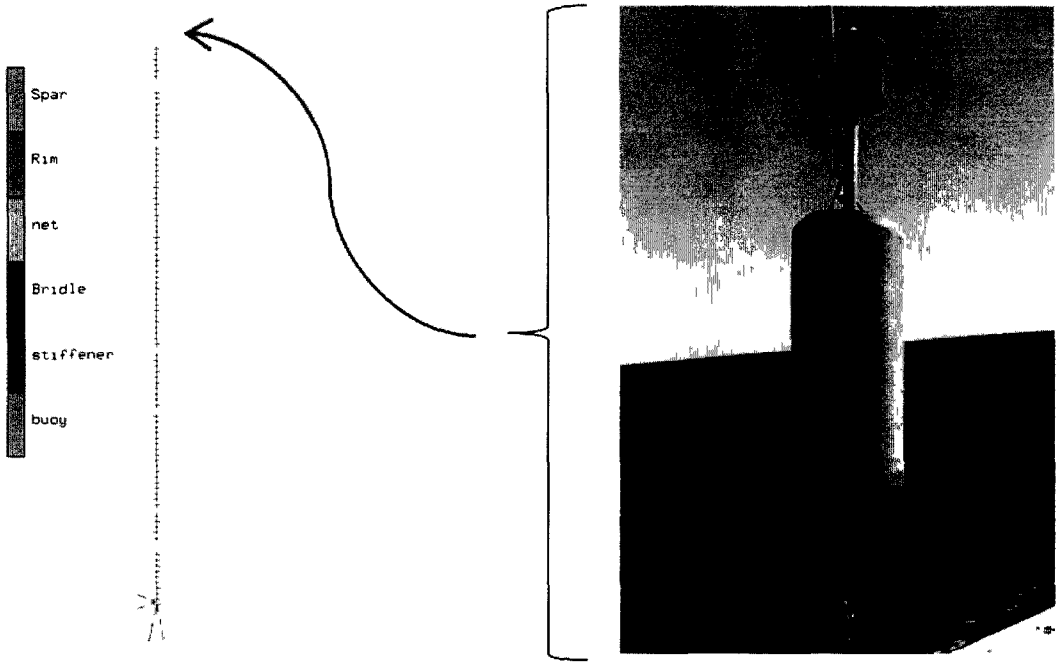

Figure 2.19: The offshore site boundary marker analyzed in this sensitivity study.

Table 2.9: The geometric and material properties of the buoy and mooring analyzed in this sensitivity study.

Component	Parameter	Value
Line	Effective Density	1004 kg/m^3
	Young's Modulus	1.03 x 10^9 Pa
	Cross sectional Area	7.917 x 10^{-4} m^2
Truss	Effective Density	356.9 kg/m^3
	Young's Modulus	2.0 x 10^{11} Pa
	Cross sectional Area	2.92 x 10^{-1} m^2

The second model consisted of a more complex system: a 600 m^3 SeaStation^{TM} fish cage manufactured by Ocean Spar Technologies. The fish cage is constructed of a central spar buoy and an octagonal rim held together by tensioned stays woven into the net. The spar buoy acts as

a variable buoyancy chamber, allowing the system to remain on or below the water surface. For this analysis, the net pen was positioned in the water column with one meter of freeboard on the spar. Two models of the fish cage were constructed: one with and one without a net chamber. The two models allow for the direct comparison of the netting's influence on the structure. The geometric and material properties of the system are shown in Table 2.10 and models can be seen in Figure 2.20.

Table 2.10: The geometric and material properties of the SeaStation™ fish cages analyzed in the sensitivity study.

Component	Parameter	Value
Line	Effective Density	1004 kg/m^3
	Young's Modulus	1.03 x 10^9 Pa
	Cross sectional Area	7.917 x 10^{-4} m^2
Spar	Effective Density	1025 kg/m^3
	Young's Modulus	8.59 x 10^9 Pa
	Cross sectional Area	6.64 x 10^{-1} m^2
Rim	Effective Density	1025 kg/m^3
	Young's Modulus	1.82 x 10^{10} Pa
	Cross sectional Area	5.85 x 10^{-2} m^2
Net	Effective Density	1025 kg/m^3
	Young's Modulus	1.00 x 10^{10} Pa
	Cross sectional Area	3.63 x 10^{-6} m^2
	repetitions	98
Stiffener	Effective Density	1025 kg/m^3
	Young's Modulus	2.00 x 10^{11} Pa
	Cross sectional Area	2.00 x 10^{-7} m^2

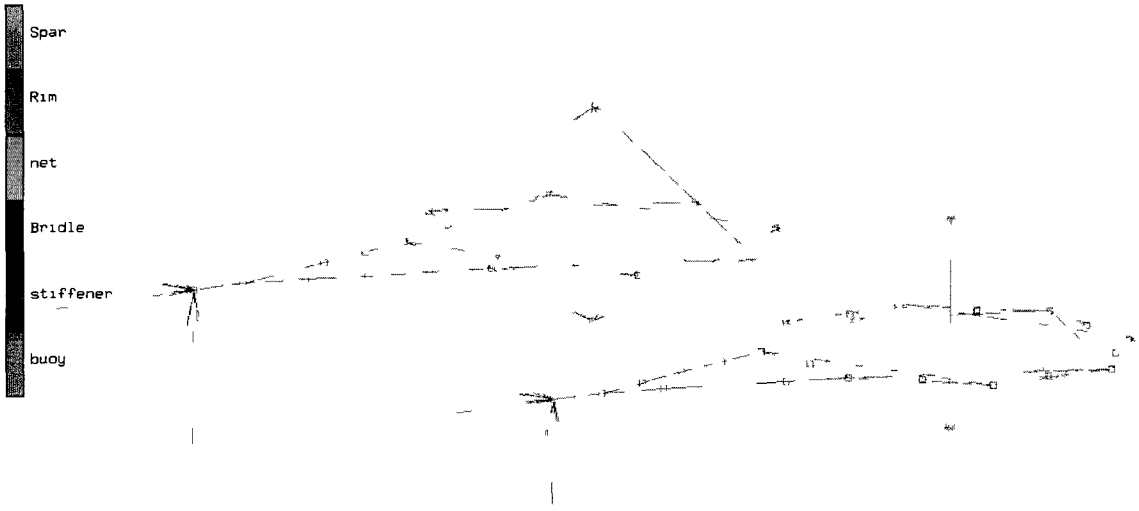

Figure 2.20: FEA models of two SeaStation™ fish cages were constructed in Aqua-FE. One had a net chamber (lower right), where the second one only had the rims and tensioned stays (upper left).

Both models were run under constant-with-depth water velocities of 1 and 2 ms^{-1}. The mooring line tension and buoy tilt angle was monitored for the site marker simulation. The fish cage mooring tension was also recorded. The net pen's motion response was not examined due to the simplified mooring system employed in the analysis. The results of the analysis are shown in Figures 2.21 through 2.24 and summarized in Table 2.11.

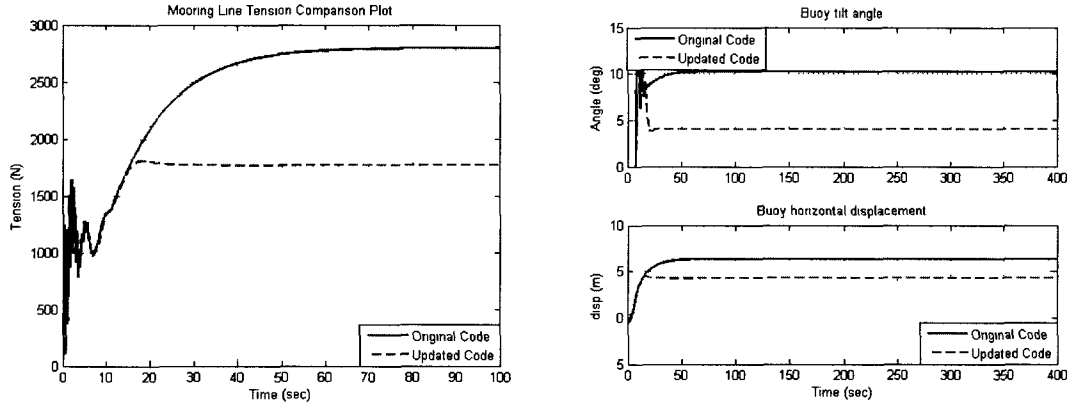

Figure 2.21: The site marker mooring tension and buoy tilt angle under the 1 m/s water velocity. The system was analyzed with the original and updated software.

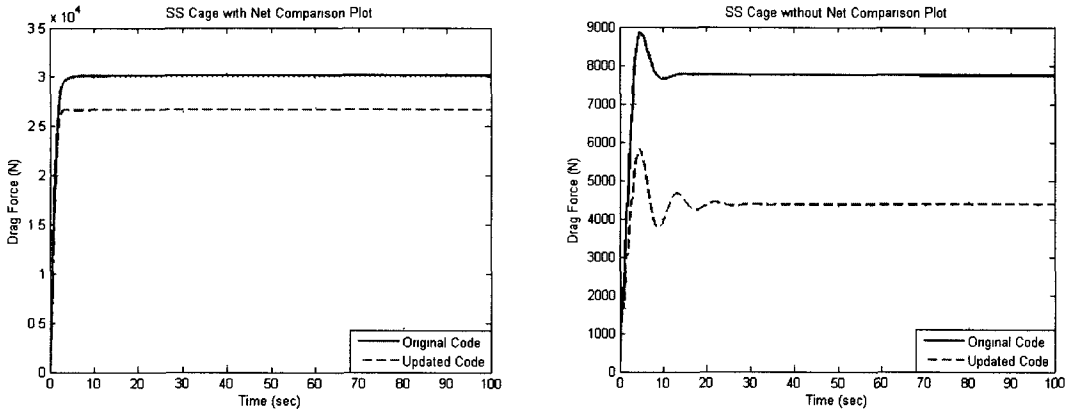

Figure 2.22: The fish cage drag force results under the 1 m/s water velocity. The cage with a net chamber (on left) and without (on right) was analyzed with the original and updated Aqua-FE software.

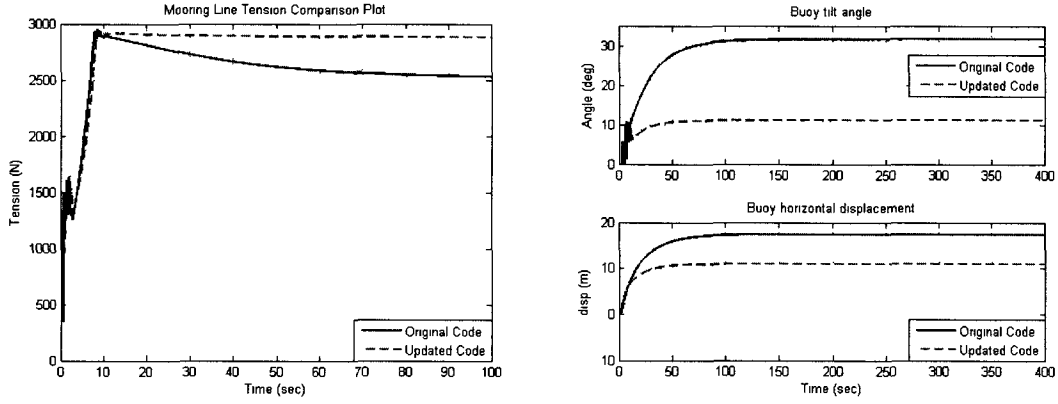

Figure 2.23: The site marker mooring tension and buoy tilt angle under the 2 m/s water velocity. The system was analyzed with the original and updated software.

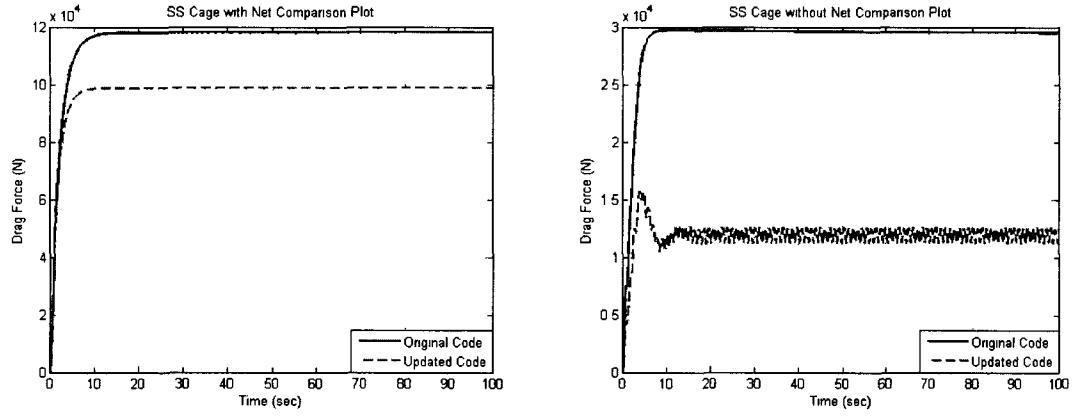

Figure 2.24: The fish cage drag force results under the 2 m/s water velocity. The cage with a net chamber (on left) and without (on right) was analyzed with the original and updated Aqua-FE software.

The steady state mooring tension results for both models are summarized in Table 2.11. The following observations can be made:

- The enhanced code predicts reductions in mooring force (36%), buoy tilt (approximately 50%) and horizontal displacement (29%) for the 1 ms^{-1} simulation.
- Similar results can be seen for the buoy under 2 ms^{-1}. However, the mooring tension predictions are increased for the upgraded software. This is a result of the significant decrease in buoy tilt angle, exposing more of the area to the oncoming flow, increasing the system drag.
- The updated code shows similar results in regards to the fish cages. Drag on the cages with and without the net chamber is reduced due to the decrease in coefficient of drag on the large diameter components spar and rims).
- It is interesting to note the influence of the net chamber on the total system drag. For the 1 ms^{-1} and 2 ms^{-1}, the net chamber accounts for 83.6% and 87.9% of the drag force, respectively.
- The netting also damps the cage system's response, as seen in Figure 2.23.

Table 2.11: Summarized output mooring tension results of the simulations.

Model	Environmental Loading	Original Code (N)	Updated code (N)	% Diff
Site Marker Buoy	Static	628.28	628.28	0.00
	1 m/s current	2799.1	1766.4	36.8
	2 m/s current	2518.7	2885.3	-14.5
Sea Station w/ Net Chamber	1 m/s current	30151	26677	11.5
	2 m/s current	118060	98728	16.3
Sea Station w/o Net Chamber	1 m/s current	7733.3	4374.9	43.4
	2 m/s current `	29507	11862	59.8

CHAPTER 3

CASE STUDY. FIELD TESTS AND NUMERICAL MODELING OF A SPHERICAL FISH CAGE SYSTEM

A case study was initiated to validate the Aqua-FE software upgrades by investigating the drag forces on a prototype aquaculture net pen in steady flows. A 450 m^3 spherical shaped Aquapod^{TM} cage system, developed by Ocean Farm Technologies (www.oceanfarmtech.com), was towed from Portsmouth Harbor to UNH's Open Ocean Aquaculture (OOA) site, located 15 km offshore in the Gulf of Maine, by the R/V Meriel B in September 2005. The OOA site location relative to the NH coast is shown in Figure 3.1. Water velocity and tow line tension measurements were recorded for 16 minutes with the cage fully submerged. Two sets of water velocity measurements were made, one by a Marsh-McBirney electro-magnetic current meter located on the tow vessel and the second by an Aquadopp Acoustic Doppler current meter located within the cage structure. The towline tension was measured by a Sensing Systems 53 kN (12,000 lbf) load cell. The drag of the fish cage at various water velocities was measured and compared to numerical model predictions under similar conditions. Portions of this work were presented in the IEEE/MTS Oceans'06 conference in Boston, Massachusetts and was published in the conference proceedings (see DeCew et al., 2006).

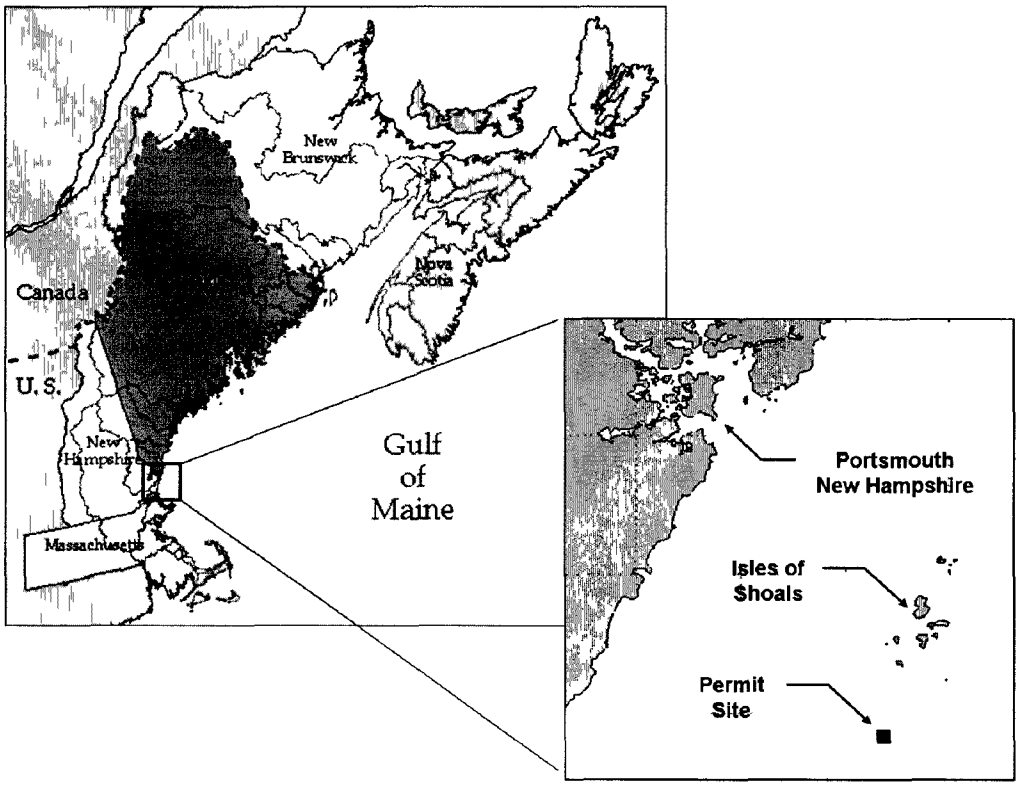

Figure 3.1: The open ocean aquaculture site is located off the coast of New Hampshire, USA in the southwest corner of the Gulf of Maine (Figure downloaded from http://spo.nos.noaa.gov and annotated).

3.1 Marine Fish Cage System

The Aquapod™ cage system, developed by Ocean Farm Technologies Inc, is different from traditional cage designs (Figure 3.2). Whereas typical gravity fish cages have upper and lower rims supporting a deformable cylindrical net chamber, the Aquapod™ system has a rigid spherical net containment structure. The 450 m^3 cage is constructed of 80 triangular panels, connected with galvanized hardware, forming a spherical chamber with a diameter of 9.75 m (32 ft). The Aquapod's 16 gauge (2 mm diameter) vinyl coated galvanized wire, 2.54 cm square mesh net is integrated within each triangular panel. The net has solidity of 16% (not including the cage framework), where the solidity is the ratio of projected area of the net over the outline

area, normal to the water flow. The deployed system was a 1:3 scale version of the full size system (volume of 3250 m^3) with a mass of 4040 kg (8900 lb).

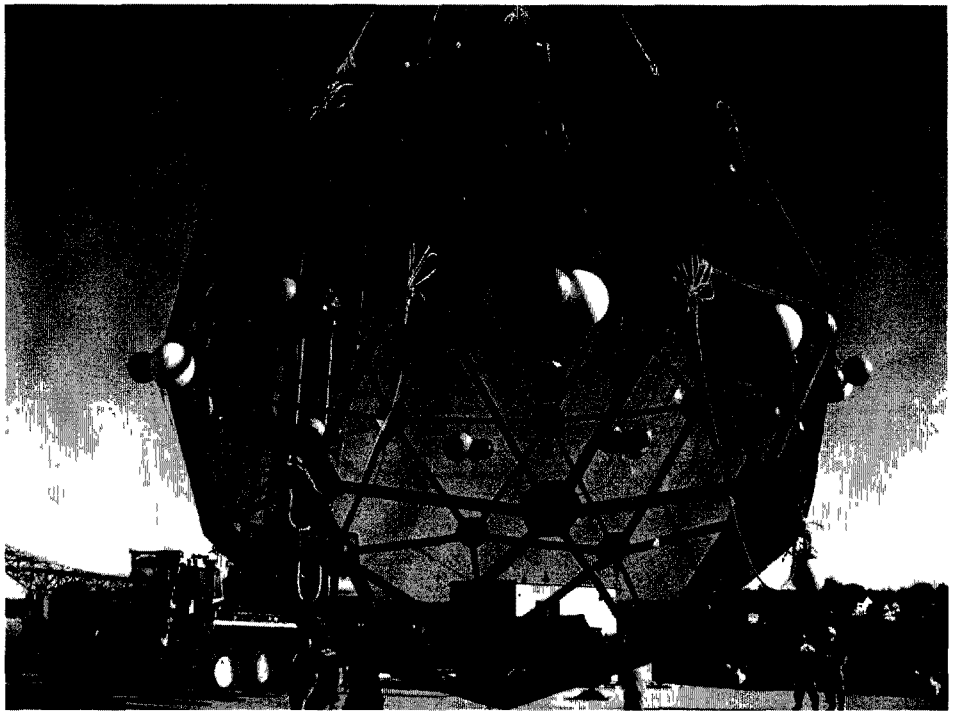

Figure 3.2: The 9.75 meter Aquapod™ fish cage.

3.2 Instruments and Calibration

Three instruments were used to measure the water velocity and towline tension. A Marsh-McBirney current meter was utilized to record the water velocity relative to the cage and was located on the tow vessel. An Aquadopp current meter was placed inside the cage structure to obtain water velocities inside the net pen. A Sensing Systems 53 kN (12000 lbf) load cell recorded the towline tensions (also located on the vessel).

The Marsh-McBirney current meter determines the water flow by measuring the voltage generated by the water moving through a magnetic field. The instrument outputs a voltage which is a linear measurement of water velocity. Prior to the tow experiment, this

instrument was calibrated in the UNH Ocean Engineering Wave/Tow tank. The current meter was towed at 7 different velocities, ranging from 0 to 1.71 m/s. The resulting calibration curve was linear and given by:

$$U = 2.8012v + 0.0217 \qquad (3.1)$$

where U is the water velocity (m/s) and v is the output voltage (volts). The calibration curve had a correlation value (R^2) of 0.999. The sampling rate was set to 10 Hz.

A Nortek Aquadopp current meter was the second water velocity measuring instrument employed in the tow test. The Aquadopp is a Doppler instrument which transmits acoustic signals that are reflected off particulates in the water column and utilizes the Doppler shift to determine the water velocity. The Aquadopp measures and averages the water velocity within a sampling volume 0.35 m to 1.5 meters from the instrument (most of the measurement occurs 1.1 m from the Aquadopp). This instrument is not suited for tank calibration due to lack of acoustic reflectors (particles) in the tank, so a field comparison between the Aquadopp and the Marsh-McBirney was performed in Great Bay, NH. Both instruments were deployed to measure the incoming tide over a 20 minute period. The Aquadopp's sampling rate was set at 1 Hz (maximum rate allowed). Table 1 lists the current meter results from this test. The values shown were averaged over 5 minute intervals. As can be seen from the table, the difference between the instrument measurements was less than 4.1% with the Aquadopp reading lower than the Marsh-McBirney. This difference was considered acceptable due to the different sampling methods utilized by each instrument.

Table 3.1: Comparison test results between the Marsh-McBirney and Aquadopp current meters.

Marsh-McBirney (m/s)	Aquadopp (m/s)	% Difference
0.5622	0.5437	3.3 %
0.5703	0.5470	4.1 %
0.5537	0.5404	2.4 %
0.5653	0.5452	3.5 %

A 53 kN Sensing Systems load cell was utilized to measure the drag of the cage system. The load cell was calibrated prior to the tow test at the Woods Hole Oceanographic Institution (WHOI). The load cell was placed within the WHOI Rigging Shop's Baldwin Material Testing Machine S/N 1010 and loaded statically in steps from 0 to 53 kN (12,000 lbf). Similar to the Marsh-McBirney current meter, the calibration curve was used during post-processing. The calibration curve for the load cell S/N 012, used in this experiment, is described by:

$$T = 18.94v + 1.482 \qquad (3.2)$$

where T is the tension (kN) and v is the output voltage (volts). The instrument was set to a 10 Hz sampling rate.

3.3 Preparation and Set-up

The Marsh-McBirney current meter and load cell were located on the tow vessel with the Aquadopp current meter located inside the cage (the Aquadopp is capable of recording the tension data on an internal memory card whereas the Marsh-McBirney is not). The Marsh-McBirney current meter was deployed away from the side of the vessel with a horizontal 2 meter (6.5 ft) I-beam and a vertical 1.5 meter (5 ft) aluminum pole (Figure 3.3). The I-beam was bolted to the vessel's gunwale, extending approximately 1 meter from the starboard side of the

vessel. A 2.5 cm diameter aluminum pole was secured to the end of the I-beam and extended to the water surface. The Marsh-McBirney meter was then attached to a 1.3 cm diameter stainless steel rod that protruded 1 meter into the water.

The load cell was located at the stern of the vessel (Figure 3.4). A tow support line was secured around the base of the vessel's knuckle-boom crane (not shown). The load cell, secured to a 222 kN (50,000 lbf) strong back, was shackled in-line with the tow line. The power cable, which carried the supply and output voltage for the load cell, ran to an Analog to Digital (A/D) board and a Labview Virtual Interface (vi) program, located at the bow of the vessel. This program provided the instruments with the required voltage (12 volts DC) and recorded the output voltages. It then applied the calibration curve and plotted the data for viewing on a laptop PC. Power for the auxiliary equipment (computer, power supply, etc) was provided by the ship's generator. A 183 meter (600 ft), 51 mm (2 in) Polysteel tow line was used to tow the cage system. The length was selected to minimize the vessel's propeller wash from affecting the net pen during the tow. Since the line was not continuous, sections of the line were shackled together and supported by floats.

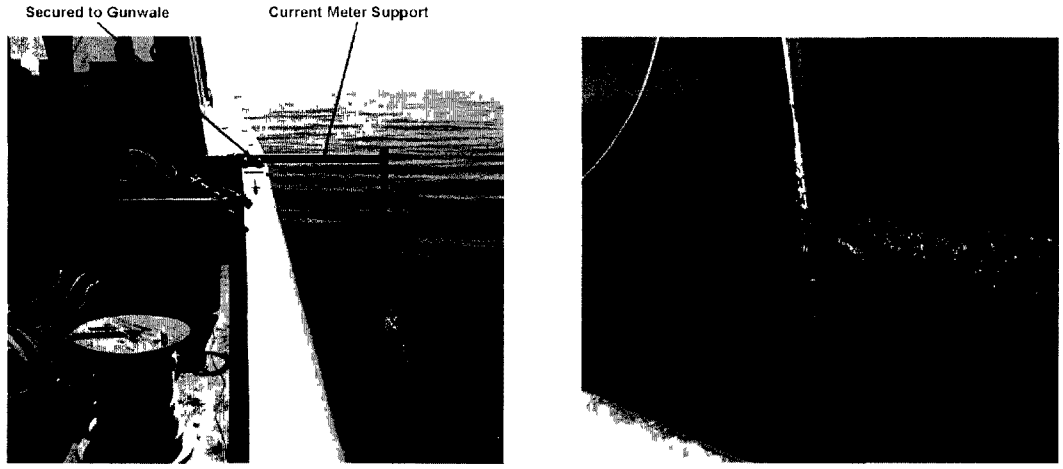

Figure 3.3: View of the Marsh-McBirney current meter and support.

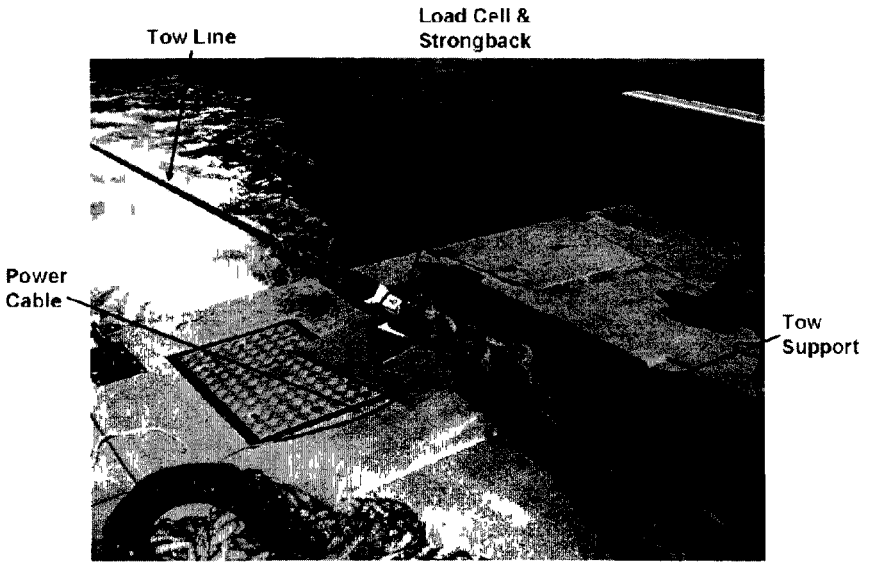

Figure 3.4: The load cell and tow line components.

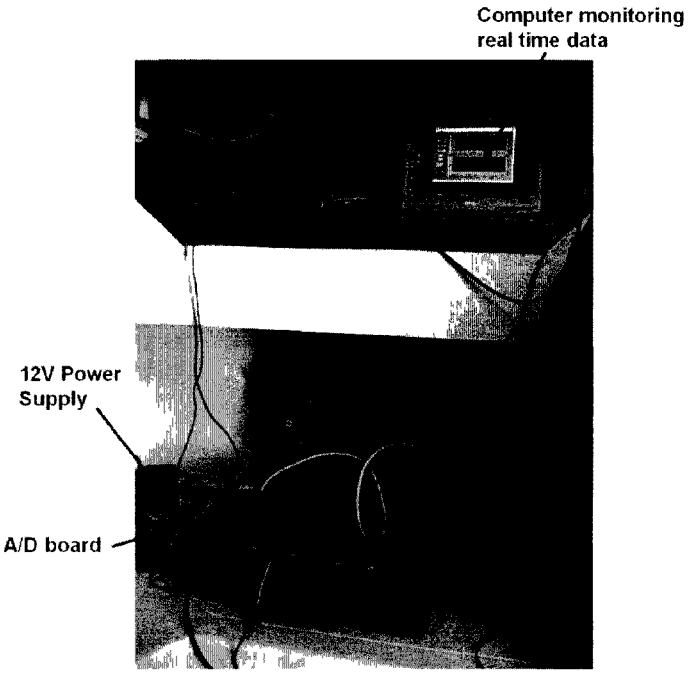

Figure 3.5: The A/D and vi utilized during the tow test. The power cables for the instruments ran to the A/D board, which was powered by the power supply. The data was then sent to the computer for viewing and analysis.

One important aspect of the tow test was to record the water velocity inside the cage structure. Understanding this "reduced" or altered water velocity will assist in the modeling of these types of structures as well as provide valuable information regarding the water blockage (if any) that occurs. The current velocity within the cage was recorded by the Aquadopp current meter. The current meter was secured within the cage with three lines (Figure 3.6). Two lines held the instrument vertically, with the third running to the front of the cage to keep the current meter from spinning. The current meter was located approximately 6 meters (20 ft) from the bow of the cage, along the "equator" or middle of the cage. The Aquadopp was installed within the cage during construction when the interior of the cage was easily accessible. In addition, this allowed the current meter to be properly oriented to the incident water flow.

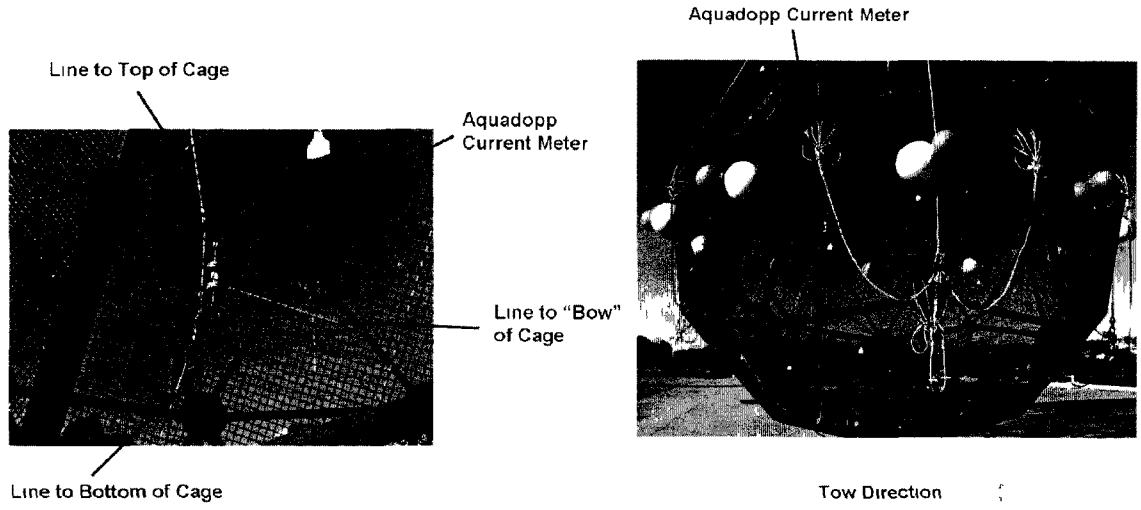

Figure 3.6: The Aquadopp current meter placed in the Aquapod™ cage (left) and orientation of the device to the tow direction (right).

3.4 Towing of the Cage

On September 21, 2005, the Aquapod™ cage system was towed from Portsmouth Harbor to the UNH's Open Ocean Aquaculture site by the R/V Meriel B. To reduce the draft and drag of the structure, thirty floats (twenty with a 72 lb net buoyancy and ten with a 140 lb net

buoyancy) were added to the middle or "equator" of the cage for the majority of the tow (Figure 3.7). The cage had approximately 5.5 m (18 ft) of draft in the water with the added flotation (normal draft ranges from 9.0 - 9.75 m). The original experiment plan was to tow the cage multiple times at a variety of water velocities. However, time constraints due to length of the tow, tide considerations, and operational concerns (attachment of the cage within the grid) limited the tow test. Therefore, only one tow test was conducted for approximately 15 minutes. Prior to the test, the floats around the center of the cage were removed, bringing the waterline to within 15 cm of the top of the structure. In an effort to conserve time, the vessel engine output (measured in revolutions per minute, RPM) was used to obtain a "speed" (as opposed to adjusting the RPM to obtain a certain water velocity). The vessel RPM was increased in six increments over the length of the test. The tow line tensions and water velocities, at the boat and within the cage, were measured throughout the entire test.

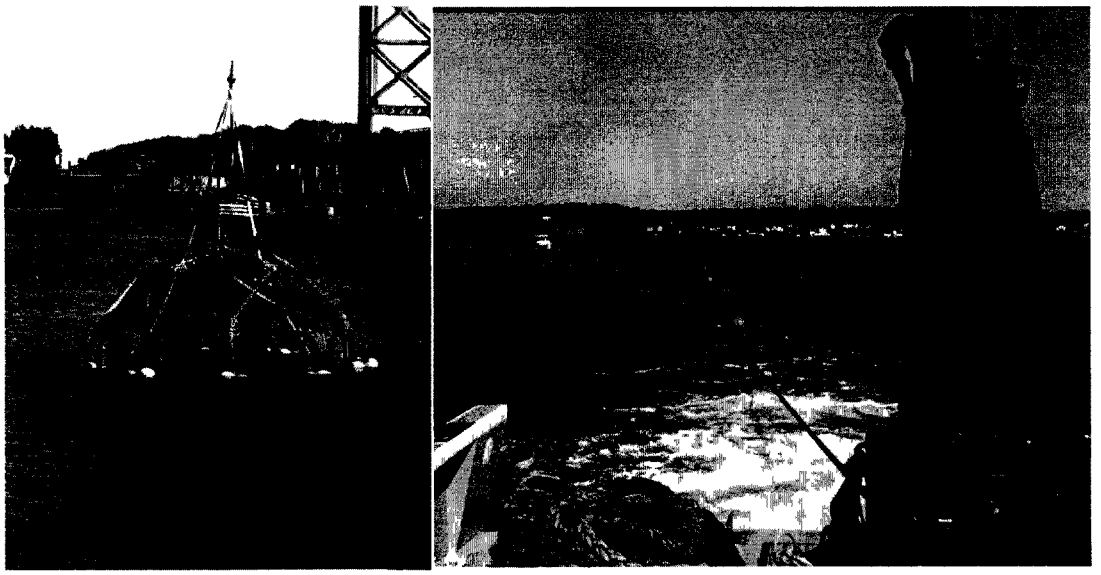

Figure 3.7: The cage was deployed from the NH Port Authority and towed out to the UNH Open Ocean Aquaculture Farm site with the R/V Meriel B.

3.5 Results of Tow Test

The water velocity measured by the Marsh-McBirney current meter and tensions measured by the load cell during the tow test are shown in Figure 3.8. Distinctive load "plateaus" can be seen throughout the first 10 minutes of the test, corresponding to a change in the vessel's RPM. The water velocity, although following the same trends, is not as well defined. The mean drag of the system ranges from 6.1 kN (1370 lbf) at 0.56 ms^{-1} to 32.2 kN (7250 lbf) at 1.05 ms^{-1}. Recall that these tensions include the drag force of the tow line.

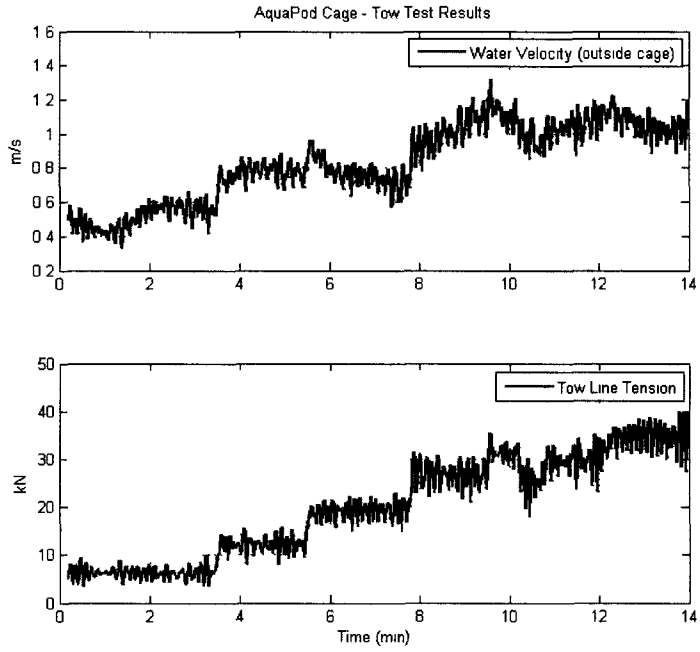

Figure 3.8: Water velocity and load cell readings during the experiment.

Detailed variations in water velocity and tension measurements can be seen in the subset time series results, shown in Figure 3.9. The sinusoidal pattern shown is attributed primarily to the waves present. The average time between peak tension forces is approximately 8 seconds, similar to the dominant wave period measured at that time (Figure

3.9). This phenomenon occurred throughout the test, regardless of water velocity. Waves were measured by the Gulf of Maine Ocean Observing System (GOMOOS) buoy B0120, located on the western Maine shelf (Figure 3.10).

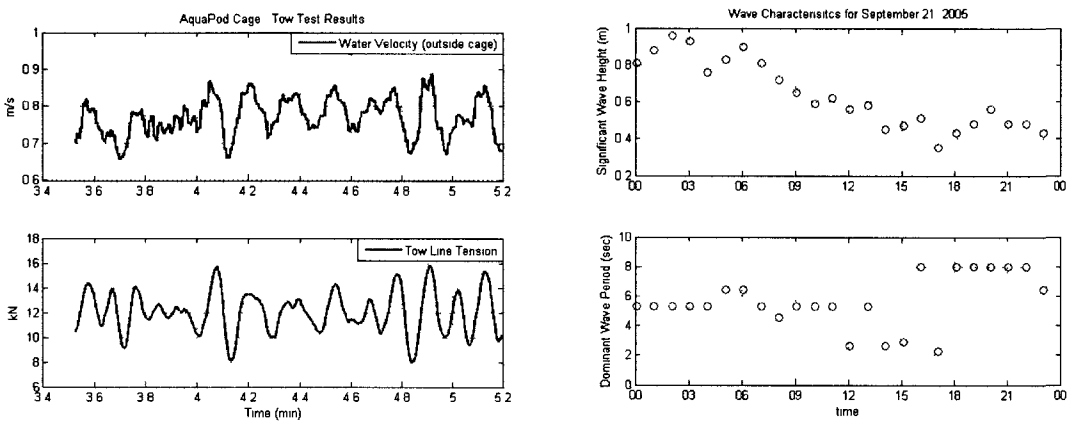

Figure 3.9: A subset of load cell tension measurements and wave characteristics present of the day of the tow. The tow test was initiated at 16:00 EST.

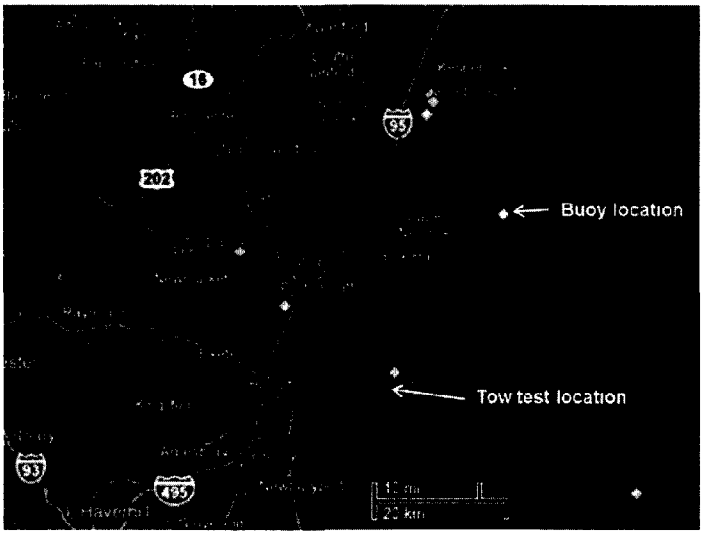

Figure 3.10: The GOMOOS buoy was located at 70° 25'40'' W, 43° 10'51'' N, approximately 22 km to the Northeast of the tow test site.

The water velocities at the vessel and within the cage are compared in Fig. 3.11. The two time series data sets follow similar trends throughout the test, although the water velocity

within the cage is reduced. Due to different sampling rates between the instruments, the Marsh-McBirney data set (water velocity at the vessel) was filtered by taking a 10-point average. For the first 6 minutes of the test, a distinctive water velocity reduction takes place inside the cage. For example, average current velocities drop from 0.56 and 0.77 ms^{-1} to 0.21 and 0.32 ms^{-1} for the Marsh-McBirney and Aquadopp current meters, respectively. This represents a water velocity reduction of 63.2% and 57.8%.

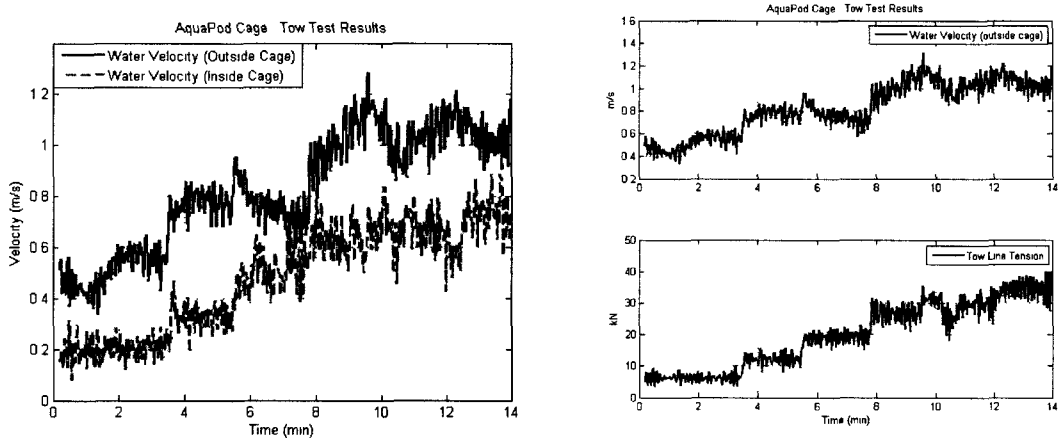

Figure 3.11: The measured water velocity reduction and tow line tension.

From the 6th to 8th minute, however, a different trend is evident. The exterior water velocity decreases slightly (below 1.5 knots), but the interior velocity increases to an average of 1.21 knots. The tow line tension shows a similar result with the load increasing to an average of 18.99 kN at approximately the same water velocity. One explanation for this is the effect of the vessel's propeller wash on the cage. One of the main assumptions with this test set-up is that the water velocity at the vessel is the same velocity that the cage is experiencing. Therefore, any change in water velocity (such as propeller wash or a different current field at the cage, as opposed to the water velocity at the tow vessel), will affect the data. Propeller wash, in general, is a turbulent flow generated by the vessel's propeller moving through the water column. This

area of increased water flow typically extends aft of the vessel (which can be seen in Figure 3.7). This flow dissipates with time into the surrounding environment. However, if the flow was present at the cage, the water velocity affecting the cage was greater than that measured at the tow vessel.

This consistent velocity increase within the cage, found at minute 6, suggests in part, that the water velocity outside the cage (but not at the tow vessel) was increased. The final stages of the test (minutes 12 through 14) support this theory, showing a slight increase in the tow line tension and interior water velocity, with a slight decrease in the water velocity outside the cage. It is important to note that at minute 9.5, the vessel did decrease its speed for approximately 1 minute due to operational concerns. This might have had an effect of not bringing the cage into a steady state load regime, and therefore the data from this time interval was not included in the discussion below.

Table 3.2: Water velocities measured by Marsh-McBirney and Aquadopp current meters during the first six minutes of the experiment.

Water Velocity (at vessel) knots	Water Velocity (inside cage) knots	% Reduction
0.0000	0.0000	0.00 %
1.0824	0.3982	63.2 %
1.4972	0.6314	57.8 %

3.6 Tow Test Discussion

Water velocity data at the tow vessel and within the cage, as well as associated tow tensions, were successfully collected. A current reduction was observed inside the net pen. However, the test was limited in scope due to time constraints. As a result, information

regarding the drag force of the fish cage at high water velocities was limited. The following observations related to improvement of such tests in the future can be made. The 183 meter line used to tow the cage was possibly not long enough to allow the system to escape the propeller wash entirely. In addition, time constraints only allowed one test to be performed, instead of multiple runs at set velocities as planned. In the future, steps can be taken to insure a more successful test. For example, the tow line can be lengthened and the test can be performed in "stages," where the vessel can come up to speed for a short period of time (assuming steady state loads can be obtained), record the necessary data, and slow down to a minimal forward velocity. This will allow the propeller wash to dissipate after each burst. Mounting an "outside" current meter directly in front of the cage would also be useful. Finally, the tension measurements presented in this paper include the drag of the tow line. A separate experiment should be performed prior to the next tow test to determine the line's drag.

Regardless of any propeller wash effect, the obtained data did provide insight into the cage's internal velocity reduction. In addition, the obtained load measurements validate the structural integrity of the system. These results will help the next generation of Aquapod™ structures for use in the open ocean aquaculture industry.

3.7 Numerical Model Comparison

The Aqua-FE software updates, described in Chapter 2, were then validated using the obtained *in-situ* fish cage drag and velocity reduction measurements. A numerical model of the Aquapod™ fish cage and tow line was constructed using 176 nodes and 399 elements, as seen in Figure 3.12. The towline floats were also placed in similar locations as those in the field. The end of the tow line was fixed at the height representing the stern of the tow vessel. The geometric and material properties of the model are shown in Table 3.3.

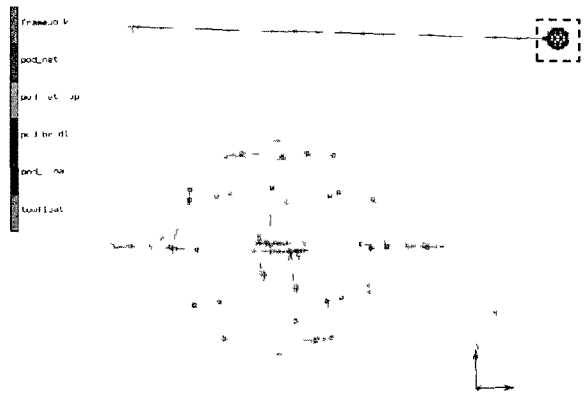

Figure 3.12: The field test set-up was recreated in Aqua-FE. The cage in the dotted box is zoomed in above.

Table 3.3: The fish cage and tow line properties utilized in Aqua-FE.

Component	Parameter	Value
Framework	Effective Density	830.3 kg/m^3
	Young's Modulus	2.758 x 10^9 Pa
	Cross sectional Area	1.06 x 10^{-2} m^2
Net	Effective Density	11040 kg/m^3
	Young's Modulus	2.0 x 10^{11} Pa
	Cross sectional Area	3.234 x 10^{-6} m^2
	Repetitions	64
Stiffeners	Effective Density	1025 kg/m^3
	Young's Modulus	2.5 x 10^{11} Pa
	Cross sectional Area	1.50 x 10^{-6} m^2
Tow line	Effective Density	963.5 kg/m^3
	Young's Modulus	1.06 x 10^9 Pa
	Cross sectional Area	5.067 x 10^{-4} m^2
Float	Effective Density	1014 kg/m^3
	Young's Modulus	2.0 x 10^{11} Pa
	Cross sectional Area	1.10 x 10^{-2} m^2
Tow Float	Effective Density	117.63 kg/m^3
	Diameter	0.419 m

The simulations were performed for three water velocities, as seen Table 3.4. The first two water velocities were similar to the lower velocities observed in the tow test results. However, due to propeller wash effects observed in the field experiment, the third water velocity was selected to be a current of 1 ms^{-1}.

To accurately model the field conditions, it was important to take into account the component shadowing observed in the field testing. To validate the effectiveness of the new hydrodynamic "shadowing" feature in Aqua-FE, the model was analyzed with and without an internal water velocity reduction. For one set of simulations, the water velocity affecting the aft portions of the cage (shown in Figure 3.13) was reduced to the values measured in the field (Table 3.4). The second set of numerical investigations did not reduce the interior water velocities. The predicted tension in the tow line was recorded for comparison to the field test results.

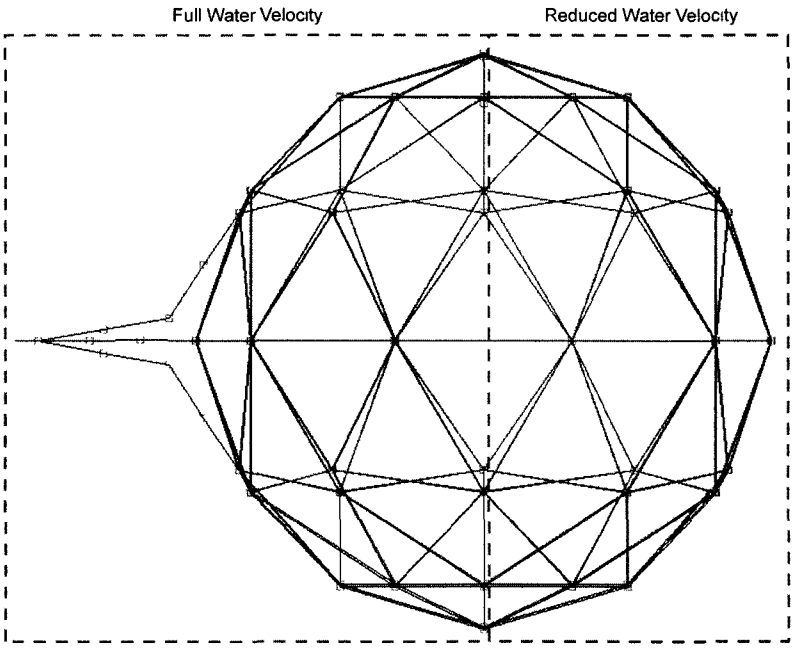

Figure 3.13: The full ambient water velocity was applied to the front half of the cage system. The water velocities measured inside the cage were applied to the aft portions of the model.

The output tension results are shown in Table 3.4. The water velocity inside and outside the cage system are shown along with the measured tow line tension from the field experiment. The field measurement data is then compared to the numerical model predictions with and without the shadowing effects applied to the system.

Table 3.4: Comparing the average drag force with the predicted numerical model

Incident (Exterior) Water Velocity (ms^{-1})	Reduced (Interior) Water Velocity (ms^{-1})	Field Measurement[a] (kN)	Numerical Model Prediction with velocity reduction (kN)	% Diff	Numerical Model Prediction w/o velocity reduction (kN)	% Diff
0.56	0.21	6.10	5.54	9.18 %	9.29	34.33 %
0.77	0.33	12.00	10.75	10.71 %	17.44	31.19 %
1.00	0.40	----	17.61	----	28.92	----

[a] Average tension result shown in the table.

It can be seen in the table that the implementation of the shadowing effect in Aqua-FE improved the model's predictions showing the importance of this numerical model upgrade. When the water velocity reduction was applied to half the fish cage, the numerical model predicted results within approximately 10% of the measured tensions. It is important to note that the measurement differences between the current meters and the assumption of the choice of the "shadowed" portion of the cage will affect the output results. Therefore, this accuracy is considered acceptable for such tests as there were uncertainties in the field experiment. In contrast, when the water velocity shadowing approach was not utilized, Aqua-FE over-predicted the drag forces by 30%. This difference is significant, and when designing or deploying marine equipment, would result in increased mooring sizes, costs, and structural integrity requirements of the fish cage system. Taking this decreased velocity into account is important in order to obtain accurate numerical model predictions and provide critical

information for field operation decisions. By incorporating this specific reduction into Aqua-FE, the loads and motions on similar Aquapod™ systems can be predicted more accurately. In the field, this reduction translates into a lower mooring line load, less current for fish to swim against and increased feed retention within the net chamber.

CHAPTER 4

CASE STUDY. DYNAMICS OF SINGLE POINT MOORED FISH CAGE

A second case study was performed to better understand the coupled motion and load response of a small scale fish cage secured in a single point mooring (SPM). In this study, the dynamic behavior of the Ocean Cage Aquaculture Technology (OCAT) system, developed by the American Soybean Association International Marketing (ASAIM) and the U.S. Soybean Export Council (USSEC), under various current regimes was investigated as a function of net solidity. The model was validated with data obtain from a series of tow tests using a Froude scaled physical model. The test results were compared to numerical model predictions under similar conditions. Once this validation was complete, the cage and mooring system was analyzed with the numerical model under various current profiles. The submergence depth of the cage and mooring component tension as a function of net chamber solidity was investigated. Note that portions of this research were originally published in Aquaculture Engineering (DeCew et al., 2010).

4.1 Introduction to Single Point Moorings

Single point mooring of offshore aquaculture fish cages has recently been under investigation as an alternative to the traditional grid array (presented, for example, in Baldwin et

al., 2000; Fredriksson et al., 2007) or fixed multipoint mooring (described in DeCew et al., 2005; Loverich and Forester, 2000). There are several advantages to this mooring configuration consisting of a lone anchor point connected to a fish cage by a mooring chain or cable. Typically, one or two intermediate floats are present to prevent entanglement and provide reduction of the wave-induced loading on the anchor (see Figure 4.1 for a particular fish cage/mooring system analyzed in this chapter). One of the advantages is a substantial reduction in benthic accumulation of waste products as compared to the traditional grid mooring system due to distributing fish waste over a larger area (see Goudey et al., 2001 and Goudey et al., 2003). Another advantage is a possible reduction in mooring costs per cage which can be as much as two-fold, as in the example considered by Goudey et al. 2001. From the engineering point of view, a potentially beneficial property of the SPM system is its ability to align with the prevailing current or weather direction minimizing the projected area and, correspondingly, the environmental loading and stresses in mooring components. Structural performance and reliability of the SPM with a gravity cage under several environmental loading scenarios was rigorously studied by Huang et al. 2009 utilizing numerical and physical model testing. Even more improvements in structural reliability can be obtained if the cage buoyancy is set such that the net pen naturally, on its own, submerges when environmental loading exceeds a certain threshold.

There are several intrinsic drawbacks of the SPM system that have to be taken into account by the mooring designers, installers, and fish farmers. First of all, the SPM lacks redundancy allowed by the traditional mooring configurations, so increased safety factors have to be used in the selection of anchors, mooring lines and other structural components. Secondly, the mooring experiences significantly more motion. This increases the possibility of damage due to friction, possibly exacerbated by biofouling. In particular, excessive motion may

lead to the failure of connecting hardware, and the integrity of the mooring can be lost as described in Goudey et al. 2003. The mooring scope (the ratio of the mooring line length to the water depth) appropriate for the chosen anchoring configuration results in a certain watch circle, so special care should be taken to avoid collision or entanglement with other components of the fish farm, e.g. other net pen systems, feed buoys, feed hoses, or service platforms. Lastly, adoption of the SPM results in periodic changes in the direction of tension applied to the anchor. This variability must be taken into account while designing the anchoring system. Two possible approaches, proposed by Goudey at al. 2003, include a properly selected dead-weight or a cluster of opposing drag-embedment anchors.

4.2 Description of the Small-Volume Ocean Cage Aquaculture Technology System

The OCAT design is a small volume, high fish stocking density cage system secured by a single point mooring (see Figure 4.1). The system was proposed by the American Soybean Association International Marketing (ASAIM) and the U.S. Soybean Export Council (USSEC) to increase opportunities for utilizing soy-based feeds for the aquaculture industry. Standing 4.5 meters high with a lower square base panel of 7 by 7 meters, the truncated pyramid design incorporates a volume of roughly 100 cubic meters (Goudey, 2004). The cage has been deployed with a fish density approaching 60 kg/m^3, whereas standard practice has a density of 20 kg/m^3. The cage's small size allows for an increased water flushing rate, reducing areas of low oxygen zones that can occur in large net pens. The increased stocking density employed by this cage system was shown to not negatively impact the fish growth or health (Cremer et al., 2003). The cage frame is constructed of HDPE pipe sections and galvanized steel corner weldments. A

pendant chain is suspended centrally from the bottom of the cage by means of an equidistant rope bridle. Each HDPE pipe section can be fully or partially flooded with water to increase or decrease the system's flotation. The net chamber is secured to each corner, minimizing deformation and providing a fixed volume for fish activity.

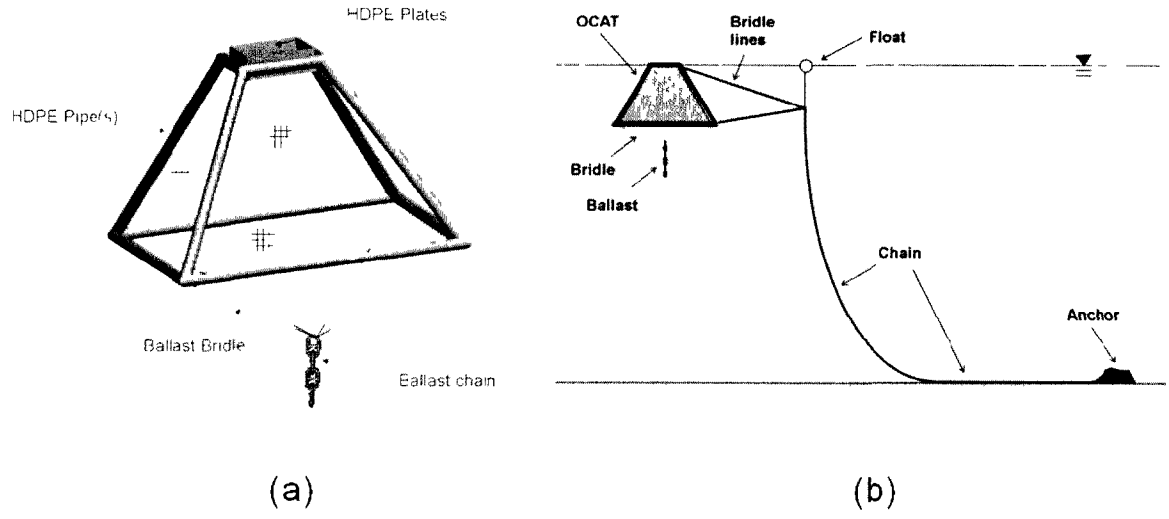

Figure 4.1: (a) The OCAT truncated pyramid cage frame constructed with HDPE pipes. Ballast hangs below the system providing additional stability to the system. (b) The single point mooring secured with a deadweight anchor, mooring chain, surface float and two pairs of bridle lines.

The system is anchored by a single point mooring. A 5000kg concrete deadweight anchor secures the system to the seafloor (Figure 4.1b). Three lengths of chain (25 mm and 19 mm diameters stud link and 13 mm long link) run from the anchor to a 2.2 kN float. Finally, upper and lower bridle lines secure the cage to the mooring resulting in an overall mooring scope of 3.45:1. The single point mooring configuration permits the cage to align with prevailing currents. The cage buoyancy was set such that the waterline bisects the top rim (resulting in a total cage reserve buoyancy of 1.33 kN). This waterline is achieved by flooding the lower HDPE rims with water increasing its mass. These adjustments allow the system to self-submerge in

extreme storm events such as typhoons. More information on the system can be found in Risso (2007). Cage and mooring details are presented in Table 4.1.

4.3 Physical Model and Experimental Setup

To validate the numerical model, tow tests on a scaled physical model were performed. A 1/10 Froude scaled model of the cage frame was constructed using PVC pipe sections for the top and bottom rims and wooden dowels for the diagonals. The top pipe sections were capped off to provide buoyancy, and the lower rims were flooded to obtain proper cage hydrostatics. The scale model cage is shown in Figure 4.2. Once the frame construction was complete, the bridle lines, ballast bridle and ballast chain were assembled. The model parameters are shown next to their full scale counterparts in Table 4.1. The cage center of gravity (CG) and center of buoyancy (CB) locations of the full and model scale systems were scaled and matched accordingly.

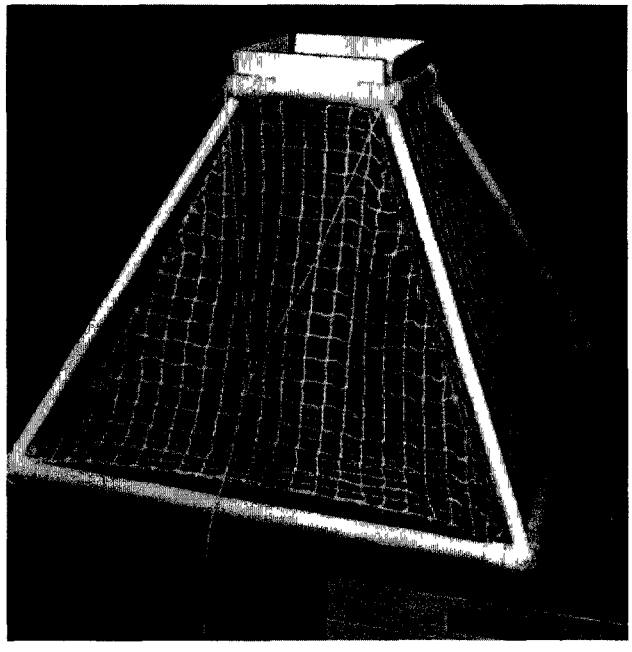

Figure 4.2: 1:10 Froude scale model of the OCAT cage

Table 4.1: The cage and mooring full and model scale components.

Cage Component		Full Scale	Model Scale
Lower Rim	Length	7 m	0.70 m
	Diameter	0.28 m	0.028 m
Angled Rim	Length	5.7 m	0.57 m
	Diameter	0.20 m	0.02 m
Top Rim	Length	2.0 m	0.20 m
	Diameter	0.28 m	0.028 m
Splashboards	Length	2 m	0.2 m
	Width	0.3 m	0.03 m
	Thickness	0.01 m	0.001 m
Ballast Bridle	Length	5 m	0.05 m
	Diameter	0.025 m	0.0025 m
	Material	Nylon	Nylon
Ballast Chain	Length	3 m	0.3 m
	Diameter	0.032 m	0.0032 m
	Mass	96 kg	0.096 kg
Net	Mesh Size	0.03 m	0.03 m
	Twine Diameter	0.0025 m	0.0025 m
	Solidity	14.8 %	14.8 %
Lower mooring chain	Length	46 m	4.6 m
	Diameter	0.025 m	0.0025 m
	Mass	655.0 kg	0.655 kg
Upper mooring chain	Length	20.5 m	2.05 m
	Diameter	0.019 m	0.0019 m
	Mass	167.2 kg	0.167 kg
Buoy chain	Length	3 m	0.3 m
	Diameter	0.013 m	0.0013 m
	Mass	10.7 kg	0.011 kg
Float	Diameter	1 m	0.1 m
	Buoyancy	2.2 kN	2.2 N
Upper Bridle Extension	Length	12.4 m	1.24 m
	Diameter	0.024 m	0.0024 m
	Material	Polyester	Nylon
Upper Bridle line	Length	3.57 m	0.36 m
	Diameter	0.018 m	0.0018 m
	Material	Polyester	Nylon
Lower Bridle Line	Length	12.66 m	1.27 m
	Diameter	0.018 m	0.0018 m
	Material	Polyester	Nylon

The compliance of the mooring lines was not replicated in the physical model because it was not critical for analysis of the steady state drag forces generated on the cages by constant currents. Accurate modeling of the mooring compliance is critical in oscillating loads, such as waves, which were performed in a separate study (Risso, 2007).

One of the principal forces acting upon the fish cage of the considered design is the drag associated with the net, making modeling the net important. Drag performance of the net is usually characterized by its solidity (Aarnses et al., 1990), defined as the projected area of the net divided by the overall outline of the net area. For a square mesh, for example, the Solidity (S) is given by:

$$S = \frac{2Ld - d^2}{L^2} 100\% \qquad (4.1)$$

where L is the side mesh length and d is the twine diameter. A net with a high solidity has more water "blockage" than one of a lower solidity.

In this study, the model net solidity was taken to be the same as that of the full scale system without geometrically reducing thread diameter and mesh size. This was done to better represent the Re – dependent frictional drag forces on the net. Otherwise, flow around the net threads would be more viscous (corresponding to lower Reynolds number), contributing to possible greater net drag. This phenomenon is discussed in more detail in Palczynski (2000) and Fredriksson (2001). The net used in the study had a square mesh size of 0.03 m, twine diameter of 0.0025 m and solidity of 14.8%.

Physical model tow testing was completed in the UNH wave/tow tank (36.5 m long by 3.05 m wide by 2.44 m deep). The model was towed through the water via a carriage system that travels above the tank (see Figure 4.3). A towing staff was fabricated from a 170 cm by 19

cm by 1.2 cm aluminum beam. A submersible load cell (SENTRAN® IP67 rated ZB1 S Beam 222 N load cell) was attached at the bottom of this staff, in-line with the towing direction. The load cell was placed 30 cm below the waterline. At full scale, this matched the bridle connection point of the single point mooring. The model cage was attached to the staff via the mooring bridle. An extension line was added to move the cage away from the immediate effect of the load cell staff.

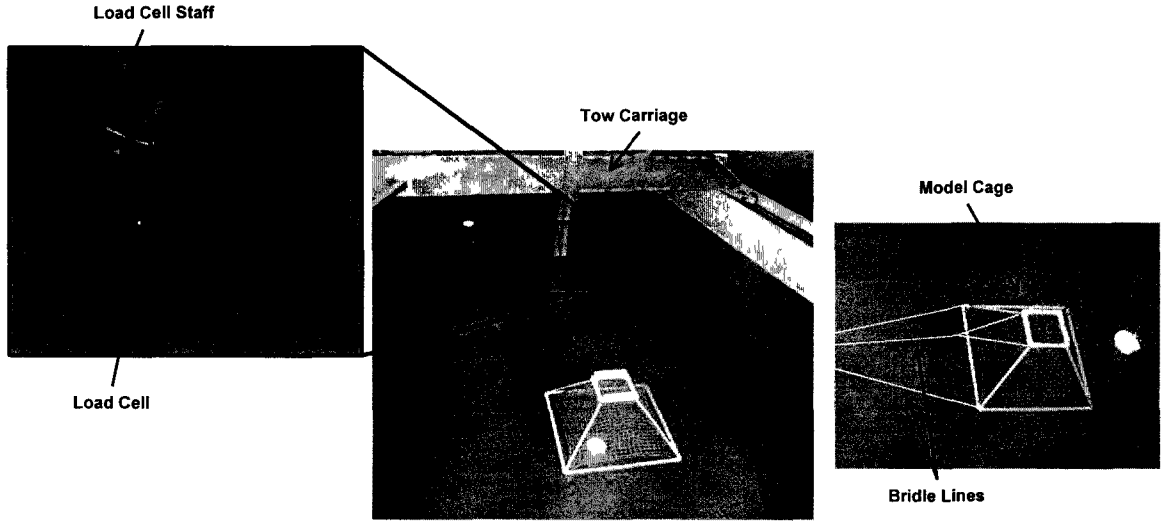

Figure 4.3: The experimental setup for physical scaled model current testing. Note that bridle lines (left) were digitally enhanced for viewing purposes.

The output load cell voltages ran through an A/D converter to a computer. National Instruments® and LABVIEW® software packages were used to view and record data. Calibration of the specified 50lbf (222 N) capacity load cell was completed prior to tow testing and proved to be linear. The load cell has a resolution of 0.044 N and was sampled at a rate of 10 Hz.

4.4 Fish Cage and Mooring Numerical Model

Similar to the previous case study, the Aqua-FE program was utilized to predict the net pen system behavior in a marine environment. Two finite element analysis models were

constructed for this study: one for scale physical model tow test comparison, and the second to investigate the full scale OCAT cage and mooring response to various current profiles. The first model is shown in Figure 4.4. The cage and bridles were simulated using 164 nodes and 288 elements. The bridle connection point location was similar to that in the physical model. The net solidity of the physical model was recreated in the numerical model (14.8%) using 30 consistent net elements, developed in Tsukrov et al. 2003.

As discussed in Chapters 2 and 3, a water velocity reduction occurs as the fluid flows through a net pen. This shadowing effect has been documented and quantified on several cage systems and net solidities (see, for example, DeCew et al., 2005; Fredriksson et al., 2001; Patursson, 2008) and should be taken into consideration. To account for this, a reduced velocity was applied to aft portions of the net chamber. From previous testing at UNH and the U.S. Naval Academy it was found that a net panel in the 15% solidity range would cause a reduction in current of roughly 12.7% (Patursson, 2008). Thus, in numerical modeling, 100% of the current velocity was applied to the front net panel and cage frame and 87.3% of the current velocity to the remaining fish cage components.

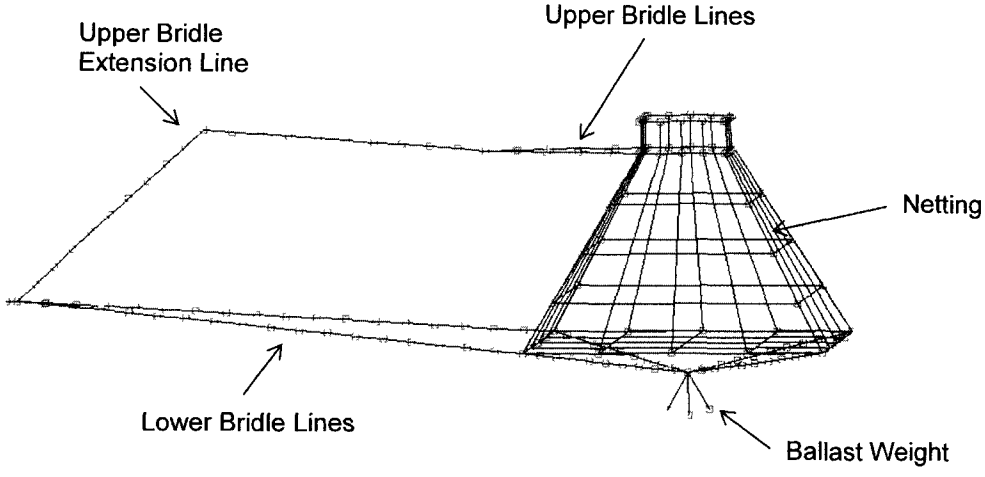

Figure 4.4: Finite element model of the cage and bridle line components.

Once the comparison test was complete, the full mooring was assembled in Aqua-FE to perform a submergence study. Note that the same FEA model of the cage was utilized in both sets of numerical simulations. The additional components increased the number of nodes and elements to 210 and 335, respectively. The full cage and mooring system is shown in Figure 4.5. The cage's top rim motion was recorded to obtain the submergence depth of the system. The tension in the mooring was monitored in the lower mooring chain (near the anchor) and in the three bridle lines connecting the cage to the SPM (upper bridle extension and lower bridles).

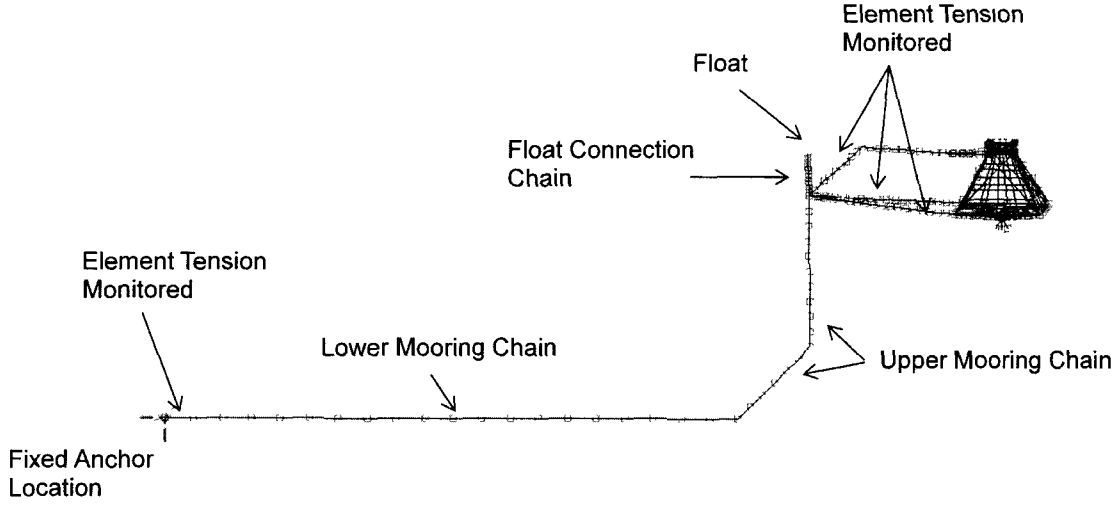

Figure 4.5: Finite element model of the full OCAT cage and single point mooring system. The cage and bridle line components are similar to those shown in Figure 6. The tensions within four elements were recorded to provide mooring component tension.

Three different net solidities representative of the actual nets utilized in aquaculture operations were used in this study to investigate the effect of the net chamber solidity on the systems dynamic response: 8.1%, 16% and 23.8%. Net Systems (www.net-sys.com) Ultra Cross 4 ply and 16 ply netting parameters were used for the 8.1% and 23.8% solidities, respectively. The

16% net was selected to represent a generic net for comparison and is not based upon an actual product. The corresponding geometric properties are listed in Table 4.2.

Table 4.2: Net pen solidities utilized in the numerical model submergence study.

Parameter	Value
Solidity	8.1%
Twine diameter	1.12 mm
Square mesh side length	26.8 mm
Solidity	16%
Twine diameter	2.5 mm
Square mesh side length	30 mm
Solidity	23.8%
Twine diameter	2.73 mm
Square mesh side length	21.6 mm

4.5 Load Cases

The cage's response to increasing currents is essential for analyzing its single point mooring design as well as the effectiveness of the cage and mooring system as a "self submerging" system. Eight water velocities, ranging from 0.25 m/s to 2 m/s in 0.25 m/s increments, were applied to the system in the scale physical model testing. The full and model scale values are shown in Table 4.3. Three tests for each tow velocity were conducted to ensure repeatability of measurements. All experiments for the physical and numerical model were conducted in a representative water depth (full scale) of 24 meters.

Table 4.3: Current velocity input parameters for physical scaled model testing.

Current Regime (#)	Full Scale Velocity (m/s)	Model Scale Velocity (m/s)
1	0.25	0.08
2	0.50	0.16
3	0.75	0.24
4	1.00	0.32
5	1.25	0.40
6	1.50	0.45
7	1.75	0.56
8	2.00	0.60

4.6 Validation of Numerical Model

Validation of the numerical model was conducted by comparing its predictions with the scaled physical model measurements. Figure 4.6 provides full scale numerical model predictions with the physical model measurements recalculated to full scale. In both cases, the total drag force acting on the system as a function of current velocity is provided for the netting of 14.8% solidity. A minimum least squares fit was used to present the quadratic dependence of the drag force T (tension in the tow line) on water velocity U:

$$T = kU^2 \tag{4.2}$$

where k is a coefficient calculated based upon data points U_i and T_i as follows:

$$k = \frac{\sum_i U_i^2 T_i}{\sum_i U_i^4}. \tag{4.3}$$

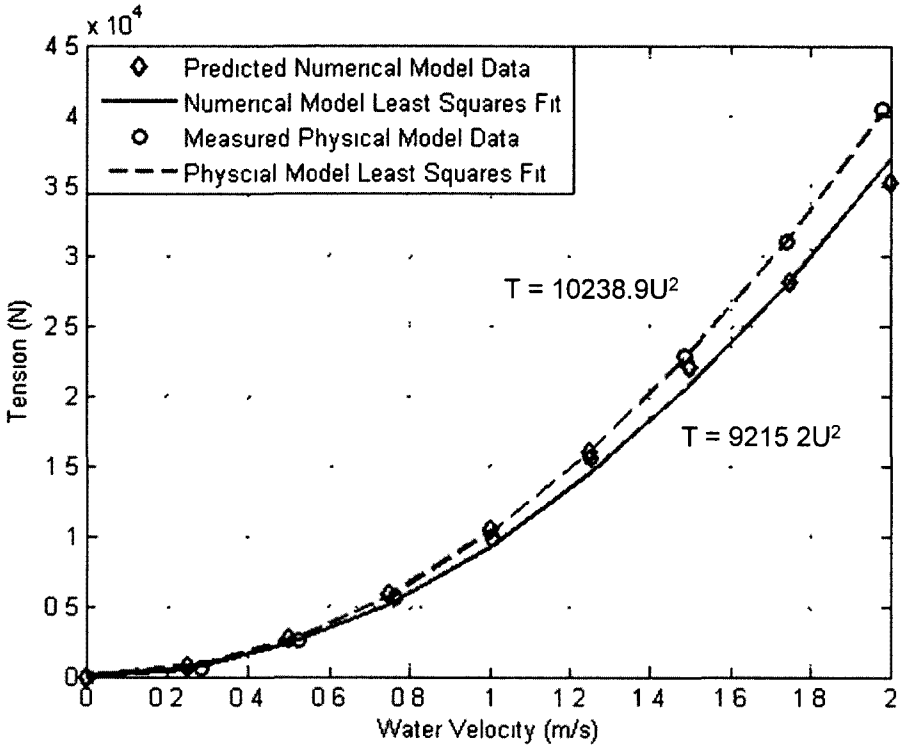

Figure 4 6. Comparison between full scale numerical and (recalculated to full scale) physical model predictions of the drag on the OCAT cage system.

As can be seen from Figure 4.6, a good agreement between the two models is observed with the numerical and physical predictions being within 3.6% from each other up to 1.5 m/s. At higher velocities, the numerical model predicts lower drag than the physical model with a maximum difference of 12.9% at 2 m/s. This can be attributed to the physical model's reduced Reynolds number and associated increased drag coefficient at these velocities. Taking the critical Reynolds numbers to be 2.33 $x10^5$ (see Figure 2.17) the water velocity required to enter critical flow for the full scale system is 1.22 m/s, compared to 12.2 m/s for the physical model. At 1.5 m/s, the frame pipe Reynolds numbers for the numerical and physical models are 3.81e5 and 1.21e4, respectively. From Figure 2.17, the structural frame pipes of the physical model had drag coefficient values roughly 1.7 times higher than those in the full scale structure.

Note that several other physical effects were not included in the models. In particular, the numerical model did not include any surface effects, so that the contribution of corresponding wave generation forces were not reproduced. Also, the compliance of the mooring lines was not replicated in the physical model. Based on the previous studies that included field observations and measurements of full scale aquaculture installations (Fredriksson, 2007), these effects can be neglected for the considered dynamic loading of the OCAT system.

4.7 Numerical Model Results and Discussion

The single-point moored OCAT cage described in Section 4.2 was designed to submerge under high currents to minimize environmental forces and preserve structural integrity. This feature of the design was analyzed by conducting numerical experiments for three different values of net solidity corresponding to low, intermediate and high values for netting used in aquaculture operations, namely 8.1%, 16% and 23.8%. Each net solidity was investigated at current speeds up to 1.5 m/s representing the highest velocities at deployment areas of interest. In addition, several other values of the net solidity were investigated at the maximum 1.5 m/s current to get more insight into the submergence behavior. These net solidities were also based on netting used in the industry. The simulations were performed for a water depth of 24 m. In most simulations, the current distribution through depth was assumed to be constant; however, one simulation with current linearly decreasing from 1.5 m/s at the surface to 0 m/s at the sea floor was conducted.

Figure 4.7 shows the submergence depth, defined as the vertical distance from the top rim to the water surface, as function of the current velocity. The deformed configuration of the

mooring cage at 1.5 m/s current for each net solidity is presented in Figure 4.8. The following observations can be made.

1. At water velocities up to 0.75 m/s, the cage system remains at or near the surface regardless of the net chamber solidity.
2. If a 1 meter vertical deflection is defined as the initiation of submergence, this threshold is achieved by the cages at 0.75, 1, and 1.2 m/s for the 23.8%, 16% and 8.1% solidity net cages, respectively.
3. From approximately 1 m/s to 1.5 m/s the cage, for the considered range of solidities, is in the unstable submergence regime when small changes in the systems design, e.g. solidity of netting, result in significant changes in the numerically predicted submergence. This is demonstrated, for example, by a 7.5 m difference between the submergence of a cage with a net solidity of 8.1% and 9% at 1.5 m/s currents.
4. The transition into the critical flow region is captured by the numerical model, see the behavior of 8.1% solidity net cage near 1.2 m/s water velocity.
5. The uniform current profile is not typically seen in the field. To evaluate the dependence of the submergence depth to the exact distribution of current, one simulation was performed for a linear changing velocity profile on the 16% solidity net pen. As expected, the submergence of the cage was reduced by a significant amount (8.7 m) as compared to the constant 1.5 m/s current. This depth corresponds to velocities of 1.1 m/s acting on the center of the cage which agrees well with the submergence predictions for constant currents.

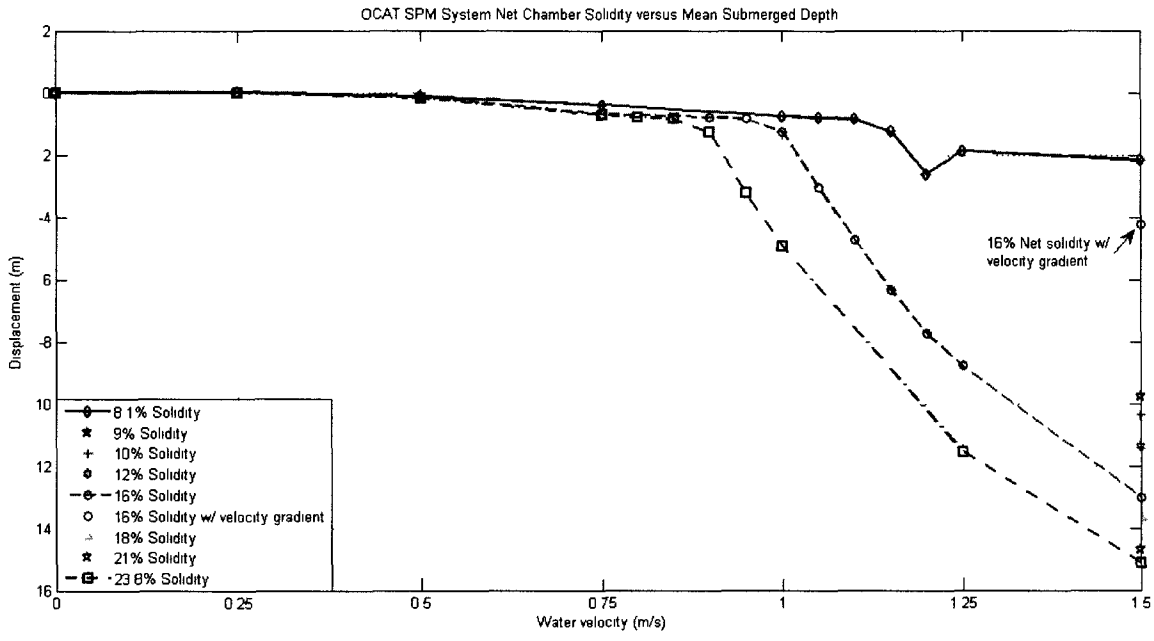

Figure 4.7: Submergence depth of the OCAT system for various netting solidities and water velocities. Note that the 9%, 10%, 12%, 16% with velocity gradient, 18% and 21% solidities were only examined at 1.5 m/s.

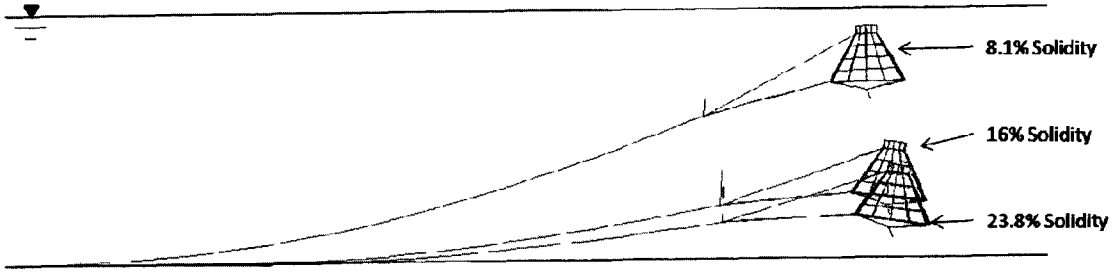

Figure 4.8: Submerged configurations of the OCAT system at 1.5 m/s currents.

The tension in the mooring components was also examined. The loads within the lower mooring chain (near the anchor) as well as the sum of the three bridle lines loads (representing the cage drag) were extracted from the numerical model for each analyzed water velocity and net solidity. It was observed that the drag associated with the lower and upper mooring chain

and spherical float had minimal influence on the total mooring system load (less than 10% at velocities below 0.5 m/s and less than 5% at higher water velocities).

The anchor chain tensions are presented in Figure 4.9. It can be seen that at the currents corresponding to the initiation of submergence, the tension-deflection curve temporarily changes its character from quadratic to linear. This is caused by the changes in the system's geometry – rearrangements in orientation of components to reduce the drag force and minimize the potential energy. After this realignment, the system enters the unstable submergence regime where variations in submergence depth do not produce significant changes in the total potential energy. For example, cages with 8.1% and 9% net solidities experience very close mooring tensions (around 18 kN) for substantially different submergence depths (approximately 2 m for the 8.1% solidity versus 10 m for the 9% net solidity).

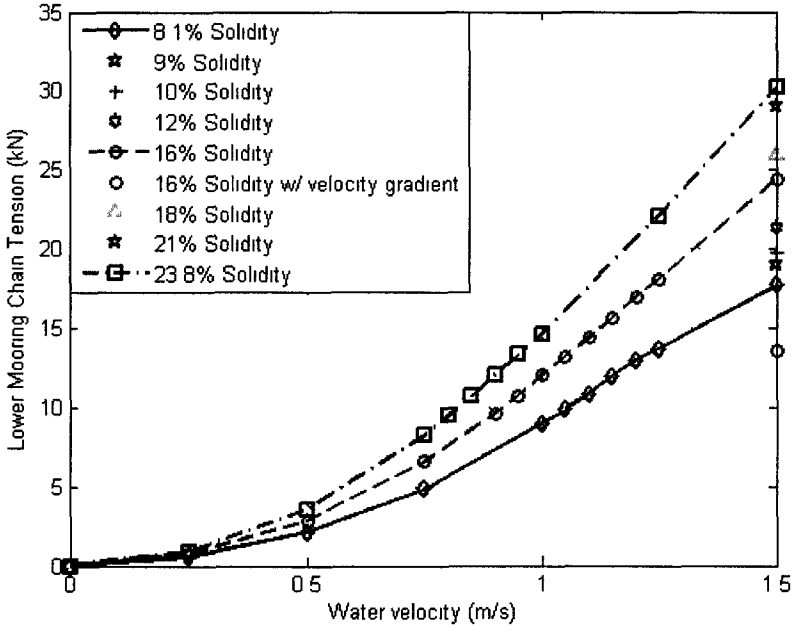

Figure 4.9: Variation of the mooring chain tension with water velocity for different net solidities.

4.8 Conclusions

A small volume aquaculture cage system secured in a single point mooring was analyzed under a variety of currents. The submergence depth and mooring tensions were investigated as a function of net solidity. The numerical model was validated by comparison with scaled physical model tow tests and demonstrated good agreement. However, it was observed that the Froude scale physical testing can over-estimate drag forces on cylindrical components at high Reynolds numbers. This is a caused by the decrease in Reynolds number when the actual component's boundary layer becomes fully turbulent, thus moving back the location of the flow speration point, while the scale model of the component is still in laminar flow, leading to a larger coefficient of drag. The system was found to remain at the surface, regardless of solidity, at water velocities less than 0.75 m/s. The submergence studies show a significant unstable regime in the response of the cage where slight modifications in the net solidity or current produce large variations in the predicted depth of submergence. This can have significant impacts in the field, as the net pen was designed to be self-submerging. The mooring tension was not linearly dependent on the cage submersion depth. The output tension data showed that cages with similar net solidities could have significant differences in submersion depth yet similar mooring loads. Further studies are needed to combine the net solidity and the total system buoyancy effects on cage submergence to fine tune the cage and mooring for different environments.

CHAPTER 5

DEVELOPMENT OF STRUCTURAL MODELING TECHNIQUES

Finite element analysis (FEA) techniques were developed to determine the structural capabilities of high-density polyethylene (HDPE) net pen flotation structures. The modeling approach uses shell elements and localized failure criteria to predict critical loading conditions. FEA simulations were performed using values for the Young's Modulus for HDPE determined from tensile tests. Standard manufacturer's values of Poisson's ratio and the yield stress were assumed. To investigate the effectiveness of the method, a series of experiments were performed in the laboratory by testing circular sections of HDPE pipe to localized failure ("kinking"). The same test was replicated with the FEA. A FEA model was then built to represent the complex geometry of a net pen flotation structure deployed at an operational fish farm located in Eastport, ME, USA. Simulations were performed using attachment line tension values measured at the site. The goal was to assess flotation pipe stress levels for typical operational conditions. Simulations were also performed to investigate the maximum capabilities of the net pen structure with different attachment line configurations. Quantifying the operational limits becomes more important as these systems are considered for more exposed, energetic environments. Portions of this research were published in Fredriksson et al. 2007b.

5.1 Previous Technical Work: Structural Modeling in Marine Aquaculture

Most of the open ocean aquaculture engineering research conducted in the world has focused on the development of adequate mooring systems (Colbourne, 1997; Lee and Pei-Wen, 2000; DeCew et al., 2005) and understanding and proper modeling of netting (Aarsnes et al., 1990; Gignoux et al., 1999; Tsukrov et al., 2003; Zhan et al., 2005; Lader et al., 2006). However, very little research has been done on the reliability of cage frames (see, for example, Suhey et al., 2005). According to the Directorate of Fisheries in Norway, HDPE cage rim integrity loss was the cause of 30% of net pen failures in Norway from 2001 through 2006 (see Figure 5.1).

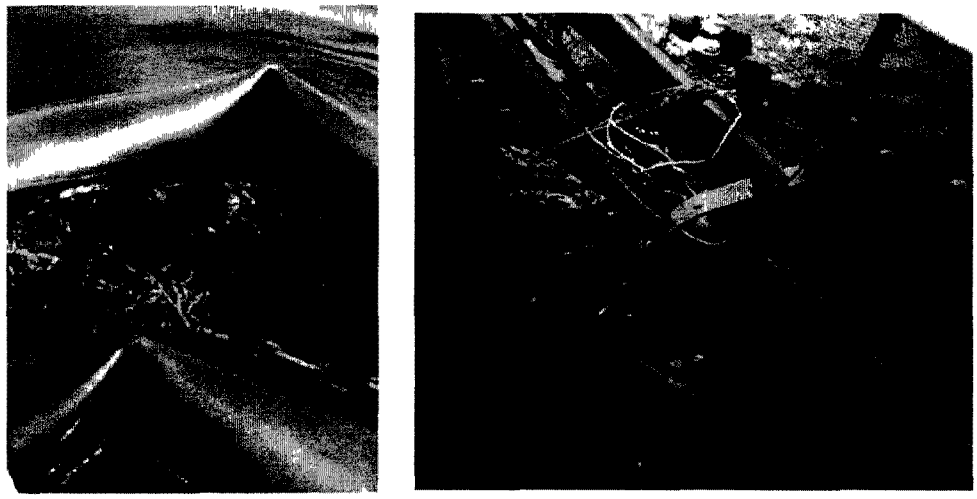

Figure 5.1: Two failed cage rims, resulting in a loss of structural integrity. The rims were constructed of standard HDPE material and deployed in near-shore farms.

There are three main FEA models used to numerically investigate the structural performance and failure of cage frames under hydrodynamic loads: beam/truss elements, 2D shell, and 3D brick elements. Figure 5.2 shows a section of pipe represented by these element types.

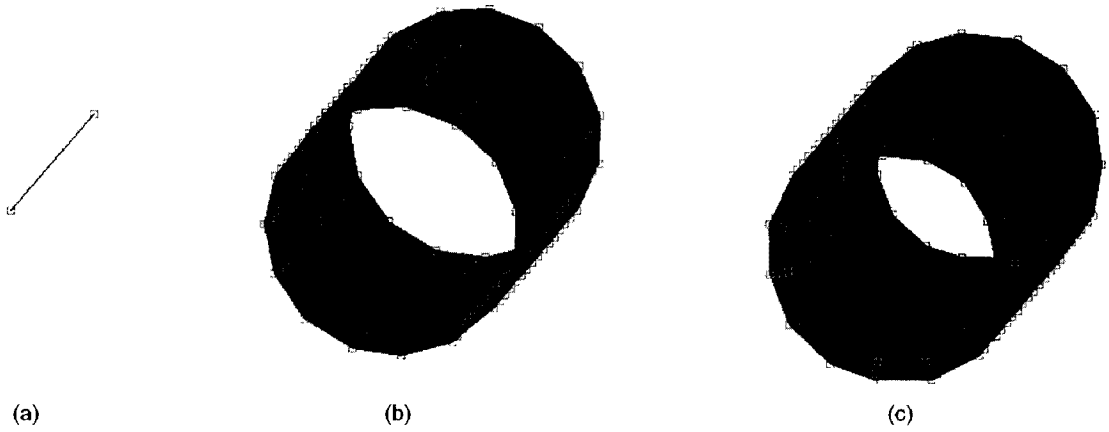

Figure 5.2: Three element types representing the same length of pipe. (a) 2 node line element, (b) 2D shell elements, and (c) 3D brick elements.

Beam/truss models are typically represented by a 2 node line elements. The elements are good for modeling the overall behavior of the structure. They can also capture the major loading and motions of the system. However, they are not appropriate to analyze stress concentrations and material failure. 2D elements are appropriate to study the deformation and buckling of shells, such as HDPE pipe. Local deformations and stress concentrations can also be monitored. These elements are not efficient for overall behavior and are not useful for hydrodynamic loading as the details of fluid pressure distribution are not usually known. 3D elements have the potential to most accurately model the structure, especially in the connection and attachment areas. However, there are a few drawbacks to these elements. 3D elements are extremely computationally intensive, especially for dynamic problems. There are

also mesh compatibility issues; the mesh-per-thickness required for accuracy lead to elements with poor thickness to length ratios, making the model difficult to converge. In addition, it is difficult to model large deformations typical for buckling (the model needs to be re-meshed after each time step). In the analysis presented in this chapter, the 2D shell elements are used to model structural behavior and buckling of cage rims.

Analysis of the buckling process of HDPE cage frames becomes complicated due to the material's viscoelastic behavior. Extensive research has been conducted examining nonlinear and viscoelastic numerical modeling techniques to effectively represent HDPE under various loadings such as tension and compression (see for example, Dusunceli and Colak, 2006; Kwon and Jar, 2008; Lai and Bakker, 1995a, 1995b; Qi et al., 2005; Drozdov and Christiansen, 2007; Colak and Dusunceli, 2006; Joseph, 2005; Klompen, 2005). Zhang and Moore (1997a, 1997b, 1998) developed nonlinear FEA models to predict performance limits of buried HDPE pipe. These models have been compared to analytical calculations and laboratory experiments with good results. However, the techniques offered by the researchers require accurate understanding of HDPE's material properties at the associated strain rates, and may be more complicated than necessary, significantly influencing the computational time when modeling a large complex fish cage frame. This chapter presents a new approach to model buckling in pipes, using a procedure which monitors the development of localized high deformation zones and simplified material property information.

5.2 Aquaculture in Broad Cove, Maine

The structural integrity of a surface gravity cage system was investigated as part of a comprehensive study working with a marine aquaculture company facility with 20 deployed net pens. The project included the installation of current meters and load cells to measure the

forcing and resulting loads in components of the farm (Fredriksson et al., 2006). The components consisted of anchor leg assemblies, net pen attachment lines and HDPE net pen structures. As part of the project, Aqua-FE was used with the field measurements to assess mooring gear operational limits (Fredriksson et al., 2007b). In this chapter, the structural capabilities of the HDPE net pens used to contain the finfish product are examined.

The study was conducted for an operational facility located in Eastport, ME, USA. The Eastport site was positioned in Broad Cove near the border of New Brunswick, Canada (Figure 5.3). Deployed at the site is an array of net pens configured in a 5 by 4 near-surface mooring grid system. It is oriented in a north–south direction and held up with flotation elements (Figure 5.4). The surface portion of the farm has the approximate dimension of 219m by 274 m. Each of the net pens has a nominal radius of 15.9 m.

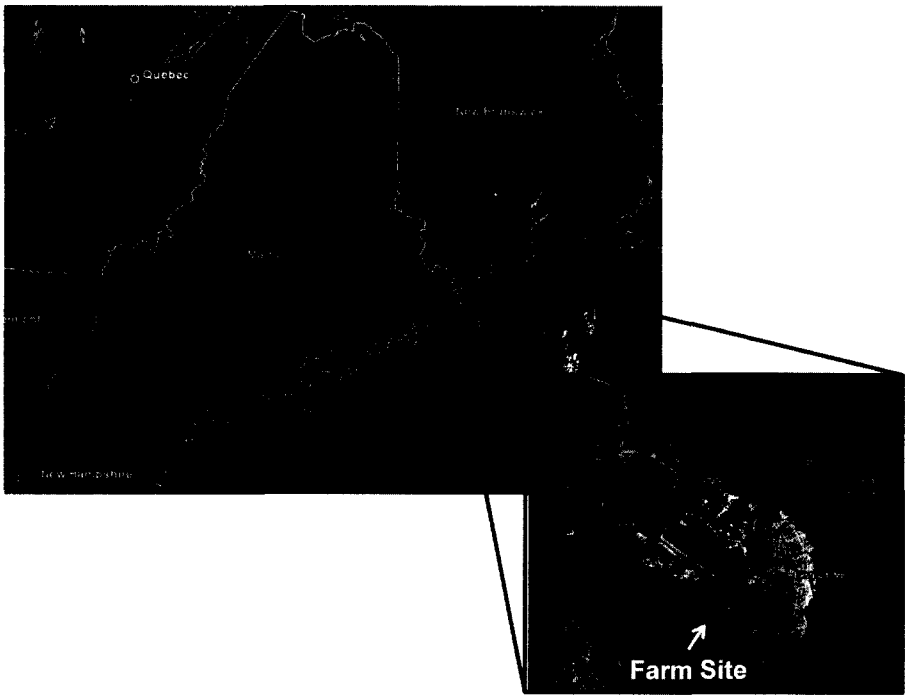

Figure 5.3: The farm was located in Broad Cove, Eastport, Maine.

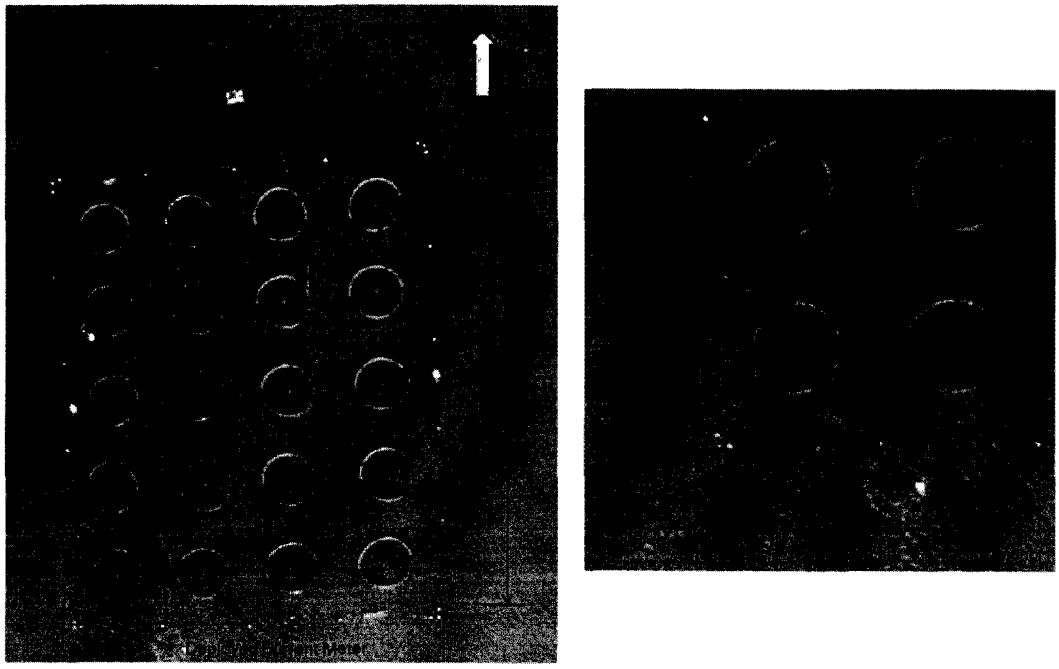

Figure 5.4: The fish farm consisted of 20 net pans each with an approximate diameter of 31.8 m. Instrumentation was deployed in the southwest portion of the farm. Load cells were installed on the SW anchor and bridle lines.

The aquaculture site in Broad Cove is influenced by the extreme tides of the Bay of Fundy (Dudley et al., 2000). The predominant forcing on the farm components is a result of the tidal currents. The tidal currents interact with the nets and HDPE pipe components to create drag forces. The loads on each net pen are transferred to the mooring grid system, ground tackle and anchors using sets of attachment lines (y-lines). To quantify the forcing at the site, a current meter was installed at an exterior farm location (see the focus area in Figure 5.4). In addition to the current meter, four load cells were installed on the West (W), Southwest (SW), East (E) and Southeast (SE) y-lines. Instrument positions and y-line components are shown superimposed on the aerial photograph in figure.

Each of the 20 net pens at the site is circular and is constructed with HDPE pipe. The surface flotation rim structure of each net pen consists of two concentric rings of pipe with a

nominal diameter and thickness of 323 and 19.8 mm, respectively (see Figure 5.5). The pipes are held together by passing them through 48 brackets constructed of two larger pipe sections (diameter of 406 mm, thickness of 6.9 mm). The brackets also incorporate a handrail support assembly made with 114mm diameter pipe with a thickness of 5.7mm with vertical and angled members through which a circular "handrail" is passed. These components are shown in Figure 5.5 (a load cell recorder strapped to one of the net pen stanchions is also shown in the figure).

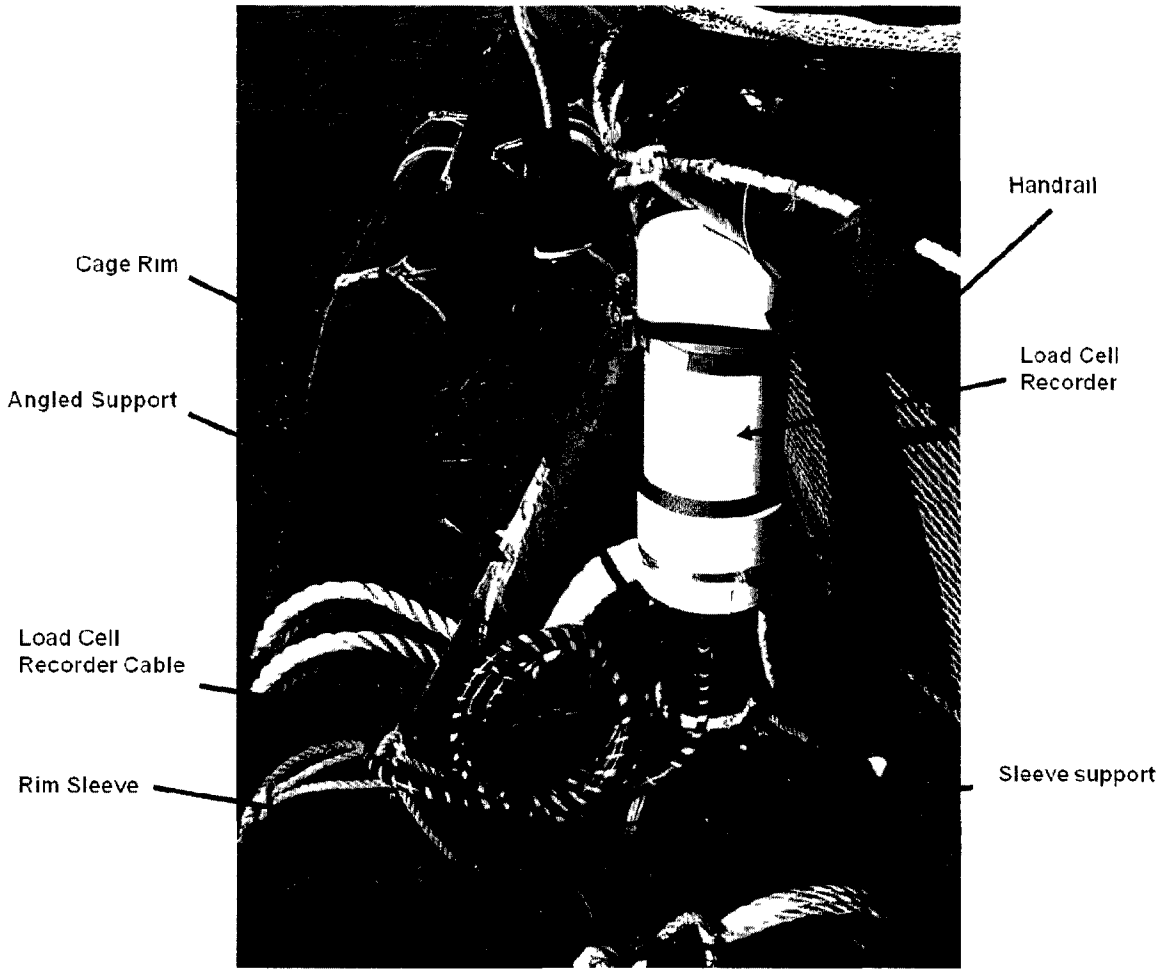

Figure 5.5: The cage frame and brackets are shown (with a attached bridle line load cell recorder).

For most deployments at this site, the net pen components were specified empirically based on years of operational experience. However, the actual capabilities of these components

were rarely quantified. If the same structures are to be deployed in a more energetic environment, the point of failure would need to be predicted to prevent escapement, which can have dire economic and environmental consequences. Therefore, the objective was to develop a technique for predicting the structural integrity of the flotation structure of HDPE net pens. The technique was developed utilizing a combination of laboratory and computer model experiments. Using the technique, FEA simulations were performed for loading conditions at the Broad Cove site. The same model was then used to investigate maximum loading conditions at estimated yield values for the material.

The first step in the approach was to carry out a series of laboratory tensile tests to determine the Young's Modulus for samples of weathered HDPE using a range of loading rates. The next step was to develop the modeling procedure for HDPE pipe, including stress–strain characteristics and FEMA techniques. This was done by utilizing shell elements and employing localized failure criteria. Circular ring laboratory experiments were then performed where five samples of actual pipe were tested to localized failure. The laboratory tests were replicated using FEM simulations. The results were then compared. Finally, the FEM approach was applied to the more complex geometry of the pen flotation structure deployed at the Broad Cove site. Calculations were performed to examine the stresses in the pipe during operation at the farm and to investigate the maximum load the net pen pipe assemblies can withstand.

5.3 Finite Element Procedure and Material Modeling

Unlike linear elastic materials such as steel, HDPE is considered viscoelastic because its mechanical response is time-dependent. A slowly applied load will cause the HDPE to undergo large deformations as the polymer bonds of HDPE "settle" and "unwind." However, if the same load is applied quickly, the bonds do not have sufficient time to react, resulting in less

deformation. As a result, the Young's Modulus relating stress and strain can be substantially larger at higher strain rates. Net pens located in exposed marine environments where waves and currents are prevalent may have a range of loading rates that are structure and site specific. To investigate the elastic characteristics of weathered HDPE, a series of tensile tests were performed using samples of pipe weathered for several years (stored in areas of direct sunlight). Since the actual loading rates at the fish farm site were not determined, three standard loading rates of 0.0127, 0.127 and 1.27 mm/s (typical of tensile testing procedures) were used in the experimental tests.

Ten pieces of the HDPE were machined into the standard ASTM D638 "dog bone" shape having an initial (total) length of 12.7 cm and a test length of 5.08 cm (Figure 5.6). Three sets of stress–strain tests (each with three replicates) were conducted at the three loading rates in an Instron® Schenk Testing System (Model 1350). Also shown in Figure 5.6 is the machine with a specimen prior to testing. The stress–strain results for the tests are shown in Figure 5.7 for the 0.0127, 0.127 and 1.27 mm/s loading rates, respectively. For each set of loading rate tests, a Young's Modulus was determined by linearizing the results. The values are provided in Table 5.1. Also provided in Table 5.1 are the standard deviation and average of the Young's Modulus values. Tensile testing results show a dependence on the loading rate, though the results from using specimen 2 were lower than those of specimens 1 and 3 for each of the test sets. It is possible that the difference can be attributed to varied weathering conditions. The average value of the Young's Modulus for the slowest loading rate, equal to 6.67×10^8 Pa, was used as input for the FEM calculations. It should be noted that a value 8.00×10^8 Pa was used by Vikestad and Lien (2005) to examine the bending stiffness of fish cage collars.

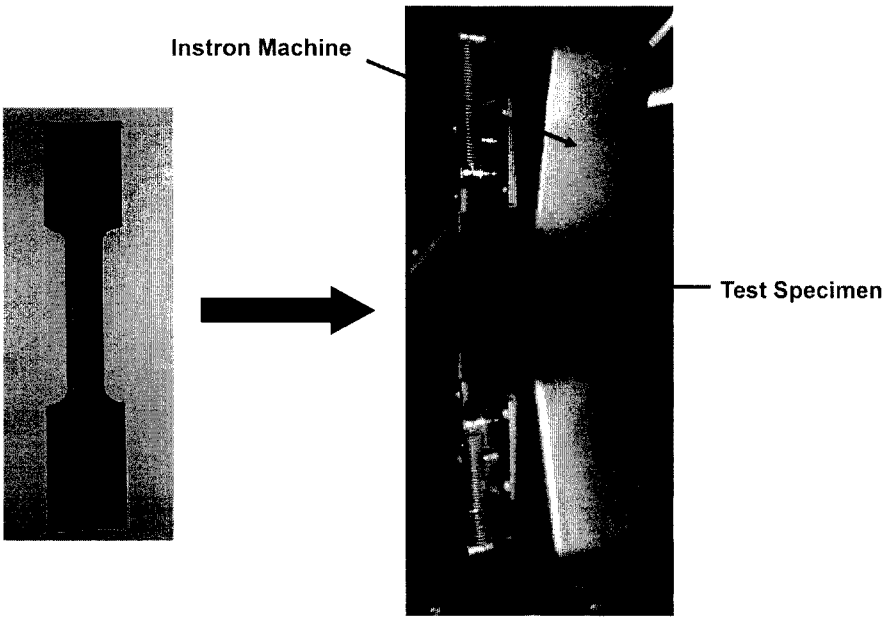

Figure 5.6: Samples of HDPE pipe were placed in an Instron tensile testing device.

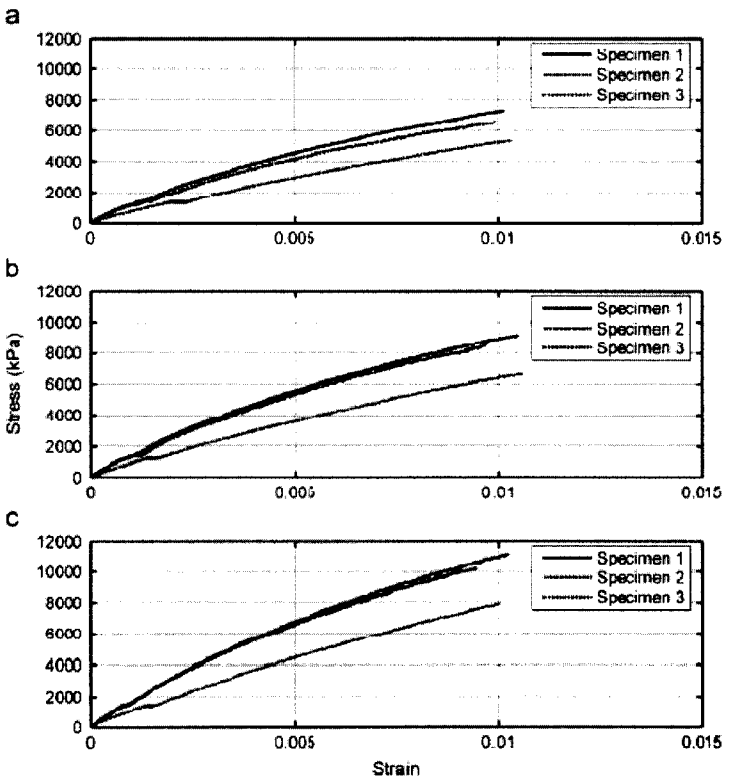

Figure 5.7: Stress strain data results when loaded at 0.0127mm/s, 0.127 mm/s and 1.27 mm/s.

Table 5.1: Young's Modulus values obtained during tensile testing using weathered HDPE samples

Sample	Young's Modulus (Pa)		
	Rate 1, 0.0127 mm/s	Rate 2, 0.127 mm/s	Rate 3, 1.27 mm/s
1	7.80×10^8 Pa	9.52×10^8 Pa	1.18×10^9 Pa
2	5.10×10^8 Pa	6.73×10^8 Pa	7.72×10^9 Pa
3	7.13×10^8 Pa	9.27×10^8 Pa	1.17×10^9 Pa
S.D.	1.41×10^8 Pa	1.54×10^8 Pa	2.33×10^8 Pa
Average	6.67×10^8 Pa	8.37×10^8 Pa	1.04×10^9 Pa

5.4 Finite Element Analysis of HDPE Pipes

Numerical modeling of the HDPE pipes was performed by utilizing shell elements developed to analyze thin structural components with high bending stiffness. These elements combine both membrane and bending resistance to applied loads. It is assumed that the flexural deformation of the shell occurs according to the Kirchhoff-Love hypotheses, so that bending stresses and strains are proportional to the distance from the mid-surface of the shell. The bilinear four-node thin-shell elements used in the analysis have six degrees of freedom per node as illustrated in Figure 5.8. In the figure, U_x, U_y, U_z and r_x, r_y, and r_z are the components of nodal displacements and rotations, respectively. Bilinear approximation of the displacements provides continuity of the displacement functions through the boundary of the element (see, for example, Zienkewicz et al., 2005). Using these elements, numerical models were developed in the commercially available finite element program MSC.MARC (www.mscsoftware.com). Geometric properties were assigned based on the actual dimensions of structures, and the material was chosen to have the nonlinear stress-strain behavior of HDPE.

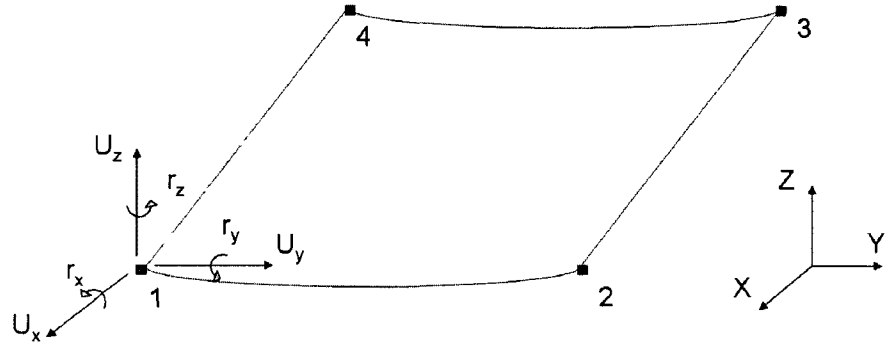

Figure 5.8: The four-node shell element with 6 degrees of freedom per node.

To model the HDPE pipes used as net pen structural members, a simplified material model was used. The Young's Modulus of the material was assumed to be constant as long as the material is within its elastic region (i.e. stress is not larger than the material yield limit). The yield strain of a typical ductile polymer ranges from 5% - 10% strain (where a metal yields at less than 0.1% strain). Once the stress in the material passes the yield stress, plastic deformation begins to occur. The material then follows a stress-strain relationship similar to that shown by the dashed curve on Figure 5.9. The material will eventually fail or fracture as the strain increases. Modeling the stress-strain characteristics is possible but requires an extensive number of tests to resolve the plasticity of the material under various loading rates (see Chapter 6). Therefore a simplified structural model, shown as the solid curve on Figure 5.9, was chosen to represent the HDPE behavior. In this case, the critical point to determine failure is the yield stress, σ_y.

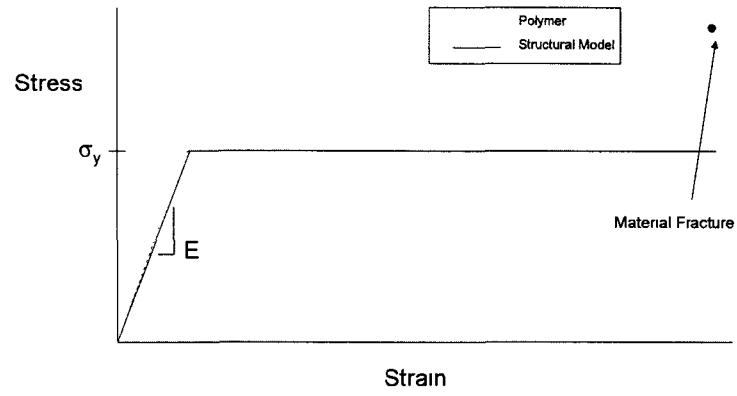

Figure 5.9: Approximation of polymer material behavior by linearly elastic – perfectly plastic curve.

Thus, finite element analysis of the HDPE pipe requires the following material parameters: Young's Modulus, Poisson's ratio and yield stress. The Young's Modulus was determined from a series of tensile tests using weathered HDPE samples as described previously. Value for the Poisson ratio was taken from a provided manufacturer's value of 0.42. A sensitivity study was performed changing the Poisson ratio value in a series of FEM simulations and the results compared. It was found that the results did not vary significantly at the time steps used in the model. This result was similar to that found by Suhey et al. (2005) in their numerical model study of membrane structures used for open ocean aquaculture cages. Yield stress was taken as the standard manufacturer published value of 2.413 (10^7) Pa. In this study, weathered HDPE components were considered, but according to Ollick and Al-Amir (2003), weather does not significantly affect the yield stress of HDPE.

5.5 Circular Ring Experiments

To investigate the failure modes and maximum loads, a set of experiments was conducted using circular rings of HDPE pipe. Tests were first conducted in the laboratory where

circular rings of HDPE pipe were deflected until "kinking" was observed. Then the laboratory tests were simulated using the FEM technique.

The laboratory experiment consisted of five individual pull tests performed on 3.66 meter diameter circular rings of HDPE pipe (SDR 15.5) having the same exposure as the material used in the tensile tests. The rings were fixed at two locations on one side spaced approximately 2.8 meters apart along the arc. On the other side, a single rope with an inline load cell was attached to the ring. A photograph of the set up is shown in Figure 5.10. A "come-a-long" was slowly used until local failure ("kinking") was observed (Figure 5.11) and the test was stopped. Five individual tests were conducted. The results of the circular ring's change in diameter are shown in Figure 5.12. Tests 2-5 showed similar results with localized failure occurring at a load of approximately 1557 N (350 lbf).

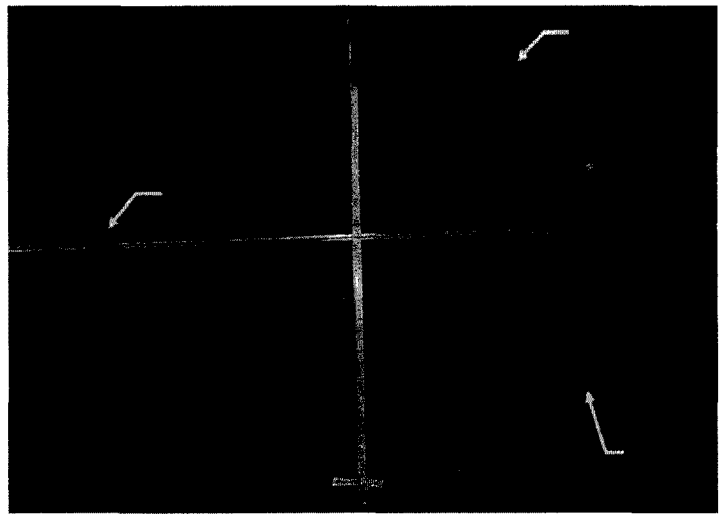

Figure 5.10: Experimental test set-up of the circular ring experiments.

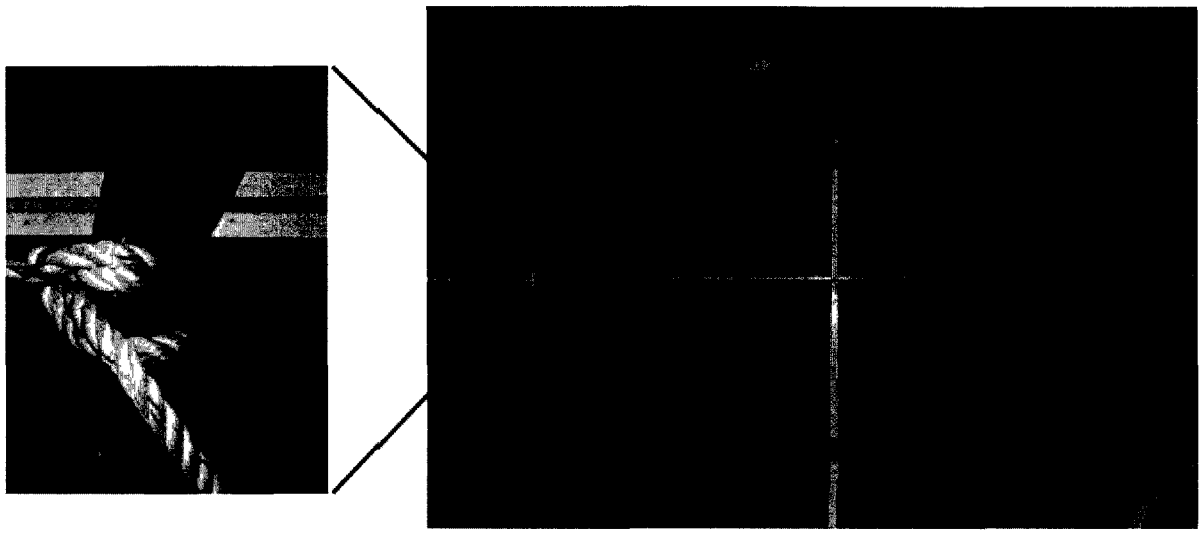

Figure 5.11: The tensioning connection point with a localized failure observed.

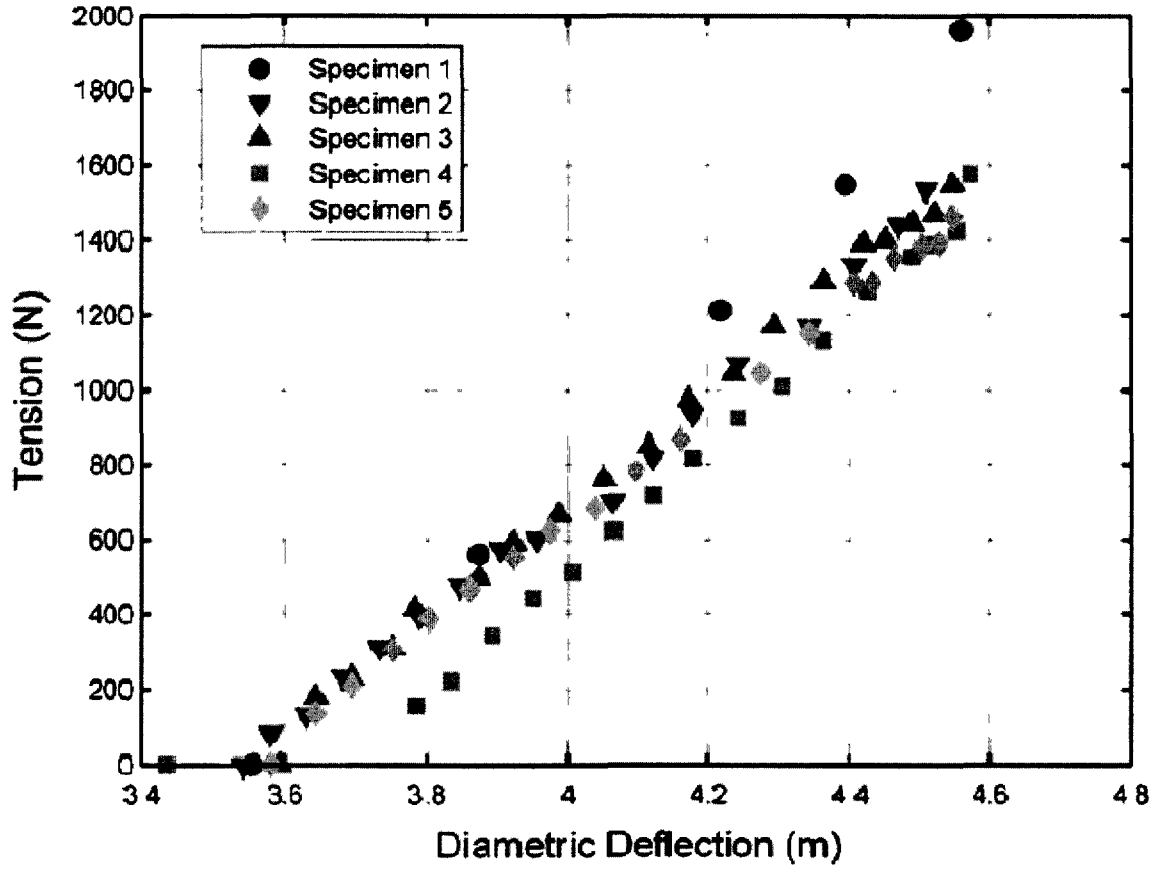

Figure 5.12: The results of the circular ring experiment. The force and associated circular ring diameter are shown. The diametric deflection was measured with a tape measure between the load application point and midpoint between the supporting bridles.

The next step was to perform numerical simulations of the circular ring laboratory tests using the MSC.MARC finite element modeling software and compare results. The finite element model was constructed using the geometric properties of the SDR 15.5 pipe from the circular ring laboratory tests. The material properties used in the model consisted of the published values for yield stress of 2.413 (10^7) Pa, a Poisson ratio of 0.42 and a Young's Modulus equal to 6.67 (10^8) Pa obtained from the tensile tests. Parameters and values used in the FEM simulation are provided on Table 5.2. The fixed and point load boundary conditions were set in the same location as the laboratory tests.

Table 5.2: Geometric and material properties of HDPE pipe used in the FEM calculations for the weathered ring experiments.

Parameter	Value
Overall Diameter	3.66 m
Pipe Diameter	8.89 cm
Wall Thickness	0.574 cm
Material	HDPE
Young's Modulus	6.67×10^8 Pa
Poisson's Ratio	0.42
Yield Stress	2.412×10^7 Pa

The model was constrained by fixing one line location in the x, y and z directions. However, to replicate the degrees of freedom of the ring in the laboratory tests, the other line attachment location was only fixed in the direction of the point load (Figure 5.13). This allowed the model to bend and flex due to the application of the load and not restrict any motion. The load on the circular ring was simulated with applied point forces, distributed over 27 nodes. It is important to note that the load in the FEM simulations was applied quasi-statically so that the rate of loading was accounted for by the choice of material parameters only.

In the FEM procedure, a localized failure criterion is applied as follows. The load acting on a set of closely spaced shell elements is slowly increased. When the yield stress of the element at the load application is reached, the model distributes the load to surrounding elements (effectively decreasing the stress at the time step). The load is increased, and the procedure is repeated until enough elements, consisting of approximately half the circumference of the pipe, reach the yield stress. At this point it is assumed that the cross-section of the pipe fails, and the simulation is terminated. Using this simplified representation had the effect of over-predicting material failure (conservative approach) because the polymer may still have limited load bearing capabilities above the tensile strength, whereas the model will not.

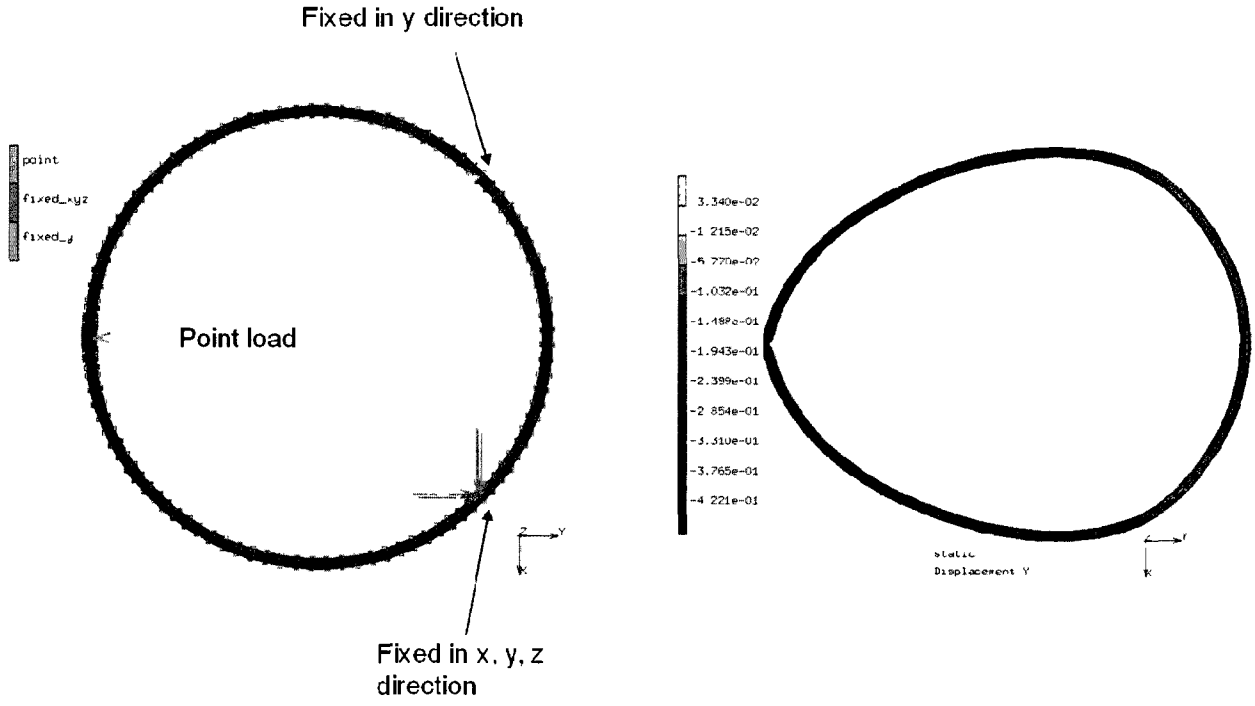

Figure 5.13: Using the values in Table 5.2, FEM calculations were performed to simulate the weathered ring experiments. Note that the ropes pull inward, present in the laboratory experiment, was not replicated in the FEM. The displacement, in meters, in the horizontal position (Y) is shown along the deformed geometry (right).

During the simulation, the rim deformed until the localized failure criterion is met. The before loading and deformed models of the rim are shown in Figure 5.13. The load at failure was calculated to be 1877 N, approximately 16% greater than the laboratory tests. Figure 5.14 shows a visual comparison of the "kinking" observed from both the laboratory and the computer model tests.

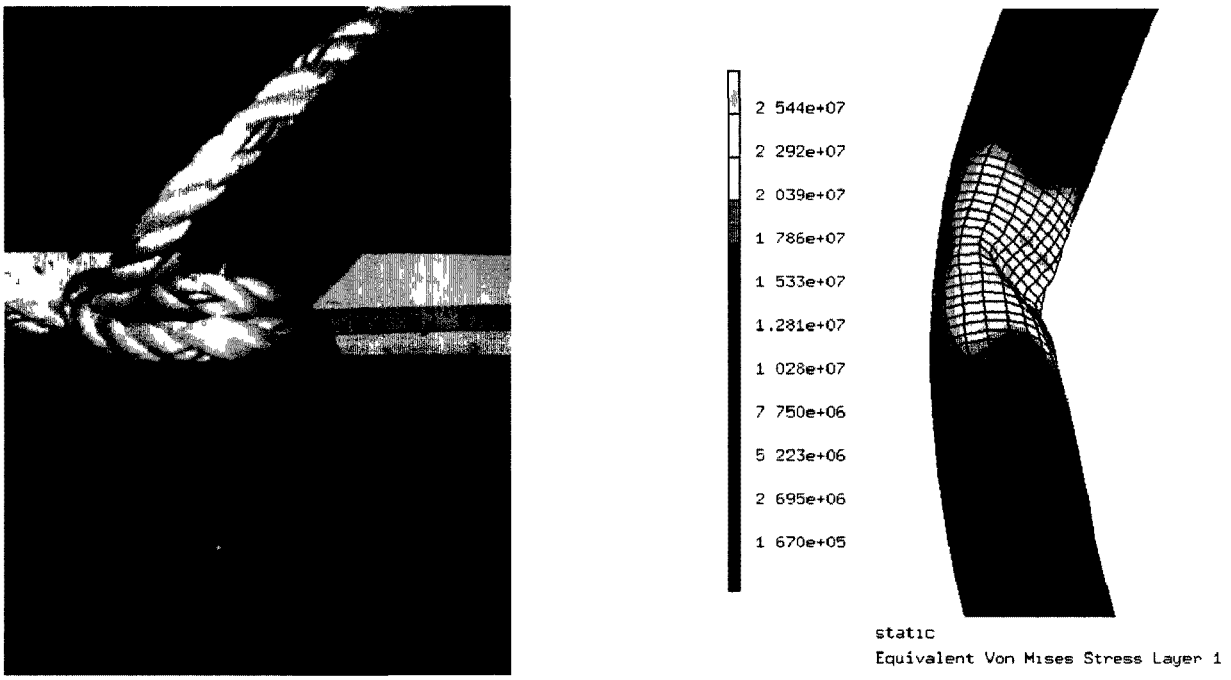

Figure 5.14: A visual comparison between the kinking and localized failure of the circular ring. Note that the yield stress of HDPE is 2.417×10^7 Pa.

Although in the study the failure criterion is set when ½ the pipe circumference elements yield, the yielding of a few elements can constitute concern. Figure 5.15 shows the total applied load on the rim versus the percent of pipe circumference undergoing plastic deformation. This plot shows the amount of yielding as a function of load, at the load application point. It can be seen that once yielding occurs in 25% of the pipe, the load is near its

maximum value, and total collapse occurs shortly thereafter. From these results, a certain amount of confidence was obtained using this modeling approach.

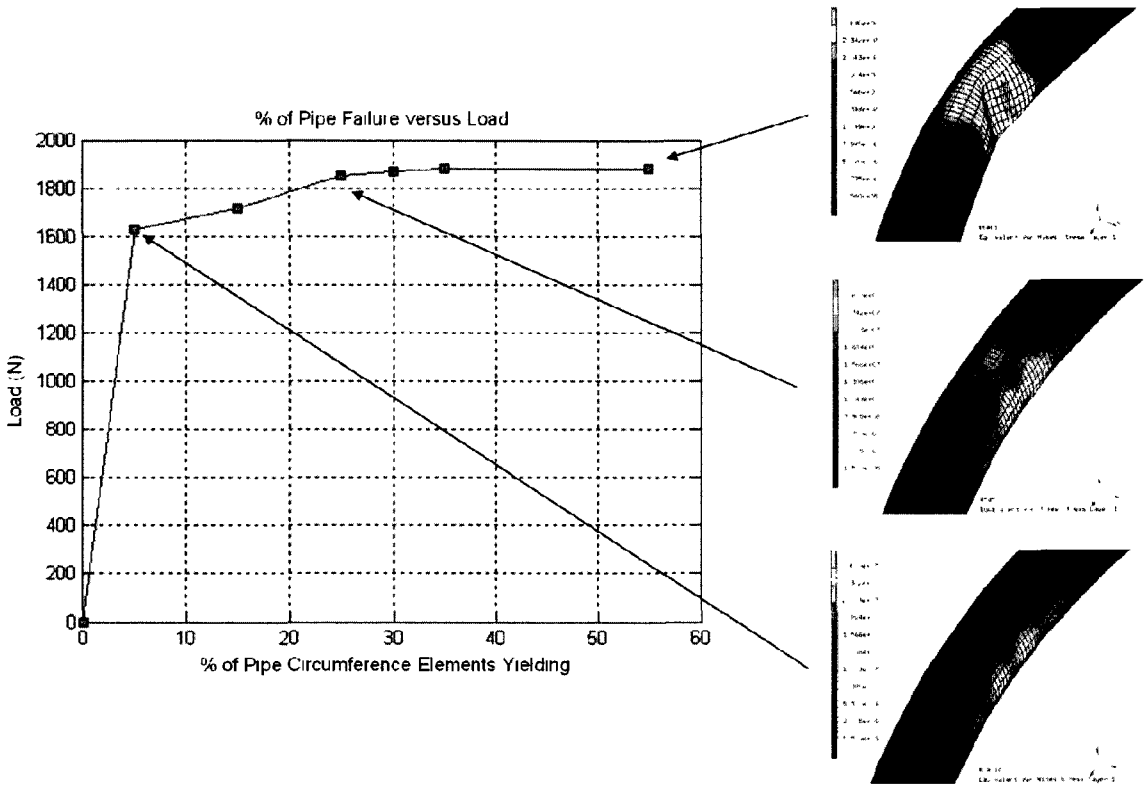

Figure 5.15: The load versus percentage of pipe circumference element failure. The progression of stress contours using the localized failure technique is also shown.

5.6 Boundary Conditions and Geometric and Material Properties

A numerical model of the net pen flotation structure was then built using the geometric and material properties described for HDPE (Table 5.3). Shell element dimensions varied depending upon the component. The inner and outer flotation pipe assemblies were modeled with shell elements (see Figure 5.8) having the dimensions of 294.8mm by 79.3 mm. A total of 24,864 nodes and 25,824 elements were used in the model. The finite element model of the net pen is shown in Figure 5.16. Boundary conditions for the model were similar to those used for

the circular ring laboratory tests, but the load application was modified. When deployed in the field, the primary loads on a net pen are the drag forces associated with the net and the equal and opposite, counteracting y-line tensions. It is difficult to model the distributed load of the net (around the rim) and localized forces due to the y-lines simultaneously. Therefore, two load cases were used to investigate each scenario. Together these load cases should bracket the predicted stresses on the system.

Table 5.3: The geometric and material properties of the net pen flotation structure FEM

Component	Parameter	Value
Cage	Overall Diameter	31.8 m
	Circumference	100 m
	Material	HDPE
	Young's Modulus[a]	6.67 (10^8) Pa
	Poisons ratio[a]	0.42
	Yield Stress[a]	2.41 (10^7) Pa
Flotation Pipe (inner and outer)	Pipe diameter	0.3238 m
	Thickness	0.0198 m
Rim Sleeve	Pipe diameter	0.4064 m
	Thickness[b]	0.0690 m
Sleeve Support	Pipe diameter	0.3238 m
	Thickness	0.0198 m
Handrail	Pipe diameter	0.1143 m
	Thickness	0.0057 m
Handrail Sleeve	Pipe diameter	0.1413 m
	Thickness[b]	0.0242 m
Vertical Support	Pipe diameter	0.1413 m
	Thickness	0.0134 m
Angled Support	Pipe diameter	0.1143 m
	Thickness	0.0108 m

[a] All components used in the model has the same Young's Modulus, poisons ratio and yield stress.
[b] Sleeves take the rim or handrail pipe thickness into account.

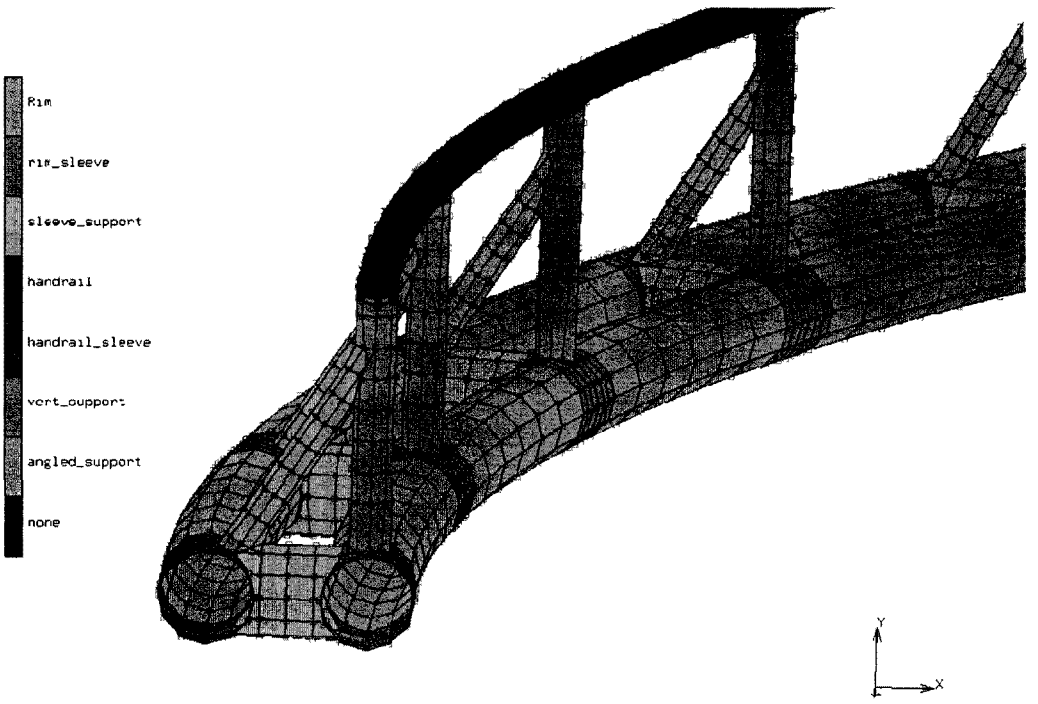

Figure 5.16: An FEM model of a portion of the surface rings used in a net pen.

The first load case examined the system from a "global" perspective. It utilized a distributed load representing the drag forces of the net chamber, with fixed and supported boundary conditions representing the y-line attachment points (Figure 5.17). Similar to the circular ring, one attachment point was fixed in the x, y and z direction and the other was restricted in the load application direction. The linear distance (around the rim) between points was dependent upon the input loading scenario (for example, if one or two y-lines were supporting the system in the field). The load representing the drag of the nets was assumed to be distributed evenly over the inner and outer rims. A force was applied to over 474 nodes that increased linearly with time at a quasi-static rate (note that the loads were only distributed over the "major arc" of the cage frame). Modeling the rim in this manner allowed for the proper distribution of the load. Note that the weight of the nets and coinciding buoyant force of the rims was not taken into consideration when modeling these structures.

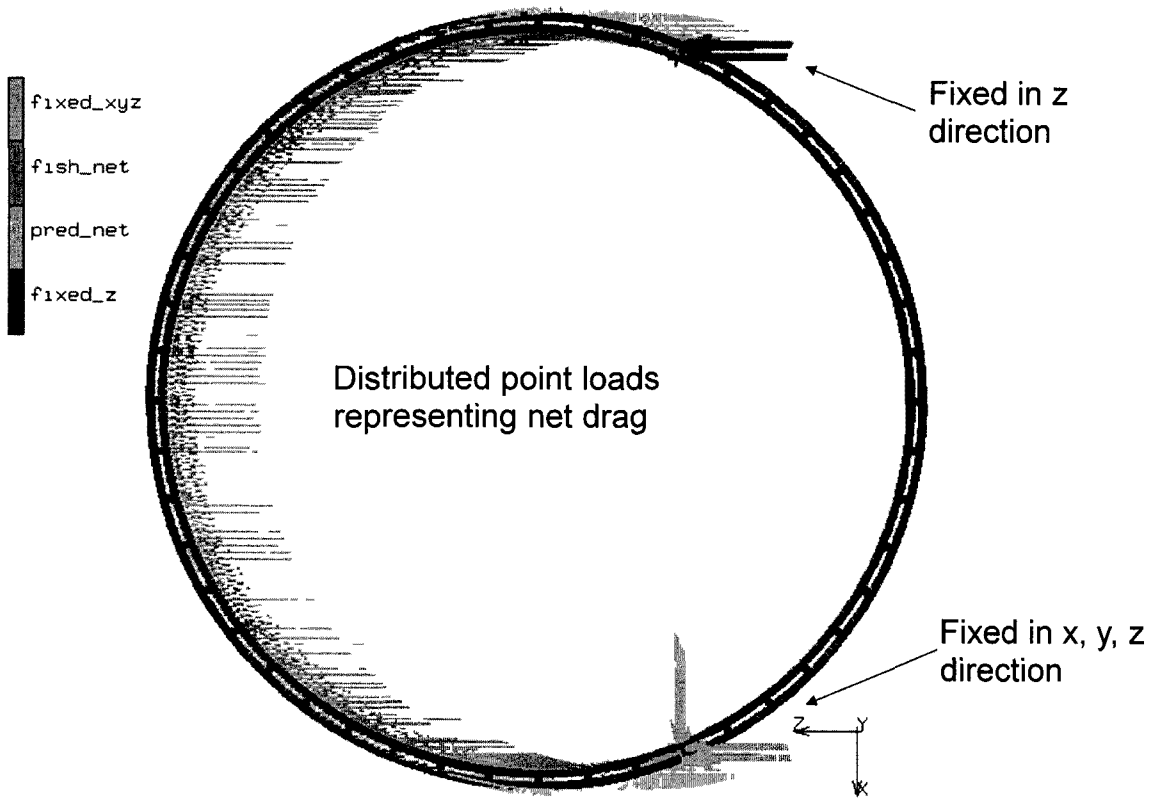

Figure 5.17: The first load case: the drag was assumed to be evenly distributed over "major arc" the inner and outer rims. The two additional bridle line supports (would be present in the "minor arc" of the cage frame), were not taken into consideration for this analysis.

The second load case investigated the response of the system due to y-line tensions. The model was fixed similar to the previous load case. However, in place of a distributed load, four sets of point loads were applied to the rim (Figure 5.18). Modeling the structure in this manner allowed more accurate representation of the attachments and localized stresses. In addition, these four sets of point loads can have different magnitudes, representing more "field-like" conditions. Both load cases, however, do assume the y-line locations (either as constraints or load application points) are symmetrically located around the rim. For each load case scenario, the geometric and material properties were assumed to be the same. In both of these

load cases, the major mechanism of kinking (the most dangerous) was examined. Therefore, certain loads and boundary conditions were neglected: additional bridle line supports, contribution from drag on the minor arc (mostly compensated by the attachment reaction forces, and out-of-plane components of reaction force.

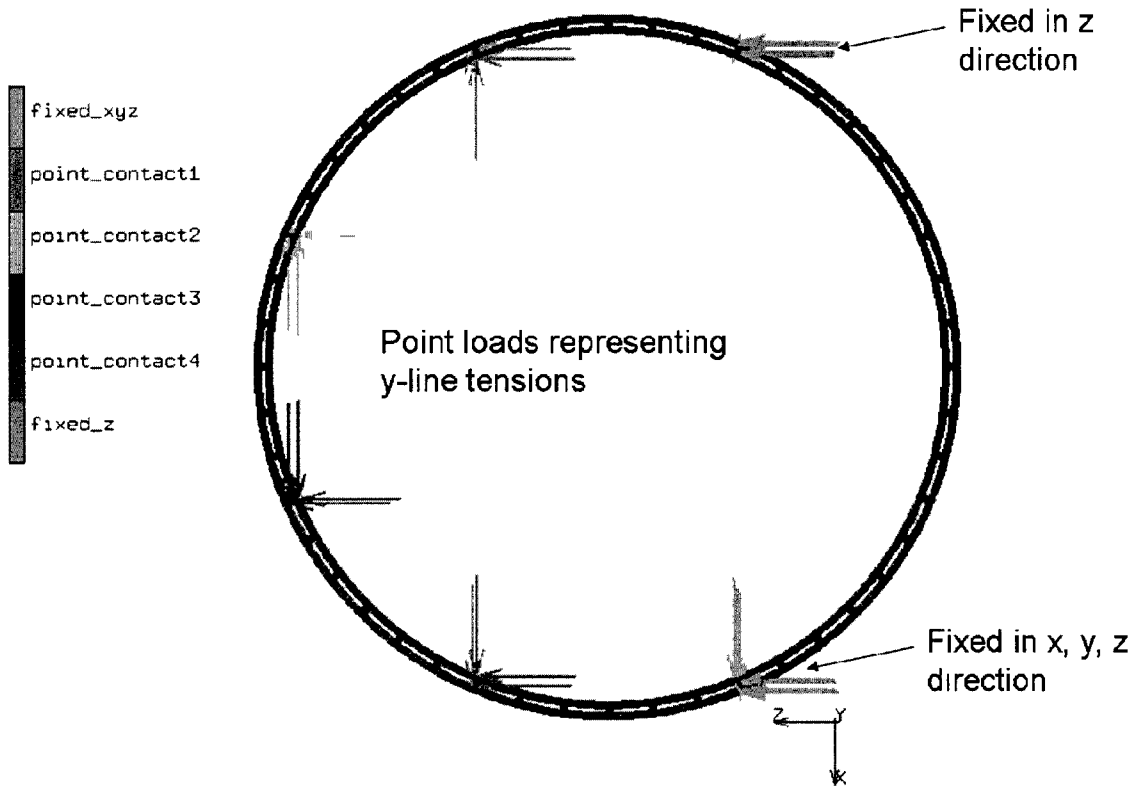

Figure 5.18: The tensions in the mooring line are represented by point loads applied to ½ the pipe circumference and evenly distributed on the inner and outer rims. The two additional bridle line supports (would be present in the "minor arc" of the cage frame), were not taken into consideration for this analysis.

5.7 Broad Cove Farm Case Study

As part of the field program, current meters and load cells were deployed at the site during three distinct operating conditions. These conditions consisted of deployment of net pens with (1) standard predator and smolt nets, (2) standard predator and fish nets and (3)

predator and fish nets fouled with biological material. Net pen attachment line (y-line) load cells were deployed during conditions (1) and (2). Since the smolt nets have a higher solidity than the standard fish nets, tension values during this condition were used in this study.

The current direction was an important factor in selecting the load cases. To accurately predict the stresses in the rims, the environmental conditions at the site had to be replicated in the model. Therefore, cases were chosen in which the cage would set back against the bridle lines due to the oncoming current, insuring that these lines were taking the majority of the load. Two data sets with these loading conditions occurred between 1400-1420 UTC on 5-May-04 and 2200-2220 UTC on 16-May-04 where forcing velocities were relatively steady in time (Table 5.4).

Table 5.4: The current velocity measurements obtained from the current meter located outside of the farm for two selected load cases.

Load Case Date	Time (UTC)	East-going (m/s)	North-going (m/s)
	1340	-0.070	0.559
5/05/2004	1400	-0.271	0.137
	1420	-0.071	0.493
	2140	-0.201	-0.004
5/16/2004	2200	-0.296	0.304
	2220	-0.268	0.258

In addition to the current velocity measurements, load cells data sets were also acquired during the same cases from the West, SW, SE and East y-lines (see Figure 5.4). Note that these y-line locations coincide with the applied boundary conditions presented in Figure 5.18. The instruments were programmed to measure net pen attachment loads at a rate of 5 Hz for 20 minutes each hour. The time series results for each load case are shown on Figures 5.19 and 5.20. The average and maximum loads are provided on Table 5.5. The maximum loads are

used as input to the structural model to calculate net pen rim stresses typical of normal operation.

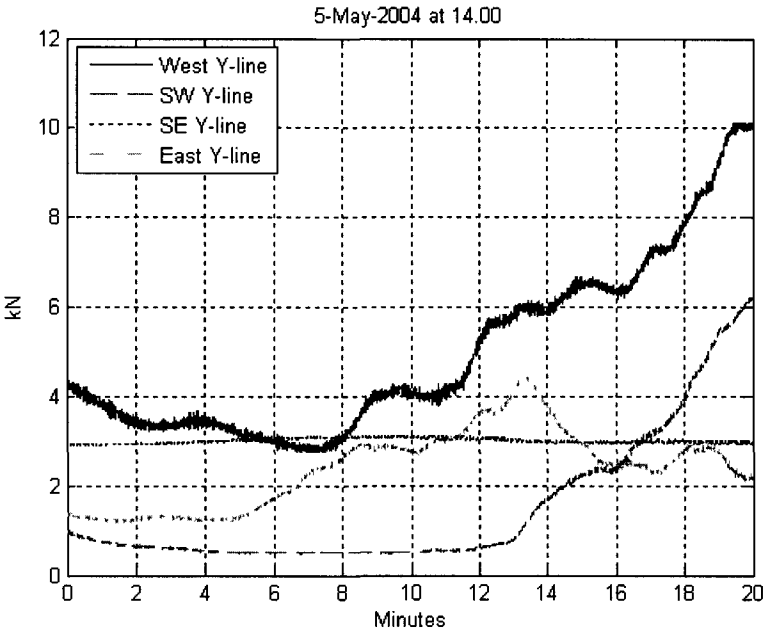

Figure 5.19: The load cell data sets from 5-may-2004 at 1400 UTC.

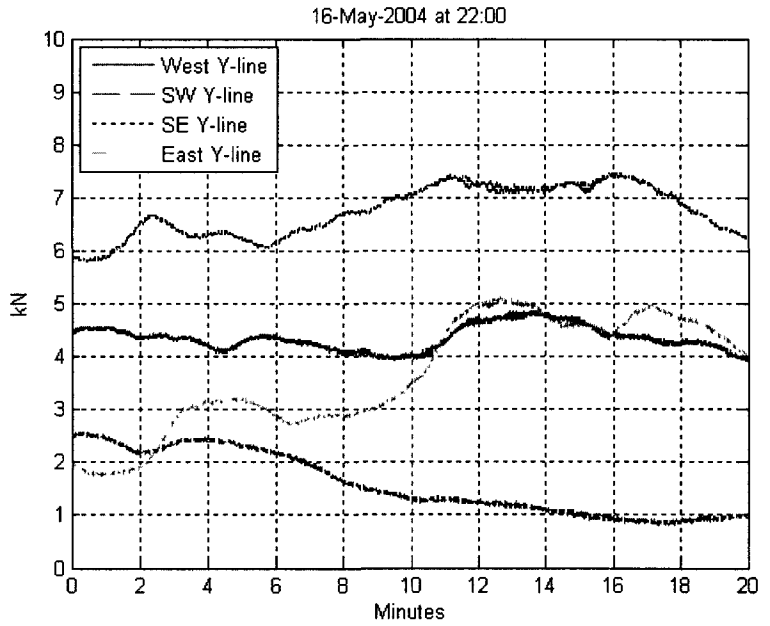

Figure 5.20: The tensions in the y-lines measured on 16-may-2004 at 2200 UTC.

Table 5.5: The average and maximum load cell results from each of the Y-line attachments.

Date Time		W Y-line (kN)	SW Y-line (kN)	SE Y-line (kN)	E Y-line (kN)
5/05/04	Average	3.21	1.50	2.95	2.41
1400	Maximum	8.39	6.26	3.10	4.46
5/16/04	Average	2.56	1.56	6.60	3.69
2200	maximum	3.07	2.58	7.32	5.13

5.8 Structural Modeling Results

Using shell elements, the localized failure criterion, and the previously described boundary conditions, case studies were performed to examine loads on the net pen structure in normal Broad Cove environmental conditions. The rims were subjected to a distributed load having a resultant equal to the vector sum of the two y-line load vectors (load case 1), and individual y-line attachment forces (load case 2). To model the worst-case scenario, the maximum load of each recorded value was utilized as provided in Table 5.5. The results from the structural model calculations yielded conservative Von Mises stress values for each load case as provided on Table 5.6.

Table 5.6: The Von Mises Stress calculated using the structural model for each load case and boundary condition.

Date Time (UTC)	Boundary Conditions	Von Mises Stress
5/05/2004	LC #1	2.17 (10^6) Pa
1400	LC #2	4.22 (10^6) Pa
5/16/2004	LC #1	2.14 (10^6) Pa
2200	LC #2	3.55 (10^6) Pa

A visual representation of rim stress for each of the load cases is shown in Figures 5.21 through 5.24. The maximum Von Mises stress obtained using the structural model was 4.23 (10^6) Pa, which is less than 1/5 of the 2.41 (10^7) Pa yield value for HDPE. This result is expected since during normal operation, the net pen rims rarely fail. However, the modeling technique now allows the operational limits to be quantified.

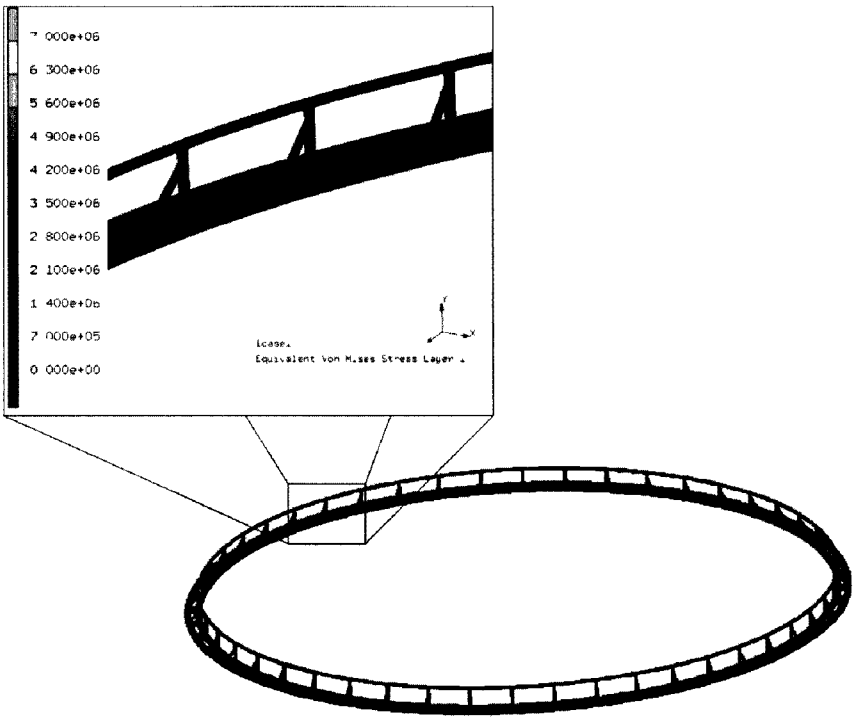

Figure 5.21: Von Mises Stresses in the net pen structure using environmental loading data of 5-may 2004 at 1200 with the 1st load case boundary conditions. The maximum stress occurred on the inside rim in the middle of the distributed loads as seen in Figure 5.18.

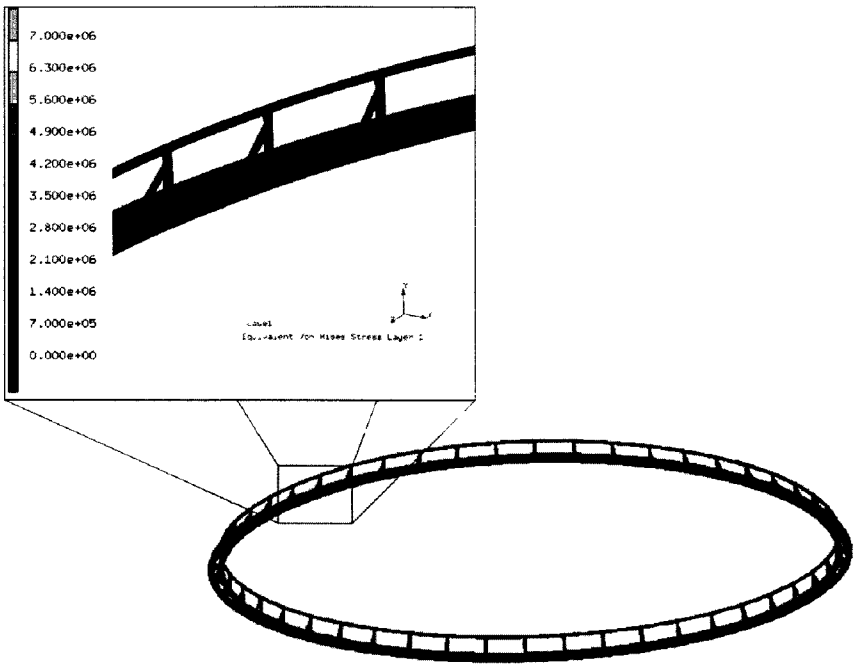

Figure 5.22: Von Mises Stresses in the net pen structure using environmental loading data of 5-may 2004 at 1200 with the 2nd load case boundary conditions. The maximum stress occurred at the SW y-line load application point (maximum y-line tension).

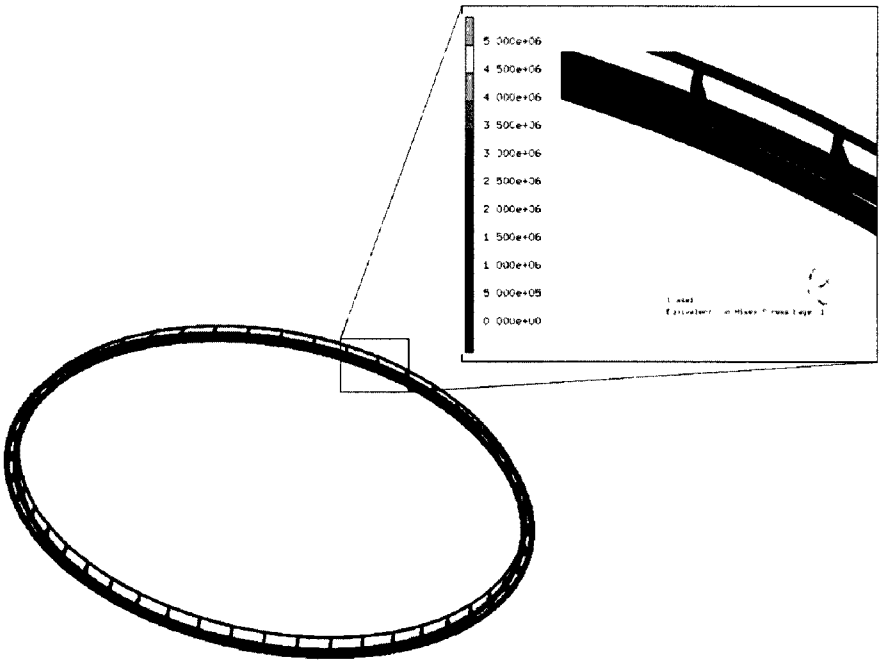

Figure 5.23: Von Mises Stresses in the net pen structure using environmental loading data of 16-may 2004 at 2200 with the 1st load case boundary conditions. The maximum stress occurred on the inside rim in the middle of the distributed loads as seen in Figure 5.18.

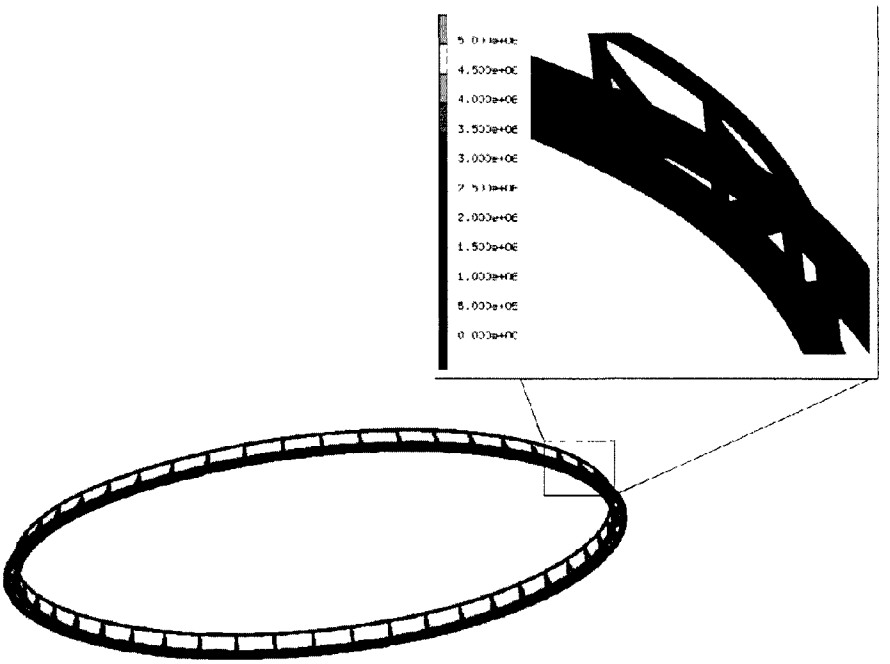

Figure 5.24: Von Mises Stresses in the net pen structure using environmental loading data of 16-may 2004 at 2200 with the 2nd load case boundary conditions. The maximum stress occurred at the SE y-line load application point (maximum y-line tension).

5.9 Estimated Maximum Load

The next step was to use the structural modeling technique to determine an estimated failure load of the net pen rim under various operational circumstances. Using shell elements and the localized failure criterion, simulations were performed for the three attachment configurations where the net pen was secured with (a) a single attachment point, (b) two attachment points and (c) four attachment points, as shown in Figure 5.25.

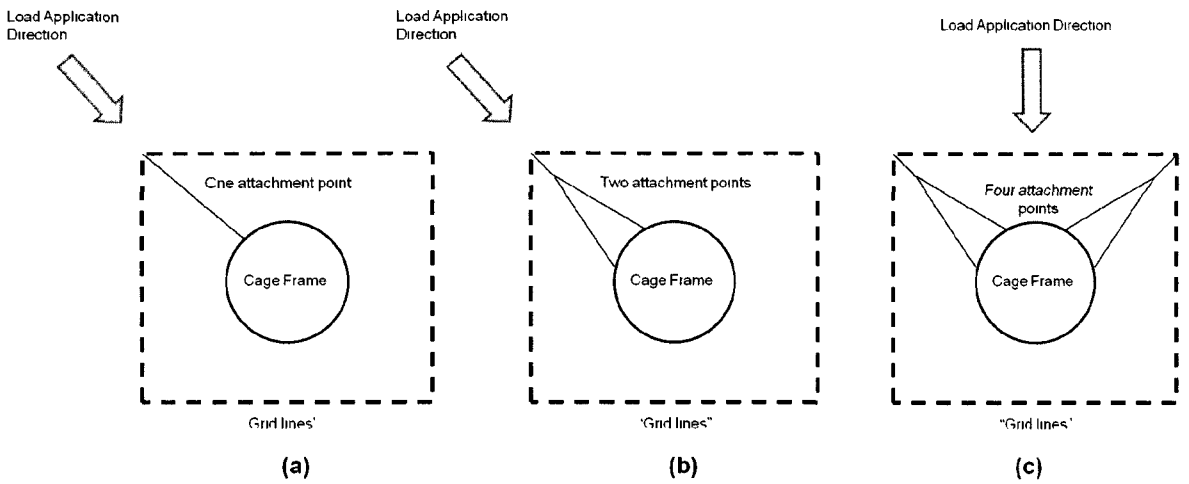

Figure 5.25: The attachment configurations were modeled where the net pen was secured with one (a), two (b) and four (c) point locations.

These configurations can represent three situations ranging from a worst-case scenario (a) to normal cage securement (c). In each one of these load cases, forces were applied to the cage frame similar to the first boundary condition until the localized failure criterion was met. The net pen rim was fixed in the x, y, z directions at one, two or four locations. Any other y-line attachments were presented by fixing the model in 1 direction (opposite direction of the load). The results of the model tests are provided in Table 5.7.

Table 5.7: The estimated failure loads for the three attachment locations

Load Case Configuration	Y-line attachment points	Failure Load kN	lbf
(a)	1	53.0 kN	11919 lbf
(b)	2	98.6 kN	22178 lbf
(c)	4	>444 kN	> 99815 lbf

With one y-line attachment point, the cage rim failed at 53 kN. However, it is rare that a net pen is secured by only one point. Typically, this situation exists if there is a line failure or the cage is temporarily secured for various operational reasons. Figure 5.26 shows the results when only one y-line attachment point was examined. The failure load increased to 98.6 kN when distributed over one full y-line (or two attachment points), as seen in Figure 5.27. When two y-lines were used, the failure load increased dramatically. Yield stresses in stanchions and over sections of the main rims were visible at 288 kN. However, the pipe still had some structural integrity at this point. The rims finally "buckled" at a load of over 444 kN (Figure 5.28). These cage loading conditions can occur regularly at a farm site if the correct environmental conditions exist. Fortunately, when examining the failure load for attachment configuration (b) and the rim loads and associated stresses, the forcing needed to obtain the failure load (98.6 kN) is significant.

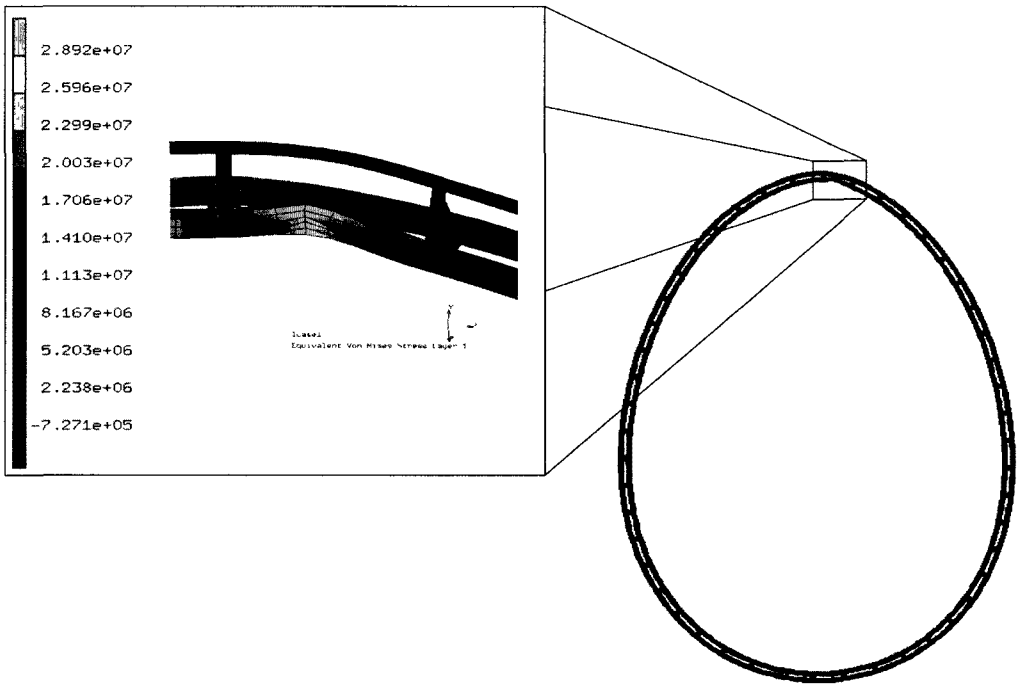

Figure 5.26: The von mises stress distribution on the net pen rim when 53 kN is applied as a distributed load.

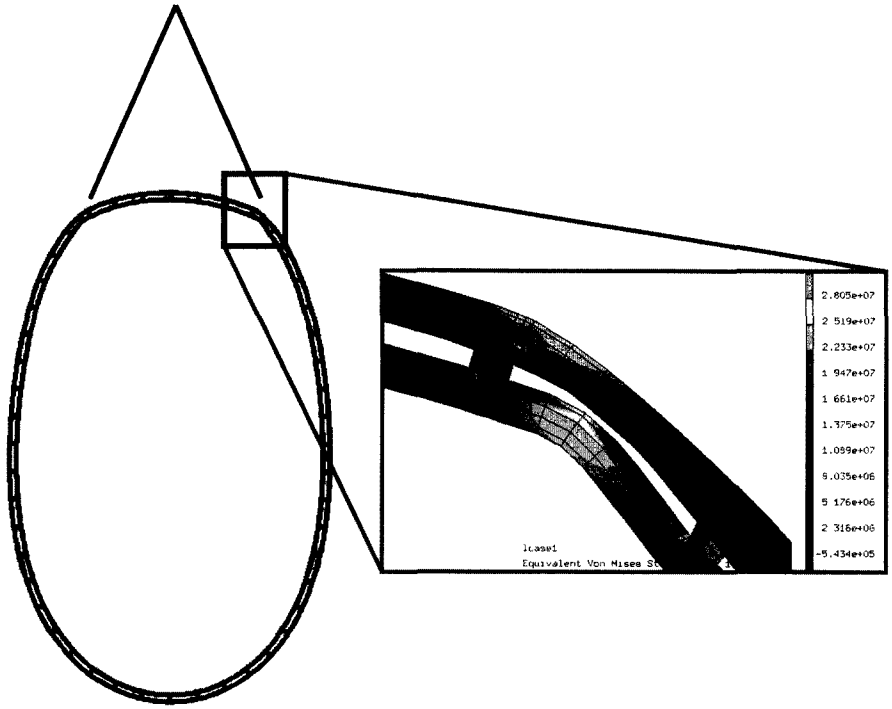

Figure 5.27: The von mises stress distribution on the net pen rim when one full y-line (shown superimposed above the results) is utilized.

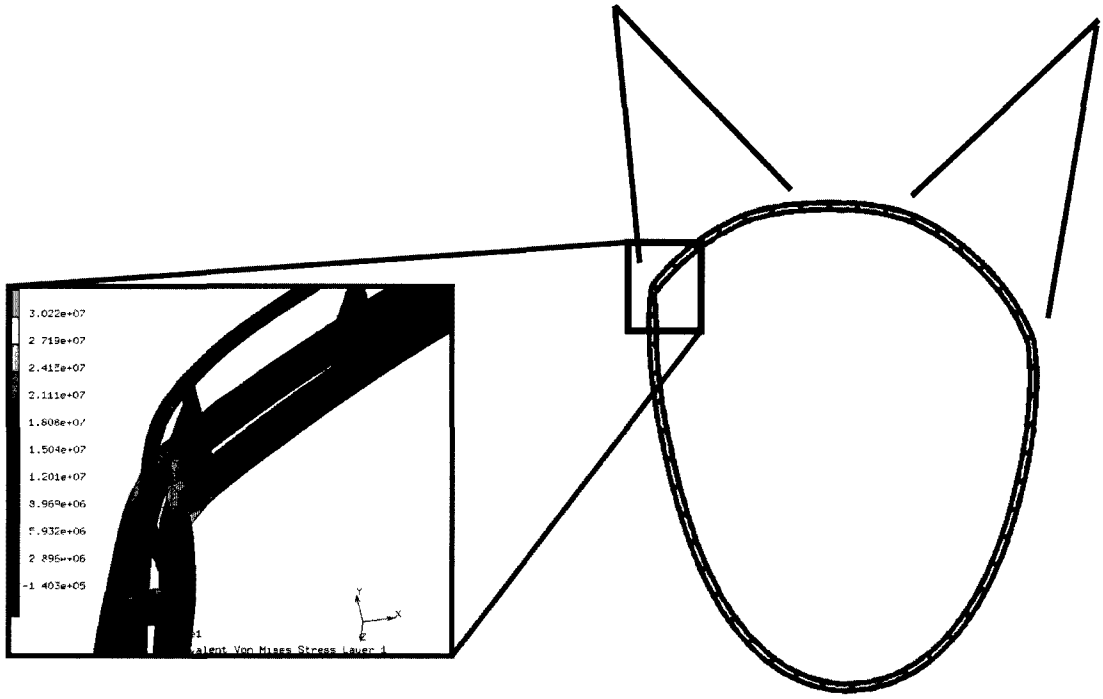

Figure 5.28: The von mises stress distribution on the net pen rim when two, symmetrical y-lines (shown superimposed above the results) are utilized.

It is important to recall that the boundary conditions used in the model are located symmetrically around the cage rim. In the field, however, operation personnel do not secure the cages at set locations (equally distributed along the rim), rather by "eye" and approximate distances between the y-lines. To investigate the effect of the y-line placement and failure of the pipe, a model was tested similar to LC #1 and y-line attachment configuration (c), except that the two "inside" y-line attachment points was separated by an additional 4.5 meters along the cage circumference (original separation was 12.9 meters), towards the undisturbed y-line locations. The results showed that although still adequate for the site, the failure load decreased by 31% (Figure 5.29).

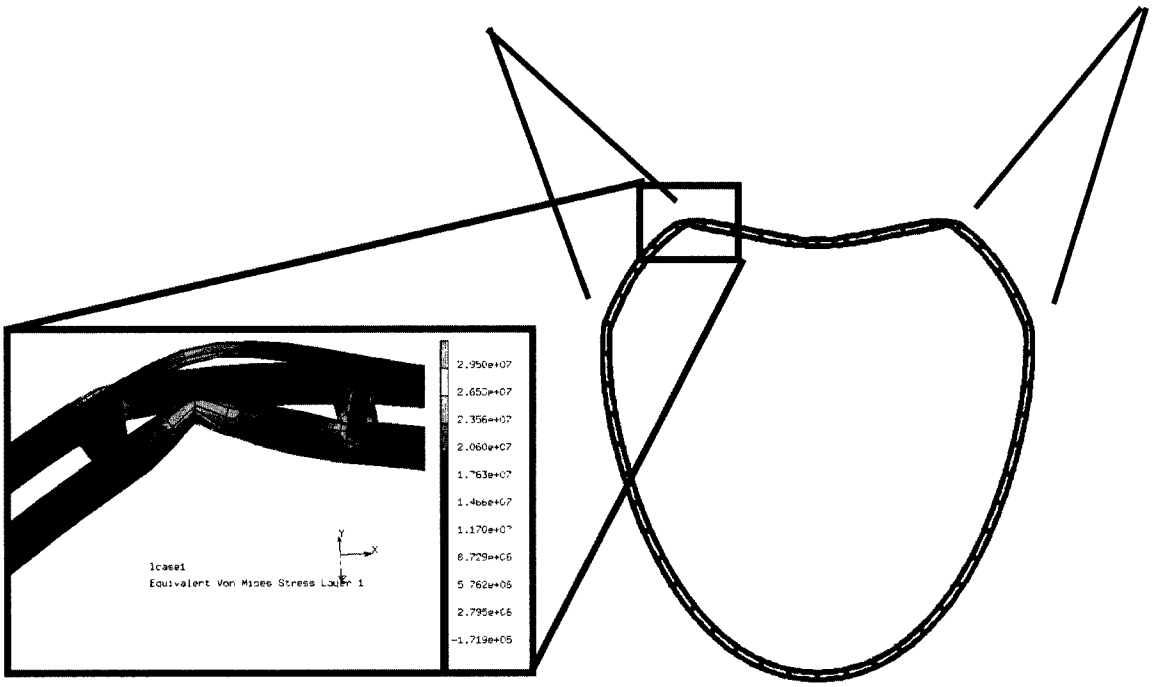

Figure 5.29: The stress distribution on the cage frame when y-lines are moved such they are not longer equally spaced around the cage circumference.

5.10 Conclusions

The technique to structurally model HDPE pipe used in fish farm net pens showed promise as an effective tool for specifying these components. As with many modeling applications, however, these results must be considered approximate. For example, the value of 6.67×10^8 Pa used for the Young's Modulus may have been underestimated and should be further investigated by performing additional tensile tests with a larger number of samples. In addition, the failure criteria are subjective and the boundary conditions simplified. The question also remains as to the appropriate loading rate, which affects the Young's Modulus for viscoelastic materials. Chapter 6 investigates this phenomena further.

Quantifying the load rate in environments with waves and currents may not be trivial. This will become more important if these structures are considered for more exposed or open ocean environments. For example, tidal currents are often considered to be quasi-static, since forcing periods are on the order of hours. In this condition, slower loading rates may be considered. In conditions where intense waves exist, forcing periods are on the order of seconds, so a faster load rate may be appropriate. At many open ocean sites, both waves and currents provide dominant forcing components, so a combination may also need to be considered. It is clear that since the structural integrity of HDPE pipe is related to the loading rate, future work should be conducted to optimize the approach.

Nevertheless, this present study showed that the HDPE pipe used for this near-shore fish farming application is appropriate. The structural modeling techniques developed, however, enabled the evaluation of acceptability margins. In the Broad Cove case, the estimated operational von Mises stress values were less than 1/5 of the yield stress. For the maximum load condition, it was necessary to consider the attachment configuration, where the worst-case

situation would occur as a point load. Utilizing two sets of y-lines (four attachment locations) minimizes the chance of this occurring. Using the developed techniques, additional studies can be conducted to optimize net pen designs and attachments for specific environments, especially if similar technologies are considered for more exposed, open ocean conditions.

CHAPTER 6

MECHANICAL BEHAVIOR OF HDPE IN MARINE APPLICATIONS

High density polyethylene (HDPE) is the dominant material used to build cage frames in the aquaculture industry. The fundamental engineering issues with HDPE are associated with how the material changes its stiffness and strength depending upon the service life, load rate and temperature. A preliminary investigation of the load rate dependence was presented in Chapter 5. In this chapter, this research is expanded to determine the mechanical behavior of HDPE during its service in marine environments, specifically, its sensitivity to strain rates. The majority of research into HDPE has focused on new material and strain rates associated with static terrestrial applications (e.g. buried pipe). Materials utilized in marine structures, however, are subjected to dynamic environmental forces (such as waves) and as a result, load the material at a much faster rate. In addition, aquaculture equipment is typically recycled from previous systems and the degradation or enhancements of the material properties in these conditions are not known. Thus, tensile tests were performed on new and pre-fatigued HDPE components, obtained from fish farms, in a laboratory setting at strain rates expected in open ocean environments.

The HDPE material parameters relevant to proper analysis of HDPE cage components under hydrodynamic loading were investigated. To accomplish this, numerical models were first

employed to predict and analyze structural performance of fish cages in an open ocean environment. The modeling effort included analysis of the overall dynamic behavior of a fish farm under various sea conditions and the associated stress within the structural components of fish cages made of HDPE material. The results were used to evaluate the HDPE material's strain rate. This information was then used to help identify the required displacement rates in laboratory experiments to obtain the relevant material properties. This task included mechanical testing of HDPE specimens made of new and "weathered" cage components which were subjected to several years of cyclic (fatigue) loading and exposure to elements during regular service in marine environments. The samples were tested in uniaxial tension under the strain rates predicted by the numerical model. The Young's Modulus and tensile strength at yielding were obtained. This preliminary research will help identify the important mechanical characteristics of previously deployed HDPE cage frame material.

6.1 Previous HDPE Research

HDPE is an extremely versatile material that has been used extensively in land based piping systems (Janson, 2003). This popular material has therefore been studied for a wide range of applications. Ogorkiewicz (1970) and Smith (1977) for example, provide a good review of the general material properties of thermoplastics and elastomers, respectively. Elleuch and Taktak (2005), Plummer et al. 2001, and Dasari et al. 2003 performed various tensile loading experiments. HDPE stress-strain relationship's were also investigated by Zahedi et al. 2008, Hillmansen et al. 2000, Ohashi et al. 2002, and Patlazhan et al. 2008. Dasari and Misra (2003b) present the tensile strength as a function of strain rate at a fixed temperature. The effect of manufacturing and joining processes and extended field deployment of HDPE mechanical properties were investigated by Dusunceli and Colak (2008), Chen et al. 1997, Gloor (1958), and

Ollick and Al-Amir (2003). The load rate influence on material fracture of HDPE was studied by Khan (2006), van der Wal and Gaymans (1997), and Gensler et al. 2000. Creep and fatigue properties were examined by Lai and Bakker (1995), Barker (1980), Parsons et al. 1999, Findlan (2007), and Jo et al. 1992. The effects of temperature on HDPE have been investigated by Nakayasu et al. 1961, Ghazanfari et al. 2008, Bilgin et al. 2007, and Merah et al. 2006. Dasari and Misra (2003) examined strain rates up to 10^{-1} sec^{-1} for new HDPE specimens. However, the material properties were for new materials and they were obtained at rates less than what preliminary investigations predict a cage system will experience (10^{-2} sec^{-1}).

6.2 Evaluation of Strain Rates in HDPE Cage Frames

The material characteristics of HDPE are needed to accurately predict the structural response of marine HDPE components. The approach taken was to use computer models to predict the load rates acting on a HDPE cage frame in marine environment and the associated strain rate of the material. Two numerical models were employed to estimate the strain rates acting within an HDPE gravity net pen in waves. In the first model, the Aqua-FE software (see section 2.1.1), was utilized to predict the variation of mooring forces acting on the cage superstructure. This information was then used as input to a second FEM software package, MSC.MARC Mentat (see section 5.5), to obtain the strain rate within the cage frame. The strain rate information predicted by the FEM was then used to help identify the testing rates for the mechanical testing experiments.

A standard circular gravity fish cage, common in the United States and Canada, was selected for this analysis. A model of the cage was placed in a simple mooring grid and analyzed under a series of regular wave conditions. To insure that the resulting mechanical testing included strain rates applicable to a variety of gravity cage systems, several factors that may

influence the cage frame's load and material strain response were investigated. These included several wave regimes applied to the system and variations in the mooring's compliancy, the fish cage net solidity, and the frame's pipe wall thickness.

6.2.1 Aqua-FE Mesh

A 100 meter circumference, surface gravity fish cage model was first constructed in Aqua-FE. The net pen consisted of 2 HDPE rings, stanchions, and handrail supporting a 9 meter deep net chamber. The system was of similar materials and construction to that described in Chapter 5. The net was tensioned with a weighted lower rim (HDPE filled with sand). These systems are used commonly for the grow-out of salmon in downeast Maine, USA. A picture of the fish cage is shown in Figure 6.1. The cage's geometric and material properties are provided in Table 6.1.

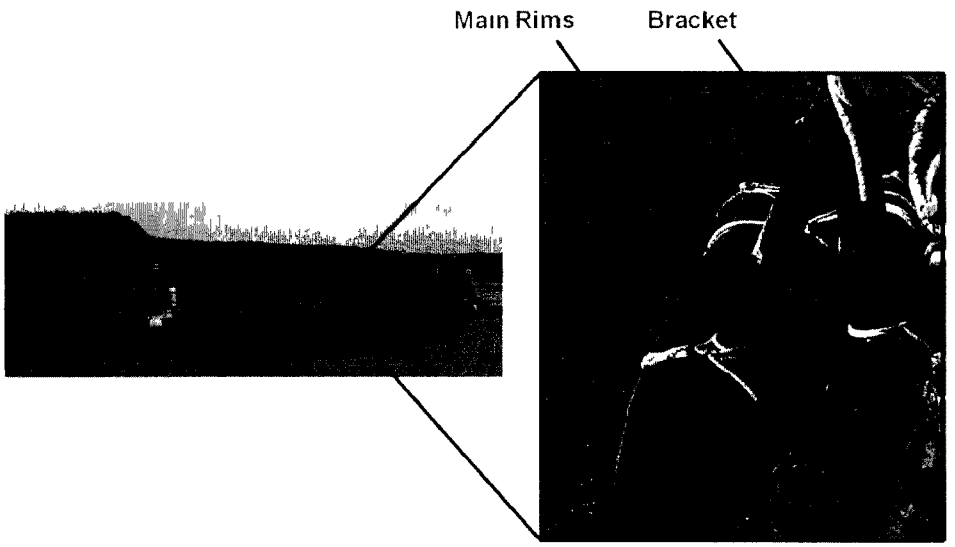

Figure 6.1: A standard circular gravity fish cage. Two main flotation pipes are connected by brackets, forming the upper superstructure.

Table 6.1:Geometric and material properties of a standard gravity net pen

Component	Parameter	Value
Cage	Overall Diameter	31.8 m
	Circumference	100 m
	Material	HDPE
	Net Chamber Depth	9 m
Flotation Pipe (inner and outer)	Pipe diameter	0.3238 m
	Thickness	0.0198 m
	Interior	Air
Brackets[a]	Number	48
Handrail	Pipe diameter	0.1143 m
	Thickness	0.0057 m
Lower rim[b]	Pipe diameter	0.3238 m
	Thickness	0.0198 m
	Interior	Sand

[a] Brackets are formed of various HDPE pipe sizes and lengths.

[b] Lower rim not shown in figure above. Lower rim consists of a single HDPE pipe filled with sand.

The net pen was assembled in Aqua-FE using 346 nodes and 492 elements. To simplify the Aqua-FE model construction, the mass contributions of the handrail and bracket components were combined into the main rims (the buoyancy contributions were neglected as the cage remained on the water surface). A grid mooring was constructed to secure the cage (Figure 6.2). This single bay grid was similar to that presented in Tsukrov et al. 2000 consisting of 4 grid lines and anchor legs, supported by submerged flotation. However, the scope of the system was increased to 4:1 by lengthening the anchor and grid lines. Each anchor leg consisted of 160 meters of 28 mm Polysteel® line, 27.4 meters of 94 mm chain and a drag embedment anchor (modeled as a fixed point). The mooring grid was submerged 18 meters below the surface and was supported by four 9.68 kN flotation elements. Bridle lines secured the top rim of the cage to the grid below. The water depth was set to 45 meters. The cage and mooring geometric and material properties are listed in Tables 6.2 and 6.3.

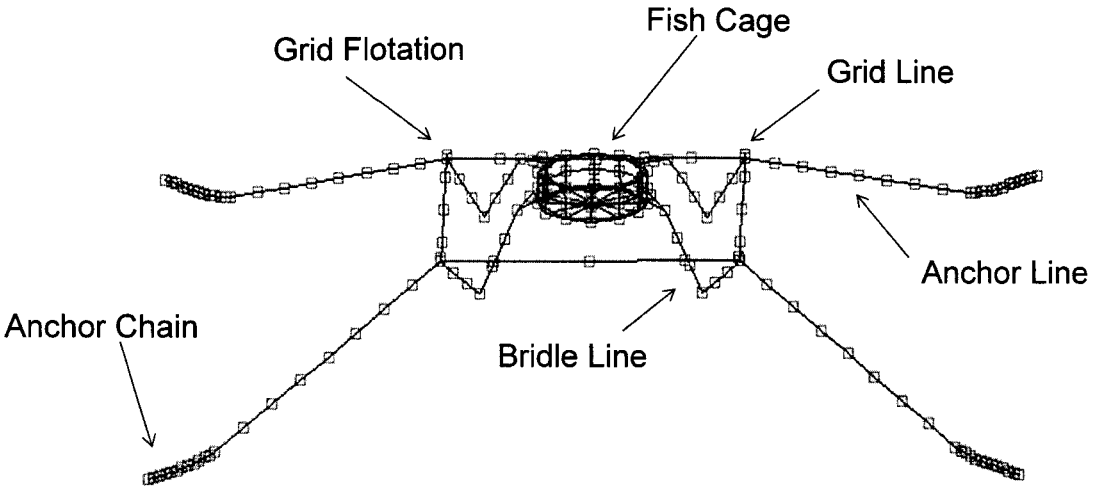

Figure 6.2: The Aqua-FE cage-grid mooring system model. A gravity fish cage was placed in a submerged grid, 18 meters below the surface in 45 meters of water. The lower ends of the anchor chain were fixed points.

Table 6.2: Geometric and material properties of the cage system used in the sensitivity study.

Component	Parameter	Value
Fish Cage Upper Rim	Effective Density	289.9 kg/m^3
	Young's Modulus	1.172×10^9 Pa
	Cross sectional Area	8.200×10^{-2} m^2
Fish Cage Lower Rim	Effective Density	1738 kg/m^3
	Young's Modulus	1.172×10^9 Pa
	Cross sectional Area	2.200×10^{-2} m^2
Fish Cage Net Chamber	Effective Density	1025 kg/m^3
	Young's Modulus	2.00 x 1010 Pa
	Cross sectional Area	[b]
	Repetitions	[b]
Stiffener	Effective Density	1025 kg/m^3
	Young's Modulus	2.5×10^{11} Pa
	Cross sectional Area	7.000×10^{-6} m^2

Table 6.3: Geometric and material properties of the mooring system used in the sensitivity study.

Component	Parameter	Value
Anchor Line	Effective Density	1380 kg/m^3
	Young's Modulus	8.687 x 10^9 Pa
	Cross sectional Area	6.583 x 10^{-4} m^2
	Length	160 m
Anchor Chain	Effective Density	6610 kg/m^3
	Young's Modulus	2.0 x 10^{11} Pa
	Cross sectional Area	7.024 x 10^{-3} m^2
	Length	27.4 m
Grid line	Effective Density	940 kg/m^3
	Young's Modulus	1.830 x 10^{09} Pa
	Cross sectional Area	1.257 x 10^{-4} m^2
	Length	90 m
Grid Float	Effective Density	291.0 kg/m^3
	Young's Modulus	2.0 x 10^{11} Pa
	Cross sectional Area	0.963 m^2
Bridle line	Effective Density	1025 kg/m^3
	Young's Modulus	[a]
	Cross sectional Area	1.140 x 10^{-3} m^2
	Length	45 m

[a] Various bridle line Young's Modulus values were investigated.

[b] Various net chamber solidities were examined.

Recall that the purpose of the numerical model was to determine strain rates in the frame so that the material characteristics of HDPE could be measured in the laboratory at the rates associated with marine loading conditions. To help insure that the obtained data would be useful for a variety of cage and mooring systems in different environments, several loading conditions and combinations of cage and mooring components were examined, specifically those which could influence the loading rate on the net pen (and therefore the strain rate of the HDPE material). These included investigating the fish cage response to various regular wave regimes, bridle line compliance, net solidities and the cage frame pipe wall thickness.

To quantify the effect of environmental conditions on the structure's load rate, three sets of waves were applied to the system. Currents were not investigated as current forces tend to apply a slow, steady load, thus producing lower strain rates (compared to wave forces). The wave steepness, wave height (H) over wave length (L), was set at 1/15, corresponding to small amplitude waves. The selected environmental loadings cover conditions that can be experienced near shore and at exposed aquaculture sites. To obtain a worst case scenario, wave direction was aligned with one mooring and bridle leg as seen in Figure 6.3. Regular waves with the following characteristics were applied to the model:

- T = 4.0 sec, L = 24.93 m, H = 1.66 m
- T = 8.0 sec, L = 99.73 m, H = 6.65 m
- T = 12.0 sec, L = 202.68, H = 13.512 m

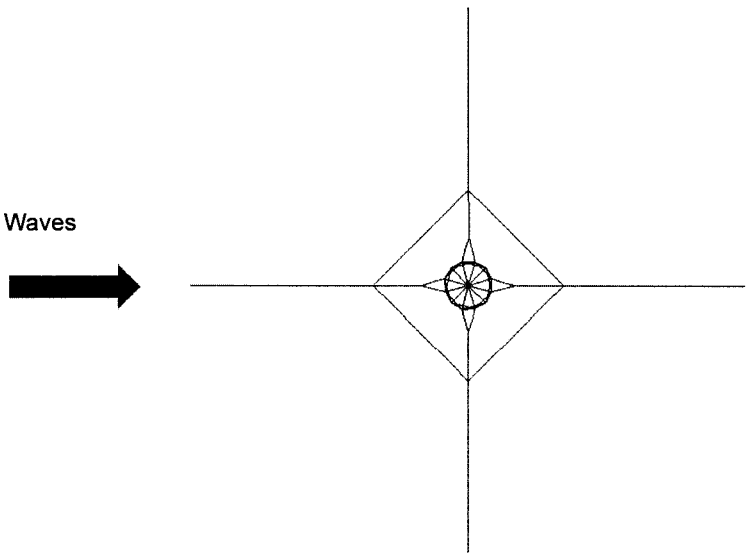

Figure 6.3: Wave direction was aligned with one sole anchor leg in each simulation.

Bridle line compliance and drag associated with the fish cage can also influence the structure's strain rate. Thus, numerical simulations were performed with three bridle line

stiffness values and net solidities. The mooring compliance was investigated considering the fish cage secured with bridle lines having different material properties: nylon line (common elastic mooring member, E = 6.315 x 10^8 Pa), polysteel® line (standard aquaculture equipment, E = 3.431 x 10^9) and steel cable (without bending resistance, E = 2.0 x 10^{11}). The remainder of the mooring parameters remained the same as those listed in Table 6.2.

As shown in chapter 2, the drag force of an aquaculture cage system is dominated by the net chamber. Therefore, to examine the influence of net pen drag on the cage frame strain rate, the net solidity was set to 8%, 16% and 24% (similar to those used in Chapter 4). The net material and geometric properties applied to the model are shown in Table 6.4.

Table 6.4: The net properties utilized in the Aqua-FE sensitivity study.

Component	Parameter	Value
8 % Solidity Net Chamber	Effective Density	1150 kg/m^3
	Young's Modulus	2.00 x 10^{10} Pa
	Cross sectional Area	9.809 x 10^{-7} m^2
	Repetitions	309
16 % Solidity Net Chamber	Effective Density	1150 kg/m^3
	Young's Modulus	2.00 x 10^{10} Pa
	Cross sectional Area	4.909 x 10^{-6} m^2
	Repetitions	260
24 % Solidity Net Chamber	Effective Density	1150 kg/m^3
	Young's Modulus	2.00 x 10^{10} Pa
	Cross sectional Area	5.91 x 10^{-6} m^2
	Repetitions	342

The final parameter analyzed in this study was the pipe wall thickness. Two values representing standard (18 mm) and thick wall (36 mm) pipe were investigated. This parameter was modified during the structural analysis of the cage frame, discussed in section 6.2.3. Twenty seven dynamic simulations were performed, summarized in Table 6.5. Each model

configuration was run for 400 seconds to insure a steady state mooring load response. The output bridle line tensions were then used as input to the structural model of the fish cage.

Table 6.5: The environmental conditions, bridle line materials and net chamber solidities analyzed in the sensitivity study.

Applied Waves	Bridle Line Material	Net Chamber Solidity	Load Case
Wave Height: 1.66 m Wave Period: 4 sec	Nylon	8 %	1
		16 %	2
		24 %	3
	Polysteel	8 %	4
		16 %	5
		24 %	6
	Steel	8 %	7
		16 %	8
		24 %	9
Wave Height: 6.65 m Wave Period: 8 sec	Nylon	8 %	10
		16 %	11
		24 %	12
	Polysteel	8 %	13
		16 %	14
		24 %	15
	Steel	8 %	16
		16 %	17
		24 %	18
Wave Height: 13.51 m Wave Period: 12 sec	Nylon	8 %	19
		16 %	20
		24 %	21
	Polysteel	8 %	22
		16 %	23
		24 %	24
	Steel	8 %	25
		16 %	26
		24 %	27

6.2.2 Dynamic Modeling Results

The steady state bridle line tensions were obtained from the load-bearing line in each simulation. Output tension results for the gravity cage from load cases 1, 4 and 7 (lowest tensions) and 19, 22, and 25 (highest tensions) are shown in Figure 6.4. It can be seen that the steel cable bridle lines produced the largest amplitude loads in both wave regimes. This is expected as the line is not as compliant, thus similar forcing will incur a larger component stress. In addition, the fish cages with high net solidities produce higher mooring tension compared to those with lower net solidities, which is consistent with previous analysis (Chapter 4).

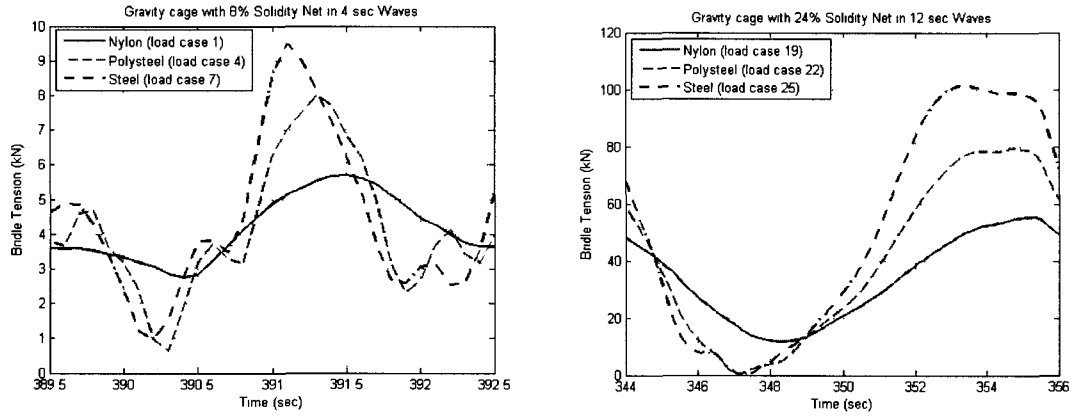

Figure 6.4: The output bridle line tension results with 2 net solidities under two regular wave regimes. The 8% solidity net chamber in 4 second, 1.66 meter waves (left) and 24% solidity in 12 second, 13.5 meter waves (right).

To obtain the strain rates in the cage frame, the loading predicted from the hydrodynamic model must be transferred to the structural model. This was accomplished by approximating the average steady state amplitude and period of the bridle tension by a sinusoidal curve. This representative bridle force equation was then used as input for the structural MSC.MARC model. The following sinusoidal equation was utilized:

$$F(t) = A_{load} \sin(ct) \qquad (6.1)$$

where F is the time dependent bridle load, A_{load} is the load amplitude, $c = 2\pi/T$ (rad/sec), T is the period, and t is time. These parameters for each simulation are shown in Table 6.6. The maximum and minimum load rates, shown in the shaded boxes, were selected for input into the structural model.

Table 6.6 : The output parameters for the forcing equation required for the structural analysis.

waves	**Bridle Line material**	**Net Chamber Solidity**		
		8 %	**16 %**	**24 %**
Height: 1.66 m Period: 4 sec	Nylon	A_{load} = 1180 c = 1.57	A_{load} = 1450 c = 1.57	A_{load} = n/a [a] c = 1.57
	Polysteel	A_{load} = 2650 c = 1.57	A_{load} = 2333 c = 1.57	A_{load} = n/a [a] c = 1.57
	Steel	A_{load} = 4000 c = 1.57	A_{load} = 2150 c = 1.57	A_{load} = n/a [a] c = 1.57
Height: 6.65 m Period: 8 sec	Nylon	A_{load} = 11200 c = 0.785	A_{load} = 4400 c = 0.785	A_{load} = 2900 c = 0.785
	Polysteel	A_{load} = 8842 c = 0.785	A_{load} = 8400 c = 0.785	A_{load} = 9200 c = 0.785
	Steel	A_{load} = 10400 c = 0.785	A_{load} = 10000 c = 0.785	A_{load} = 12000 c = 0.785
Height: 13.5 m Period: 12 sec	Nylon	A_{load} = 15600 c = 0.5235	A_{load} = 19998 c = 0.5235	A_{load} = 17100 c = 0.5235
	Polysteel	A_{load} = 19998 c = 0.5235	A_{load} = 29100 c = 0.5235	A_{load} = 32100 c = 0.5235
	Steel	A_{load} = 24000 c = 0.5235	A_{load} = 34500 c = 0.5235	A_{load} = 49800 c = 0.5235

[a] The resulting output tensions were noisy and not sinusoidal in nature. Therefore, this data set was not utilized in the study.

6.2.3 Structural Modeling of the Cage Frame

The output load rates obtained from Aqua-FE were used as input for the structural FE model. The mesh of the entire net pen flotation structure was constructed in MSC.MARC/Mentat using the geometric and material properties provided in Table 6.7. As previously noted, two pipe wall thicknesses were considered. Shell elements, type 139, were

employed throughout the mesh. The inner and outer flotation pipe assemblies were modeled with elements having the dimensions of 294.8mm x 79.3 mm. A total of 24,864 nodes and 25,824 elements were used in the model. A portion of the FEM of the net pen is shown in Fig. 6.5.

Table 6.7: The geometric and material properties of the net pen flotation structure FEM.

Component	Parameter	Value
Cage	Overall Diameter	31.8 m
	Circumference	100 m
	Material	HDPE
	Young's Modulus[a]	6.67 (10^8) Pa
	Poisons ratio[a]	0.42
	Yield Stress[a]	2.41 (10^7) Pa
Flotation Pipe (inner and outer)	Pipe diameter	0.3238 m
	Thickness 1[c]	0.018 m
	Thickness 2[c]	0.0037 m
Rim Sleeve	Pipe diameter	0.4064 m
	Thickness[b]	0.0690 m
Sleeve Support	Pipe diameter	0.3238 m
	Thickness	0.0198 m
Handrail	Pipe diameter	0.1143 m
	Thickness	0.0057 m
Handrail Sleeve	Pipe diameter	0.1413 m
	Thickness[b]	0.0242 m
Vertical Support	Pipe diameter	0.1413 m
	Thickness	0.0134 m
Angled Support	Pipe diameter	0.1143 m
	Thickness	0.0108 m

[a] All components used in the model has the same Young's Modulus, poisons ratio and yield stress.

[b] Sleeves take the rim or handrail pipe thickness into account.

[C] Two wall thickness were investigated in this study to represent a thin and thick walled structure.

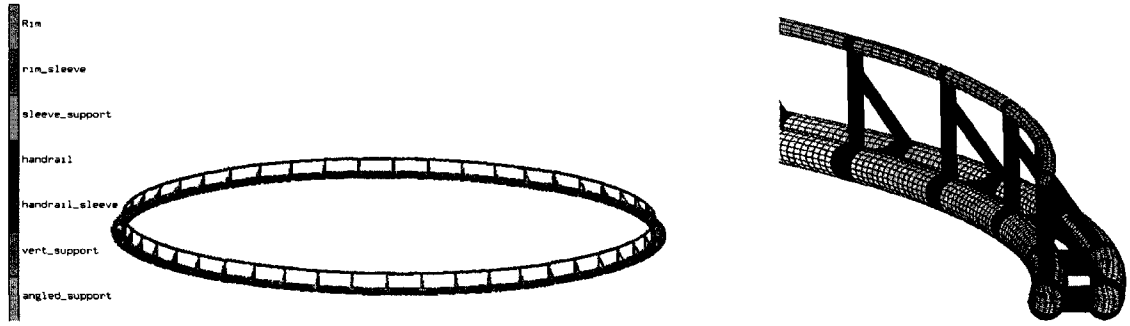

Figure 6.5: The FEM constructed in MSC.MARC/Mentat. The full rim is shown on left, a portion of the mesh on right.

The boundary conditions utilized in this study were similar to those presented in load case 2 in section 5.6. In the FEM model, the tensions in the bridle lines were represented by point loads which were applied to 1/2 the pipe circumference and distributed on the inner flotation pipe in a single location (Figure 6.6). This load case investigated the response of the system due to the localized forces of the bridle line tensions predicted by the Aqua-FE software. The model also contained two fixed points. The first restricted the model in the x, y and z directions. The second restricted the mesh in the x direction only. The fixed points were symmetrically located around the cage frame, 45 degrees apart. Note that these point loads (and associated reaction forces the boundary conditions) represent the effects of cage inertia and net drag.

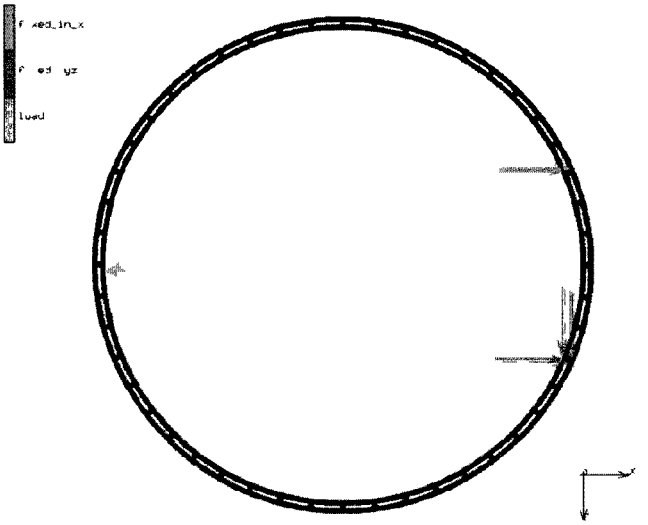

Figure 6.6: The boundary conditions applied to the FEM.

The following equations were used as input for the point loadings, as determined from the dynamic analysis:

$$F(t) = 1180\sin(1.57t) \tag{6.2}$$

$$F(t) = 49800\sin(0.5235t) \tag{6.3}$$

Each of the load equations was applied to the cage rims with wall thickness of 18 mm and 36 mm. Strains and strain rates are different for different points on the frame. Four points along the fish cage frame were chosen for monitoring, as shown in Figure 6.7. These locations were selected due to the proximity to the load application point, as well as being in the areas of expected high strain. Three components of strain were recorded: axial ε_{xx}, ε_{yy} and $\varepsilon_{equivalent}$, where $\varepsilon_{equivalent} = \sqrt{\frac{2}{3}(\epsilon_{xx}^2 + \varepsilon_{yy}^2 + \varepsilon_{zz}^2)}$. Linear elastic analysis was assumed.

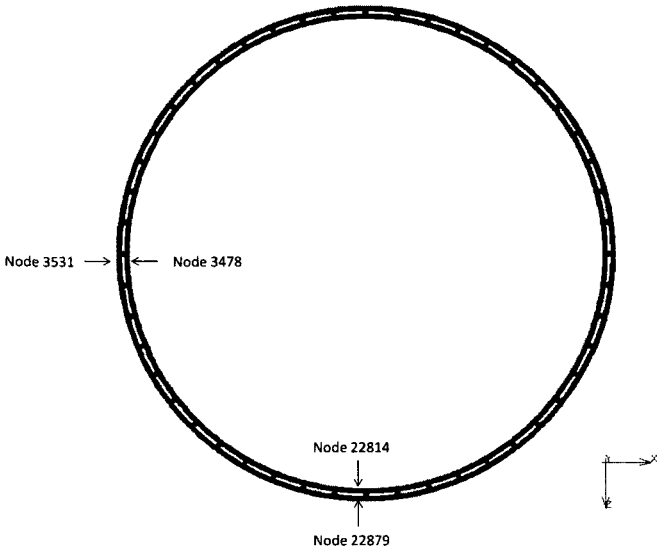

Figure 6.7: Strain in the material was monitored in four nodal positions along the cage frame.

Figures 6.8 and 6.9 present variations of strain corresponding to the applied load described by equations 6.2 and 6.3 on the thin-walled pipe system. It can be seen that the combination of sinusoidal load and linear elastic analysis assumption produces consistent cyclic results.

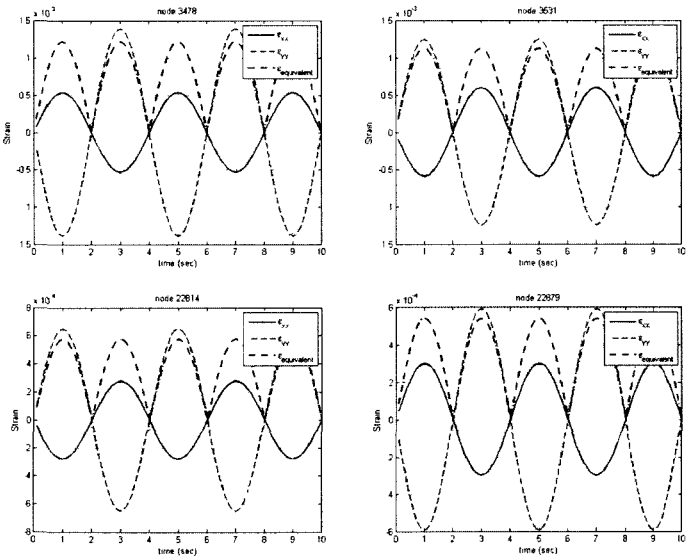

Figure 6.8: The output strain results from the structural analysis of the thin wall pipe under forcing described by equation 6.2.

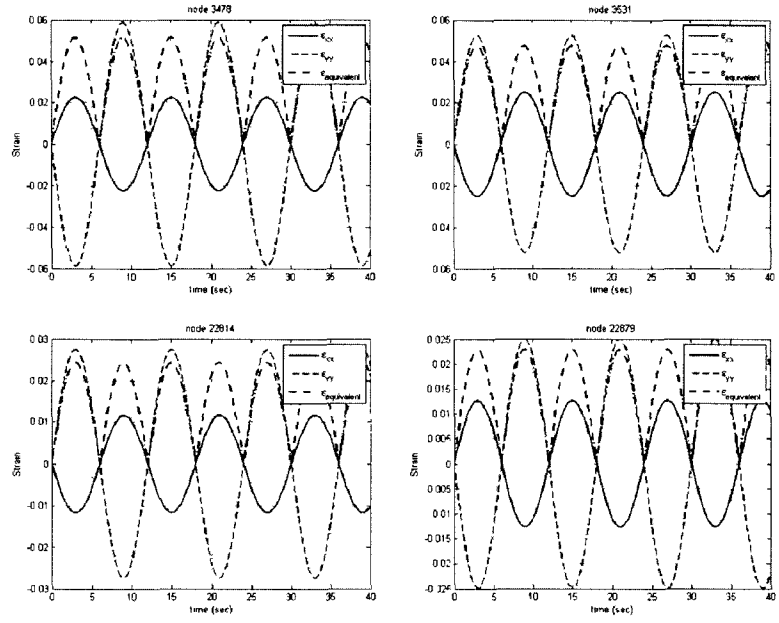

Figure 6.9: The output strain results from the structural analysis of the thin wall pipe under forcing described by equation 6.3.

The strain rate, $\dot{\varepsilon}$, of the material was obtained from the FEM's strain predictions using

$$\dot{\varepsilon} = \frac{2\pi A_{strain}}{T} \cos\left(\frac{2\pi}{T} t\right) \tag{6.4}$$

where A_{strain} is the strain amplitude, T is the period, and t is the time. The oscillatory (cos) term can be dropped to obtain the maximum strain rate. Table 6.8 lists the predicted strain rates in the thin and thick wall pipes in each wave regime loading. It can be seen that the thinner wall pipe experienced higher strain rates due to less material in the rim.

Table 6.8 : The predicted strain rate, as defined by equation 6.4, from the structural analysis. The maximum and minimum values are highlighted.

Strain Comp.	Loading Equation	Strain Rate (s^{-1})							
		Thin Wall Pipe				Thick Wall Pipe			
		Node 3478	Node 3531	Node 22814	Node 22879	Node 3478	Node 3531	Node 22814	Node 22879
ε_{xx}	6.2	5.33e-4	5.94e-4	2.76e-4	2.99e-4	3.34e-4	3.46e-4	1.66e-4	1.73e-4
ε_{yy}		1.40e-3	1.20e-3	6.49e-4	5.92e-4	8.42e-4	7.52e-4	3.93e-4	3.57e-4
ε_{equiv}		1.20e-3	1.1e-3	5.77e-4	5.41e-4	7.40e-4	6.76e-4	3.49e-4	3.24e-4
ε_{xx}	6.3	7.5e-3	8.4e-3	3.9e-3	4.2e-3	4.7e-3	4.9e-3	2.3e-3	2.4e-3
ε_{yy}		1.95e-2	1.75e-2	9.1e-3	8.3e-3	1.19e-2	1.06e-2	5.5e-3	5.0e-3
ε_{equiv}		1.71e-2	1.58e-2	8.1e-3	7.6e-3	1.04e-2	9.5e-3	4.9e-3	4.6e-3

The maximum and minimum strain rates predicted by the model were 1.95×10^{-2} s^{-1} and 1.66×10^{-4} s^{-1}, respectively. Since information on the HDPE material properties at strain rates near the latter value are available for unused HDPE (for example, Dasari and Misra, 2003), the lower strain limit was not investigated in this study. As a result, the following strain rates were selected for the experimental program, insuring that the upper strain rate of interest was bracketed:

- Rate 1: 1.0×10^{-3} s^{-1}
- Rate 2: 1.0×10^{-2} s^{-1}
- Rate 3: 1.0×10^{-1} s^{-1}

These strain rates were utilized in the tensile testing experiment to determine the material characteristics of the new and previously used HDPE.

6.3 Experimental Program

Using the strain rates predicted by the FEA models, the material properties of the new and previously deployed HDPE specimens were measured. It has been shown that exposure to

UV light and rain does not significantly change HDPE's material properties (Ollick and Al-Amir, 2003). However, any effect of cyclic loading, due to the daily tidal current or wave events on the material was not known. Therefore, new and previously deployed specimens of HDPE were uniaxially tested to determine their mechanical properties under the strain rates chosen in the previous section. Previously fatigued material was obtained from 3 fish farms. For comparison, new, unused pipe was also acquired for this experiment. Twenty common "dog bone" shaped specimens were then fabricated from the HDPE material and tensile tested in an Instron® Schenk Testing System (Model 1350). The material's Young's Modulus and tensile strength at yielding for selected strain rates were determined.

6.3.1 HDPE Specimens

The pre-used HDPE material was obtained from the main rims of surface gravity cage systems from 3 fish farms located in the Faeroe Islands, British Columbia and New Hampshire. The unused material was obtained from a local supplier of HDPE pipe. To properly quantify the material properties of each specimen, a detailed chemical composition and deployment history of the pipe would be required. Unfortunately, the composition was not known, and only anecdotal evidence was available for some of the samples in regards to the duration of deployment and environmental conditions at the farm sites. Whereas it is common practice to keep detailed records of net chambers (due to cleaning, maintenance, replacement, etc), it is not the case for the cage frame, and it is common for sections of pipe to be recycled into new systems. This limits any direct comparison that can be made between samples. As a result, the information gained from this study will be qualitative and provide "seed" research results for future, more thorough, investigations.

The goal of the experiments, therefore, was to determine if any trends were present that suggest that previously deployed material had significant differences in the material

properties. Table 6.9 lists the geometric properties, origin, and known information regarding the deployment history of each pipe sample obtained from the aquaculture farms.

Table 6.9: The geometric properties, origin and deployment history for the acquired pipe specimens.

Pipe Sample	Pipe Dimensions	Origin	Known Deployment History
A1[a]	L = 62.2 cm D = 31.75 cm T = 17.5 mm	Iceland / Faeroe Islands	Deployed in Iceland in 2002 at an exposed site. Towed to the Faeroe Islands in 2006 and placed in a semi-exposed farm. Pipe is PE80. Pipe specimens courtesy of Fiskaaling.
A2[a]	L = 61.8 cm D = 31.75 cm T = 17.5 mm	Iceland / Faeroe Islands	Deployed in Iceland in 2002 at an exposed site. Towed to a farm in the Faeroe Islands in 2006 to a semi-exposed farm. Pipe is PE80. Pipe specimens courtesy of Fiskaaling.
B	L = 92.7 cm D = 21.9 cm T = 11.1 mm	New Hampshire, USA	Cage subjected to a 5 month deployment in Gulf of Maine at the UNH OOA Demonstration site. Pipe specimens courtesy of JPS Industries.
C	L = 114.3 cm D = 21.9 cm T = 9.525 mm	British Columbia, Canada	Deployed at Eggerton Farm, a protected site, for approximately 17 years. Site experiences 10 significant storms a year, with H_s of 0.75 to 1 meter. Pipe specimens courtesy of Marine Harvest.
D	L = 129.5 cm D = 27.3 cm T = 17.5 mm	British Columbia, Canada	Deployed at Paradise Bay Farm for 12-17 years. Wave climate is unknown. Pipe specimens courtesy of Marine Harvest.
N	L = 137.6 cm D = 11.43 cm T = 11.43 mm	ISCO Industries, USA	New, unused pipe. Shelf life unknown. Purchased from ISCO Industries.

[A] Pipe samples are from the inner and outer rims of the same cage system.

Tensile tests were performed to obtain the materials Young's Modulus and tensile strength at yielding. Twenty type V specimens, specified by ASTM D638, were fabricated from each pipe segment. The type V geometry was chosen due to the planned strain rate ranges and limited piston stroke of the Instron machine. The specimens were taken from the pipe as shown in Figure 6.10. In an effort to keep specimens flat and uniform among the different pipe

samples, all specimens were machined on an end mill. The gage cross sectional area of the neck of each specimen was then measured with calipers and recorded.

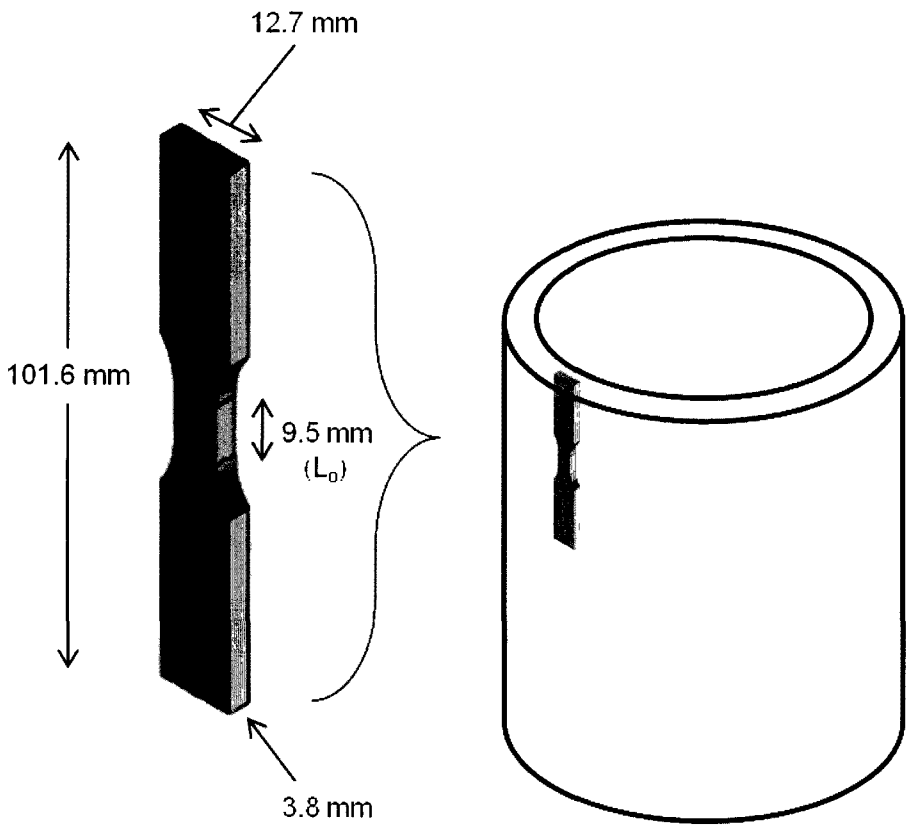

Figure 6.10: Twenty specimens were fabricated from each pipe segment. The samples were 101.6 mm long, 12.7 mm wide and 3.8 mm thick. The testing gage length, L_o, was 9.5 mm.

6.3.2 Experimental Procedure

Each specimen was tested in tension under a constant displacement rate in the Instron® Schenk Testing System. The displacement rates were selected using:

$$\dot{u} = \dot{\varepsilon} L_o \qquad (6.5)$$

where $\dot{\varepsilon}$ is the strain rate obtained from the FEA results, L_o is the gage length of the samples and $\dot{u}$ is the displacement rate. Table 6.10 presents displacement rates utilized in the experimental

program calculated using equation 6.5. Note that this relationship assumes that the gauge length is the only area of elongation during testing.

Table 6.10 : The displacement rates utilized for the material testing.

Strain rate, $\dot{\varepsilon}$ (s^{-1})	Gage Length, L_o (mm)	Displacement Rate, $\dot{u}$ mms^{-1}
1.0×10^{-1}		9.525×10^{-1}
1.0×10^{-2}	9.525	9.525×10^{-2}
1.0×10^{-3}		9.525×10^{-3}

The stress and strain within the HDPE specimen must be measured to obtain the Young's Modulus and tensile strength at yielding. Note that the HDPE's Young's Modulus was investigated only in the linear elastic region of the material's stress-strain curve. The engineering stress within each sample was calculated by dividing the tension (applied by the Instron) by the undeformed cross-sectional gage area of the specimen. The tension was measured by a calibrated Futek 890 N load cell (model LSB303).

Three methods were evaluated for obtaining the specimen's strain: an extensometer, the Instron cross-head movement and a Digital Imaging Correlation (DIC) system. Preliminary experiments were performed investigating the feasibility of utilizing an extensometer on the small HDPE samples. It was found that the sharp extensometer grips "knifed" into the soft material and caused visible localized stress concentrations. Therefore the extensometer was not used in the experiments.

Specimen strain can also be obtained from the Instron cross head movement. To obtain the strain, the displacement of the grips is assumed to be equal to the elongation of the specimen. This calculation is based on the assumption that the reduced cross sectional gage area of the specimen is the only material deforming. In addition, strain measurements can be

influenced by slippage of the specimen in the grips and unknown compliance in the machine (at the joints, connection, etc).

The final method to measure the strain in the HDPE specimen employed Digital Imaging Correlation (DIC) technology. DIC utilizes a high resolution digital camera to record the specimen under load and a mathematical correlation analysis to determine the strain range over the surface of the sample (Cintrion and Saouma, 2008). This technique is non-invasive, produces the strain over the entire surface area of the specimen and has been used in a variety of experiments with good results (Hild and Roux, 2006; Hilburger and Nemeth, 2005; Pan et al., 2008).

It was determined to utilize a combination of the cross-head movement and DIC techno logy for specimen strain measurement. The experimental set-up utilized for the uniaxial tensile testing is shown in Figure 6.11. The HDPE specimens were placed in the Instron crosshead grips, as shown. The 890 N load cell was placed below the lower crosshead and connected to the Instron for data acquisition. The DIC camera was placed approximately 30 cm from each specimen and rotated 45^{o} to increase the number of pixels over the dog-bone test area as well as provide the largest recording view for the deformation process. The load cell and cross head movement were synchronized and recorded by the Instron machine. The DIC was recorded on a separate computer. The sampling rates of both instruments for each displacement rate are shown in Table 6.10. Note that the Instron has a minimum sampling rate of 1 Hz.

The DIC instrumentation required the specimens to be "speckled" in contrasting paint. Therefore, the dog bones were lightly coated in a fine spray-paint mist, as can be seen in Figure 6.12. Five replicates of each displacement rate (from each pipe sample) were performed, as recommended by ASTM D638, resulting in 90 tensile tests. The DIC was not utilized, however,

for every sample due limited computer space, availability of the instrument and periods of inadequate lighting. Therefore, some tests only have three of five specimens with DIC results.

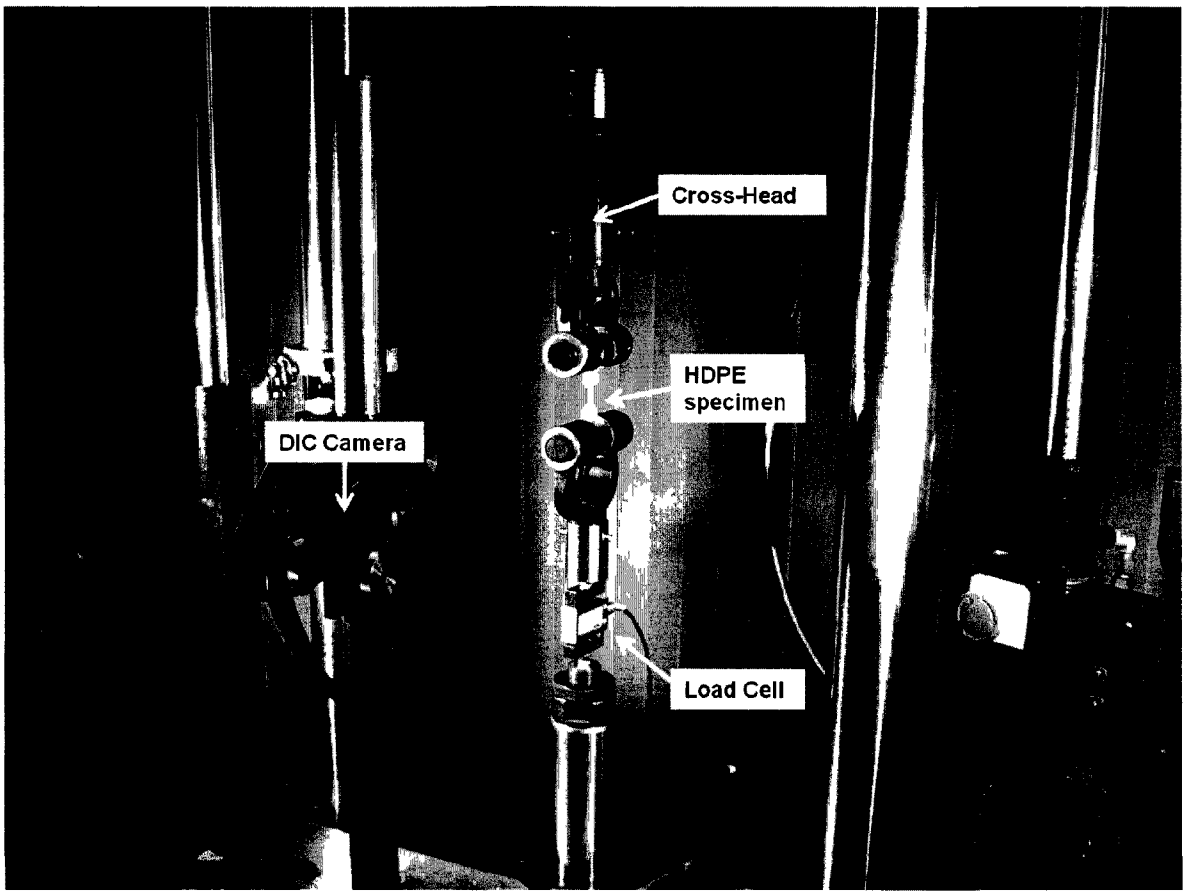

Figure 6.11: The test set-up of the experiments performed on the Instron tensile testing machine. The force straining the HDPE specimen was recorded from the load cell. The specimens strain was calculated from the Instron cross head movement and DIC measurements

Table 6.11: The sampling rates of the instruments utilized in the tension testing.

Displacement Rates	Displacement Rate, $\dot{u}$	Instron Sampling Rate	DIC Sampling Rate
1	9.525×10^{-1} mms^{-1}	20 Hz	20 Hz
2	9.525×10^{-2} mms^{-1}	5 Hz	5 Hz
3	9.525×10^{-3} mms^{-1}	1 Hz[a]	0.2 Hz

[a] The Instron had a minimum sampling rate of 1 Hz.

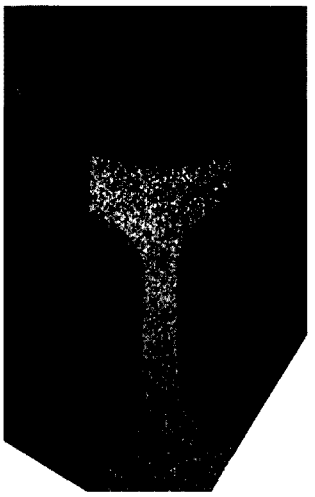

Figure 6.12: The specimens were speckled in contrasting paint for DIC measurement.

6.3.3 Data Processing

The Young's Modulus and tensile strength were determined based on the measurements described in section 6.3.2. The Young's Modulus was obtained by plotting the specimen's stress–strain curve, as shown in the schematic Figure 6.13. The slope of the linear portion of the curve was utilized to calculate the Young's Modulus. Preliminary experiments found that the "linear" portion of the curve was limited to strain values of 0.5 and 2.5%.

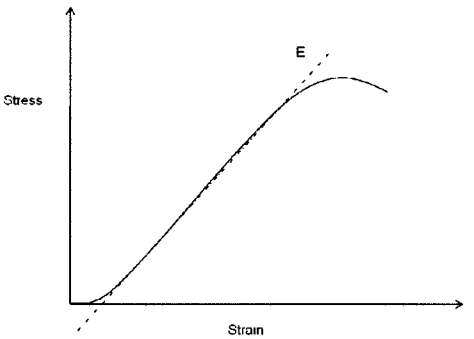

Figure 6.13: The linear portion of the stress-strain curve was utilized to calculate the Young's Modulus, E.

The tensile strength was assumed to correspond to the maximum value from the region of the curve shown in Figure 6.14. The strength values were found for all specimens and displacement rates.

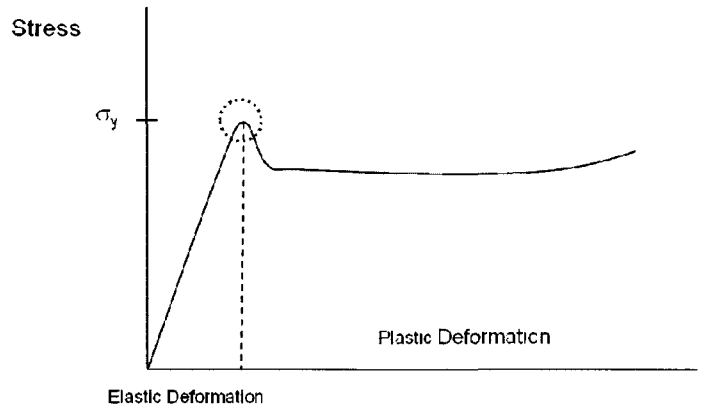

Figure 6.14: The tensile strength at yielding, σ_y, was obtained for each specimen.

6.3.4 Results

The 90 specimens were tested at three displacement rates in the Instron tensile testing machine. The majority of the specimens were found to elongate over 700% (to the maximum travel distance of the Instron), regardless of displacement rate. The full deformation of a sample is shown in Figure 6.15. Sixteen of the eighty-seven samples fractured during the experiments. Of these fractures, 87% occurred at the faster displacement rates (Rate 1: 9.525×10^{-1} mms^{-1}, Rate 2: 9.525×10^{-2} mms^{-1}). Data on the stress and strain was recorded for the entire deformation process. However, only the information from the linearly elastic portion was utilized in this research.

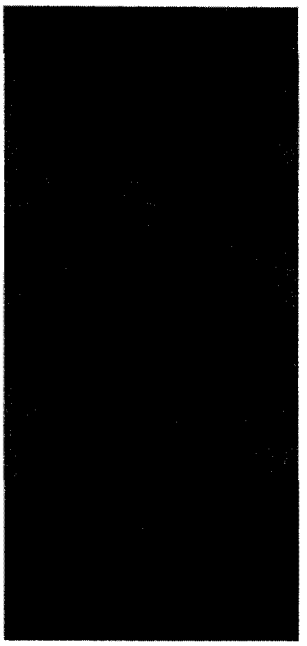

Figure 6.15: An undeformed and deformed specimen tested subjected to uniaxial tensile loading.

The first steps performed upon the completion of the tensile tests were to verify the output data. This included (1) determination of the proper DIC settings, (2) verification of the DIC accuracy and strain distribution throughout the specimen under load and (4) comparison of the strain values obtained from the DIC and crosshead movement techniques.

When processing the DIC data, it was necessary to balance the accuracy and subsequent computational processing time. The DIC uses a software package called *VIC-2D* to collect and process the strain measurements. The software has two primary parameters to allow user control over the quality and quantity of the data set: *subset* and *step.* The *subset* parameter controls the reference area (in pixels) that the DIC software utilizes for the displacement measurement accuracy. A larger subset provides greater system accuracy by tracking larger number of data points within the reference area, but is the least efficient computationally. The *step* parameter adjusts the distance (in pixels) the software utilizes to search and track the paint speckle movements from the initial undeformed specimen to the subsequent images of the

loaded specimen. To determine the optimal settings of these parameters, a sensitivity study was performed on one sample where the *subset* and *step* parameters were varied over the values listed in Table 6.12. The examined parameter values were limited to those shown based upon user experience and a desire to track 4000 points on the surface of each specimen.

Table 6.12: The subset and step parameter values examined in the DIC sensitivity study.

Load Case	Subset value	Step value (in pixels)	Number of Tracked Points[a]
1	23	1	29890
2	23	2	7650
3	23	3	3405
4	25	1	30125
5	25	2	7710
6	25	3	3405

[a] Refers to the number of points tracked for analysis over the tracked surface of the specimen.

Using the extensometer feature in the DIC software, the strain (over the gage length) of the specimen was compared for each subset and step increment. The results of the analysis are shown in Figure 6.16. Similar output values can be seen for all 6 settings. The difference becomes apparent near the end of the test at strains approaching 700%. Using these results as a guide, the *subset* and *step* values of 23 and 2, respectively, were used for the rest of the analysis.

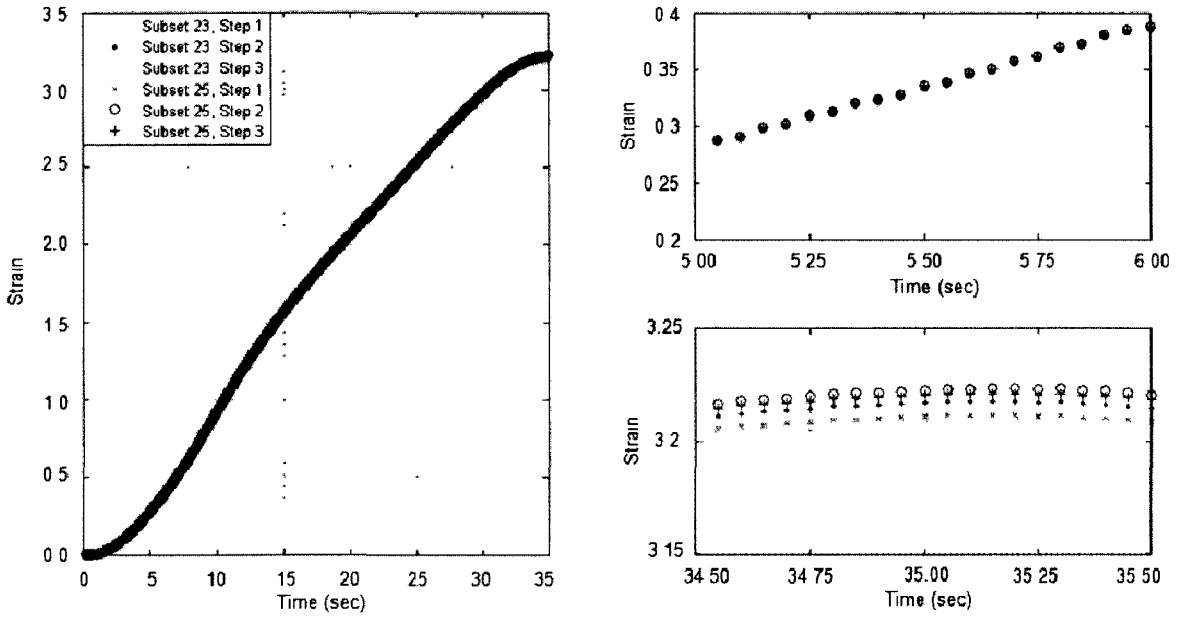

Figure 6.16: Sensitivity test results comparing the strain in a sample from the unused pipe at displacement rate 1, 9.525 x 10^{-1} mms^{-1} for the 6 load cases. Left: The total specimen strain. Top Right: The strain in the linear elastic region of the specimen. Bottom Right: The strain at the yield stress.

The next steps examined the accuracy and confidence of the DIC measurements based upon the incremental statistics (i.e. per each time step) reported by the software such as correlation coefficient and Standard Error of Estimate (SSE) for analyzed regions of the image. The employed DIC system has a displacement measurement error of approximately +/- 0.01 pixel (reported SSE was in the range 0.008 - 0.012). The sub-pixel accuracy is obtained by internal interpolation routines of the DIC software than compares grey values of the pixels. For the current study, positioning of the DIC camera together with its focal length resulted in 0.075 mm/pixel scale. Optical distortions of the lens were studied and found to be negligible. A strain measurement accuracy of +/-0.016% (95% confidence) was obtained when comparing this value to the 9.5 mm gage length of the specimen. More information of the accuracy of the DIC can be found in Pan et al. 2008.

The strain distribution under tension was then examined. It can be observed that the strain is concentrated in the necked portion of the specimen, which supports the assumption that the sole area of deformation is located in this narrow region. The results of this analysis are shown in Figure 6.17, verifying the strain concentration in the gage portion of the specimen.

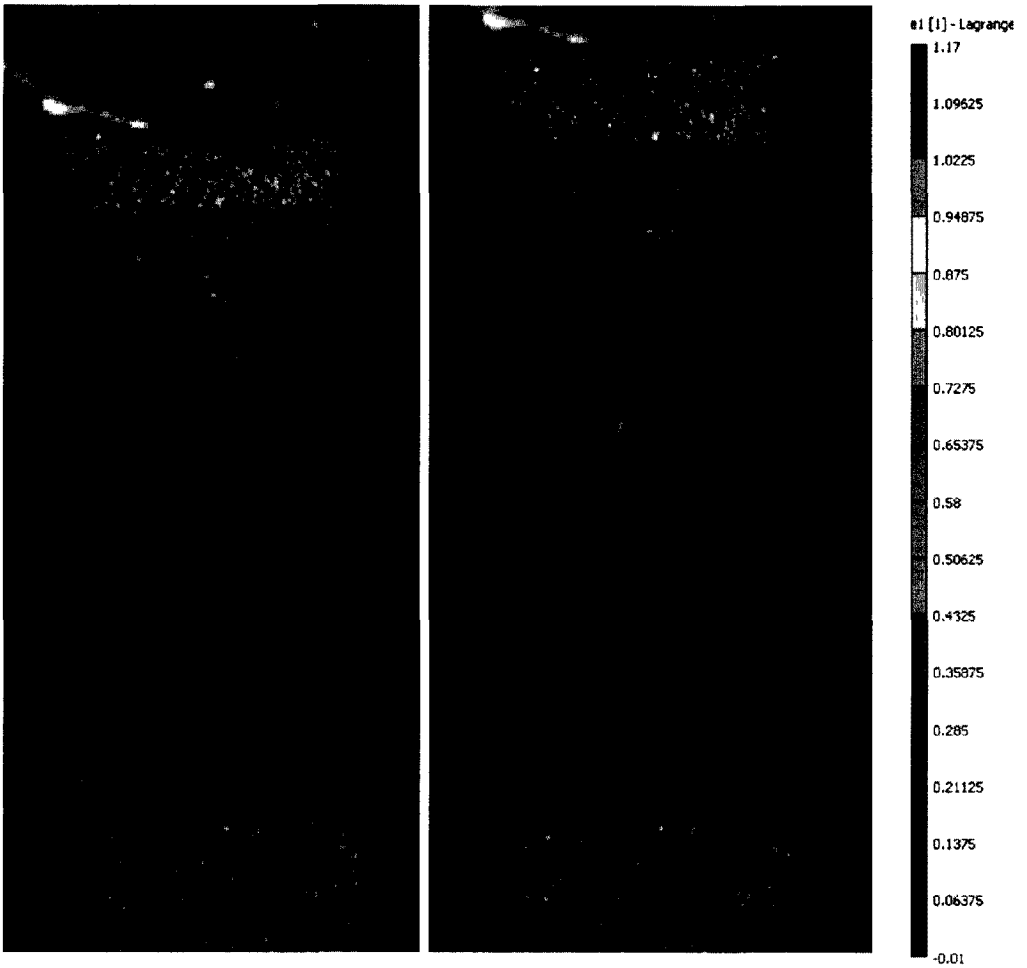

Figure 6.17: The axial strain distribution of the specimen under load. From left to right: The unloaded, undeformed specimen; and strain distribution during the linearly elastic deformation.

The final verification compared the DIC strain measurements to the cross-head movement, and subsequent, strain calculations. The output results from one representative sample are shown in Figure 6.18. It can be seen that the crosshead calculations produce greater strain compared to the DIC measurements. The difference is probably a result of the initial compliance of the Instron system (joints, connection, etc) having to settle out before the

specimen reaches yielding. This, combined with the small gage length of the specimen, produced greater apparent strains than that occurring in the specimen itself. The difference in strain measurement compromised the use of the crosshead movement as a strain measurement source. This proved to be costly as the DIC was not utilized in every test, resulting in a decrease in the number of analyzed specimens.

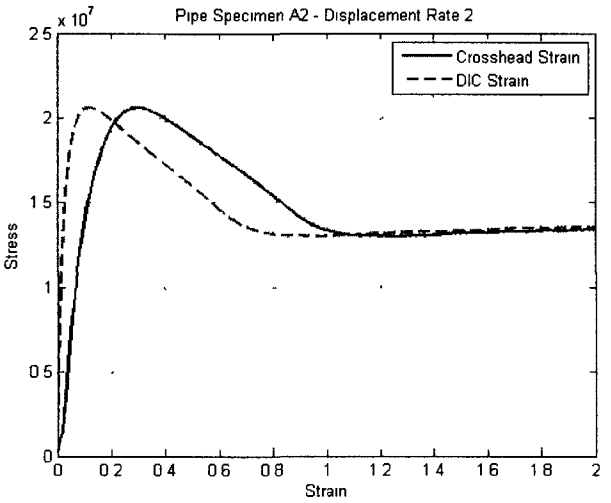

Figure 6.18: The stress-strain curves for a specimen obtained from pipe sample 2 under displacement rate 2. The curves were obtained using the calculated crosshead and DIC measured strains.

With the initial investigations complete, the Young's Modulus of the specimens were obtained. Figure 6.19 displays the results from one of the experiments. A linear approximation of the slope of the curve between strain of 0.5 and 2.5% was obtained. The resulting Young's Modulus values for each specimen can be seen in Tables 6.13-6.18.

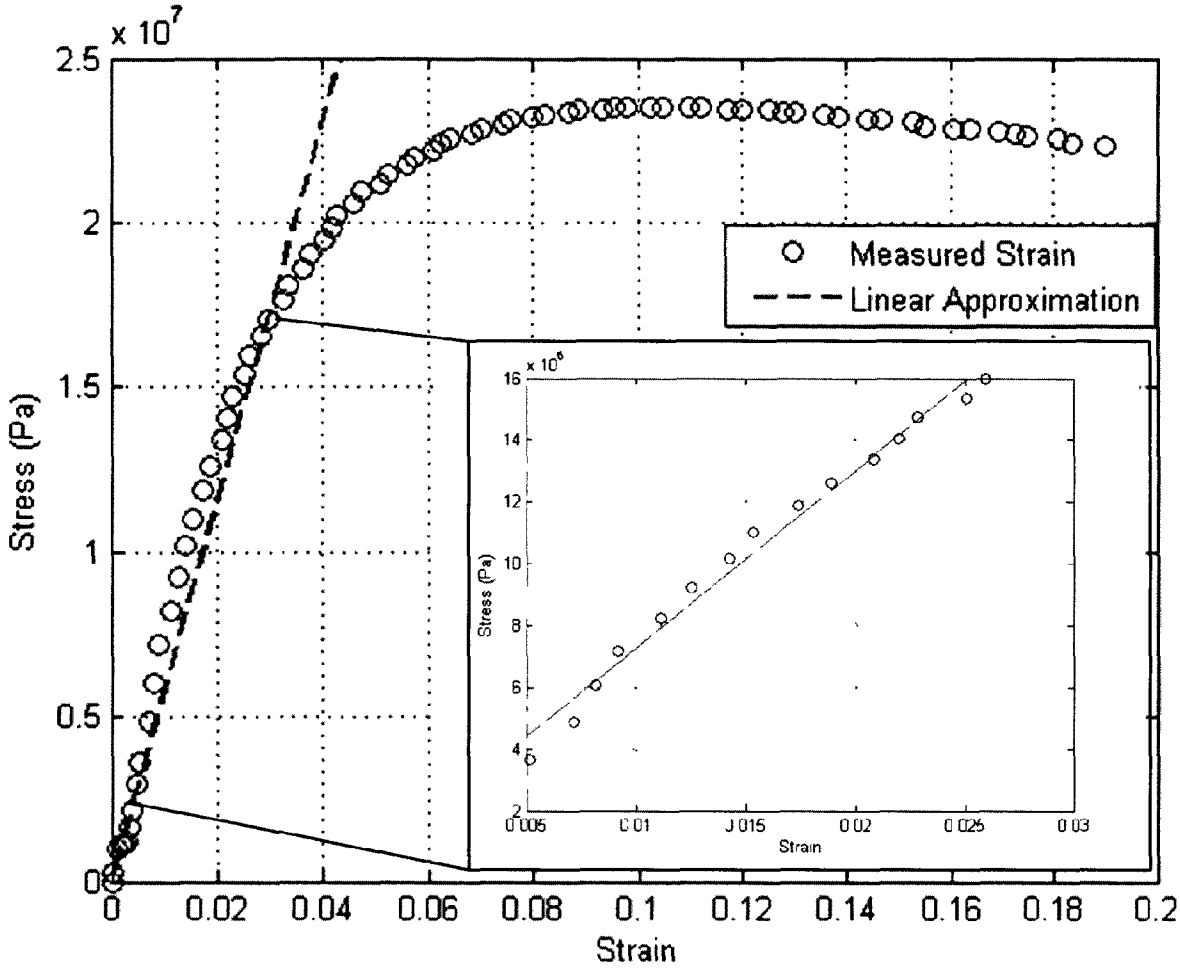

Figure 6.19: The stress-strain curve obtained from tensile testing of HDPE specimen 1 of Pipe A1.

Table 6.13: The Young's Modulus results of specimen obtained from PIPE A1.

Rate 1: 9.525×10^{-1}		**Rate 2: 9.525×10^{-2}**		**Rate 3: 9.525×10^{-3}**	
Specimen	E (Pa)	Specimen	E (Pa)	Specimen	E (Pa)
1	5.76E+08	6	----	11	3.90E+08
2	5.61E+08	7	----	12	3.61E+08
3	4.95E+08	8	5.34E+08	13	4.14E+08
4	4.77E+08	9	5.86E+08	14	----
5	6.69E+08	10	5.48E+08	15	----
Ave	5.56E+08	Ave	5.56E+08	Ave	3.88E+08
Std	7.61E+07	Std	2.69E+07	Std	2.65E+07

Table 6.14: The Young's Modulus results of specimen obtained from PIPE A2.

Rate 1: 9.525×10^{-1}		**Rate 2: 9.525×10^{-2}**		**Rate 3: 9.525×10^{-3}**	
Specimen	E (Pa)	Specimen	E (Pa)	Specimen	E (Pa)
1	5.28E+08	6	3.61E+08	11	4.57E+08
2	5.36E+08	7	5.71E+08	12	3.48E+08
3		8	4.46E+08	13	3.09E+08
4	5.41E+08	9	----	14	----
5	5.14E+08	10	----	15	----
Ave	5.30E+08	Ave	4.59E+08	Ave	3.71E+08
Std	1.18E+07	Std	1.06E+08	Std	7.67E+07

Table 6.15: The Young's Modulus results of specimen obtained from PIPE B.

Rate 1: 9.525×10^{-1}		**Rate 2: 9.525×10^{-2}**		**Rate 3: 9.525×10^{-3}**	
Specimen	E (Pa)	Specimen	E (Pa)	Specimen	E (Pa)
1	5.24E+08	6	4.70E+08	11	3.05E+08
2	4.07E+08	7	4.58E+08	12	3.39E+08
3	4.81E+08	8	5.31E+08	13	----
4	6.19E+08	9	----	14	----
5	5.16E+08	10	----	15	---
Ave	5.09E+08	Ave	4.86E+08	Ave	3.22E+08
Std	7.67E+07	Std	3.91E+07	Std	2.40E+07

Table 6.16: The Young's Modulus results of specimen obtained from PIPE C.

Rate 1: 9.525×10^{-1}		**Rate 2: 9.525×10^{-2}**		**Rate 3: 9.525×10^{-3}**	
Specimen	E (Pa)	Specimen	E (Pa)	Specimen	E (Pa)
1	5.41E+08	6	4.23E+08	11	4.09E+08
2	4.91E+08	7	5.24E+08	12	3.49E+08
3	5.20E+08	8	5.11E+08	13	3.45E+08
4	---	9	---	14	---
5	---	10	---	15	---
Ave	5.17E+08	Ave	4.86E+08	Ave	3.68E+08
Std	2.51E+07	Std	5.49E+07	Std	3.59E+07

Table 6.17: The Young's Modulus results of specimen obtained from PIPE D.

Rate 1: 9.525×10^{-1}		**Rate 2: 9.525×10^{-2}**		**Rate 3: 9.525×10^{-3}**	
Specimen	E (Pa)	Specimen	E (Pa)	Specimen	E (Pa)
1	4.87E+08	6	4.72E+08	11	3.32E+08
2	4.87E+08	7	3.74E+08	12	3.13E+08
3	5.09E+08	8	3.87E+08	13	3.99E+08
4	4.97E+08	9	---	14	3.82E+08
5	6.14E+08	10	---	15	---
Ave	5.19E+08	Ave	4.11E+08	Ave	3.57E+08
Std	5.40E+07	Std	5.32E+07	Std	4.06E+07

Table 6.18: The Young's Modulus results of specimen obtained from PIPE N (new, unused).

Rate 1: 9.525×10^{-1}		**Rate 2: 9.525×10^{-2}**		**Rate 3: 9.525×10^{-3}**	
Specimen	E (Pa)	Specimen	E (Pa)	Specimen	E (Pa)
1	4.59E+08	6	4.81E+08	11	2.27E+08
2	4.17E+08	7	3.84E+08	12	3.48E+08
3	5.03E+08	8	3.45E+08	13	---
4	4.95E+08	9	---	14	---
5	---	10	---	15	---
Ave	4.69E+08	Ave	4.03E+08	Ave	2.88E+08
Std	3.93E+07	Std	7.00E+07	Std	8.56E+07

The tensile strength at yield was also obtained for each sample. The results from each experiment can be seen in Tables 6.19 through 6.24.

Table 6.19: Tensile Strength at Yielding for specimens obtained from PIPE A1.

Rate 1: 9.525×10^{-1}		**Rate 2: 9.525×10^{-2}**		**Rate 3: 9.525×10^{-3}**	
Specimen	Tensile Strength (Pa)	Specimen	Tensile Strength (Pa)	Specimen	Tensile Strength (Pa)
1	2.351E+07	6	2.492E+07	11	1.886E+07
2	2.343E+07	7	2.428E+07	12	1.708E+07
3	2.373E+07	8	2.175E+07	13	1.838E+07
4	2.416E+07	9	2.229E+07	14	1.993E+07
5	2.416E+07	10	2.213E+07		
Min	2.343E+07	Min	2.175E+07	Min	1.708E+07
Ave	2.380E+07	Ave	2.307E+07	Ave	1.856E+07
Std	3.481E+05	Std	1.425E+06	Std	1.184E+06

Table 6.20: Tensile Strength at Yielding for specimens obtained from PIPE A2.

Rate 1: 9.525×10^{-1}		**Rate 2: 9.525×10^{-2}**		**Rate 3: 9.525×10^{-3}**	
Specimen	Tensile Strength (Pa)	Specimen	Tensile Strength (Pa)	Specimen	Tensile Strength (Pa)
1	2.404E+07	6	2.285E+07	11	1.768E+07
2	2.459E+07	7	2.463E+07	12	1.723E+07
3	2.475E+07	8	2.186E+07	13	1.652E+07
4	2.391E+07	9	2.279E+07	14	2.139E+07
5	2.360E+07	10	2.125E+07		
Min	2.360E+07	Min	2.125E+07	Min	1.652E+07
Ave	2.418E+07	Ave	2.268E+07	Ave	1.821E+07
Std	4.806E+05	Std	1.279E+06	Std	2.175E+06

Table 6.21: Tensile Strength at Yielding for specimens obtained from PIPE B.

Rate 1: 9.525×10^{-1}		**Rate 2: 9.525×10^{-2}**		**Rate 3: 9.525×10^{-3}**	
Specimen	Tensile Strength (Pa)	Specimen	Tensile Strength (Pa)	Specimen	Tensile Strength (Pa)
1	2.139E+07	6	2.117E+07	11	1.503E+07
2	1.676E+07	7	2.240E+07	12	1.937E+07
3	2.106E+07	8	2.011E+07	13	1.522E+07
4	2.262E+07	9	2.081E+07	14	1.635E+07
5	2.149E+07	10	1.971E+07	15	1.837E+07
Min	1.676E+07	Min	1.971E+07	Min	1.503E+07
Ave	2.048E+07	Ave	2.076E+07	Ave	1.733E+07
Std	2.259E+06	Std	1.045E+06	Std	1.927E+06

Table 6.22: Tensile Strength at Yielding for specimens obtained from PIPE C.

Rate 1: 9.525×10^{-1}		**Rate 2: 9.525×10^{-2}**		**Rate 3: 9.525×10^{-3}**	
Specimen	Tensile Strength (Pa)	Specimen	Tensile Strength (Pa)	Specimen	Tensile Strength (Pa)
1	2.080E+07	6	2.231E+07	11	1.699E+07
2	2.260E+07	7	2.246E+07	12	1.606E+07
3	2.333E+07	8	2.074E+07	13	1.635E+07
4	2.499E+07	9	1.969E+07	14	1.914E+07
5	2.574E+07	10	2.006E+07	15	1.779E+07
Min	2.080E+07	Min	1.969E+07	Min	1.606E+07
Ave	2.416E+07	Ave	2.074E+07	Ave	1.734E+07
Std	1.960E+06	Std	1.276E+06	Std	1.239E+06

Table 6.23: Tensile Strength at Yielding for specimens obtained from PIPE D.

Rate 1: 9.525×10^{-1}		**Rate 2: 9.525×10^{-2}**		**Rate 3: 9.525×10^{-3}**	
Specimen	Tensile Strength (Pa)	Specimen	Tensile Strength (Pa)	Specimen	Tensile Strength (Pa)
1	2.211E+07	6	2.209E+07	11	1.634E+07
2	2.255E+07	7	2.254E+07	12	1.680E+07
3	2.179E+07	8	2.060E+07	13	1.743E+07
4	2.248E+07	9	2.058E+07	14	1.776E+07
5	2.270E+07	10	1.925E+07	15	----
Min	2.179E+07	Min	1.925E+07	Min	1.634E+07
Ave	2.238E+07	Ave	2.074E+07	Ave	1.733E+07
Std	3.694E+05	Std	1.317E+06	Std	6.365E+05

Table 6.24: Tensile Strength at Yielding for specimens obtained from PIPE N (New, unused).

Rate 1: 9.525×10^{-1}		**Rate 2: 9.525×10^{-2}**		**Rate 3: 9.525×10^{-3}**	
Specimen	Tensile Strength (Pa)	Specimen	Tensile Strength (Pa)	Specimen	Tensile Strength (Pa)
1	2.169E+07	6	2.045E+07	11	1.577E+07
2	1.980E+07	7	2.063E+07	12	4.333E+06
3	2.073E+07	8	1.941E+07	13	1.834E+07
4	2.044E+07	9	1.954E+07	14	1.483E+07
5	2.163E+07	10	1.739E+07		
Min	1.980E+07	Min	1.739E+07	Min	4.333E+06
Ave	2.065E+07	Ave	1.924E+07	Ave	1.250E+07
Std	8.048E+05	Std	1.290E+06	Std	6.171E+06

6.4 Discussion

The HDPE material parameters relevant to proper analysis of HDPE cage components under hydrodynamic loading were investigated. Numerical models were employed to estimate strain rates in the HDPE components of fish cages in an open ocean environment. First, the overall dynamic behavior and mooring line tensions were investigated. The tension then were used as loading conditions on a FEM of a standard HDPE cage frame. Based on this information the laboratory testing procedures were specified to obtain the relevant material properties. The Young's Modulus and tensile strength was measured in the pipe specimens tested at three different displacement rates.

The following observations from the tensile test results can be made:

1. A large variation in the data can be seen. Young's Modulus values, from specimens of one pipe sample tested at similar displacement rates showed greater variability than expected. For example, samples tested from pipe A1 at displacement rate 1 varied from 4.15×10^8 Pa to 6.69×10^8 Pa. Similar variations in tensile strength were also present within and between samples. This could be a result of samples being taken from different portions of the pipe circumference and thus having unequal loading histories when in the field.
2. A strain rate dependence in the Young's Modulus and Tensile strength at yielding is present. This was evident throughout the samples, and was amplified between the faster displacement rates (1 and 2) and the slowest one (3). For example, the average Young's Modulus values of specimens from pipe C were 5.17×10^8 Pa, 4.86×10^8 Pa, and 3.68×10^8 Pa for displacements rates 1, 2 and 3, respectively. Similarly, average tensile strength values of specimens from pipe B were 2.05×10^7 Pa, 2.08×10^7 Pa, and 1.74×10^7 Pa for displacements rates 1, 2 and 3, respectively.

3. The new, unused pipe had the lowest average Young's Modulus and tensile strength values compared to the fatigued pipe. Note that Klompen (2005) found a similar trend for aged polymers where the yield stress increased over time.
4. Published Young's Modulus values ranged from 8.0 – 10.0 x 10^8 Pa, depending upon the chemical composition the material. The displacement rate associated with these values was not known. The Young's Modulus data obtained from these experiments are on the order of 30-65% less. This could be a result of using fatigued material or a difference between the displacement rates utilized for the previously published values and those investigated in this research.
5. The published value of the HDPE yield stress is 2.417x 10^7 Pa. The results of the tensile tests showed similar results, ranging from 2.0–2.4 x 10^7 Pa at the faster rates to 1.25–1.82 x 10^7 Pa at the slowest.

It is important to note that the information gained from the tensile experiments is limited. Recall that the service history and chemical composition of the pipes were not known. In addition, the history of the "new" pipe could also not be verified. This led to qualitative, as opposed to quantitative, observations.

CHAPTER 7

DESIGN CONSIDERATIONS AND PRACTICAL APPLICATIONS OF FLEXIBLE STRUCTURES IN MARINE ENVIRONMENTS

The enhancements of the Aqua-FE software developed in chapter 2 provide a versatile tool to investigate flexible system response. The numerical model can be used not only to examine small scale systems (Chapters 2, 3, 4), but to assist in the design and analysis of large complex systems as well. For example, Aqua-FE was utilized extensively in the design and analysis of the mooring systems deployed at the UNH site (Figure 3.1). Initially, these consisted of two single mooring grids containing two independent 600 m3 Sea Station™ fish cages (Tsukrov et al., 2000; Fredriksson et al., 2000; Baldwin et al., 2000). These moorings were replaced with a larger four grid mooring system that enabled the deployment of additional containment structures (seen in Figures 7.2 and 7.3). The mooring system geometries, subsurface flotation and pretension requirements were first specified using analytical techniques, which included standard chain catenary equations and equilibrium analysis. Mooring gear and ground tackle were then sized, in part, by modeling the designed system with Aqua-FE. This chapter will focus on the design, analysis and deployment of the four cage grid. This mooring was deployed in 2003 and used as a platform to conduct a series of engineering

and biological studies, advancing the state of the art in offshore aquaculture. The mooring was recovered and examined in 2010 after seven years of continuous use.

The objective of this chapter is to describe the engineering design process used to specify components of the four-grid mooring system, including the numerical modeling and review the success or failure of the approach at the end of the seven year field deployment. The design process included a review of the specific design criteria for the open ocean site including the conceptual design, application of standard analytical methods to investigate the system hydrostatic characteristics, construction of a numerical model and comparison of static simulations with values calculated analytically and analyzing the results of dynamic simulations using a deterministic design wave condition with a superimposed, co-linear current. Using the results of the model simulations, along with practical experience, a design mooring component force was determined, components specified, procured and the system deployed. To evaluate the success/failure of the mooring, a brief description of the environmental conditions and research conducted at the site is presented and followed by the mooring recovery and inspection. Portions of the work presented in this chapter were published in *Aquaculture Engineering Journal* (Fredriksson et al., 2004) and *Oceans 2010 Conference Proceedings* (DeCew et al., 2010).

7.1 Design Criteria

Design criteria specific for the site off the coast of NH were established prior to the engineering analysis and specification of components. First, it was required that the entire system fit into the site boundaries specified in the government permit for the two separate mooring grids (30 total acres). It was also necessary that the new mooring be able to

accommodate two existing SS600 cages and have space for additional fish containment structures. The gear had to be able to withstand the waves and currents that occur at the site, especially those associated with extreme storms. The mooring also had to be versatile, have straightforward installation and recovery of structures and components, be diver accessible and have minimal maintenance requirements. Finally, the mooring system needed to be designed to minimize entanglement with marine mammals.

The first design constraint required that the new mooring system be deployed in the existing permitted site approximately 10 km from the shore. The site is in 52 meters of water and has a 30 acre (12.41 hectare) area. The bottom composition consists of relatively heterogeneous materials, which include bedrock outcroppings, gravel and muddy sands (Grizzle et al., 2003). The site is fully exposed from nearly all directions, though a small set of islands was located approximately 2 km to the north (Figure 3.1). In this study, a deterministic wave height of 9 meters with a period of 8.8 seconds was used with a co-linear current of 1 m/s for design purposes. The design wave height of 9 meters is estimated to be the energy based significant wave height (H_{mo}) of a 50 year storm at the site (Fredriksson, 2001). The design wave period is approximately the average dominant wave period of the most frequent wave directional band. Included in the design condition was a superimposed, a co-linear current of 1 m/s (constant with depth). Although the largest velocity measured in two years of observation was 0.6 m/s (due to internal waves), the design coastal current value was chosen to encompass other coastal current components due to tidal forcing, surface winds and storm surge.

The mooring system was specified to have a four-cage capacity to help insure future flexibility of the mooring capabilities. Two of the cages consisted of the previously deployed SS600 fish cages (see Figure 7.1). For mooring design purposes, two 3000 m^3 *Sea Stations*™ (SS3000) were considered for the other two cage locations, though other commercial fish cages

could be accommodated. The operational plan, however, was to deploy one SS3000 and reserve the fourth cage location for future deployments of experimental systems. Both the SS600 and SS3000 have a similar construction. The cages are built around a central spar buoy and rim, both made of galvanized steel and can be submerged by flooding a chamber inside the central spar. The structure is held in a semi-rigid configuration by tensioning stays between these primary components. The containment net is woven into the stays, therefore maintaining a constant volume. Component details can be found in Fredriksson et al. 2003 and Kurgan (2003) for the SS600 and SS3000 cages, respectively.

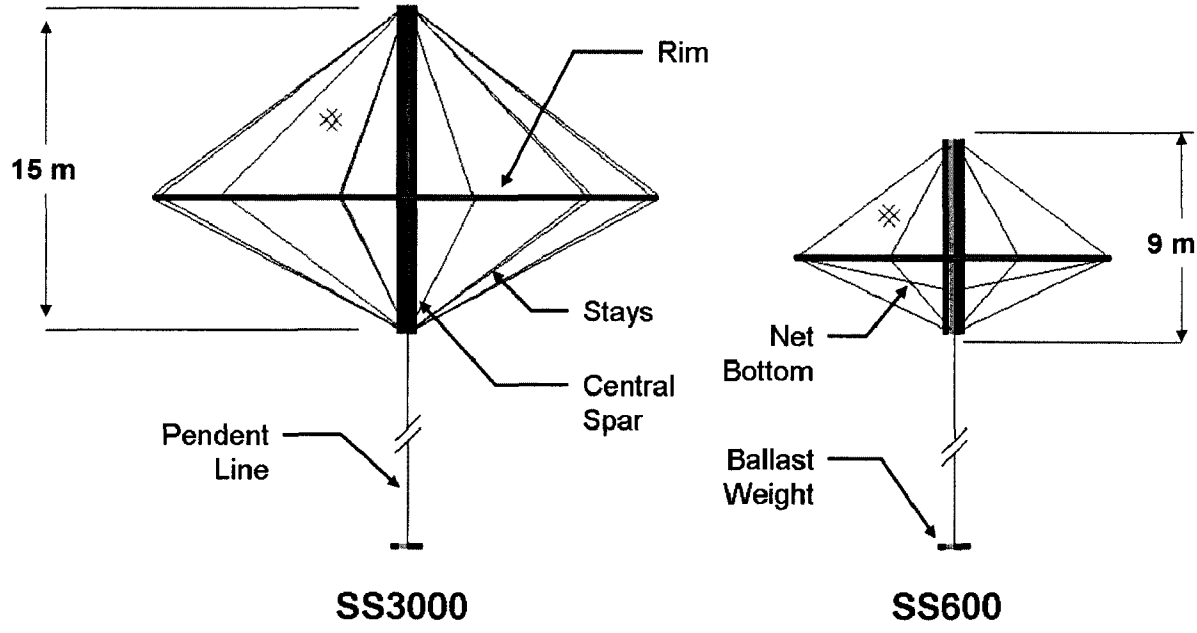

Figure 7.1: The SS600 and SS3000 cages each consist of a central spar and rim held together with tensioned stays. The spar on the SS600 has a length of 9 meters, while the spar on the SS3000 is about 15 meters. The nominal rim diameter of the SS600 is 15 meters, while on the SS3000 it is 25 meters. Each cage incorporates a ballast weight suspended with a pendent line from the spar weighing 19 and 53 kN (dry) for the SS600 and the SS3000 cages, respectively.

Another important consideration is marine mammal entanglement. Though no gear deployed in the open ocean will eliminate this serious issue, efforts must be made to

incorporate designs that minimize the effect on the marine mammal population. One approach utilizes a submerged grid using large diameter ropes (44-52 mm) that are pre-tensioned in the deployment process. In the previously deployed single-cage submerged grid (Baldwin et al., 2000), the design (minimum) pre-tensioned value was estimated at 2.2 kN (Fredriksson et al., 2000). In the four year deployment period, not one entanglement occurred. While it is recognized that few large marine mammals actually enter the site, the criteria was doubled in the design of the four-grid mooring system.

The mooring grid was designed to be placed at a depth of approximately 18 meters and consisted of nine nodes (Figures 7.2 and 7.3). Four sets of bridle lines connected each cage to the submerged grid. The grid was anchored to the bottom using 12 mooring legs each incorporating co-polymer rope and a chain catenary. Tension in the system was maintained using subsurface flotation at the nine nodal locations. Due to the 12 anchor design, flotation elements at the corners were required to be larger than those at the grid sides to accommodate the weight of chain for two anchor legs. During the deployment process, the anchors were set to form the required geometry, which submerged the flotation elements down to the desired depth and lifted chain up off the bottom. The chain catenary in the anchor legs provided compliance to the system, while maintaining static pre-tensioning. Having a submerged mooring reduced the wear on the system (compared to employing flotation at the high energy surface environment) and kept a constant pre-tension in the gear. In addition, the depth was diver accessible, yet deep enough to mitigate excessive biological growth.

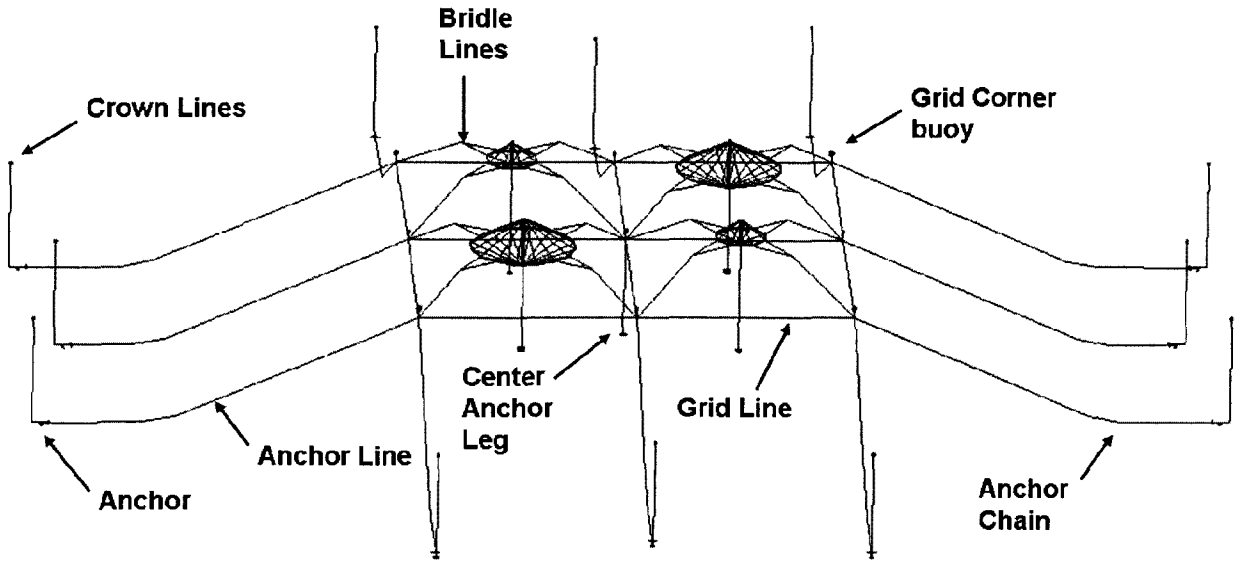

Figure 7.2: An isometric view of the submerged 4-cage grid system.

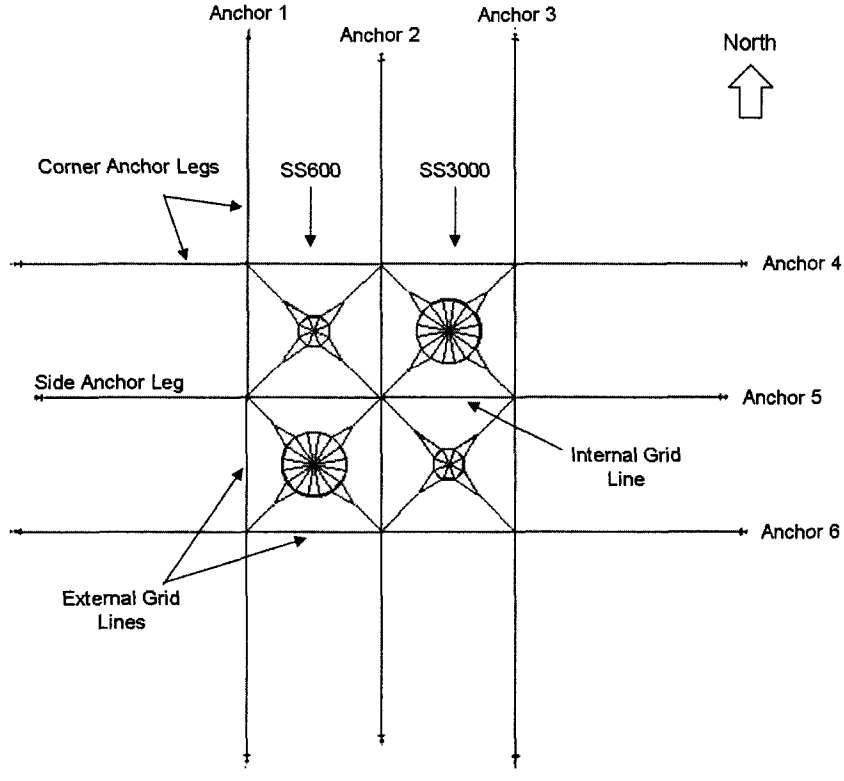

Figure 7.3: A top view of the submerged grid mooring system. It consisted of 8 corner anchor legs, 4 side anchor legs, 1 center anchor line, 12 grid lines, and 16 bridle lines. The anchors on the north and east sides are numbered for load identification.

7.2 Engineering Analysis

Using the design concepts introduced in the previous section, the hydrostatic and geometric configuration of the submerged grid mooring was estimated using a standard analytical approach. Tension loads in the anchor legs and the desired geometry of the system to maintain the static shape of the grid were estimated using the inextensible cable (catenary) equations (see, for example, Faltinsen, 1990). A similar approach was used in the design of a double submerged grid aquaculture mooring as described in Fredriksson et al. 1999 and Fredriksson et al., 2001. These equations were also used to specify the chain forming the catenary in the anchor leg and the submerged flotation at the grid. The schematic shown on Figure 7.4 defines the components of one anchor leg of the mooring system. For the four-grid mooring configuration, it was required to have the pre-tensioned subsurface grid at a depth of 18 m for relatively easy diver serviceability.

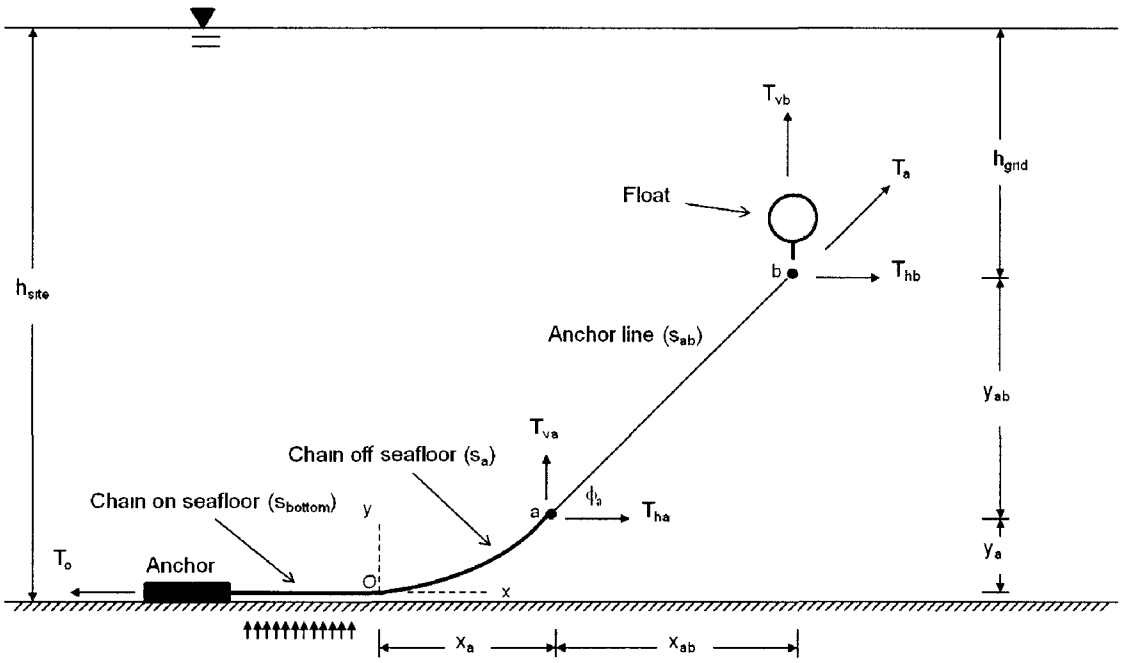

Figure 7.4: Anchor leg definition schematic. Note that the float assembly consists of the float, a length of chain and the rope ring corner connections (not shown).

In general, the approach assumed a certain geometric configuration. For instance, since the average depth of the water at the site is 52 meters, the grid plane is approximately 34 meters off the bottom ($y_a + y_{ab}$ on Figure 7.4). The anchor legs, which are made of rope (s_{ab}) and chain (s_a), are not identical. It was decided that the eight corner legs were to be made up of 36.5 m of chain and 78 m of rope resulting in a scope (anchor leg length to depth ratio) of 3.1. The four side anchor legs, however, were different, being composed of 27.4 m of chain and 78 m of rope and therefore having a scope of 2.9. The horizontal component of the corner and side anchor legs ($s_{bottom}+x_a+x_{ab}$) was defined to be 107 and 96 m so that the entire system could fit into the 30 acre (12 hectares) site, assuming that the grid lines are 65 m.

Using these and other predetermined design values (summarized in Table 7.1), the static pre-tension and the geometry of the submerged grid mooring was determined by employing the following analytical equations. First, the vertical force acting on the grid corner, T_{vb}, and associated chain suspended off the seafloor, s_a, was determined by:

$$T_{vb} = B_{float} + B_{25\,mm\,chain} + B_{rope\,ring} = T_{va} \tag{7.1}$$

$$s_a = \frac{T_{vb}}{p} \tag{7.2}$$

where B_{float} is the net buoyancy of the float acting on one anchor leg, $B_{25\,mm\,chain}$ is the net buoyancy of the chain securing the float, $B_{rope\,ring}$ is the net buoyancy of the rope ring (corner connection element), T_{va} is the vertical force acting on the chain, and p is the wet weight of the chain. For the static condition, it was then established that 20-30% of the anchor chain should be suspended off the seafloor. Using this as a guide, the tension at the anchor, T_o, the horizontal and vertical positions of position of point A, x_a and y_a, respectively, could be found using:

$$s_a = \frac{T_o}{p}\sinh\left(\frac{px_a}{T_o}\right) \tag{7.3}$$

$$y_a = \frac{T_o}{p}\left[\cosh\left(\frac{px_a}{T_o}\right) - 1\right] \tag{7.4}$$

$$T_o \tan(\phi_a) = T_{vb} \tag{7.5}$$

where ϕ_a is the angle formed at the top of the catenary. The tension in the anchor line, T_a, and grid line, T_g, could then be found using equilibrium analysis:

$$\frac{T_{vb}}{\sin(\phi_a)} = T_a \tag{7.6}$$

$$T_o = T_{hb} = T_g \tag{7.7}$$

Once these values were calculated, the remaining system geometry, such as y_{ab}, s_{ab}, x_{ab} could be found.

Table 7.1: Pre-determined design values utilized in the catenary analysis. These parameters were established due to geometric constraints (for example, permit area), availability of equipment and past experience.

Parameter	Value	Description
Water depth (h_{site})	52 m	UNH offshore site water depth
Mooring grid depth (h_{grid})	18 m	Depth of the grid was selected as part of design process
Length of grid line (l_{grid})	65 m	Length selected to insure future versatility of mooring
Mooring scope	3.1 (corner) 2.9 (side)	System was designed to have approximately a 3:1 scope
Lengths of anchor line	78 m (corner) 78 m (side)	Determined from scope and site permit area
Lengths of anchor chain	36.5 m (corner) 27.4 m (side)	Selected upon cost considerations, availability and to insure horizontal force is applied to the anchors
Chain length off the seafloor (s_a)	11 m (corner) 6 m (side)	Design constraint; ideally only 20-30% of the anchor chain to be suspended off the seafloor in static condition
Wet weight of chain (p)	460 N/m	Selected based upon availability from previous individual moorings and strength/weight characteristics
Float buoyancy	11 kN (corner) 3.2 (side)	Floats were selected based upon available sizes, costs and submergence depths of the component
Rope ring buoyancy	222 N	Calculated based upon the physical and geometrical properties of the rope ring
25 mm chain buoyancy	243 N	Calculated based chain physical and geometrical properties

7.4 Results

7.4.1 System Hydrostatics

To size the grid flotation elements and to determine the required geometry and pre-tension values of the mooring, the analytical techniques described in Section 7.3 were applied. Using a total vertical force of 5.1 and 2.8 kN for the corner and side grid flotation nodes, the anchor tensions, T_o, and geometric characteristics of the suspended chain were calculated using equations 7.3 through 7.5. The static anchor line tensions for the corner and side legs, were found using equation 7.6 resulting in values of 12.52 kN and 6.62 kN, respectively. At the grid node locations, equation (7.7) was applied to obtain grid line tensions of 11.4 kN and 6.01 kN for the exterior (outside square) and interior (connecting to the center node) grid lines, respectively.

The next step was to build a numerical model of the entire system and perform a hydrostatic simulation (i.e. no wave or current loading was applied). Geometric and material properties used in the model were based on the components described in Section 7.3 and the properties calculated as part of the analytical analysis (i.e. the size of the corner floats and geometry). Cage characteristics used in the model are discussed in Section 7.2. Note, however, that the cage system's bridle lines were slack in this analysis, thus the cages did not affect the grid tensions. For the hydrostatic numerical model tests, the entire fish cage and mooring system was allowed to come to static equilibrium for a period of 30 seconds. Tensions in the anchor and grid lines were calculated and the results provided in Table 7.2. After the transient portion of the simulation, the corner and side anchor line pretension values were calculated to be 12.84 kN and 7.30 kN, respectively. The exterior and interior grid lines were determined to have tensions of 11.69 kN and 6.67 kN, respectively. Results of the numerical model compared reasonably well (within 10%) with those calculated analytically. Note that the difference is due

to stretch in the mooring lines. When the anchor and grid line stiffness is increased (for example, to values similar to steel cable) the analytical and numerical values are within 1%. The static tension results were different for the two methods because the analytical approach utilizes inextensible catenary equations while the numerical approach considers mooring line elasticity. The geometric difference due to stretching the mooring lines slightly changes the static tension.

Table 7.2: Analytical and Numerically modeling static load results.

	Analytical (kN)	Numerical (kN)	% Difference
Corner Anchor Line	12.52	12.84	2.5
Side Anchor Line	6.62	7.30	9.3
Grid Line (Outside Edges)	11.41	11.64	1.9
Grid Line (Interior)	6.01	6.67	10.0

7.4.2 Dynamic Simulations

Dynamic simulations were performed using the UNH design condition consisting of a deterministic wave with a height of 9 meters and a period of 8.8 seconds coming from the northeast direction. Model simulations were used to calculate mooring line loads. Time series results for the anchor line tension from the numerical model are shown on Figure 7.5. Maximum steady state values were calculated to be 147 and 132 kN for the side (2 and 5) and corner (1, 3, 4 and 6) anchor line assemblies, respectively. One advantage of the data set resulting from performing numerical model simulations was that the tension from a variety of components in the mooring system could be analyzed. From this data set grid line tensions were also investigated. This information was important in the understanding of how the cages transfer loads to the anchor legs and the ground tackle. It was found that the grid line tensions in the northeast quadrant of the mooring were major load bearing components with values ranging from 70 to 120 kN when the design condition was applied (Figure 7.6). In addition, it

was found that a majority of the southwest SS3000 cage loads were transferred through the grid to the two side anchors. This information was vital to determining how the loads were distributed throughout the grid so each component could be specified.

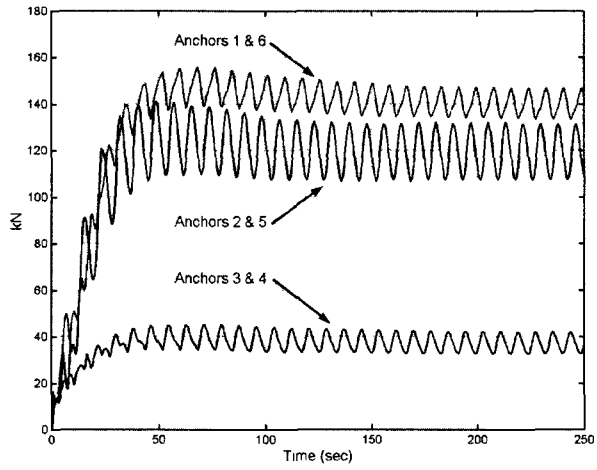

Figure 7.5: Selected mooring line load results using one of the UNH design conditions. Anchors are identified in Figure 7.3.

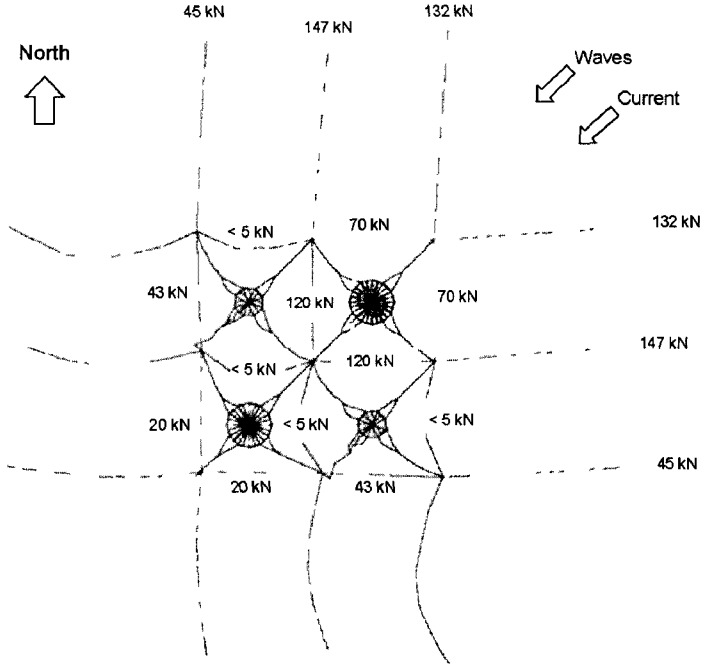

Figure 7.6: The maximum load distribution in the mooring using one of the UNH design conditions. The current and waves are applied from the northeast direction.

7.5 Component Specification and Deployment

The use of the numerical model was important during the design of these mooring systems. It was imperative, however, to understand that the tension values calculated were only approximations. Modeling variability associated with choosing correct material and geometric properties, appropriate forcing and other physical characteristics (not necessarily represented), creates some uncertainty. For example, the numerical modeling approach did not take into account shadowing effects discussed in Chapters 2, 4 and 5 or the change in drag and mass due to biological fouling. Therefore, developing an appropriate design mooring component force also incorporates knowledge obtained from practical experience. A team of engineering and operational personnel discussed the modeling results, along with deployment and maintenance implications. Based on these discussions, the maximum loads calculated with the numerical model were increased by 17% to obtain a design mooring component force of 178 kN. Along with the cost and operational factors, this design force was used to specify mooring system components.

Many of the mooring parts used in the previous single-cage grid deployments, including eight of the twelve embedment anchors (and chain), as well as four of the side flotation elements, were reused to reduce costs. The anchors were chosen to have the smallest safety factor relative to other mooring components. Even though conservative environmental conditions were used in the design process, often more extreme or unplanned events could occur at the site. If a more extreme event was encountered, the intent was to have the anchors "drag" to relieve system stress before actual structural damage occurred in the other components (e.g. mooring rope, shackles). Depending upon the direction of the waves and currents, the grid lines are important members for the transfer and distribution of loads to the

anchor lines. Therefore, all of the mooring rope (grid and anchor) were sized using the same design force (178 kN) requirements. This also helped to reduce costs since the rope could be purchased in bulk quantities. The lines were held in place by 38 mm shackles, which have been found to be the limit of easy diver serviceability. Prior to deployment, each shackle pin was welded to prevent them from becoming undone. The grid corner flotation was sized not only to tension two anchor legs, but also to offset any biological fouling that may occur, allowing greater flexibility in routine cleaning operations. The mooring system components along with the minimum breaking loads (M.B.L.) and factors of safety (compared to the design force) are listed in Table 7.3. It is important to note that line, chain and shackles typically have a "working" load and a minimum breaking strength. In this system, the M.B.L. was employed to limit the size of the equipment and associated cost of the mooring grid. For reference, typically working loads are approximately 5 times lower than the M.B.L. Schematics of the grid corner and side and center anchor leg assemblies are shown in Figures 7.7 through 7.9. Figure 7.10 presents the crown line assembly located on each anchor.

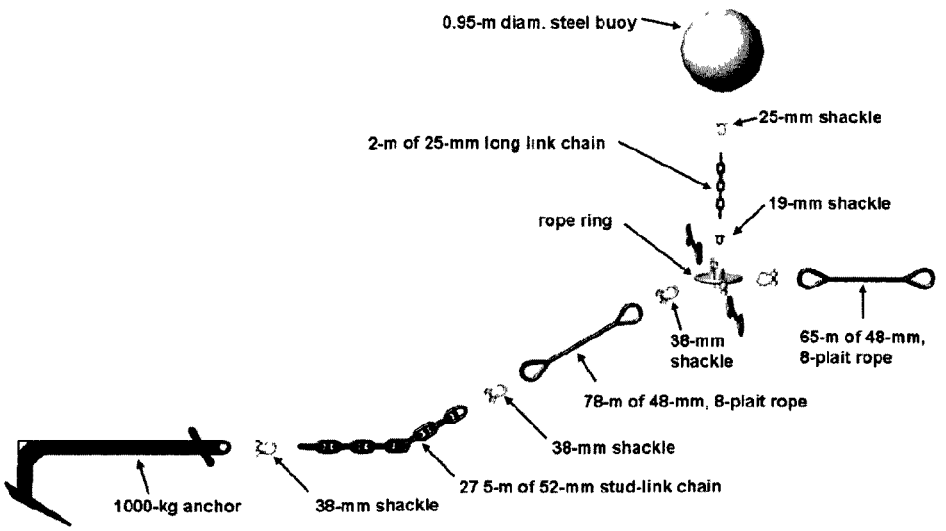

Figure 7.7: Component details of the side grid mooring assembly. Some items are not to drawn to scale.

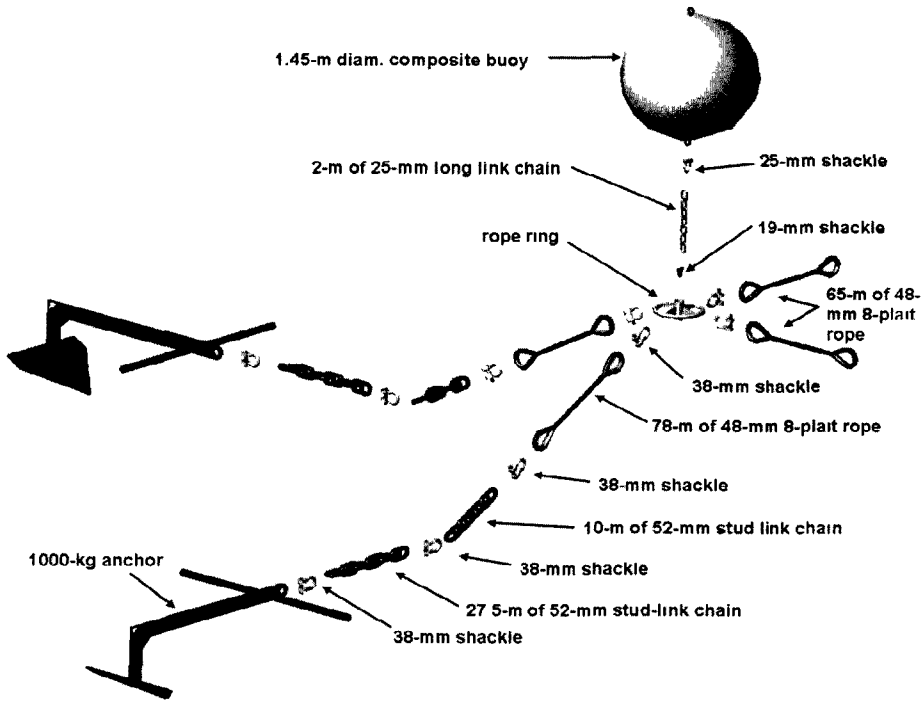

Figure 7.8: Component details of the corner grid mooring assembly. Some items are not to drawn to scale.

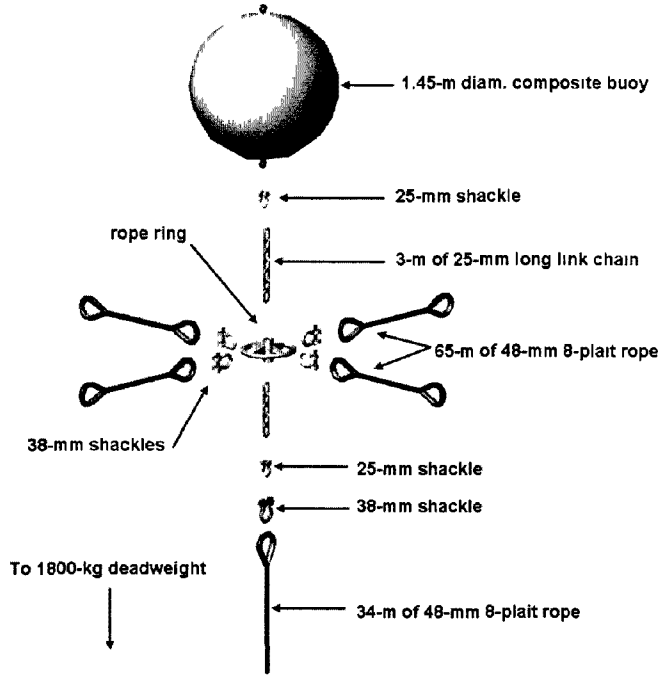

Figure 7.9: Component details of the center grid mooring assembly. Some items are not to drawn to scale. The center node is held down by a 1800 kg steel deadweight.

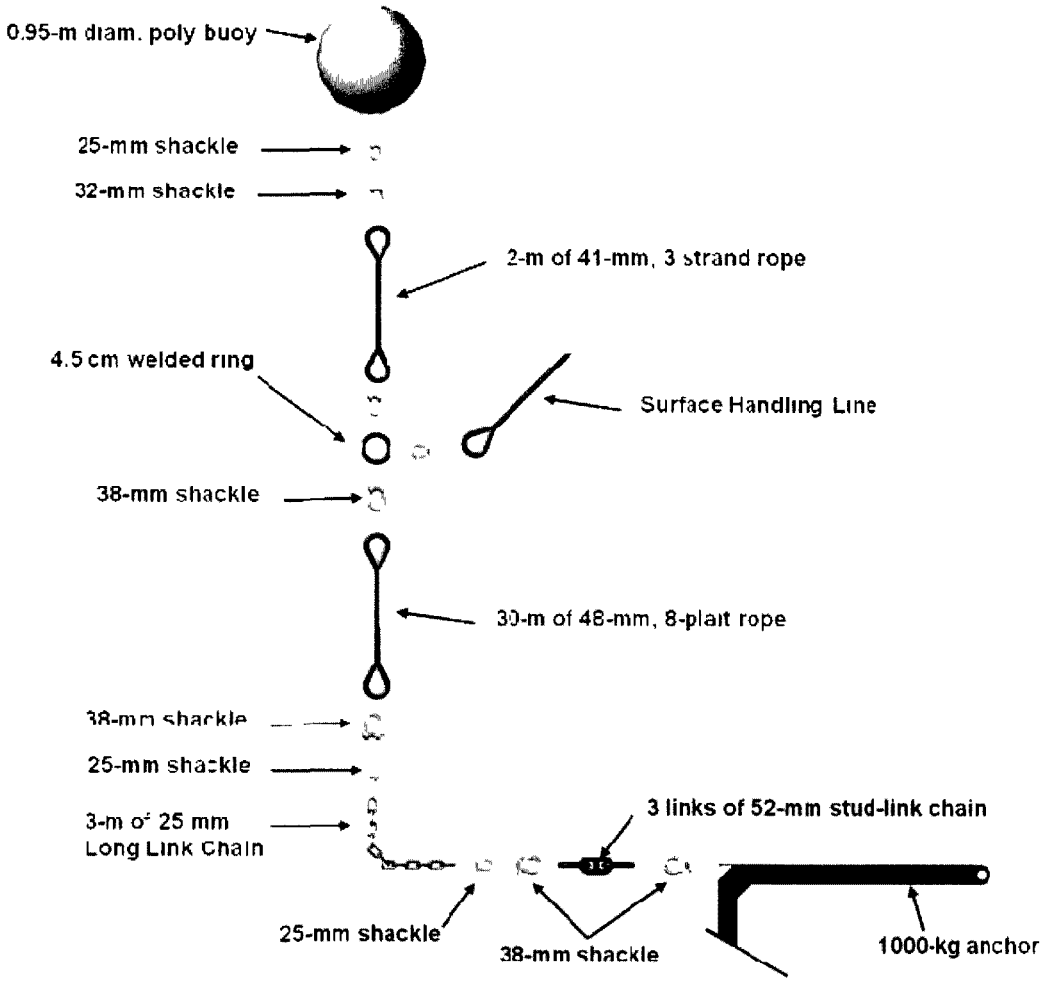

Figure 7.10: Component details of the crown line assembly. Some items are not to drawn to scale.

Table 7.3: The mooring system particulars.

Component	Description	M.B.L.[a]	Safety Factors[e]
ANCHOR (12)			
Construction Mass	Drag Embedment 1000 kg	178 kN[b]	1.0
SIDE ANCHOR CHAIN (4)		894 kN	5.0
Construction Length Mass	Stud-Link 27.4 m 706 kg/m		
CORNER ANCHOR CHAIN (8)		894 kN	5.0
Construction Length Mass	Stud-Link 37.5 m 706 kg/m		
ANCHOR LINE (12)		390 kN	2.2
Construction Length Specific Gravity Diameter	8-plait co-polymer 78 m 0.94 48 mm		
SIDE GRID FLOTATION (4)		370 m[c]	---
Construction Mass Diameter	Steel 136 kg 0.9525 m		
CORNER and CENTER GRID FLOTATION (5)		47 m[c]	---
Construction Mass Diameter	Urethane Foam Comp. 295 kg 1.45 m		
CORNER ROPE RING/CHAIN		444 kN[d]	2.5
Construction Mass Length	25.4 mm steel long-link 61.33 kg 2.0 m		
GRID LINE		390 kN	2.2
Construction Length Specific gravity Diameter	8-plait co-polymer 65 m 0.94 48 mm		
SHACKLES		756 kN	4.2
Construction Mass Diameter	Galvanized Steel 7.25 kg 38 mm		

[a] Minimum Breaking Load
[b] Holding power
[c] The flotation elements are rated at working depth.
[d] The corner rope ring was tested by manufacturer to a load of 444 kN without failure.
[e] Safety factor utilized the 178 kN design force.

The location of the mooring grid within the permitted site was determined using bottom topography information obtained courtesy of the Center for Coastal and Ocean Mapping /Joint Hydrographic Center (CCOM/JHC). The gear was successfully deployed the first week of July 2003, using the F/V Nobska operated by Stommel Fisheries from Woods Hole, MA (Figures 7.11 and 7.12). Anchor locations were first determined using Differential Global Positioning System (GPS) instrumentation based on the design geometry calculated using the catenary equations (Rice 2006). The gear was deployed "slack" with each of the grid floats at the surface (Figure 7.13). A 15 meter line with indicator floats was attached to each of the grid floats. Next, using the crown lines, the anchors were pulled out with the fishing vessel to the predetermined positions. The anchors were set when only the indicator floats of the 15 meter lines were visible, "indicating" that the grid was at the proper depth. This technique allows the vessel operator to accurately position the anchors and grid since the inextensible catenary equations do not take into consideration stretching of the rope and bottom contour variability.

Figure 7.11: The F/V Nobska, operated by Stommel Fisheries, deployed the four-grid mooring.

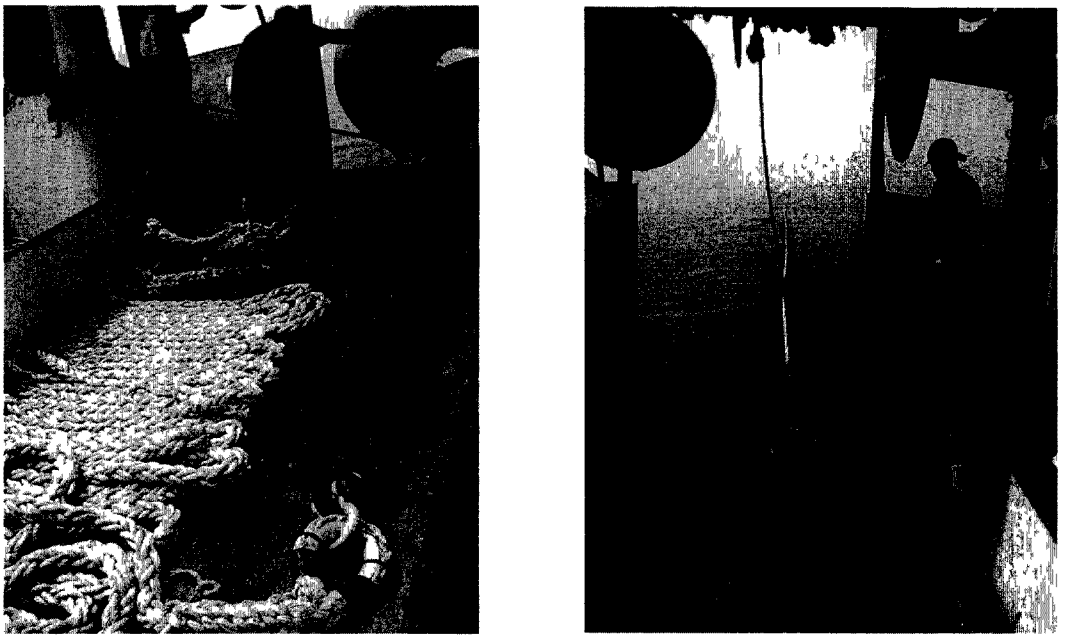

Figure 7.12: The gear was faked on the deck and streamed behind the deployment vessel

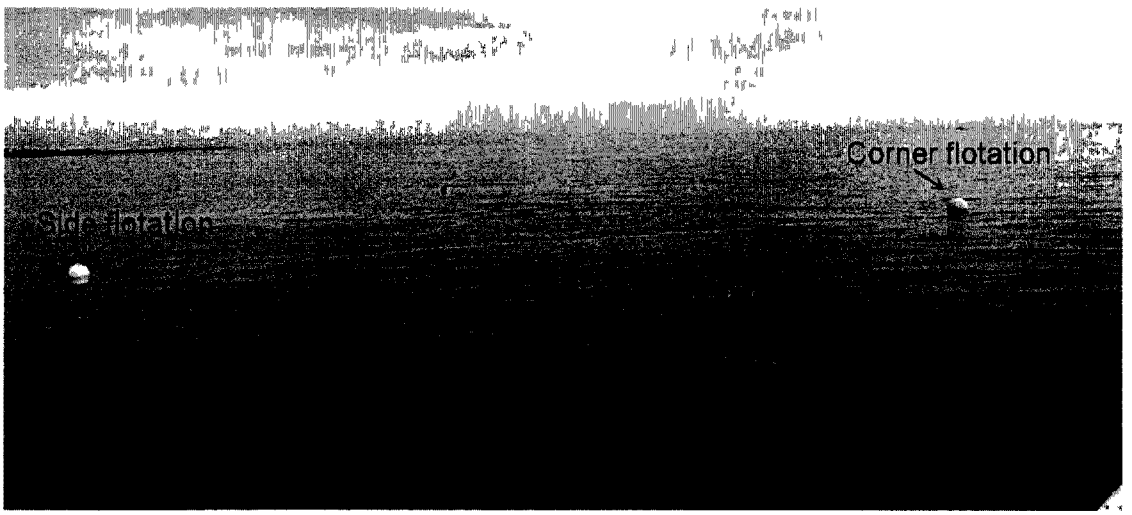

Figure 7.13: The grid lines can be seen organized on the water surface.

Once the installation was complete, the designed anchor locations were compared to the deployed anchor positions, determined by temporarily mooring up to the crown lines and recording the positions using GPS. The resulting locations are displayed in Figure 7.14. The numerical values listed on the figure present the linear separation distance of the two anchors.

It can be seen that the anchors were pulled further out from the grid than designed. This was likely a result of the loose construction (lay) of the line. It is important to note that some error may be incorporated into the measurements, depending upon the scope of the line attached to the corners and anchors. The grid depth, however, was flat, submerging approximately 15 meters below the surface. A detailed description of the grid deployment process as well as *in-situ* static line tensions can be found in Rice (2006).

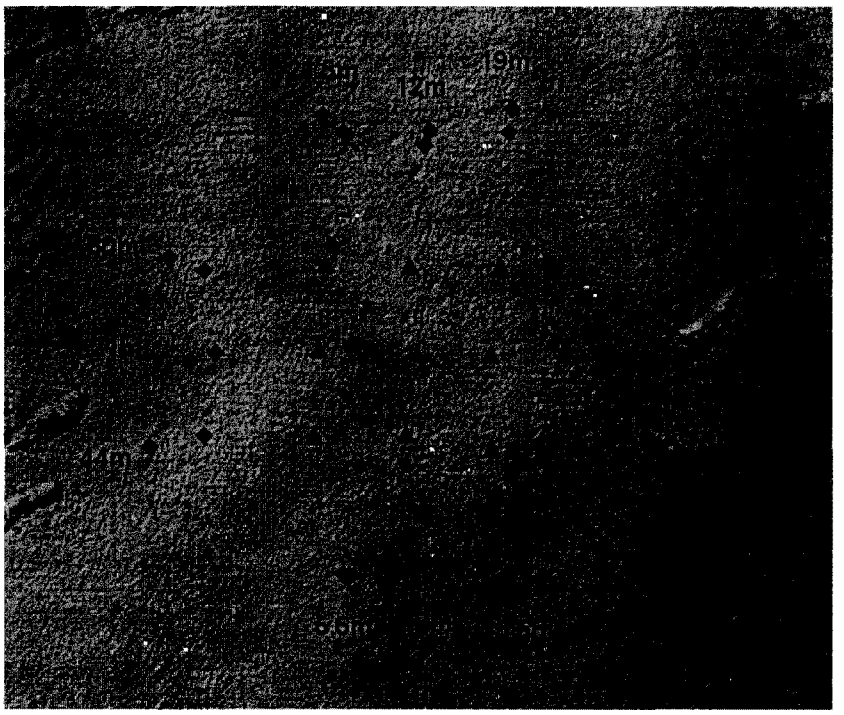

Figure 7.14: The mooring corner and anchor locations depicted on the UNH site bathymetry. The solid black diamonds represent the designed location of the anchors. The pink are the deployed locations as measured from the vessel GPS. The numbers are the distances between the deployed and designed positions. During deployment, it became apparent from the indicator floats that the designed anchor locations were not sufficient to get the grid to the designed depth. As a result, the anchors out further than designed.

7.6 Research Activities and Environmental Conditions at the Submerged Mooring

The submerged grid mooring provided a platform to conduct engineering and biological research projects at an exposed site in the Gulf of Maine. Numerous cage systems were at one point secured in the mooring such as the SS600 and SS3000 *SeaStations*™ by Ocean Spar Technologies, the Aquapod™ by Ocean Farm Technologies, the American Soybean Association's OCAT system, JPS Industries prototype submersible net pen and standard surface nursery cages (DeCew et al., 2006; Fredriksson et al., 2005; Celikkol et al., 2007, 2009). A few of these systems can be seen in Figure 7.15. Tensions in the grid and anchor lines were measured (Rice, 2006) as well as those in the bridle lines for the prototype gravity net pen (Santamaria et al., 2007). These *in-situ* measurements were used to verify the numerical modeling predictions from Aqua-FE. Studies were conducted monitoring the marine growth (biofouling) on traditional nylon nets, anti-fouling painted nets and emerging net technologies such as copper alloy materials (Celikkol et al., 2007; Greene and Grizzle, 2007; and Langan 2004).

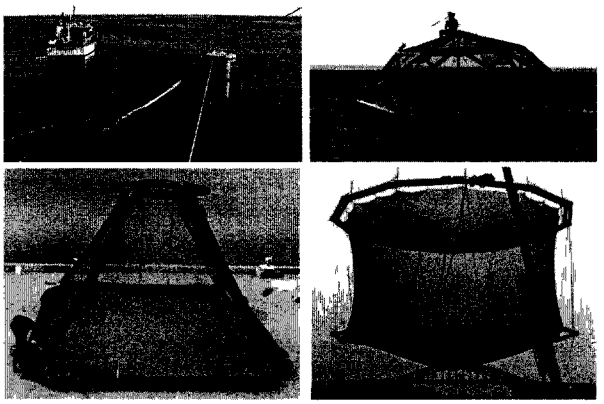

Figure 7.15: Cage systems deployed at the site include the SeaStation™ (top left), Aquapod™ (top right), OCAT (lower left), and the JPS prototype (lower right).

The mooring was also used to secure surface structures. Three fish feeding buoys were deployed in and around the grid (Figure 7.16). These fully automated buoys remotely fed fish in submerged cages secured in the grid mooring (Fullerton et al., 2004; Turmelle et al., 2009; Boduch and Irish, 2006; and Irish and Boduch, 2006). Two of these buoys (1/4 ton and 1 ton feed capacity) were attached directly to the grid using traditional and elastic mooring members. The third buoy with a 20-ton feed capacity had an external mooring, but was coupled to the grid with elastic feed hoses. More information regarding the buoy dynamics, mooring components tensions and operability can be found in (Rice et al., 2003; Fullerton et al., 2004; Turmelle et al., 2009; Irish et al., 2001; Irish and Fredriksson et al.; 2003 and Horton, 2008).

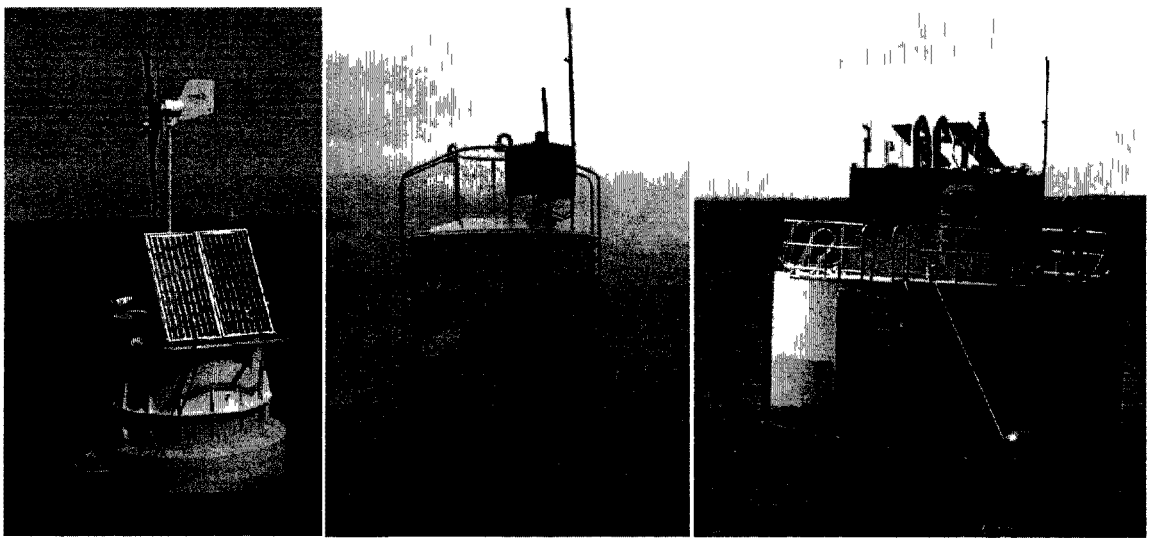

(a) (b) (c)

Figure 7.16: Feeding buoys deployed within or coupled to the grid: (a) 1/4 ton feed capacity, (b) 1 ton feed capacity or (c) 20 ton feed capacity.

In parallel to the engineering studies, a series of biological experiments were conducted. Fish growth studies on a variety of species using various feed diets were performed on species such as Atlantic Halibut (*Hippoglossus hippoglossus*), Atlantic Cod (*Gadus morhua*), Haddock (*Melanogrammus aeglefinus*), Summer Flounder (*Paralichthys dentatus*) and Steelhead Trout

(*Oncorhynchus mykiss*) (Chambers et al., 2007; Howell and Chambers, 2005; and Chambers and Howell, 2006). Some of these fish species are shown in Figure 7.17. Fish distribution, swimming speed and feeding behavior were observed in the submerged cages utilizing acoustic tags and hydrophones (Rillahan et al., 2009; 2011). Operational methods were also developed for open sea live harvesting of cod (Chambers et al., 2003).

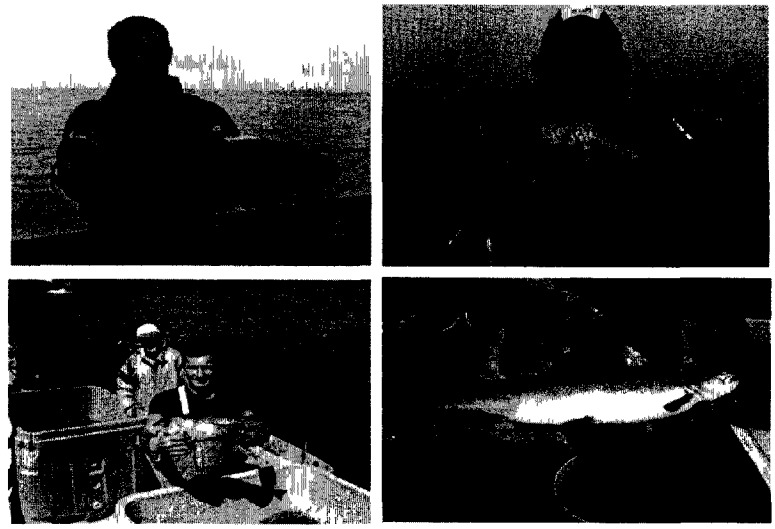

Figure 7.17: Several of the fish species grown at the site include Atlantic halibut (top left), Atlantic cod (top right), Haddock (lower left), and Steelhead Trout (lower right).

In support of these research activities, the environmental conditions at the site were monitored with a wave riding buoy (Figure 7.18) secured in a single point mooring (Irish et al., 2001; Irish and Fredriksson et al., 2003; Irish et al., 2004). To provide a better platform for measuring waves, compliant elastic tethers were incorporated into the mooring, which allowed the buoy to move freely with the waves with limited movement of the oceanographic equipment located in the water column (Irish and Fredriksson et al., 2003, Ahern 2002). Currents were recorded by an Acoustic Doppler Current Profiler (ADCP) placed in the mooring

near the seafloor. Various water parameters, such as the temperature, salinity, etc were also measured.

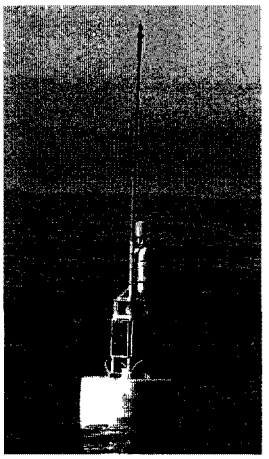

Figure 7.18: The environmental monitoring buoy deployed at the offshore site.

The waves at the site were measured by the environmental monitoring buoy with a Summit Technologies accelerometer (model number 34102A). The recorded accelerations were utilized to estimate the non-directional significant wave height (SWH) and dominant wave period. The SWH was found to be smallest during the summer months (typical SWH and dominate period values of 1-2 meters and 5-7 seconds, respectively) and larger during the winter (SWH and dominate period values of 4-6 meters and 6-8 seconds, respectively). Figure 7.19 shows the significant wave heights for the 2006 winter season. It was found that the largest storm waves generally originated from "northeasters." Two of the largest storm events were observed in March 2001 (SWH of 7.5 m) and April 2007 (SWH of 9 m). Figure 7.20 shows the significant wave height history for the latter, representing a 50-year storm event for the region, capable of re-suspending sediments on the seafloor. In addition, time series data from this event showed surface elevation fluctuations of 30 m (single wave trough to crest distance).

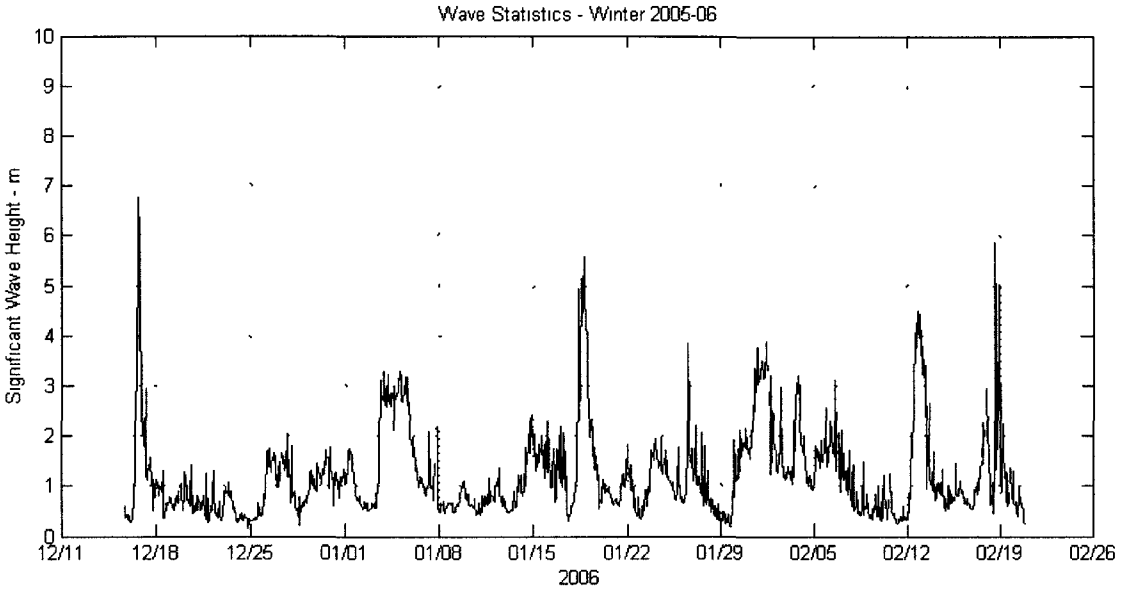

Figure 7.19: Typical winter storm waves in 2005-2006 with significant wave heights of 4 to 6 m.

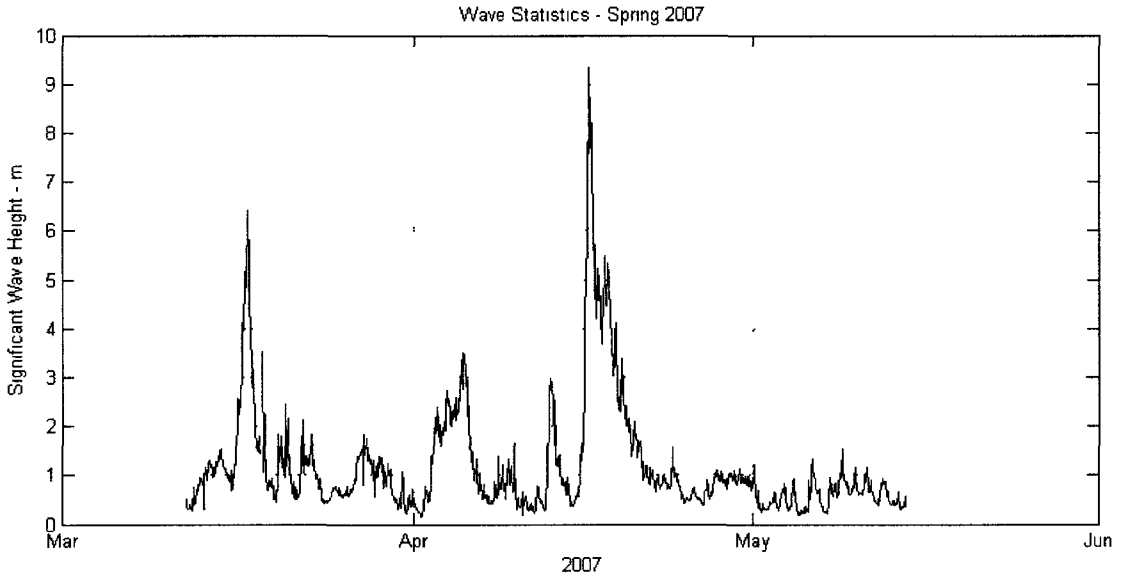

Figure 7.20: The April 2007, 9 meter, 12 second storm event at the UNH offshore site.

Currents at the site were measured with an upward looking RD Instruments 300 kHz ADCP secured in the mooring (Irish et al., 2004). Tidal currents in the region were found to be nearly uniform with depth, ranging from 0.02 m/s – 0.05 m/s. Storm driven currents were

measured to be strongest near the surface and decreased with depth, with maximum magnitudes of 0.5 m/s (1 knot). An example of a tidal water velocity time series in March 2004 is shown in Figure 7.21.

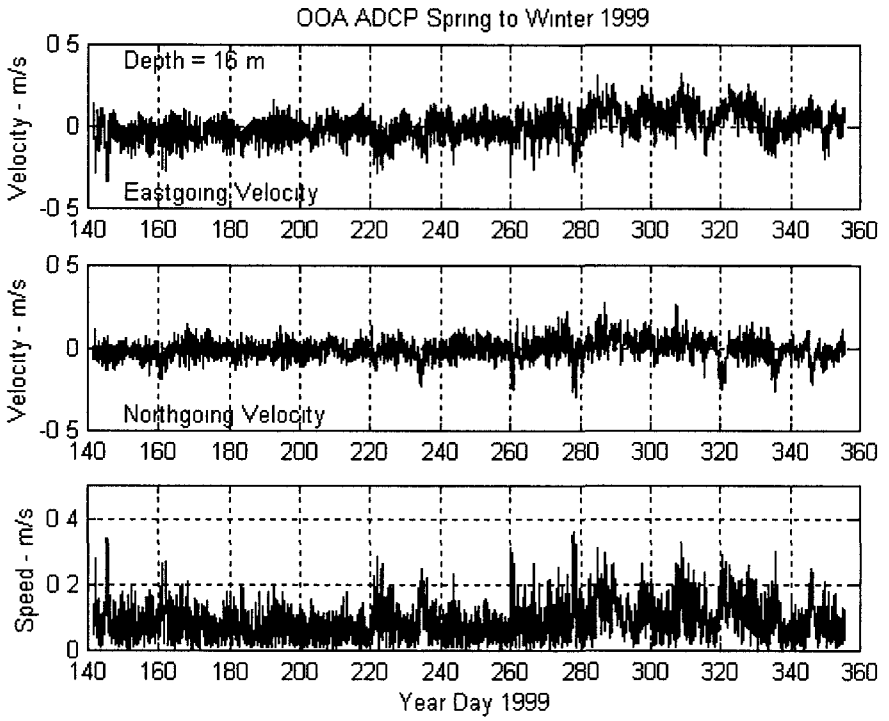

Figure 7.21: The observed currents at the UNH site over one year.

7.7 Mooring Recovery and Inspection

In June 2010, the submerged mooring was recovered by Riverside and Pickering Marine of Elliot, ME using a barge (w/ crane) and tug vessel. The mooring components were then transported to shore with the UNH R/V Meriel B. The original deployment plan called for the crown lines to be used to release the pre-tension in the system, allowing the grid to rise to the surface. Unfortunately, the majority of the crown lines sank to the seafloor at some point during the seven years the mooring was in place. Therefore, the two southwest mooring lines were cut by divers, producing a similar result. With the grid at the surface to ease accessibility, each

anchor leg was systematically disconnected from the rope rings and removed from the water. The grid lines and floats remained secured at the surface with the center deadweight anchor. Once the anchors were recovered, the surface lines and floats were removed. Finally, the center deadweight was recovered, all the equipment organized and transported to shore.

Upon recovery, the mooring components were inspected and documented. Anchors, chain and other critical components were pressure washed and organized. The following observations regarding the state of the critical components were made:

Anchors - The majority of the anchors were in good shape, with some still having the original paint on the shaft and flukes (Figure 7.22). "Mud lines" and areas of biological growth helped determine that each anchor was well set into the seafloor sediment. One anchor had a bent stock, possibly occurring during deployment. Two of the anchors showed excessive material loss due to corrosion on the tip of the flukes. However, the corrosion did not threaten the operability or integrity of the anchor.

(a) (b)

Figure 7.22: Two anchors recovered from the mooring. Some of the anchors were in excellent shape, with paint present on the flukes and little material loss (a), whereas others had some material loss at the edges of the flukes (b).

Chain – The chain utilized with each anchor was in good shape. The majority of the chain was covered in mud, helping to reduce any corrosion. The chain near the anchor line attachment, and thus out of the seafloor sediment, displayed more evidence of long term exposure to seawater with an additional 2-3 mm of material loss (compared to the remainder of the chain). Quantitative comparisons of the chain's material loss that occurred during the deployment between anchor legs could not be made because "used" chain was utilized in the original mooring and measurements of the wire diameter were not made.

Mooring Lines – The recovered grid lines were fouled with mussels upon recovery. Once cleaned off, the line had minimal abrasion and wear along its length. Anchor lines had significantly less mussel growth and were in similar condition. However, rope fraying was evident around the thimbles at rope ring connections, mostly in the northeast quadrant of the grid (dominate storm bearing direction). The lines showed wear around the thimbles (Figure 7.23) where contact could occur with the steel rope ring. The anchor line – anchor chain connection did not show any line fraying. Therefore, it is assumed that relative motion, present at the grid level, caused some wear between the line and rope rings.

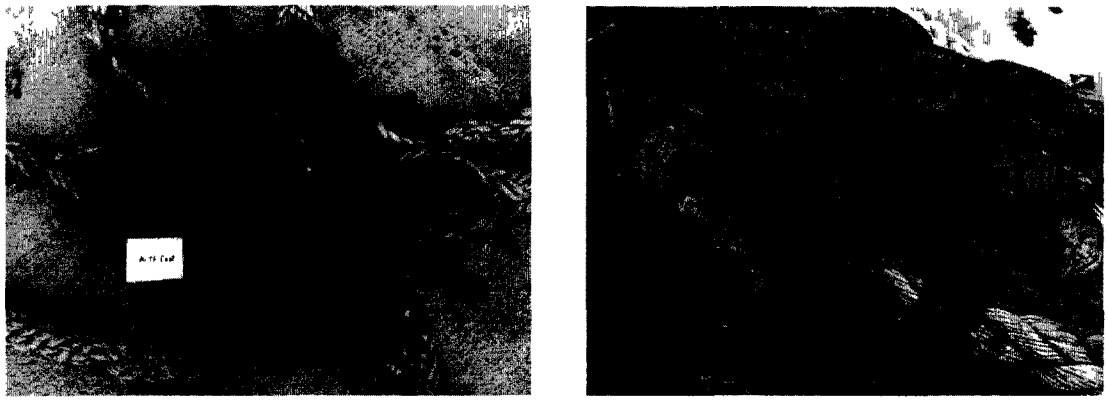

Figure 7.23: The grid lines were found to have some wear around the thimbles, near the rope rings. The lines must have come in contact with the rope rings, fraying the line over the seven year deployment.

Rope Rings / Shackles – These components were all in good shape. A few rope rings (shown in Figures 7.7, 7.8, and 7.9) had evidence of slight wear (rust worn off, a few flat spots at connection points). The shackles in the majority of the system had minimal wear. The shackles located on the northeast corner, had some wear in the bow of the shackle. However, none threatened the structural integrity of the mooring.

Figure 7.24: The center connection rope ring and shackles. The rope rings and shackles were found to be in good shape, with minimal wear.

Subsurface Floats – The floats were all in good condition. The attachment points located on the bottom of the flotation elements had little wear and were structurally sound (Figure 7.25). Both types of floats (urethane foam and steel) were fouled with biological growth but were otherwise in re-usable shape.

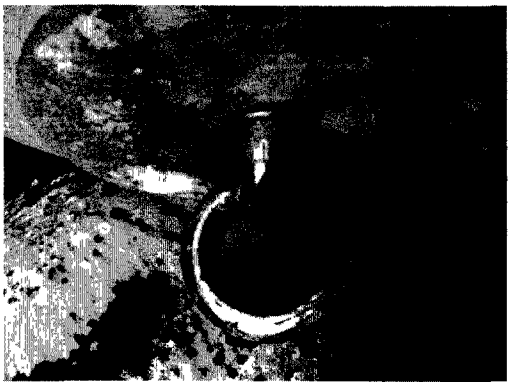

Figure 7.25: The connections on the floats were found to be in excellent condition.

7.8 Review of the System

A submerged grid mooring was designed, analyzed and deployed for seven years in the western Gulf of Maine. The design procedure included analytical calculations and numerical model simulations. A large portion of the design effort involved the interpretation of the numerical model results. Efforts were made to accurately model the system by comparing static simulation values to those obtained using inextensible catenary equations. Results from the dynamic simulations were employed to size the mooring gear and factors of safety. The grid was utilized as a scientific platform, hosting a series of engineering and biological studies. The system proved to have minimal maintenance requirements over its lifetime. The dominant maintenance procedure was the yearly removal of mussels from the grid lines and flotation elements and the occasional addition of zincs to the steel subsurface floats. The submerged platform survived numerous extreme environmental conditions, including a 9-meter significant wave height storm in 2007. The system's pre-tension and depth below the surface minimized wear between components due to relative motion. No marine mammal entanglements were observed over the mooring deployment, even though minke and fin whales were spotted in the vicinity of the grid.

A majority of the crown line flotation was lost at some point during the system's lifetime. This could be a result of excessive biofouling on the components over time (these were not cleaned as part of the maintenance schedule), slowly sinking the lines until pressure collapsed the floats. Without access to these lines for recovery, the removal of the system took longer than expected.

The minimal amount of wear on steel components was unanticipated. Although the mooring design utilized the submerged system's pretension to reduce the relative motion between components (unlike surface moored systems), more material loss was expected at the grid corners and float connection points. The reduced water particle velocity (due to waves) and current magnitudes at depth helped facilitate this result. With largely steel components, the corrosion was minimal and much of the life of shackles, rings, thimbles was remaining after seven years.

The submerged grid mooring proved to be a reliable, stable working platform for a variety of ocean structures. The success of the seven-year deployment with no structural integrity issues, no loss of fish cages or surface feed buoys highlights the importance of a sound engineering approach taken in the design process.

CHAPTER 8

RESEARCH CONCLUSIONS

Numerical modeling tools and techniques were developed to effectively predict flexible system response in marine environments. The Aqua-FE software package was enhanced by increasing the element library and implementing new hydrodynamic effects. Two case studies, involving laboratory and field experiments, were performed evaluating these software modifications. Aqua-FE was used as the primary tool in the design and analysis of the UNH offshore submerged mooring system. New structural modeling techniques were proposed, to evaluate the strength and predict localized failure in HDPE components. The mechanical behavior of new and previously deployed HDPE specimens, obtained from marine fish farms was investigated via tensile testing.

The following conclusions result from the conducted research:

- Enhancements in the UNH developed software package Aqua-FE improves the performance of the software when compared to laboratory and field experiments.
- The expansion of the element library to include spherical elements and incorporation of Stokes 2nd Order waves increases the versatility of the program by providing new geometries and non-linear wave capabilities to the software.
- An approach to simulate velocity shadowing effects is proved to be adequate to represent reduced water velocities inside and behind aquaculture cage systems.

- The cylindrical element's coefficient of drag enhancement is shown to improve the software predictions for drag forces and motion dynamics in the critical region of the drag coefficient as a function of Reynolds number curve (Figure 2.17).
- Application of the modeling approach shows that the single point moored fish cage system experiences an unstable submergence regime in a certain current range. This region is characterized by significant changes in depth for small variations in the system's design, e.g. solidity of netting.
- The modeling approach to predict localized failure is effective and shows good agreement to laboratory experiments.
- A method to predict the strain rate within a HDPE net pen is proposed that incorporates influencing cage frame strain rate factors such as net solidity, mooring compliance and environmental loading.
- HDPE's material properties are found to have a rate dependence and, therefore influence the structural capabilities of net pen frames.

This research exposed several areas of required further work. The velocity shadowing approach described in Chapter 2, required knowledge of the incident and "reduced" water velocities around the cage and the regions/areas of reduced water flow. Therefore, empirical measurements are required for different system geometries or net solidities. It would be useful to determine "reduced" water velocity approximations associated with various geometries in certain flows for integrations into the Aqua-FE software. In addition, the method used in this research applied he reduced water velocity to half the cage system. This may be oversimplifying the problem and future research into a more accurate representation of the shadowed portions is necessary. In the case study of the net pen secured by a single point mooring (Chapter 4), the

effect of the net pen's buoyancy on the submergence depth was not studied should be investigated to determine this effect on the system's dynamic response.

The structural modeling techniques can also be enhanced with future studies (Chapter 5). Investigations to determine the proper boundary conditions for net pens (y-line attachment, net load distribution, buoyancy forces, etc) should be initiated. Although significant progress was made in determining HDPE material properties at strain rates associated with marine environments (Chapter 6), there were two limitations to the research: (1) the initial strain rates selected for analyses were determined using linear elastic analysis and (2) the service history of the material was not known. A second iteration analyzing the cage frame strain rate should be conducted, utilizing the data gained in the mechanical testing experiments, to determine if the strain rates originally developed are adequate. Secondly, investigation of the HDPE material properties should be revisited when more information of the materials length of deployment and environmental conditions are obtained.

The modeling tools and techniques researched in this study have applications outside the aquaculture industry. The Aqua-FE software can be utilized to investigate the motion and mooring load dynamics of a variety of structures such as wave buoys, wind turbines and acoustic tethers. The structural modeling approach and HDPE material property data can be applied to marine pipelines, barrier system and other complaint structures. Testing these modeling techniques on these types of systems would be an interesting extension of this research.

LIST OF REFERENCES

Aarsnes, J.V., Rudi, H., Loland, G. (1990). *Current Forces on Cage, Net Deflection.* In: Engineering for Offshore Fish Farming. London: Thomas Telford, pp.137-152.

Ahern, J. (2002). *Validation of a Wave Measurement Buoy.* Dissertation submitted to the University of New Hampshire in partial fulfillment of the Masters of Science in Ocean Engineering Degree. Durham, NH.

Airy, G. B. (1845). *"Tides and Waves."* Encyclopedia Metropolitan, London, pp. 241-396.

Baldwin, K. Steen, R., Michelin, D., Muller, E., Lavoie, P., (2000). *Open Aquaculture Engineering: Mooring and Net Pen Deployment.* Mar Technol Soc J. 34, 1, 53-58.

Barker, M., Bowman, J., Bevis, M., (1980). *Fatigue Properties of High Density Polyethylene Pipe Systems.* Journal of Materials Science, Vol 15, No 1, pp 265-268.

Berteaux, H.O. (1991). Coastal and Oceanic Buoy Engineering. Published by the author. Woods Hole, Ma. 285 p.

Bessonneau, J.S. and Marichal, D., (1998). *Study of the Dynamics of Submerged Supple Sets (Applications to Trawls).* Ocean Eng. 25 (27), 563-583.

Bilgin, O., Stewart, H., O'Rourke, T., (2007). *Thermal and Mechanical Properties of Polyethylene Pipes.* Journal of Materials in Civil Engineering, Vol 19, no 12, pp 1043-1052.

Boduch, S., J. Irish, (2006). *Aquaculture Feed Buoy Control – Part 1: System Controller.* In: Proc. Oceans '06, Boston.

Celikkol, B., DeCew, J., Swift, M.R., Tsukrov, I., Baldwin, Risso, A., Despins, R., Irish, J., (2007). Construction and Deployment of an OCAT Cage in the Gulf of Maine. Final report submitted to the ASAIM and USSEC for Activity 7515.

Celikkol, B., DeCew, J., Drach, A., Chambers, M. (2009). Construction and Deployment of an OCAT Fish Cage with Copper Alloy Netting. Final report submitted to the ASAIM, USSEC and ICA.

Chambers, M.D., W.H. Howell, R. Langan, B. Celikkol and D. Fredriksson, (2003). *Status of Open Ocean Aquaculture in New Hampshire.* Open Ocean Aquaculture, From Research to Commercial Reality. The World Aquaculture Society.

Chambers, M.D. and W.H. Howell, (2006). *Preliminary Information on Cod and Haddock Production in Submerged Cages off the Coast of New Hampshire USA.* ICES Journal of Marine Science, 63(2).

Chambers, M.D., R. Langan, W. Howell, B. Celikkol, K., W. Watson, R. Barnaby, J. DeCew and C. Rillihan, (2007). *Recent Developments at the University of New Hampshire Open Ocean Aquaculture Site.* Bull. Aquacul. Assoc. Canada, 105(3).

Chen, H., Scavuzzo, R., Srivatsan, T., (1997). *Influence of Joining on the Fatigue and Fracture Behavior of High Density Polyethylene Pipe.* JMEPEG, Vol 6, pp 473-480.

Choo, Y.I., Casarella, M.J., (1971). *Hydrodynamic Resistance of Towed Cables*. J. Hydronautics. pp. 126–131.

Cintron, R., Saouma, V., (2008). Strain Measurements with the Digital Image Correlation System Vic-2D. Center for Fast hybrid Testing, document number CU-NEES-08-06.

Clark, P., Bettess, P., Hearn, G., Downie, M., (1991). *The Application of Finite Element Analysis to the Solution of Stokes Wave Diffraction Problems*. International Journal for Numerical Methods in Fluids, Vol 12, pp. 343-357.

Colak, O., Dusunceli, N., (2006). *Modeling Viscoelastic and Viscoplastic Behavior of High Density Polyethylene (HDPE)*. ASME, Vol 128, pp 572-578.

Cremer, M., Z. Jian and H.P. Lan, (2003). Growth Performance of Golden fin Pompano at Two Stocking Densities in Near-Shore Ocean Cages at Hainan, China. Results of ASA/China 2003 Feeding Trial 35-03-121. American Soybean Association, Beijing, China.

Coulbourne, D.B., (1997). Mooring Line Loads in a Salmon Cage. IMD Rep. LM-1997-22.

Dasari, A., Duncan, S., and Misra, R.D.K, (2003a). *Microstructural Aspects of Tensile Deformation of High Density Polyethylene*. Materials Science and Technology, Vol 19, pp244-252.

Dasari, A., Misra, R.D.K (2003b). *On the Strain Rate Sensitivity of High Density Polyethylene and Polypropylenes*. Materials Science and Engineering, A358, pp 356-371.

Dean, R.G., and R.A. Dalrymple (1991). Water Wave Mechanics for Engineers and Scientists. World Scientific Publishing Company, Singapore. 353 p.

DeCew, J., D.W. Fredriksson, L. Bougrov, M.R. Swift, O. Eroshkin, and B. Celikkol (2005). *A Case Study of a Modified Gravity Type Cage and Mooring System using Numerical and Physical Models*. IEEE Journal of Oceanic Engineering, Special issue on Open Ocean Aquaculture Engineering. Vol 30, No. 1, 47-58.

DeCew, J., S. Page, C.A. Turmelle, and J.D. Irish, (2006). *Tow Test Results of an Aquapod Fish Cage*. In Proc. Oceans06, Boston, MA.

DeCew, J., Tsukrov, I., Risso, A., Swift, M.R., Celikkol, B., (2010). *Modeling of Dynamic Behavior of a Single-Point Moored Submersible Fish Cage under Currents*. Aquacult. Eng. Vol 43, pp 38-45.

DeCew, J., Baldwin, K., Celikkol, B., Chambers, M., Fredriksson, D.W., Irish, J., Langan, R., Rice, G., Swift, M.R., Tsukrov, I. (2010). *Assessment of a Submerged Grid Mooring in the Gulf of Maine*. In: Proc. Oceans10, Seattle, WA (in press).

Donley, H. E., (1991). *The Drag Force on a Sphere*. UMAP Journal, Vol. 12, No. 1, pp. 47-80.

Dudley, R.W., Panchang, V.J., Newell, C.R., (2000). *Application of a Comprehensive Modeling Strategy for the Management of Net-pen Aquaculture Waste Transport*. Aquaculture 187 (3), 319–340.

Dusunceli, N., Colak, O., (2006). *High Density Polyethylene (HDPE): Experiments and Modeling*. Mech. Time-depend Mater, Vol 10, pp 331-345.

Dusunceli, N., Colak, O., (2008). *The Effects of Manufacturing Techniques on Viscoelastic and Viscoplastic Behavior of High Density Polyethylene (HDPE)*. Material and Design, Vol 29, pp 1117-1124.

Drozdov, A., Christiansen, J., (2007). *Cyclic Viscoplasticity of High Density Polyethylene: Experiments and Modeling*. Computational Materials Science, Vol 39, pp 465-480.

Elleuch, R., and Taktak, W. (2006). *Viscoelastic Behavior of HDPE Polymer using Tensile and Compressive Loading*. Journal of Materials Engineering and Performance, Vol 15, pp 111-116.

FAO, (2004). The State of World Fisheries and Aquaculture 2004. FAO Fisheries Department, Food and Agriculture Organization of the United Nations. Vialle delle Terme di Caracalla, Rome, Italy. P 147.

Faltinsen, O.M., (1990). Sea Loads on Ships and Offshore Structures. Cambridge University Press. New York, 328 p.

Fenton, J. (1985). *A Fifth Order Stokes Theory for Steady Waves*. Journal of Waterway, Port and Coastal and Ocean Engineering. Vol 111, No. 2, pp 216 – 234.

Findlan, S., (2007). Fatigue and Capacity Testing of High Density Polyethylene Pipe Material. EPRI, Palo Alto, CA: Technical Report 1014902.

Fredriksson, D.W., E. Muller, M.R. Swift, I. Tsukrov and B. Celikkol, (1999). *Offshore Grid Mooring/Net Pen System: Design and Physical Model Testing*. OMAE99-3064. In: Offshore Mechanics and Arctic Engineering '99. Proceedings of the 18th International Conference. St. John's, Newfoundland Canada: ASME.

Fredriksson, D.W., Swift, M.R., Muller, E., Baldwin, K. and Celikkol, B., (2000). *Open Ocean Aquaculture Engineering: System Design and Physical Modeling*. Mar. Tech. Soc. J. 34 (1), 41-52.

Fredriksson, D.W, (2001). *Open Ocean Fish Cage and Mooring System Dynamics*. Ph.D. Dissertation submitted to the University of New Hampshire in partial fulfillment of the Engineering Systems Design Program. Durham, NH.

Fredriksson, D.W., M.R. Swift, I. Tsukrov, J.D. Irish and B. Celikkol, (2003). *Fish Cage and Mooring System Dynamics using Physical and Numerical Models with Field Measurements*. Aqua Eng. Vol 27, (2), 117-270.

Fredriksson, D.W., J. DeCew, M.R. Swift, I. Tsukrov, M.D. Chambers, and B. Celikkol, (2004). *The Design and Analysis of a Four-Cage, Grid Mooring for Open Ocean Aquaculture*. Aqua. Eng. Vol 32 (1) pp 77-94.

Fredriksson, D.W., M.R. Swift, O. Eroshkin, I. Tsukrov, J.D. Irish and B. Celikkol, (2005a). *Moored Fish Cage Dynamics in Waves and Currents*. IEEE Journal of Oceanic Engineering, Vol 30, No. 1, 28-36.

Fredriksson, D.W., M.D. Chambers, J.C. DeCew, B. Fullerton, M.R. Swift, G. Rice, and B. Celikkol., (2005b). *An Open Ocean Aquaculture System for Submerged Operations in New England*. Bull. Aquacul. Assoc. Canada. (103-3). pp. 21-30.

Fredriksson, D.W., M.R. Swift, O. Eroshkin, I. Tsukrov, J.D. Irish and B. Celikkol, (2005c). *Moored Fish Cage Dynamics in Waves and Currents*, IEEE Journal of Oceanic Engineering, Vol 30, No. 1, 28-36.

Fredriksson, D.W., DeCew, J.C., Tsukrov, I., Swift, M.R., Irish, J.D., (2007a). *Development of Large Fish Farm Numerical Modeling Techniques with in-situ Mooring Tension Comparisons*. Aquacultural Engineering 36, 137–148.

Fredriksson, D.W., J. DeCew, I. Tsukrov, (2007b). *Development of Structural Modeling Techniques for Evaluating HDPE Plastic Net Pens used in Marine Aquaculture*. Ocean Engineering. Vol 34, p 2124-2137.

Fredriksson, D., Tsukrov, I., Hudson, P., (2008). *Engineering Investigation of Design Procedures for Closed Containment Marine Aquaculture Systems*. Aquaculture Engineering, Vol 2-3, pp. 91 – 102.

Fullerton, B. Swift, M.R., Boduch, S., Eroshkin, O. and G. Rice, (2004). *Design and Analysis of an Automated Feed Buoy for Submerged Cages*. Aqua. Eng. Vol 95 (1) pp. 95-111.

Garrett, D.L, (1982). *Dynamic Analysis of Slender Rods*. In Proceedings of the 1st International OMAE Conference, Dallas, pp 127-132.

Gensler, R., Plummer, C., Grerin, C., Kausch, H., (2000). *Influence of the Loading Rate on the Fracture Resistance of Isotatic Polypropylene and Impact Modified Isotatic Polypropylene*. Polymer, Vol 41, pp 3809-3819.

Ghazanfari, A., Emani, S., Panigrahi, S., Tabil, L., (2008). *Thermal and Mechanical Properties of Blends and Composites from HDPE and Date pits Particles*. Journal of Composite Materials, Vol 42, no 1, pp 77-89.

Gignoux, H., and Messier, R. (1999). *Computational Modeling for Fin-Fish Aquaculture Net Pens*. Ocean Engineering International, Vol 3, No. 1, pp. 12-22.

Gloor, W., (1958). *Service Test Data on High Density Polyethylene*. Modern Plastics, report number D542924.

Gobat, J., and Grosenbaugh, M., (2001). *A Simple Model for Heave-induced Dynamic Tension in Catenary Moorings*. Applied Ocean Research, Vol 23, pp 159-174.

Goda, Y., (1985). Random Seas and the Design of Maritime Structures. University of Tokyo Press, Japan.

Gosz, M., Kestler, K., Swift, M.R. and Celikkol, B., (1996). *Finite Element Modeling of Submerged Aquaculture Net-Pen Systems*. In: Open Ocean Aquaculture. Proceedings of an International Conference. May 8-10, 1996, Portland, ME, Marie Polk, Editor. NH/ME Sea Grant College Program Rpt #UNHMP-CP-SG-96-9. pp.523-554.

Goudey, C.A., Loverich, G., Kite-Powell, H., and Costa-Pierce, B.A., (2001). *Mitigating the Environmental Effects of Mariculture through Single-Point Moorings (SPMs) and Drifting Cages*. ICES J Mar Sci. 58, pp 497-503.

Goudey, C., Boaz, T., Bridger, C., (2003). *The Design, Installation and Performance of a Single Point Mooring for an Offshore Cage*. In Bridger (Ed.), Open Ocean Aquaculture: From Research to Commercial Reality. Baton Rouge, LA, pp 191-195.

Goudey, C, (2004). Cage and Mooring Specifications for the ASA 2 m x 4.5 m x 7 m Prototype Offshore Cage, report prepared for the American Soybean Association.

Greene, J.K. and R.E. Grizzle, (2007). *Successional Development of Fouling Communities on Open Ocean Aquaculture Fish Cages in the Western Gulf of Maine, USA*. Aquaculture 262:289-301.

Grizzle, R.E., Ward, L.G., Langan, R., Schnaittacher, G.M, Dijkstra, J.A. and J. Adams, (2003). *Environmental Monitoring at an Open Ocean Aquaculture Site in the Gulf of Maine: Results*

for 1997 – 2000. in C.J. Bridger and B.A. Costa-Pierce, editors. Open Ocean Aquaculture: From Research to Commercial Reality. The World Aquaculture Society, Baton Rouge, Louisiana, United States. pp. 105 - 117.

Haritos, N., and He, D.T., (1992). *Modeling the Response of Cable Elements in an Ocean Environment*. Finite Elements in Analysis and Design, Vol 19, pp 19-32.

Hilburger, M and Nemeth, M.m, (2005). Application of Video Image Correlation Techniques to the Space Shuttle External Tank Foam Materials. NASA/TM-2005-213944.

Hillmansen, S., Hobeika, S., Haward, N., Leevers, P., (2000). *The Effect of Strain Rate, Temperature and Molecular Mass on the Tensile Deformation of Polyethylene*. Polymer Engineering and Science, Vol 40, no 2, pp 481-489.

Hoerner, S., (1965). Fluid Dynamic Drag. Published by the author, Midland Park, N.

Horton, J., (2008). *Dynamic Responses of a 20-ton Capacity Feed Buoy in an Open Ocean Environment*. M.S. Thesis, Ocean Engineering, University of New Hampshire, Durham, NH.

Howell, W.H. and M.D. Chambers, (2005). *Growth Performance and Survival of Atlantic Halibut (Hippoglossus hippoglossus) Grown in Submerged Net Pens*. Bull. Aqua. Assoc. Canada, 9:35-37.

Huang, C., Tang, H., Liu, J., (2006). *Dynamical Analysis of Net Cage Structures for Marine Aquaculture: Numerical Simulation and Model Testing*. Aquacultural Engineering, Vol 35, pp 258-270.

Huang, C.C., Tang, H.J., Pan, J.Y., (2009). *Numerical Modeling of an SPM Cage with a Frontal Rigid Frame*. IEEE J Oceanic Eng. 34, 2, pp 113-122.

Irish, J.D., Carroll, M., Singer, R., Newhall, A., Paul, W., Johnson, C., Witzell, N., Rice, G., Fredriksson, D.W., (2001). Instrumentation of Open Ocean Aquaculture Monitoring. Woods Hole Oceanographic Institution, Technical Report WHOI-2001-15, p. 95.

Irish, J.D. and D.W. Fredriksson, (2003). *Telemetering Environmental Monitoring Buoy and Mooring*. Proc. Oceans '03, 2589-2595, San Diego.

Irish, J.D. and D.W. Fredriksson, (2003). *Compliant Mooring Technology to Separate Buoy Motion from In-Line Current Meter Observations*. Proc. 7th Current Measurements Technology Conf, 165-170, 13-15.

Irish, J.D. and D.W. Fredriksson, and S. Boduch, (2004). *Environmental Monitoring Buoy and Mooring with Telemetry*. Sea Technology, 45(5), 14-19.

Irish, J.D., M. Carroll, R. Singer, A. Newhall, W. Paul, C. Johnson, N. Witzell, G. Rice and D.W. Fredriksson, (2001). Instrumentation of Open Ocean Aquaculture Monitoring. Woods Hole Oceanographic Institution, Technical Report WHOI-2001-15. p. 95.

Irish, J., S. Boduch, (2006). *Aquaculture Feed Buoy Control - Part 2: Telemetry, Data Handling and Shore-Based Control*. Proc. Oceans '06, Boston.

Issacson M, and Cheung, K., (1994). *Correction Factors for Nonlinear Run-up and Wave Forces on a Large Cylinder*. Canadian Journal of Civil Engineering, Vol 21, pp 762-769.

Janson, L.-E. (2003). Plastic Pipes for Water Supply and Sewage Disposal. 4th Ed., Borealis, Majornas CopyPrint AB, Stockholm, Sweden.

Jo, N., Takahara, A., Kajiyama, T., (1993). *Analysis of Fatigue Behavior of High Density Polyethylene Based on Nonlinear Viscoelastic Measurement under Cyclic Fatigue*. Polymer Journal, Vol 25, no 7, pp 721-729.

Joseph, S.H., (2005). *A Method for Modeling the Nonlinear Viscoelastic Response of Polymers*. Mechanics of Time Dependant Materials, Vol 9, pp 35-69.

Kestler, K., (2004). *Development of Special Finite Elements for Dynamic Analysis of Flexible Structures in the Moving Fluid Environment*. M.S. Thesis, Ocean Engineering, University of New Hampshire, Durham, NH, 164p.

Khan, F., (2006). *Loading History Effects on the Creep and Relaxation Behavior of Thermoplastics*. ASME, Vol 128, pp 564-571.

Klompen, E., (2005). *Mechanical Properties of Solid Polymers: Constitutive Modeling of Long and Short Term Behavior*. University Press Facilities, Eindhoven, The Netherlands.

Kurgan, C., (2003). *Fish Cage and Multiple Mooring Systems Finite Element Modeling*. Master's Degree Thesis submitted in partial requirement for the Mechanical Engineering degree program. University of New Hampshire, Durham, NH.

Kwon, H., Jar, P., (2008). *On the Application of FEM to Deformation of High Density Polyethylene*. International Journal of Solids and Structures, Vol 45, pp 3521-3543.

Lader, P.F and A. Fredheim., (2003). *Modeling of Net Structures Exposed to Three Dimensional Waves and Current*. Pages 177-189 in C.J. Bridger and B.A. Coasta-Pierce, editors. *Open Ocean Aquaculture: From Research to Commercial Reality*. The World Aquaculture Society, Baton Rouge, Louisiana, United States.

Lader, P.F and A. Fredheim., (2006). *Dynamic Properties of a Flexible Nets in Waves and Current – A Numerical Approach*. Aqua. Eng. Vol 35, pp 228-238.

Lader, P., Jensen A., Sveen J.K., Fredheim A., Enerhaug b., Fredriksson F., (2007). *Experimental Investigation of Wave Forces on Net Structures*. Appl Ocean Res. 29, pp 112–127.

Lai, J., and Bakker, A., (1995). *Analysis of the Non-linear Creep of High Density Polyethylene*. Polymer, Vol 36, No 1, pp 93-99.

Lai, J., Bakker, A., (1995). *An Integral Constitutive Equation for Nonlinear Plasto-viscoelastic Behavior of High Density Polyethylene*. Polymer Engineering and Science, Vol 35, No 17, pp 1339-1347.

Langan, R., (2004). *Balancing Marine Aquaculture Inputs and Extraction: Combined Culture of Finfish and Bivalve Molluscs in the Open Ocean*. Bulletin of the Fisheries Research Agency of Japan. Supplement No.1, 51-58, 2004.

Lee, C.-H., (1995). WAMIT theory manual. MIT Report 95-2, Department of Ocean Engineering. (www.WAMIT.com).

Lee, H., Kim, S., (2006). *A Comparison of Several Wave Spectra for the Random Wave Diffraction by a Semi-infinite Breakwater*. Ocean Engineering, Vol 33, pp. 1954-1971.

Lee, Chun-Woo, Lee, J., Cha, B., Kim, H., Lee, J, (2004). *Physical Modeling for Underwater Flexible Systems Dynamic Simulation*. Ocean Engineering, Vol 32.

Lee, H.H. and Pei-Wen, W., (2000). *Dynamic Behavior of Tension-leg Platform with Net-cage System subjected to Wave Forces*. Ocean Engineering, Vol. 28, pp. 179-200.

Li, Yu-Cheng, Zhao, Y., Gui, F., Teng, B., (2006). *Numerical Simulation of the Hydrodynamic Behavior of Submerged Plane Nets in Current*. Ocean Engineering, Vol 33.

Loland, G., (1991). *Current Forces on and Flow through Fish Farms*. Ph.D. Thesis, Division of Marine Hydrodynamics at the Norwegian Institute of Technology, p. 149.

Loverich G., and J. Forster, (2000). *Advances in Offshore Cage Design using Spar Buoys*. Mar Technol Soc J. 34, 1, pp 18-28.

Merah, N., Saghir, F., Khan, Z., Bazoune, A., (2006). *Effect of Temperature on Tensile Properties of HDPE Pipe Material*. Plastics, Rubber and Composites, Vol 35, no 5, pp 226-230.

Morison, J.R., Johnson, J.W., O'Brien, M.P., Schaaf, S.A., (1950). *The Forces Exerted by Surface Waves on Piles*. Petroleum Transactions, American Institute of Mining Eng.

Nakayasu, H., Markovitz, H., Plazek, D., (1961). *The Frequency and Temperature Dependence of the Dynamic Mechanical Properties of a High Density Polyethylene*. Transactions of the Society of Rheology, Vol 5, no 1, pp 261-283.

Ogorkiewicz, R. M., ed., (1970). Engineering Properties of Thermoplastics. Imperial Chemical Industries Ltd., Plastics Division, Willey, New York.

Ohashi, F., Hiroe, T., Fujiwara, K., Matsue, H., (2002). *Strain Rate and Temperature Effects on the Deformation of Polypropylene and its Simulation under Monotonic Compression and Bending*. Polymer Engineering and Science, Vol 42, no 5, pp 1046-1055.

Ollick, A.M., Al-Amir, A.M., (2003). *Weathering Effects on Mechanical Properties of Low and High Density Polyethylene Pipes used in Irrigation Networks*. Alexandria Engineering Journal 42 (6), 659–667.

Ozbay, M., (1999). *Finite Element Analysis of Offshore Net Pen / Mooring Systems*. Master's Degree Thesis submitted in partial requirement for the Mechanical Engineering Degree program. University of New Hampshire, Durham, NH.

Palczynski, M., (2000). *Fish Cage Physical Modeling.* Master's Degree Thesis submitted in partial requirement for the Ocean Engineering program, University of New Hampshire, Durham, NH.

Pan, B., Xie, H., Wang, Z., Qian, K., Wang, Z., (2008). *Study on Subset Size Selection in Digital Image Correlation for Speckle Patterns*. Optics Express, vol 16, No 10, pp 7037-7048.

Patursson, O., (2008). *Flow Through and Around Fish Farming Nets*. Ph.D. Dissertation submitted to the University of New Hampshire in partial fulfillment of the Ocean Engineering Degree program. University of New Hampshire, Durham, NH, 146p.

Patursson, O., Swift, M.R., Tsukrov, I., Simonsen, K., Baldwin, K., Fredriksson, D., Celikkol, B., (2010). *Development of a Porous Media Model with Application to Flow through and around a Net Panel*. Ocean Engineering, Vol 37, 2-3, pp 314-324.

Parsons, M., Stepanov, V., Hiltner, A., Baer, E., (1999). *Correlation of Stepwise Fatigue and Creep Slow Crack Growth in High Density Polyethylene*. Journal of Materials Science, Vol 34, pp 3315-3326.

Patlazhan, S., Hizoum, K., Remond, Y., (2008). *Stress Strain Behavior of High Density Polyethylene below the Yield Point: Effect of Unloading Rate*. Polymer Science, Vol 50, No 5, pp 507-513.

Plummer, C., Goldberg, A., and Ghanem, A., (2001). *Micromechanisms of Slow Crack Growth in Polyethylene under Constant Tensile Loading*. Polymer, Vol 42, No 23, pp 9551-9564.

Qi, F., Huo, L., Jing, H., (2005). *Study on Fracture Behaviors of High Density Polyethylene Pipe Material based on Local Approach*. Advanced Materials Research, Vol 9, pp 101-108.

Rahman, M., (1998). *Nonlinear Hydrodynamic Loading on Offshore Structures*. Theoretical Computational Fluid Dynamics, Vol 10, pp. 323-347.

Rao, S., (2004). Mechanical Vibrations. Pearson Education, Inc. Upper Saddle River, NJ, pp 1078.

Rice, G.A., M.D. Chambers, M. Stommel, O. Eroshkin., (2003). *The Design, Construction and Testing of the University of New Hampshire Feed Buoy* in C.J. Bridger and B.A. Costa-Pierce, editors. Open Ocean Aquaculture: From Research to Commercial Reality. The World Aquaculture Society, Baton Rouge, Louisiana, United States p. 197-203.

Rice, G., (2006). *Investigation of a Submerged Four-Bay Mooring System for Aquaculture*. M.S. Thesis, Ocean Engineering, University of New Hampshire, Durham, NH, 96p.

Rillahan, C., M.D. Chambers, W. H. Howell and W.H. Watson III., (2011). *The Behavior of Cod (Gadus morhua) in an Offshore Aquaculture Net Pen*. J. Aquaculture 310, 361-368.

Rillahan, C., M.D. Chambers, W.H. Watson and W. H. Howell, (2009). *A Self-Contained System for Observing and Quantifying the Behavior of Atlantic cod, Gadus morhua, in an Offshore Aquaculture Cage*. J. Aquaculture. 293, 49-56.

Risso, A., (2007). *Structural Analysis of a Small Volume Offshore Aquaculture Cage System Utilizing Numerical Modeling and Scaled Physical Testing*. M.S. Thesis, Ocean Engineering, University of New Hampshire, Durham, NH, 158p.

Santamaria, J., C. Monahan, J. Scott, B. Celikkol, D. Fredriksson, J. DeCew, (2007). Development of a Submersible Fish Cage for Open Ocean Aquaculture. Small Business Innovation Research, SBIR Final report.

Smith, T., (1977). *Strength of Elastomers – A Perspective*. Polymer Engineering and Science, Vol 17, No 3, pp 129-143.

Stokes, G. G., (1851). *On the Effect of the Internal Friction of Fluids on the Motion of Pendulums*. Cambridge Philos. Trans. 9, 8-106.

Suhey, J.D., Kim, N.H. and C. Niezrecki, (2005). *Numerical Modeling and Design of Inflatable Structures – Application to Open Ocean Aquaculture Cages*. Aquacultural Engineering. Vol 33, Issue 4, pp 285-303.

Sumer, B., and Fredsoe, J., (1997). Hydrodynamics Around Cylindrical Structures. World Scientific Publishing Company, Singapore, 527 p.

Swift, M.R., Palczynski, M., Kestler, K., Michelin, D., Celikkol, B., and Gosz, M., (1998). *Fish Cage Physical Modeling for Software Development and Design Applications*. Proceedings of the 26th U.S.-Japan Aquaculture Symposium Nutrition and Technical Development of Aquaculture. Durham, NH: University of New Hampshire, pp. 199-206.

Tsukrov, I., Ozbay,M., Fredriksson, D.W., Swift, M.R., Baldwin, K., Celikkol, B., (2000). *Open Ocean Aquaculture Engineering: Numerical Modeling*. Mar. Tech. Soc. J., vol. 34, no. 1. Washington DC, pp 29–40.

Tsukrov, I., Eroshkin, O., Fredriksson, D.W., Swift, M.R., Celikkol, B., (2003). *Finite Element Modeling of Net Panels using Consistent Net Element*. Ocean Eng. 30, 251–270.

Turmelle, C., Swift, M.R., Celikkol, B., Chambers, M., DeCew., J., (2009). *Design of a 20-ton Capacity Finfish Aquaculture Buoy.* World Aquaculture, Vol 40, No 2, pp 35-38, 69.

Van der Wal, A., and Gaymans, R., (1999). *Polypropylene-Rubber Blends: 3. The Effect of the Test Speed on the Fracture Behavior*. Polymer, Vol 40, pp 6045-6055.

Vikestad, K., Lien, E., (2005). *Bending Stiffness of a Clamps-connected 2-rings PE Fish Cage Collar*. In: Proceedings of the 12th International Congress of the International Maritime Association of the Mediterranean *(IMAM 2005)*, Vol. 2, Lisboa, Portugal, pp. 1293–1299.

Wang, X.K., Tan., S.K., (2008). *Comparison of Flow Patterns in the Near Wake of a Circular Cylinder and a Square Cylinder placed near a Plane Wall*. Ocean Engineering, Vol 35, pp 458-472.

Webster, W.C., (1995). *Mooring Induced Damping*. Ocean Engineering, Vol 22, No. 6, pp 571-591.

White, F.M., (1999). Fluid Mechanics. 4th ed. McGraw-Hill, Boston, MA.

Zahedi, M., Ahmadi, M., Nekoomanesh, M., (2008). *Influence of Microstructure and Morphology on Stress-Strain Behavior of Commercial High Density Polyethylene*. Journal of Applied Polymer Science, Vol 110, pp 624-631.

Zhan, J.M, Jia, X., Li., Y., Sun, M., Guo, G., Hu, Y, (2005). *Analytical and Experimental Investigation of Drag on Nets of Fish Cages*. Aqua. Eng. Vol 35, pp 91-101.

Zhang, C., and Moore, I. D., (1997). *Nonlinear Mechanical Response of High Density Polyethylene. Part I: Experimental Investigation and Model Evaluation*. Polym. Eng. Sci., 37, pp. 404–413.

Zhang, C., and Moore, I. D., (1997) *Nonlinear Mechanical Response of High Density Polyethylene. Part II: Uniaxial Constitutive Modeling*. Polym. Eng. Sci., 37, pp. 413–420.

Zhang, C., Moore, I., (1998). *Nonlinear Finite ELement Analysis for Thermoplastic Pipes*. Transportation Research Record 1624, pp 225-230.

Zienkiewicz, O.C. and Cheung, Y.K., (1967). The Finite Element Method in Continuum and Structural Mechanics. McGraw Hill, 272 pp.

Zong, Z., Hao, S., Zhao, Y., Dong, G., (2008). *In-plane Hydroelastic Response of a Circular Ring in Water Waves*. Applied Ocean Research. 30(3), p 208-214.

APPENDIX A: MODIFIED AQUA-FE SUBROUTINES

FINITE ELEMENT ANALYSIS PROGRAM (FEAP)

The core Aqua-FE finite element code is written in FORTRAN. It is based on an early version of the Finite Element Analysis Program (FEAP). FEAP was originally created as a general purpose finite element program for research and educational use. The source code was written by R.L. Taylor at the University of California at Berkley (Zienkewiech and Taylor, 1988). Aqua-FE's fluid-structure interaction capabilities were added as one of the modules (Gosz et al., 1997; Swift et al., 1998).

A problem solution in FEAP is constructed using a command language concept in which the solution algorithm is written by the user. FEAP has built-in commands for linear and non-linear applications in structural mechanics, fluid mechanics, heat transfer, and other areas. Both steady state and transient problems can be analyzed. Users also may add new routines for mesh generation and manipulation; model element or material description; new command language statements to meet specific application requirements; and plot outputs for added graphical display.

The program contains a general element library. Elements are available to model one-, two- or three-dimensional problems in linear or non-linear solid mechanics. Elements provide capability to generate mass and geometric stiffness matrices for structural problems and to

compute output quantities associated with each element (e.g., stress, strain), including capability of projecting these quantities to nodes to permit graphical outputs of result contours.

Users also may add an element to the system by writing and linking a single module to the FEAP system (the approach taken, for example, with the spherical element).

OPT File Description

As mentioned in Chapter 2, Aqua-FE simulation requires data on mesh geometry, element and nodal connectivity, material properties and fluid loading information. The material properties and fluid loading information is provided in the **.opt* file. The file also relays FORTRAN MACRO controls to various subroutines to handle mesh and additional input data. An example of an **.opt* file s shown below. Descriptions of the MACRO's in the **.opt* file and the allocation of columns for data input by the FORTRAN program can be found in Keslter 2004.

```
FEAP ** Example *.opt file**
  260  412   19    3    3    2    1    1    1

MP01
filename.out

MATE
    1    1                                                  Truss element
       0     9.8062         1 1.158E+03 1.172E+09 6.158E-02
    2    2                                                 Sphere element
       0     9.8062         1 9.058E+02 6.158E-02
    3    4                                                  Net element
       0     9.8062         1 1.025E+03 1.833E+09 3.142E-06  69
    4    5                                               Non-linear element
       0     9.8062         1 7.120E+02 1.026E-02 4.8E-01
       3
       1.2e0, 7.452e5
       1.55e0, 1.692e6
       1.7e0, 2.919e6
     5    3                                               Stiffener element
       0     9.8062         1 1.025E+03 2.500E+11 5.000E-07

FDAT
```

```
analysis    itypsw =    4
sub. check    isub =    1
print check isubpr =    1
mat. type   noplot =    5
updt drag coef. ic =    1
               cdn = 1.200E+00
               cdt = 0.010E+00
                cm = 1.000E+00
               rho = 1.025E+03
             depth = 2.400E+01
            vconfx = 1.000E+00
            vconfz = 0.000E+00
            vgrdfx = 0.000E+00
            vgrdfz = 0.000E+00
               vis = 1.130E-03
wave loading iwave =    1
no. freq.    nfreq =    1
1:   height, length  1.30,30.531

END
MRCA   1
PROF
MACR
TOL           1.E-04
DT              0.01
PRIN
PARA             .25        .5
LOOP            40000
TIME
PRED
LOOP               25
FORM
TANG
SOLV
CORR
CEQS
NEXT
MRCB
HIST STRE         343         1
HIST DISP          43         1
HIST DISP          43         2
HIST DISP          43         3
NEXT
END
MRCC
STOP
```

Aqua-FE Code Modifications

This section presents the Aqua-FE code modifications implemented in the dissertation. The following MACRO's in the subroutine *pmesh* were modified to support the component shadowing feature, implementation of Stokes waves, and incorporation of the proper truss element drag coefficients at high Reynolds Numbers:

- FDAT
- WETTEST
- SURFELEV
- AVCURR
- UPDCD

The code utilized to implement these features are shown in the following sections.

MACRO - FDAT

```
C---- MACRO 'FDAT'
C---- READ IN PARAMETERS FOR FLUID LOADING
C---- This part was heavily modified to accept multiple fluid loadings
C---- Most things changed to a multi-dimensional array
C---- The if and else statements have some repeated parts and can be
C---- cleaned up... Still in debugging(4/15/05) mode so haven't gotten
C---- to it.
   25 CONTINUE
      LOADF=1
      PI = 3.141592653589793D0
      READ(1,4500)ITYPSW,ISUB,ISUBPR,NOPLOT,IC,
     +    CDN,CDT,CM,RHO,DEPTH,VCONFX,VCONFZ,VGRDFX,VGRDFZ,VIS
C---- Sets the default number of fluid loadings to 1.
      NUMLOAD = 1
C
C---- The following if statement will process either the *.wc file
C---- or if only 1 fluid loading, the standard way (else part)
C---- The *.wc file is generated in the AquaFE Editor code written in
C---- Python
      IF (ITYPSW .GT. 4) THEN
            ITYPSW=4
            READ (1,4510) WCFILENAME
            OPEN(UNIT = 37,FILE=WCFILENAME)
            IWAVE=0
            DO 481 KK = 1,25
```

```
                NFREQ(KK)= 0
C                     WRITE(6,*) 'NFREQ KK values are next'
C                      WRITE(6,'(I5)') NFREQ(KK)
481             CONTINUE
            READ (37,4601) CDUM
C           WRITE(6,'(A20)') CDUM
                READ (37,'(A4)') BLANK
            READ (37,2747) NUMLOAD
C           WRITE(6,'(I5)') NUMLOAD
            READ (37,'(A4)') BLANK
C
            DO 471 II=1,NUMLOAD
C                   WRITE(6,'(I5)') II
                              READ (37,'(A4)') BLANK
                  DO 410 I=1,100
C                   WRITE(6,*) 'In do loop'
                    READ (37,4610) NW(II),H(I,II),WAVEL(I,II),
     +                        PHI(I,II)
                    IF(WAVEL(I,II) .EQ. 0.0) GOTO 411
C
C                   WRITE(6,'(I5)') NW(II)
C                   WRITE(6,'(G11.4)') H(I,II)
C                   WRITE(6,'(G11.4)') WAVEL(I,II)
C
                    IWAVE=1
                    NFREQ(II)=NFREQ(II)+1
C                   WRITE(6,'(I5)') NFREQ(II)
410               CONTINUE
411                NCURR(II)=0
                   READ (37,'(A4)') BLANK
                   DO 420 I=1,100
                         READ (37,4610) NC(II),CURPROFD(I,II),
     +                         CURPROFX(I,II),CURPROFZ(I,II)
                         IF(NC(II) .EQ. 99) GOTO 421
C
                         WRITE(6,*) '---------------'
                         WRITE(6,'(I5)') NC(II)
                         WRITE(6,'(G11.4)') CURPROFD(I,II)
                         WRITE(6,'(G11.4)') CURPROFX(I,II)
                         WRITE(6,'(G11.4)') CURPROFZ(I,II)
                         WRITE(6,*) '---------------'
C
                         NCURR(II)=NCURR(II)+1
                         WRITE(6,*) '---------------'
                         WRITE(6,*) 'NCURR next'
                         WRITE(6,'(I5)') NCURR(II)
                         WRITE(6,*) '---------------'
420                 CONTINUE
421                 IF(NCURR(II) .EQ. 0) THEN
                         NCURR(II)=1
                         CURPROFD(1,II)=DEPTH
                         CURPROFX(1,II)=0.0
                         CURPROFZ(1,II)=0.0
                         END IF
C
      WRITE(6,4700)ITYPSW,ISUB,ISUBPR,NOPLOT,IC,
     +       CDN,CDT,CM,RHO,DEPTH,VIS,
```

```
     +        IWAVE,NFREQ(II)
C
              VFXAVE(II)=(DEPTH-CURPROFD(1,II))*CURPROFX(1,II)
              VFZAVE(II)=(DEPTH-CURPROFD(1,II))*CURPROFZ(1,II)
                    WRITE(6,*) '---------------'
                    WRITE(6,*) 'vfxave and vfzave'
                    WRITE(6,'(G11.4)') VFXAVE(II)
                    WRITE(6,'(G11.4)') VFZAVE(II)
                    WRITE(6,*) '---------------'
C
              IF(NCURR(II).GT.1) THEN
                    DO 455 I=2, NCURR(II)
                          VFXAVE(II)=VFXAVE(II)+(CURPROFD(I-1,II)-
     +                    CURPROFD(I,II))*(CURPROFX(I-1,II)+
     +                    CURPROFX(I,II))
     +                    /2.D0
                          VFZAVE(II)=VFZAVE(II)+(CURPROFD(I-1,II)-
     +                    CURPROFD(I,II))*(CURPROFZ(I-1,II)+
     +                    CURPROFZ(I,II))
     +                    /2.D0
                    WRITE(6,*) '---------------'
                    WRITE(6,*) 'vfxave and vfzave'
                    WRITE(6,'(G11.4)') VFXAVE(II)
                    WRITE(6,'(G11.4)') VFZAVE(II)
                    WRITE(6,*) '---------------'
455                 CONTINUE
              END IF
C
              VFXAVE(II)=VFXAVE(II)+CURPROFD(NCURR(II),II)*
     +        CURPROFX(NCURR(II),II)
              VFZAVE(II)=VFZAVE(II)+CURPROFD(NCURR(II),II)*
     +        CURPROFZ(NCURR(II),II)
                    WRITE(6,*) '---------------'
                    WRITE(6,*) 'vfxave and vfzave'
                    WRITE(6,'(G11.4)') VFXAVE(II)
                    WRITE(6,'(G11.4)') VFZAVE(II)
                    WRITE(6,*) '---------------'
C
              VFXAVE(II)=VFXAVE(II)/DEPTH
              VFZAVE(II)=VFZAVE(II)/DEPTH
C
              WRITE(6,*) '---------------'
                    WRITE(6,*) 'vfxave and vfzave'
                    WRITE(6,'(G11.4)') VFXAVE(II)
                    WRITE(6,'(G11.4)') VFZAVE(II)
                    WRITE(6,*) '---------------'
C
              WAMP(II)=0.D0
              IF (IWAVE.EQ.1) THEN
              DO 460 I=1,NFREQ(II)
                    WRITE(6,4800)I,H(I,II),WAVEL(I,II),phi(I,II)
                    WAVEK(I,II)=2.D0*PI/WAVEL(I,II)
                    OMEGA(I,II)=VFXAVE(II)*WAVEK(I,II)+
     +                    DSQRT(G*WAVEK(I,II)*
     +                    DTANH(WAVEK(I,II)*DEPTH))
                    FACTOR(I,II)=OMEGA(I,II)*H(I,II)/
     +                    (2.D0*DSINH(WAVEK(I,II)*DEPTH))
```

```
                              WAMP(II)=WAMP(II)+H(I,II)/2.D0
460         CONTINUE
            ENDIF


C----------beginning of updates 11/25/08 by JCD
c----------thus update will incorporate stokes waves
c----------if iwave = 2
c----------if stokes, only 1 phase allowed
c----------wavek, omega did not change
            IF (IWAVE.EQ.2) THEN
            DO 463 I=1,NFREQ(II)
C
            IF (I.GT.1) THEN
                  WRITE(6,*) '*ERROR* MULTIPLE WAVE FREQUENCIES NOT
ALLOWED'
                  GOTO 666
            ENDIF
C
                  WRITE(6,4800)I,H(I,II),WAVEL(I,II),phi(I,II)
                  WAVEK(I,II)=2.D0*PI/WAVEL(I,II)
                  OMEGA(I,II)=VFXAVE(II)*WAVEK(I,II)+
     +                  DSQRT(G*WAVEK(I,II)*
     +                  DTANH(WAVEK(I,II)*DEPTH))
                  FACTOR(I,II)=OMEGA(I,II)*H(I,II)/
     +                  ((DSINH(WAVEK(I,II)*DEPTH))**4)
                  WAMP(II)=WAMP(II)+(H(I,II)/2.D0)+
     +                  (H(I,II)**2)*WAVEK(I,II)*
     +                  (DCOSH(WAVEK(I,II)*DEPTH)/
     +                  (16.D0*(DSINH(WAVEK(I,II)*DEPTH)**3)))*
     +                  (2.D0+DCOSH(2.D0*WAVEK(I,II)*DEPTH))
463         CONTINUE
            ENDIF
C----------end of updates 11/25/08 by JCD
C----------
C----------

            WRITE(6,4810) NCURR(II)
            DO 470 I=1,NCURR(II)
                  WRITE(6,4820) I, CURPROFD(I,II), CURPROFX(I,II),
     +                  CURPROFZ(I,II)
470         CONTINUE
            WRITE(6,4900)
            READ (37,'(A4)') BLANK
471   CONTINUE
C
C----- The else processes the fluid loading only if no *wc file...
C
            ELSE
                  II = 1
C                 WRITE(6,*) '---------------'
C                 WRITE(6,'(I5)') II
C                 WRITE(6,*) '---------------'
                  NCURR(II)=2
                  CURPROFD(1,II)=DEPTH
                  CURPROFX(1,II)=VCONFX+VGRDFX*DEPTH
                  CURPROFZ(1,II)=VCONFZ+VGRDFZ*DEPTH
```

```
                CURPROFD(2,II)=0.0
                CURPROFX(2,II)=VCONFX
                CURPROFZ(2,II)=VCONFZ
                READ(1,4505) IWAVE,NFREQ(II)
C               WRITE(6,'(I5)') IWAVE
C               WRITE(6,'(I5)') NFREQ(II)
              DO 451 I=1,NFREQ(II)
C               WRITE(6,'(I5)') NFREQ(II)
                READ(1,4600) H(I,II),WAVEL(I,II),phi(I,II)
C               WRITE(6,'(G11.4)') H(I,II)
C               WRITE(6,'(G11.4)') WAVEL(I,II)
C               WRITE(6,'(G11.4)') phi(I,II)
451           CONTINUE
C
            WRITE(6,4700)ITYPSW,ISUB,ISUBPR,NOPLOT,IC,
     +       CDN,CDT,CM,RHO,DEPTH,VIS,
     +       IWAVE,NFREQ(II)
               WRITE(6,*) 'CHECK fdat ELSE2'
C
            VFXAVE(II)=(DEPTH-CURPROFD(1,II))*CURPROFX(1,II)
            VFZAVE(II)=(DEPTH-CURPROFD(1,II))*CURPROFZ(1,II)
                WRITE(6,*) '---------------'
                WRITE(6,'(G11.4)') VFXAVE(II)
                WRITE(6,'(G11.4)') VFZAVE(II)
                WRITE(6,*) '---------------'
            IF(NCURR(II).GT.1) THEN
                DO 456 I=2, NCURR(II)
                    VFXAVE(II)=VFXAVE(II)+(CURPROFD(I-1,II)-
     +              CURPROFD(I,II))*(CURPROFX(I-1,II)+
     +              CURPROFX(I,II))
     +              /2.D0
                    VFZAVE(II)=VFZAVE(II)+(CURPROFD(I-1,II)-
     +              CURPROFD(I,II))*(CURPROFZ(I-1,II)+
     +              CURPROFZ(I,II))
     +              /2.D0
                WRITE(6,*) '---------------'
                WRITE(6,'(G11.4)') VFXAVE(II)
                WRITE(6,'(G11.4)') VFZAVE(II)
                WRITE(6,*) '---------------'
456             CONTINUE
            ENDIF
            VFXAVE(II)=VFXAVE(II)+CURPROFD(NCURR(II),II)*
     +      CURPROFX(NCURR(II),II)
            VFZAVE(II)=VFZAVE(II)+CURPROFD(NCURR(II),II)*
     +      CURPROFZ(NCURR(II),II)
C
                WRITE(6,*) '---------------'
                WRITE(6,'(G11.4)') VFXAVE(II)
                WRITE(6,'(G11.4)') VFZAVE(II)
                WRITE(6,*) '---------------'
            VFXAVE(II)=VFXAVE(II)/DEPTH
            VFZAVE(II)=VFZAVE(II)/DEPTH
C
                WRITE(6,*) '---------------'
                WRITE(6,'(G11.4)') VFXAVE(II)
                WRITE(6,'(G11.4)') VFZAVE(II)
                WRITE(6,*) '---------------'
```

```
            WAMP(II)=0.D0
            IF (IWAVE.EQ.1) THEN
            DO 461 I=1,NFREQ(II)
                  WRITE(6,4800)I,H(I,II),WAVEL(I,II),phi(I,II)
                  WAVEK(I,II)=2.D0*PI/WAVEL(I,II)
                  OMEGA(I,II)=VFXAVE(II)*WAVEK(I,II)+
     +                  DSQRT(G*WAVEK(I,II)*
     +                  DTANH(WAVEK(I,II)*DEPTH))
                  FACTOR(I,II)=OMEGA(I,II)*H(I,II)/
     +                  (2.D0*DSINH(WAVEK(I,II)*DEPTH))
                  WAMP(II)=WAMP(II)+H(I,II)/2.D0
461         CONTINUE
            ENDIF


C----------beginning of updates 11/25/08 by JCD
c----------thus update will incorporate stokes waves
c----------stokes happens when iwave = 2
c----------if stokes, only 1 phase allowed
c----------wavek, omega did not change
            IF (IWAVE.EQ.2) THEN
            DO 464 I=1,NFREQ(II)
c
            IF (I.GT.1) THEN
                  WRITE(6,*) '*ERROR* MULTIPLE WAVE FREQUENCIES NOT
ALLOWED'
                  GOTO 666
            ENDIF
c
                  WRITE(6,4800)I,H(I,II),WAVEL(I,II),phi(I,II)
                  WAVEK(I,II)=2.D0*PI/WAVEL(I,II)
                  OMEGA(I,II)=VFXAVE(II)*WAVEK(I,II)+
     +                  DSQRT(G*WAVEK(I,II)*
     +                  DTANH(WAVEK(I,II)*DEPTH))
                  FACTOR(I,II)=OMEGA(I,II)*H(I,II)/
     +                  ((DSINH(WAVEK(I,II)*DEPTH))**4)
                  WAMP(II)=WAMP(II)+(H(I,II)/2.D0)+
     +                  (H(I,II)**2)*WAVEK(I,II)*
     +                  (DCOSH(WAVEK(I,II)*DEPTH)/
     +                  (16.D0*(DSINH(WAVEK(I,II)*DEPTH)**3)))*
     +                  (2.D0+DCOSH(2.D0*WAVEK(I,II)*DEPTH))
464         CONTINUE
            ENDIF
C----------end of updates 11/25/08 by JCD


            WRITE(6,4810) NCURR(II)
            DO 473 I=1,NCURR(II)
                  WRITE(6,4820) I, CURPROFD(I,II), CURPROFX(I,II),
     +                  CURPROFZ(I,II)
473         CONTINUE
            WRITE(6,4900)
      ENDIF
C
      GO TO 10
C
```

```
c*****these statements can't be reached so are c'd to prevent
warning*****c
c       INN = 0
c       INE = 0
c       WRITE(JDUMP,1003)INN,INE
c       WRITE(JDUMP,1004)NUMEL,NEN
c       DO 400 I=1,NUMEL
c       WRITE(JDUMP,1005)I,(IX(J,I),J=1,NEN)
c400    CONTINUE
c       WRITE(JDUMP,1003)NUMNP,NDM
c       DO 500 I=1,NUMNP
c       WRITE(JDUMP,1006)I,(X(J,I),J=1,NDM)
c500    CONTINUE
c       DO 600 II=1,NUMEL
c600    WRITE(KDUMP,1007)((X(J,IX(JJ,II)),J=1,NDM),JJ=1,NEN)
c       GO TO 10
c**********************************************************************
***c
c
c
c
C
C---- FORMATS
1000  FORMAT(A4,75X,A1)
1002  FORMAT(16I5)
1003  FORMAT(1X,2I5)
1004  FORMAT(/,1X,2I5)
1005  FORMAT(1X,9I5)
1006  FORMAT(I6,3X,3G15.8)
1007  FORMAT(8F8.4)
2003  FORMAT(/5X,12HMATERIAL SET,I3,17H FOR ELEMENT TYPE,I2,5X,//
     1   10X,49HDEGREE OF FREEDOM ASSIGNMENTS    LOCAL    GLOBAL   /
     2   42X, 6HNUMBER, 4X, 6HNUMBER/(36X,2I10))
2004  FORMAT(A1,20A4//5X,19HMATERIAL PROPERTIES)
2005  FORMAT(A1,20A4//5X,17HNODAL FORCE/DISPL//6X,4HNODE,9(I7,A4,A2))
2006  FORMAT(I10,9E13.3)
2747  FORMAT(I5)
3003  FORMAT(5X,'**WARNING 01** ELEMENT CONNECTIONS NECESSARY TO USE
BLO
     1K IN MACRO PROGRAM')
4500  FORMAT(5(20X,I5,/),9(20X,G10.4,/),20X,G10.4)
4505  FORMAT(20X,I5,/,20X,I5)
4510  FORMAT(20X,A50)
c
ccccccccccc
```

MACRO - WETTEST

```
c*******************************************************************
c*******************************************************************
      SUBROUTINE WETTEST(iwet,surf1,surf2,X1,Y1,Z1,X2,Y2,Z2,time,NUMB,
     +      IX)
      IMPLICIT DOUBLE PRECISION(A-H,O-Z)
c
c---- test if either node of element is below waterline
c---- return wet status and surface elevation at each node
c
      COMMON /FDATA/ G,H(100,25),WAVEL(100,25),WAVEK(100,25),
     +               phi(100,25),OMEGA(100,25),FACTOR(100,25),
     +               DEPTH,VFXAVE(25),VFZAVE(25),CURPROFD(100,25),
     +               CURPROFX(100,25),CURPROFZ(100,25),
     +               CDN,CDT,CM,RHO,VIS,WAMP(25),NCURR(25),
     +               NFREQ(25),IWAVE,ITYPSW,ISUB,ISUBPR,IC
C
      COMMON /CDATA/ NUMNP,NUMEL,NUMMAT,NEN,NEQ,IPR,
     1 NSDM,NQDM,NQUAD,NPRFL
      COMMON /NUMWC/ NUMLOAD
      INTEGER IIII
      DIMENSION IX(4,1)
c
C     WRITE(6,'(I5)') NEN
C     WRITE(6,'(I5)') NUMB
      NEN2 = NEN + 2
C     WRITE(6,'(I5)') NEN2
C     WRITE(6,*) '-----'
C     WRITE(6,'(I5)') IX(1,1)
C     WRITE(6,'(I5)') IX(2,1)
C     WRITE(6,'(I5)') IX(3,1)
C     WRITE(6,'(I5)') IX(4,1)
C     WRITE(6,*) '-----'
C---- The IX is a 4 x 1 array. The +1 is added because index from
python editor
C---- is from 0-9, not 1-10.
C
      IIII = IX(NEN2,1) + 1
C     WRITE(6,'(I5)') IIII
C
      WETMIN=DEPTH-WAMP(IIII)
C     WRITE(6,'(G11.4)') WAMP(IIII)
      WETMAX=DEPTH+WAMP(IIII)
      IF ((Y1.GT.WETMAX) .AND. (Y2.GT.WETMAX)) THEN
            IWET=4
      ELSEIF ((Y1.LT.WETMIN) .AND. (Y2.LT.WETMIN)) THEN
            IWET=3
      ELSE
            eta1=0.d0
        eta2=0.d0
        if (iwave.eq.1) then
                  do 100 i=1,nfreq(IIII)
                        eta1=eta1+h(i,IIII)*dcos(wavek(i,IIII)*X1-
     +                        omega(i,IIII)*time+phi(i,IIII))
                        eta2=eta2+h(i,IIII)*dcos(wavek(i,IIII)*X2-
     +                  omega(i,IIII)*time+phi(i,IIII))
```

```
100               continue
            endif
c

C------- start of UPDATES BY JCD ON 11/25/08
C------- INCORP OF STOKES WAVES
          if (iwave.eq.2) then
                  do 102 i=1,nfreq(IIII)
c
                        eta1=eta1+h(i,IIII)*dcos(wavek(i,IIII)*X1-
     +                        omega(i,IIII)*time)+
     +                        (h(i,IIII)**2)*wavek(i,IIII)*
     +                        (dcosh(wavek(i,IIII)*DEPTH)/
     +                        (8.D0*(dsinh(wavek(i,IIII)*DEPTH)**3)))*
     +                        (2.D0+dcosh(2.D0*wavek(i,IIII)*DEPTH))*
     +                        dcos(2.D0*(wavek(i,IIII)*X1-
     +                        omega(i,IIII)*time))
c
                        eta2=eta2+h(i,IIII)*dcos(wavek(i,IIII)*X2-
     +                        omega(i,IIII)*time)+
     +                        (h(i,IIII)**2)*wavek(i,IIII)*
     +                        (dcosh(wavek(i,IIII)*DEPTH)/
     +                        (8.D0*(dsinh(wavek(i,IIII)*DEPTH)**3)))*
     +                        (2.D0+dcosh(2.D0*wavek(i,IIII)*DEPTH))*
     +                        dcos(2.D0*(wavek(i,IIII)*X2-
     +                        omega(i,IIII)*time))

c
102               continue
            endif
c
c
C------- NOTE THAT H IS NOT DIVIDED BY 2 DUE TO COMMAND BELOW.
C------- end of UPDATES BY JCD ON 11/25/08
C------- INCORP OF STOKES WAVES
c
              surf1=depth+eta1/2.d0
              surf2=depth+eta2/2.d0
c
c
              if ((Y1.le.surf1).and.(Y2.le.surf2)) then
            iwet=3
              elseif ((Y1.gt.surf1).and.(Y2.gt.surf2)) then
            iwet=4
              elseif (Y1.le.surf1) then
            iwet=1
              elseif (Y2.le.surf2) then
            iwet=2
              endif
       END IF
c
       return
       end
```

MACRO - SURFELEV

```
C
C-----------------------------------------------------------------------
----
      DOUBLE PRECISION FUNCTION SURFELEV(XCoord,Time)
      IMPLICIT DOUBLE PRECISION(A-H,O-Z)
      COMMON /FDATA/ G,H(100,25),WAVEL(100,25),WAVEK(100,25),
     +               phi(100,25),OMEGA(100,25),FACTOR(100,25),
     +               DEPTH,VFXAVE(25),VFZAVE(25),CURPROFD(100,25),
     +               CURPROFX(100,25),CURPROFZ(100,25),
     +               CDN,CDT,CM,RHO,VIS,WAMP(25),NCURR(25),
     +               NFREQ(25),IWAVE,ITYPSW,ISUB,ISUBPR,IC
            SURFELEV=0.D0
C
C---- This applies the surface elevation of only the first profile to
C---- the model
            IF(IWAVE.EQ.1) THEN
            DO 101 I=1,NFREQ(1)
            SURFELEV=SURFELEV+H(I,1)*dcos(wavek(i,1)*
     1          XCOORD-omega(i,1)*time+phi(i,1))/2.D0
101       CONTINUE
        END IF


C------- start of UPDATES BY JCD ON 11/25/08
C------- INCORP OF STOKES WAVES
         if (IWAVE.EQ.2) THEN
            DO 102 I=1,NFREQ(1)
                  SURFELEV=SURFELEV+(h(i,1)*dcos(wavek(i,1)*
     +                XCOORD-omega(i,1)*time)/2.D0)+
     +                (h(i,1)**2)*wavek(i,1)*
     +                (dcosh(wavek(i,1)*depth)/
     +                (16.D0*(dsinh(wavek(i,1)*depth)**3)))*
     +                (2.D0+dcosh(2.D0*wavek(i,1)*depth))*
     +                dcos(2.D0*(wavek(i,1)*XCOORD-
     +                omega(i,1)*time))

102         CONTINUE
            END IF
C------- end of UPDATES BY JCD ON 11/25/08
C------- INCORP OF STOKES WAVES

      RETURN
      END
C
```

MACRO - AVCURR

```
C-----------------------------------------------------------------------
----
      SUBROUTINE
AVCURR(CentX,CentY,CentZ,Time,VFX,VFY,VFZ,AFX,AFY,AFZ,NUMB,
     + IX)
      IMPLICIT DOUBLE PRECISION(A-H,O-Z)
```

```
      COMMON /FDATA/ G,H(100,25),WAVEL(100,25),WAVEK(100,25),
     +               phi(100,25),OMEGA(100,25),FACTOR(100,25),
     +               DEPTH,VFXAVE(25),VFZAVE(25),CURPROFD(100,25),
     +               CURPROFX(100,25`),CURPROFZ(100,25),
     +               CDN,CDT,CM,RHO,VIS,WAMP(25),NCURR(25),
     +               NFREQ(25),IWAVE,ITYPSW,ISUB,ISUBPR,IC
      COMMON /CDATA/ NUMNP,NUMEL,NUMMAT,NEN,NEQ,IPR,
     1 NSDM,NQDM,NQUAD,NPRFL 6+
      COMMON /NUMWC/ NUMLOAD
      INTEGER IIII
      DIMENSION IX(4,1)
C
      NEN2 = NEN + 2
C---- The IX is a 4 x 1 array. The +1 is added because index from
python editor
C---- is from 0-9, not 1-10.
C
      IIII = IX(NEN2,1) + 1
      VFX=0.D0
      VFY=0.D0
      VFZ=0.D0
      AFX=0.D0
      AFY=0.D0
      AFZ=0.D0
      NC=NCURR(IIII)
      IF(NCURR(IIII).GT.1) THEN
            DO 101 I=1,NCURR(IIII)-1
                  IF (CURPROFD(I,IIII).LE.CentY) THEN
                        NC=I
                        GOTO 102
                  END IF
101         CONTINUE
102         VFX=CURPROFX(NC,IIII)
            VFZ=CURPROFZ(NC,IIII)
            IF(NC.GT.1) THEN
                  W1=(CentY-CURPROFD(NC-1,IIII))/(CURPROFD(NC,IIII)-
     +                  CURPROFD(NC-1,IIII))
                  W2=(CURPROFD(NC,IIII)-CentY)/(CURPROFD(NC,IIII)-
     +                  CURPROFD(NC-1,IIII))
                  VFX=CURPROFX(NC-1,IIII)*W1+CURPROFX(NC,IIII)*W2
                  VFZ=CURPROFZ(NC-1,IIII)*W1+CURPROFZ(NC,IIII)*W2
            END IF
      END IF
      IF(IWAVE.EQ.1) THEN
            DO 201 I=1,NFREQ(IIII)
            angle=wavek(i,IIII)*CentX-omega(i,IIII)*time+phi(i,IIII)
          VFX=vfx+factor(i,IIII)*dcosh(wavek(i,IIII)*CentY)*dcos(angle)
          VFY=vfy+factor(i,IIII)*dsinh(wavek(i,IIII)*CentY)*dsin(angle)
         AFX=afx+omega(i,IIII)*factor(i,IIII)*dcosh(wavek(i,IIII)*
     +     CentY)*dsin(angle)
         AFY=afy-omega(i,IIII)*factor(i,IIII)*dsinh(wavek(i,IIII)*
     +     CentY)*dcos(angle)
201         CONTINUE
      END IF


C------- start of UPDATES BY JCD ON 11/25/08
```

```
C------- INCORP OF STOKES WAVES
         if (IWAVE.EQ.2) THEN
            DO 202 I=1,NFREQ(IIII)
            angle=wavek(i,IIII)*CentX-omega(i,IIII)*time
c
c           WRITE(6,*) 'check to see what VFX is before vfx is calced'
c           WRITE(6,'(e20.5)') VFX

            VFX=vfx+(h(i,IIII)*g*wavek(i,IIII))/(2.D0*omega(i,IIII))*
     +             ((dcosh(wavek(i,IIII)*CentY))/
     +             (dcosh(wavek(i,IIII)*depth)))*dcos(angle)+
     +             (3.D0/16.D0)*h(i,IIII)*factor(i,IIII)*wavek(i,IIII)*
     +             dcosh(2.D0*wavek(i,IIII)*CentY)*dcos(2.D0*angle)
c
c           WRITE(6,*) 'check to see what VFY is before vfy is calced'
c           WRITE(6,'(e20.5)') VFY

            VFY=vfy+h(i,IIII)*g*wavek(i,IIII)/(2.D0*omega(i,IIII))*
     +             (dsinh(wavek(i,IIII)*CentY)/
     +             dcosh(wavek(i,IIII)*depth))*dsin(angle)+
     +             (3.D0/16.D0)*h(i,IIII)*factor(i,IIII)*wavek(i,IIII)*
     +             dsinh(2.D0*wavek(i,IIII)*CentY)*dsin(2.D0*angle)
c
c           WRITE(6,*) 'check to see what AFX is before afx is calced'
c           WRITE(6,'(e20.5)') AFX

            AFX=afx+(h(i,IIII)*g*wavek(i,IIII)/2.D0)*
     +             (dcosh(wavek(i,IIII)*CentY)/
     +             dcosh(wavek(i,IIII)*depth))*dsin(angle)-
     +             ((h(i,IIII)**2)*g*(wavek(i,IIII)**2)/4.D0)*
     +             (dsin(2.D0*angle)/
     +             dsinh(2.D0*wavek(i,IIII)*depth))+
     +
      (3.D0/8.D0)*h(i,IIII)*omega(i,IIII)*factor(i,IIII)*wavek(i,IIII)*
     +             dcosh(2.D0*wavek(i,IIII)*CentY)*dsin(2.D0*angle)
c
            AFY=afy+(-h(i,IIII)*g*wavek(i,IIII)/2.D0)*
     +             (dsinh(wavek(i,IIII)*CentY)/
     +             dcosh(wavek(i,IIII)*depth))*dcos(angle)+
     +             ((h(i,IIII)**2)*g*(wavek(i,IIII)**2)/4.D0)*
     +             (dsinh(2.D0*wavek(i,IIII)*CentY)/
     +             dsinh(2.D0*wavek(i,IIII)*depth))-
     +
      (3.D0/8.D0)*h(i,IIII)*omega(i,IIII)*factor(i,IIII)*wavek(i,IIII)*
     +             dsinh(2.D0*wavek(i,IIII)*CentY)*dcos(2.D0*angle)
c
c
202         CONTINUE
            END IF
c
C------- end of UPDATES BY JCD ON 11/25/08
C------- INCORP OF STOKES WAVES
c--------
      RETURN
      END
C
```

MACRO - UPDCD

```
C-----------------------------------------------------------------------
----
      SUBROUTINE UPDCD(REN,aCDN, aCDT, aCM)
      IMPLICIT DOUBLE PRECISION(A-H,O-Z)
      COMMON /FDATA/ G,H(100,25),WAVEL(100,25),WAVEK(100,25),
     +               phi(100,25),OMEGA(100,25),FACTOR(100,25),
     +               DEPTH,VFXAVE(25),VFZAVE(25),CURPROFD(100,25),
     +               CURPROFX(100,25),CURPROFZ(100,25),
     +               CDN,CDT,CM,RHO,VIS,WAMP(25),NCURR(25),
     +               NFREQ(25),IWAVE,ITYPSW,ISUB,ISUBPR,IC
C
        pi = 3.141592653589793d0


c     Code updated on 12/10/08 by JCD
c     update was to add critical Re values for truss element
c     data obtained via Hoerner. Takes effect at the critical
c     Reynolds number

        if (ic.eq.1) then
          if (ren.le.0.001d0) then
              cdn=2789.8d0
          elseif (ren.le.1.d0) then
              sfact=-0.077215665d0+dlog(8.d0/ren)
              cdn=8.d0*pi*(1.d0-0.87d0*sfact**(-2))/(ren*sfact)
          elseif ((ren.gt.1.d0).and.(ren.le.30.d0)) then
              cdn=1.45d0+8.55d0*ren**(-0.9d0)
          elseif ((ren.gt.30.d0).and.(ren.le.3.078d5)) then
              cdn=1.1d0+4.d0*ren**(-0.5d0)
c
            elseif ((ren.gt.3.078d5).and.(ren.le.3.632d5)) then
                  rena=3.078d5
                  renb=3.632d5
                  cdna=0.9717d0
                  cdnb=0.70694d0
                  call cintb(ren,rena,renb,cdna,cdnb,cdn)
c
            elseif ((ren.gt.3.632d5).and.(ren.le.3.939d5)) then
                  rena=3.632d5
                  renb=3.939d5
                  cdna=0.7069d0
                  cdnb=0.5412d0
                  call cintb(ren,rena,renb,cdna,cdnb,cdn)
c
            elseif ((ren.gt.3.939d5).and.(ren.le.4.363d5)) then
                  rena=3.939d5
                  renb=4.363d5
                  cdna=0.5412d0
                  cdnb=0.4142d0
                  call cintb(ren,rena,renb,cdna,cdnb,cdn)
c
            elseif ((ren.gt.4.363d5).and.(ren.le.4.444d5)) then
                  rena=4.363d5
                  renb=4.444d5
                  cdna=0.4142d0
```

```
            cdnb=0.3336d0
            call cintb(ren,rena,renb,cdna,cdnb,cdn)
c
      elseif ((ren.gt.4.444d5).and.(ren.le.4.920d5)) then
            rena=4.444d5
            renb=4.920d5
            cdna=0.3336d0
            cdnb=0.2429d0
            call cintb(ren,rena,renb,cdna,cdnb,cdn)
c
      elseif ((ren.gt.4.920d5).and.(ren.le.6.088d5)) then
            rena=4.920d5
            renb=6.088d5
            cdna=0.2429d0
            cdnb=0.2588d0
            call cintb(ren,rena,renb,cdna,cdnb,cdn)
c
      elseif ((ren.gt.6.088d5).and.(ren.le.7.536d5)) then
            rena=6.088d5
            renb=7.536d5
            cdna=0.2588d0
            cdnb=0.2804d0
            call cintb(ren,rena,renb,cdna,cdnb,cdn)
c
      elseif ((ren.gt.7.536d5).and.(ren.le.9.326d5)) then
            rena=7.536d5
            renb=9.326d5
            cdna=0.2804d0
            cdnb=0.2988d0
            call cintb(ren,rena,renb,cdna,cdnb,cdn)
c
      elseif ((ren.gt.9.326d5).and.(ren.le.1.154d6)) then
            rena=9.326d5
            renb=1.154d6
            cdna=0.2988d0
            cdnb=0.3185d0
            call cintb(ren,rena,renb,cdna,cdnb,cdn)
c
      elseif ((ren.gt.1.154d6).and.(ren.le.1.459d6)) then
            rena=1.154d6
            renb=1.459d6
            cdna=0.3185d0
            cdnb=0.3566d0
            call cintb(ren,rena,renb,cdna,cdnb,cdn)
c
      elseif ((ren.gt.1.459d6).and.(ren.le.1.846d6)) then
            rena=1.459d6
            renb=1.846d6
            cdna=0.3566d0
            cdnb=0.3994d0
            call cintb(ren,rena,renb,cdna,cdnb,cdn)
c
      elseif ((ren.gt.1.846d6).and.(ren.le.2.485d6)) then
            rena=1.846d6
            renb=2.485d6
            cdna=0.3994d0
            cdnb=0.4044d0
```

```
                  call cintb(ren,rena,renb,cdna,cdnb,cdn)
c
            elseif ((ren.gt.2.485d6).and.(ren.le.4.600d6)) then
                  rena=2.485d6
                  renb=4.600d6
                  cdna=0.4044d0
                  cdnb=0.4077d0
                  call cintb(ren,rena,renb,cdna,cdnb,cdn)
c
            elseif (ren.gt.4.600d6) then
                  cdn=0.4077d0
c
c
          endif
          CDT=pi*vis*(0.55d0*ren**0.5d0+0.084d0*ren**(2.d0/3.d0))
        ENDIF
          aCDN=CDN
          aCDT=CDT
          aCM=CM
      RETURN
      END
```